



HAL
open science

Spin injection into semiconductors and organic materials

Xue Gao

► **To cite this version:**

Xue Gao. Spin injection into semiconductors and organic materials. Physics [physics]. Université de Lorraine; Université de Technologie de Hefei (Anhui, Chine), 2019. English. NNT : 2019LORR0059 . tel-02328779

HAL Id: tel-02328779

<https://hal.univ-lorraine.fr/tel-02328779>

Submitted on 23 Oct 2019

HAL is a multi-disciplinary open access archive for the deposit and dissemination of scientific research documents, whether they are published or not. The documents may come from teaching and research institutions in France or abroad, or from public or private research centers.

L'archive ouverte pluridisciplinaire **HAL**, est destinée au dépôt et à la diffusion de documents scientifiques de niveau recherche, publiés ou non, émanant des établissements d'enseignement et de recherche français ou étrangers, des laboratoires publics ou privés.



AVERTISSEMENT

Ce document est le fruit d'un long travail approuvé par le jury de soutenance et mis à disposition de l'ensemble de la communauté universitaire élargie.

Il est soumis à la propriété intellectuelle de l'auteur. Ceci implique une obligation de citation et de référencement lors de l'utilisation de ce document.

D'autre part, toute contrefaçon, plagiat, reproduction illicite encourt une poursuite pénale.

Contact : ddoc-theses-contact@univ-lorraine.fr

LIENS

Code de la Propriété Intellectuelle. articles L 122. 4

Code de la Propriété Intellectuelle. articles L 335.2- L 335.10

http://www.cfcopies.com/V2/leg/leg_droi.php

<http://www.culture.gouv.fr/culture/infos-pratiques/droits/protection.htm>



UNIVERSITÉ
DE LORRAINE

C2MP



ijl
INSTITUT
JEAN LAMOUR



THÈSE

Pour l'obtention du titre de:

DOCTEUR de L'UNIVERSITÉ DE LORRAINE et

de L'UNIVERSITÉ DES SCIENCES ET TECHNOLOGIES DE CHINE

Spécialité: *Physique*

Présentée par:

Mme Xue GAO

Injection de spin dans les semi-conducteurs et les matériaux organiques

Thèse soutenue publiquement le 20 Juin 2019 à Nancy devant le jury composé de :

M. Zhongming Wei	Professeur, University of Chinese Academy of Sciences	<i>Rapporteur</i>
M. Philippe Schieffer	Professeur, Université de Rennes	<i>Rapporteur</i>
Mme. Bérangère Hyot	Ingénieur de Recherche, CEA-LETI	<i>Examinatrice</i>
M. Henri Jaffrès	Chargé de Recherche, Unité mixte de Physique CNRS Thalès	<i>Examinateur</i>
Mme. Chunping Jiang	Professeur, Suzhou Institute of Nano-Tech and Nano-Bionics, Chinese Academy of Sciences	<i>Examinatrice</i>
M. Jean-Marie George	Directeur de Recherche, Unité mixte de Physique CNRS Thalès	<i>Invité</i>
M. Yuan Lu	Chargé de Recherche, Université de Lorraine	<i>Directeur de thèse</i>
M. Mathieu Stoffel	Maitre de Conférences, Université de Lorraine	<i>Co-directeur de thèse</i>
M. Hui Yang	Professeur, Suzhou Institute of Nano-Tech and Nano-Bionics, Chinese Academy of Sciences	<i>Co-directeur de thèse</i>

Résumé élargi

Introduction générale:

La spintronique est un domaine multidisciplinaire émergent, qui considère le rôle joué par l'électron et le spin nucléaire dans la physique des solides. L'objectif principal de ces enquêtes est de développer des dispositifs qui tirent parti du spin au lieu ou en plus du degré de liberté de la charge. Cela pourrait conduire à de nouveaux dispositifs multifonctionnels offrant une non-volatilité, des vitesses de traitement plus élevées, des densités de garnissage plus élevées et une consommation d'énergie réduite. Les diodes électroluminescentes à spin et les lasers à polarisation de spin (laser à spin) constituent une classe importante de dispositifs spintroniques à semi-conducteurs. Dans ces dispositifs, des électrons (ou des trous) polarisés en spin sont injectés dans une région active où ils se recombinent de manière radicale avec des trous (ou des électrons) non polarisés pour émettre de la lumière polarisée de manière préférentielle droite ou gauche. Le lien direct entre l'injection de spin et l'émission de lumière polarisée de manière circulaire rend les sources de lumière à polarisation de spin particulièrement adaptées à de nombreuses applications. À un niveau très fondamental, les sources de lumière à spin polarisé permettent la détection directe des spins dans les hétérostructures semi-conductrices. De plus, les LED de spin codent les informations de spin des électrons en lumière polarisée de manière circulaire et montrent de fortes applications potentielles dans les technologies avancées des semi-conducteurs. On peut citer le transport optique d'informations, la cryptographie quantique, le commutateur optique en utilisant deux états de polarisation circulaire et des affichages

tridimensionnels. La lumière polarisée circulairement à gauche et à droite émise par la diode électroluminescente peut être commutée par inversion de spin, ce qui joue un rôle dans la vision binoculaire pour l'imagerie stéréoscopique par un système à obturateur optique avec lunettes à polariseur.

Très récemment, une EL à polarisation circulaire élevée a été rapportée pour un dispositif contenant une seule couche de points quantiques InAs/GaAs dopés p. L'injection de spin est réalisée à travers une électrode CoFeB. Cependant, ces travaux se sont principalement concentrés sur la polarisation de spin d'un point quantique unique, alors que le comportement de l'ensemble des points quantiques n'a pas été pris en compte. Dans cette thèse, nous avons étudié avec soin la lumière polarisée de manière circulaire provenant de l'ensemble des QD. L'effet du champ magnétique appliqué, du biais appliqué et de la température sur le degré de polarisation circulaire et l'intensité EL a été étudié et discuté à la lumière du concept de relaxation de spin compétitive et de taux de combinaison radiative des porteurs. En outre, nous avons également mis au point un injecteur de spin entièrement épitaxial en Co (0001)/MgO (111) avec anisotropie magnétique perpendiculaire sur des modèles de GaN. Des caractérisations structurales, des mesures de propriétés magnétiques et des calculs *ab initio* ont été effectués pour analyser les injecteurs de spin. Ci-après, nous avons également développé l'injecteur de spin Co (0001)/MgO (111) sur une structure de LED GaN de type n-i-p et avons étudié les propriétés d'électroluminescence résolues en polarisation.

Comparée à la spintronique inorganique, la spintronique organique est également très attrayante en raison de la longue durée de rotation des porteurs de charge ainsi que de leur coût relativement bas, de leur flexibilité et de leur diversité chimique. Le contrôle ferroélectrique de la polarisation de spin a été signalé pour la première fois dans des systèmes inorganiques. En 2010, en utilisant le BaTiO₃ (BTO) comme barrière ferroélectrique à effet tunnel dans la structure Fe/BaTiO₃ / La_{0.7}Sr_{0.3}MnO₃ (MFTJ), Garcia et al. ont été le premier groupe à démontrer une modulation de la

magnétorésistance de -17% à -3% lorsque la BTO était polarisée d'états «haut» à «bas». Bien que la modulation soit évidente, aucun changement de signe ne s'est produit dans leurs expériences. Le polyfluorure de vinylidène (PVDF), l'un des polymères ferroélectriques les plus typiques, est maintenant largement utilisé dans les systèmes et dispositifs électroniques modernes. La performance ferroélectrique dépend fortement de son contenu en phase β . Contrairement à l'oxyde de pérovskite, tel que BaTiO_3 , où le déplacement ionique produit une polarisation, l'ordre ferroélectrique du polymère de PVDF provient des dipôles permanents et la rotation coopérative à longue distance des chaînes moléculaires se produit via les interactions à courte portée de Van der Waals. De plus, le PVDF et les copolymères apparentés forment des couches ordonnées de haute qualité et présentent une ferroélectricité robuste jusqu'à l'épaisseur de la monocouche. La polarisation électrique du PVDF est comparable à celle des ferroélectriques à oxyde de pérovskite, ce qui les rend favorables pour une utilisation en tant que barrières dans les jonctions tunnel ferroélectriques (FTJ). Récemment, notre groupe a réalisé pour la première fois à titre expérimental des structures organiques MFTJ (OMFTJ) basées sur des structures $\text{La}_{0.6}\text{Sr}_{0.4}\text{MnO}_3/\text{PVDF}/\text{Co}$ en utilisant du PVDF comme barrière de tunnel. Dans ce travail, nous avons prouvé expérimentalement qu'un effet TMR de 8 à 15% combiné à un TER de 75% pouvait être mesuré à 10K dans les MFTJ organiques LSMO/PVDF/Co. L'oxyde ferroferrique de magnétite (Fe_3O_4) a récemment attiré l'attention du fait que le Fe_3O_4 en vrac présente une température de Curie élevée ($T_c \sim 850$ K) et une polarisation de spin presque complète à la température ambiante. Ces deux propriétés sont particulièrement intéressantes pour les applications dans les dispositifs magnétoélectroniques géants et à soupape de spin à base de films de magnétite. Dans certains travaux antérieurs, il a été prouvé que les nanoparticules sphériques de Fe_3O_4 sont d'excellentes charges pour les composites polymères à constante diélectrique élevée. Certains chercheurs ont également constaté une augmentation de la phase β du PVDF après l'ajout de nanoparticules de Fe_3O_4 . Nous avons fabriqué des OMFTJ à base de structures $\text{La}_{0.6}\text{Sr}_{0.4}\text{MnO}_3/\text{PVDF}:\text{Nanocomposites}/\text{Co}$. L'influence de Fe_3O_4 sur les propriétés de l'interface PVDF/Co a été étudiée.

Ce manuscrit est divisé en cinq chapitres.

Le premier chapitre est consacré à l'introduction des concepts physiques et aux connaissances de base nécessaires à l'analyse des résultats expérimentaux présentés aux chapitres 3, 4 et 5. Dans ce chapitre, l'effet de la magnétorésistance géante (GMR) considéré comme la naissance de la spintronique sera introduite en premier. Ensuite, nous présenterons quelques informations générales sur les jonctions tunnel magnétiques (MTJ). Enfin, nous présenterons quelques concepts de base en spintronique à base de semi-conducteurs.

Le chapitre 2 est consacré aux techniques expérimentales utilisées pour la réalisation de cette thèse de doctorat. La plupart des travaux présentés ici ont été réalisés à l'Institut Jean Lamour (IJL), Nancy, France. Des plaquettes de GaAs LED ont été fournies par l'Institut des semi-conducteurs (IOS), CAS, Beijing, Chine, développé par le professeur Bo Xu. Tous les modèles GaN utilisés dans cette thèse ont été développés par MOCVD de l'Institut des nanotechnologies et de la nano-bionique de Suzhou (SINANO) à Suzhou, en Chine, par le professeur Jianping Liu. Les structures de LED GaN ont été développées par le MOCVD de l'Université de Pékin, à Beijing, en Chine, fournies par le professeur Ning Tang.

Au chapitre 3, nous présenterons d'abord l'état de la technique en matière d'injection de spin dans des structures à base de GaAs. Ensuite, nous montrerons nos travaux très récents sur l'émission polarisée circulaire d'un ensemble de QD InAs/GaAs dopés p, qui présentent des propriétés intéressantes du point de vue du fonctionnement à faible courant injecté.

Au chapitre 4, nous allons d'abord présenter l'état de l'art de l'injection de spin dans les structures à base de GaN. Ensuite, nous montrerons comment développer un injecteur de spin Co/MgO présentant une propriété PMA. Enfin, quelques résultats préliminaires sur l'injection de spin dans les LED à base de GaN seront présentés.

Au chapitre 5, nous présenterons d'abord l'état de la recherche sur la spintronique organique. Ensuite, nous présenterons nos travaux récents sur LSMO/PVDF: Fe₃O₄/Co MFTJ.

Enfin, nous concluons nos travaux et présenterons quelques perspectives.

Chapitre 1: De la spintronique à base de métal à à base de semi-conducteur

Le premier chapitre est consacré à l'introduction des concepts physiques et aux connaissances de base nécessaires à l'analyse des résultats expérimentaux présentés aux chapitres 3, 4 et 5. Nous avons brièvement passé en revue quelques concepts de base de la spintronique à base de métal et de la spintronique à semi-conducteur. De grands progrès ont été accomplis dans le domaine de la spintronique des semi-conducteurs depuis la découverte de l'effet GMR, illustré à la Figure R1.1. La découverte de GMR est considérée comme le début de la nouvelle électronique à base de spin, ce qui signifie littéralement l'intégration du degré de liberté de spin dans l'électronique traditionnelle. L'injection efficace de spin dans un dispositif à semi-conducteurs, ainsi que la manipulation et la détection ultérieures de la polarisation de spin injectée, sont essentielles au développement de dispositifs de spintronique à semi-conducteurs avancés. Les expériences pionnières ont montré différentes possibilités d'étudier l'injection de spin et la détection dans les semi-conducteurs, ce qui sera utile pour comprendre les études suivantes sur l'injection et la détection de spin dans les LED de spin à base de GaAs et de GaN dans cette thèse, illustrés à la Figure R1.2-R1.7.

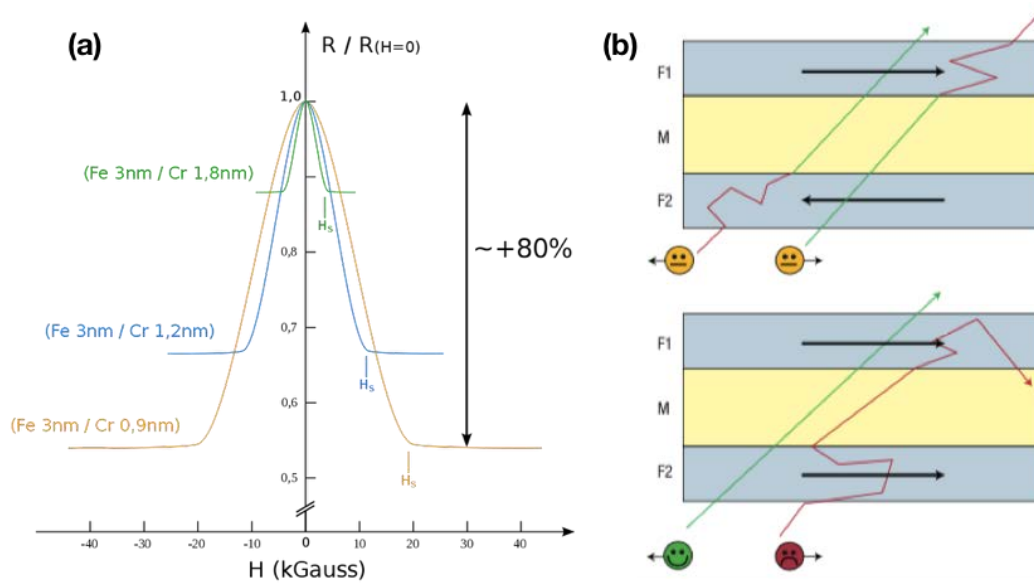


Figure R1.1: (a) Résultats fondateurs d'Albert Fert et Peter Grunberg (1988): variation de la résistance des super-réseaux Fe/Cr à 4,2 K dans le champ magnétique externe H . La flèche à droite indique la variation maximale de la résistance. H_s est le champ de saturation. (b) Schéma des processus de diffusion intervenant dans la pile de couches F1/M/F2. Le film à trois couches est constitué de deux couches ferromagnétiques identiques F1 et F2 prenant en sandwich une couche d'espacement en métal non magnétique M, le courant circulant dans le plan. Dans la configuration parallèle (schéma inférieur), les électrons de spin-up (spin parallèle à l'aimantation) peuvent traverser le sandwich presque sans dispersion, fournissant ainsi un raccourci de conductivité et une faible résistance. Au contraire, dans le cas antiparallèle (schéma du haut), les électrons de spin-up et de spin-down subissent des collisions soit en F1 soit en F2, donnant lieu à une résistance globale plus élevée.

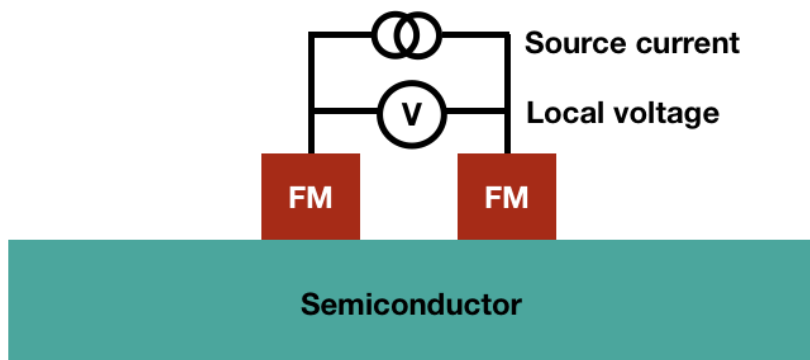


Figure R1.2: Schéma de mesure de la géométrie locale.

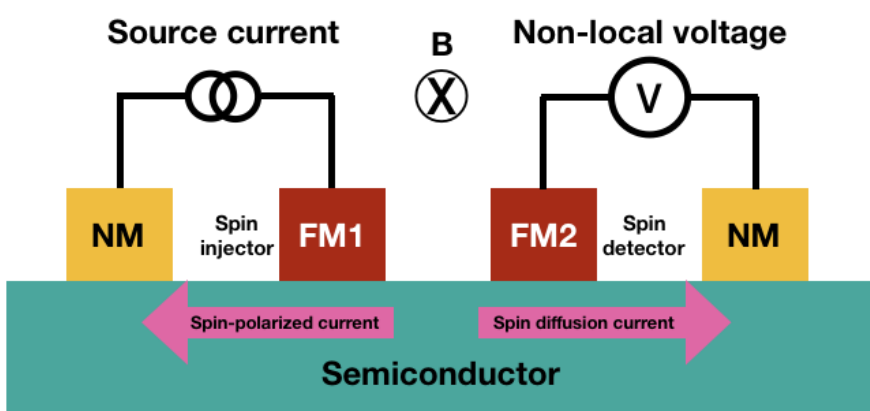


Figure R1.3: Diagramme schématique de la mesure de géométrie non locale.

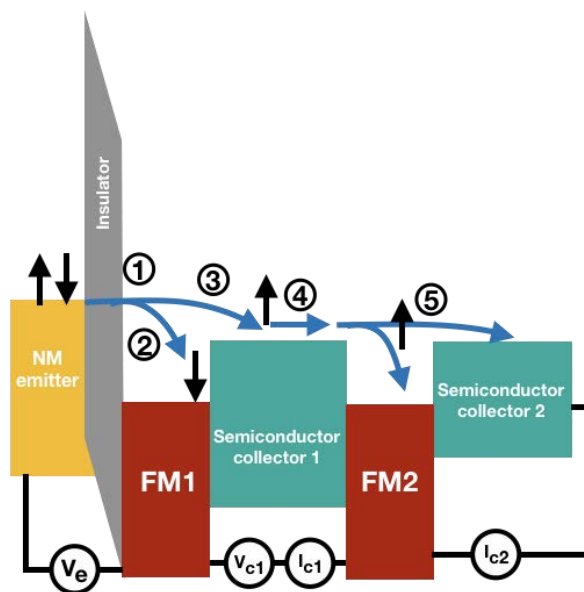


Figure R1.4: Schéma d'une jonction tunnel utilisée comme source d'injection balistique

d'électrons chauds dans une bande semi-conductrice. À une tension d'émetteur constante (V_e), le «premier courant de collecteur» (I_{c1}) au contact FM1 et le «deuxième courant de collecteur» (I_{c2}) au contact avec le substrat sont mesurés sous polarisation de tension optionnelle (V_{c1}) dans la région de dérive de semi-conducteur.

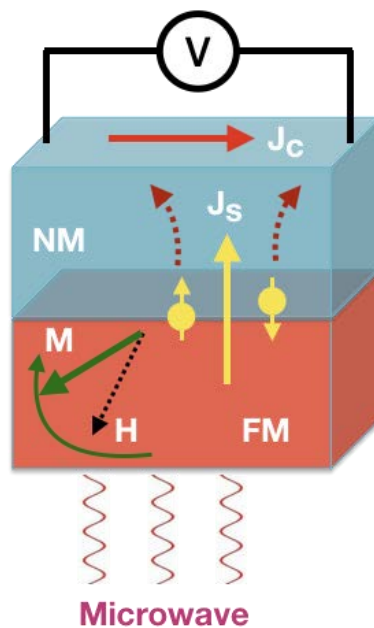


Figure R1.5: Représentation schématique du mécanisme de pompage de spin. Un courant de spin pur est injecté dans le matériau non magnétique par résonance ferromagnétique induite de la couche FM. Le courant de spin pur injecté est détecté en tant que tension de spin sur les bords de l'échantillon à l'aide de l'effet Hall à spin inverse (ISHE).

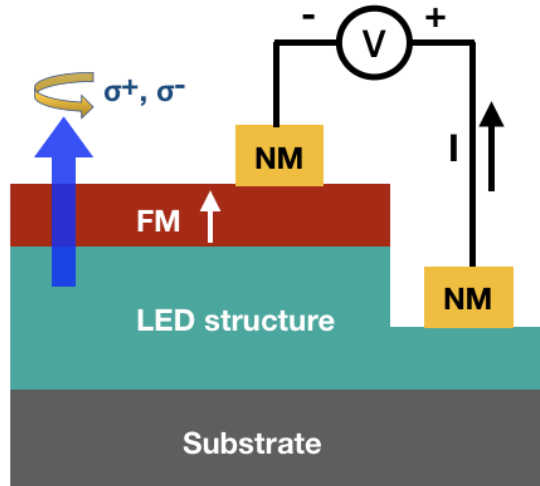


Figure R1.6: Schéma de principe de la LED de spin pour l'injection de spin électrique et la détection optique.

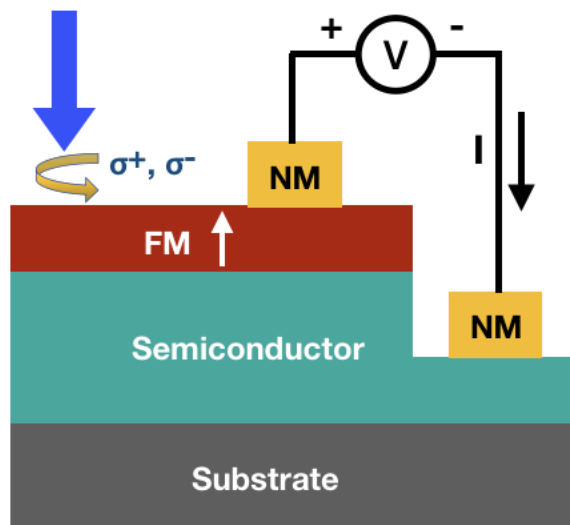


Figure R1.7: Schéma de la structure semi-conductrice utilisée pour l'injection de spin optique et la détection électrique.

Chapitre 2: Techniques expérimentales

Le chapitre 2 est consacré aux techniques expérimentales utilisées pour la réalisation de cette thèse de doctorat. La plupart des travaux présentés ici ont été réalisés

Résumé élargi

à l'Institut Jean Lamour (IJL), Nancy, France. Des plaquettes de GaAs LED ont été fournies par l'Institut des semi-conducteurs (IOS), CAS, Beijing, Chine, développé par le professeur Bo Xu. Tous les modèles GaN utilisés dans cette thèse ont été développés par MOCVD de l'Institut des nanotechnologies et de la nano-bionique de Suzhou (SINANO) à Suzhou, en Chine, par le professeur Jianping Liu. Les structures de LED GaN ont été développées par le MOCVD de l'Université de Pékin, à Beijing, en Chine, fournies par le professeur Ning Tang. Dans cette thèse, un système MECA 2000 MBE tel qu'illustré à la Figure R2.1 a été utilisé pour la fabrication de tous les échantillons. Un schéma du système MBE est présenté à la Figure R2.2.



Figure R2.1: Photo du système MECA 2000 MBE.

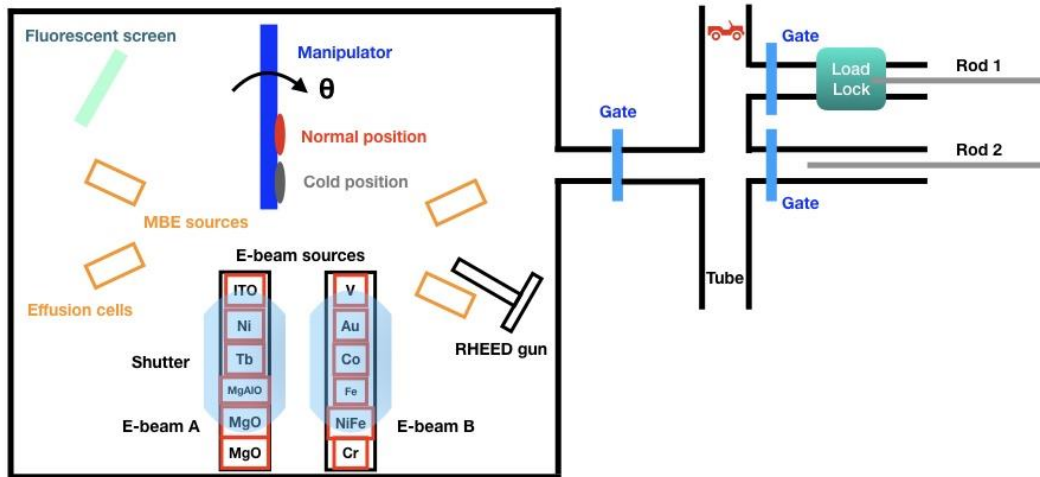


Figure 2.2: Vue de dessus du système MECA 2000 MBE connecté au tube.

Chapitre 3: LED Spin à base de GaAs

Au chapitre 3, nous avons d'abord présenté le concept de spin LED et ses applications potentielles. Nous avons ensuite passé en revue l'état de l'art des LED de spin à base de structures GaAs, qui contient des travaux de recherche sur les injecteurs de spin plans et hors-plan. En outre, nous avons également présenté nos travaux de recherche précédents sur l'injecteur de spin CoFeB/MgO PMA. Nous avons ensuite présenté nos travaux très récents sur l'électrolinescence résolue en polarisation à partir d'un ensemble de QD InAs/GaAs dopés p, qui présente des propriétés intéressantes du point de vue du fonctionnement à faible courant d'injection. La structure des couches complètes et les concentrations de dopage sont indiquées à la Figure R3.1. Nous avons constaté que PC atteint une valeur aussi élevée que 18% sous zéro champ magnétique appliqué à 10K, comme le montre la Figure R3.2. Une corrélation claire a été établie entre le degré de polarisation circulaire de la lumière émise et l'aimantation perpendiculaire de la couche d'injecteur. Une forte dépendance à la tension de polarisation a révélé un PC maximum à une polarisation optimale de 2,5 V (6 μ A) à 10K. De plus, la température de fonctionnement montre un effet important sur le PC avec un comportement différent à certaines valeurs de température. Le comportement

du PC présente des changements remarquables avant et après 60-80K. Les mesures de dépendance de courant effectuées aux valeurs de température 10K, 60K et 100K montrent une légère dépendance du PC sur le courant injecté à 60K par rapport à la forte dépendance entre les deux autres températures. L'interprétation de la dépendance du PC en fonction de la polarisation et de la température a été examinée à la lumière de la compétition entre le temps de relaxation de spin τ_s et le taux de recombinaison de la porteuse de charge. On pense que ces résultats peuvent aider à mieux comprendre le comportement collectif d'un ensemble de QD InAs/GaAs dopés par p dans différentes conditions de fonctionnement.

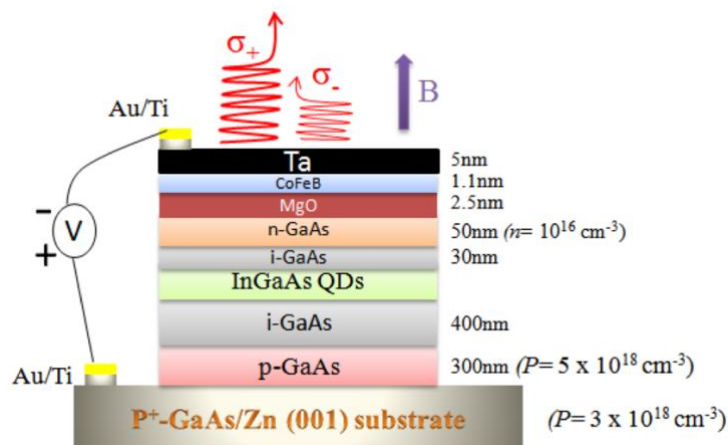


Figure R3.1: Schéma représentant la structure en couches de la LED à spin.

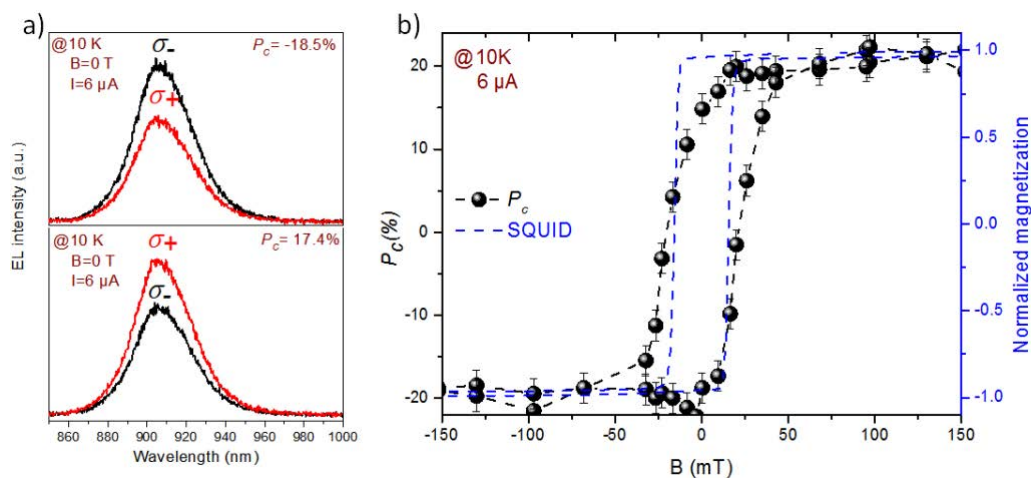


Figure R3.2: (a) Spectres EL avec composantes résolues en polarisation (σ^+ et σ^-) mesurés à 10K et à un champ magnétique appliqué nul, après la pré-saturation de négatif à zéro (panneau du haut) et de positif à zéro (en bas). (b) Degré de polarisation circulaire du EL en fonction du champ magnétique balayé du sens négatif au sens positif et inversement.

Chapitre 4: Vers des LED Spin à base de GaN

Au chapitre 4, nous avons examiné les recherches précédentes concernant l'injection de spin dans des matériaux à base de GaN. Le GaN est un semi-conducteur à large bande interdite ($\sim 3,4$ eV) qui devrait être un bon candidat pour les applications de spintronique, car il présente une faible interaction spin-orbite (≈ 15 meV) et un long temps de relaxation de spin (environ 20 ns). à $T = 5$ K et quelques centaines de nanosecondes à la température ambiante (RT)). Ces derniers sont deux ordres de grandeur plus grands que les durées de vie des spires en GaAs (environ 500 ps). C'est un avantage important du GaN car les dispositifs spintroniques nécessitent généralement un temps de cohérence de spin long. Plus récemment, des résultats de LED à spin visibles et de lasers à spin à base de GaN ont également été rapportés. Cependant, tous les résultats sont obtenus sous un certain champ magnétique, ce qui est loin d'une application réaliste. Pour les applications, il est nécessaire de réaliser des LED de spin capables de fonctionner sans champ magnétique appliqué et à température ambiante. Par conséquent, des efforts importants ont été consacrés d'abord à la réalisation d'un injecteur à spin perpendiculaire sur un gabarit en GaN. Nous avons comparé les injecteurs de spin Fe/MgO et Co/MgO. Nous démontrons une forte PMA en examinant un injecteur de spin épitaxial Co (0001)/MgO (111) sur un modèle GaN. La Figure R4.1 montre un schéma de la structure de la couche et des motifs RHEED pendant la croissance d'un injecteur de spin. Des caractérisations structurales et des mesures magnétiques ont été effectuées. La Figure R4.2 montre les propriétés magnétiques de l'injecteur de spin Co/MgO. En outre, les calculs ab initio ont également

montré que l'interface Co/MgO présente une anisotropie magnétique importante, montré à la Figure R4.3. Nous avons ensuite développé un injecteur de spin Co (0001)/MgO (111) sur une structure de LED GaN de type n-i-p. Cependant, aucune polarisation de spin n'a pu être détectée dans les mesures EL résolues en polarisation. Cela pourrait être dû à la formation d'une couche d'oxyde formée à l'interface Co/MgO ou à une structure non optimisée de LED GaN. Bien qu'aucune émission de lumière à polarisation circulaire ne puisse être détectée, nous suggérons d'utiliser la technique de collage de tranche pour réaliser une structure n-i-p à partir d'une structure normale p-i-n.

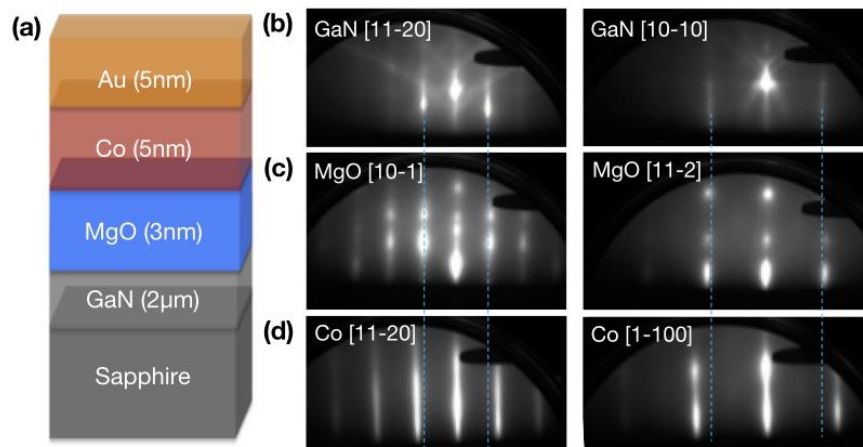


Figure R4.1: (a) Schéma de la pile multicouche. Modèles RHEED pris à 30 kV le long des azimuts [11-20] et [10-10] de (b) la surface de GaN (0001) avant dépôt, (c) après dépôt de 3 nm MgO et (d) film ultérieur de 5 nm Co suivi d'un recuit à 250 °C pendant 20 minutes.

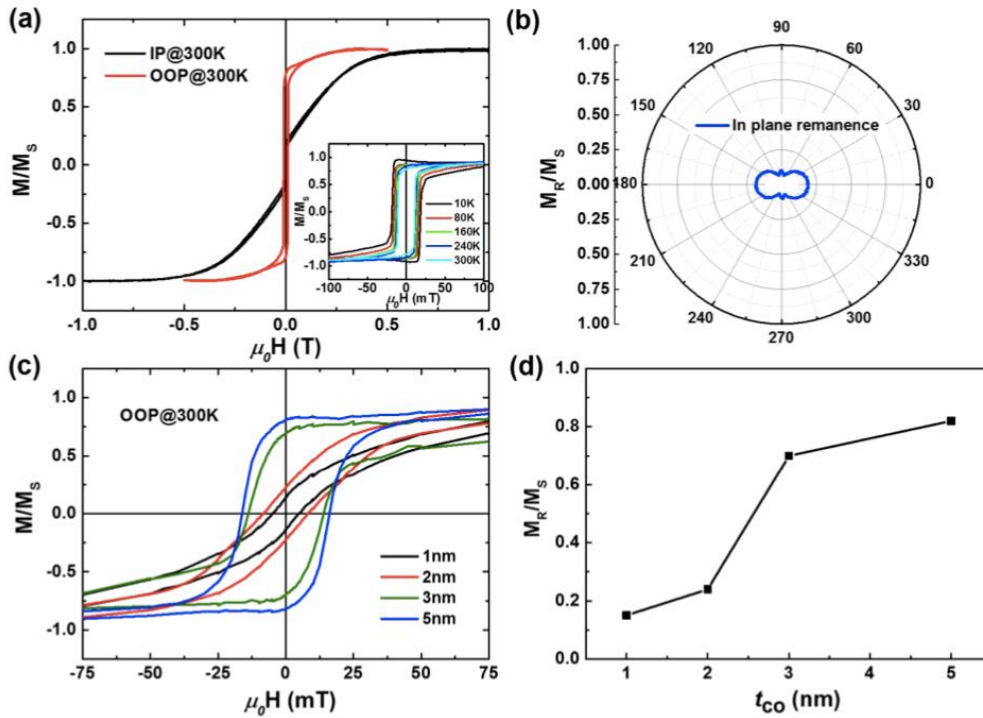
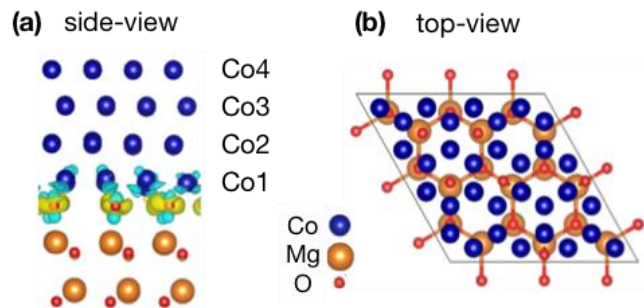


Figure R4.2: (a) Courbes M-H mesurées à la température ambiante par SQUID pour une structure de Co (4,6 nm)/MgO/GaN avec des champs magnétiques appliqués dans le plan (IP) et hors du plan (OOP). Encadré: courbes M-H à différentes températures avec champ OOP. (b) Magnétisation résiduelle dans le plan normalisée en fonction de l'angle dans le plan avec le champ magnétique. (c) Courbes M-H hors du plan de la RT pour Co/MgO/GaN avec différentes épaisseurs de Co. (d) Aimantation rémanente perpendiculaire normalisée en fonction de différentes épaisseurs de Co.



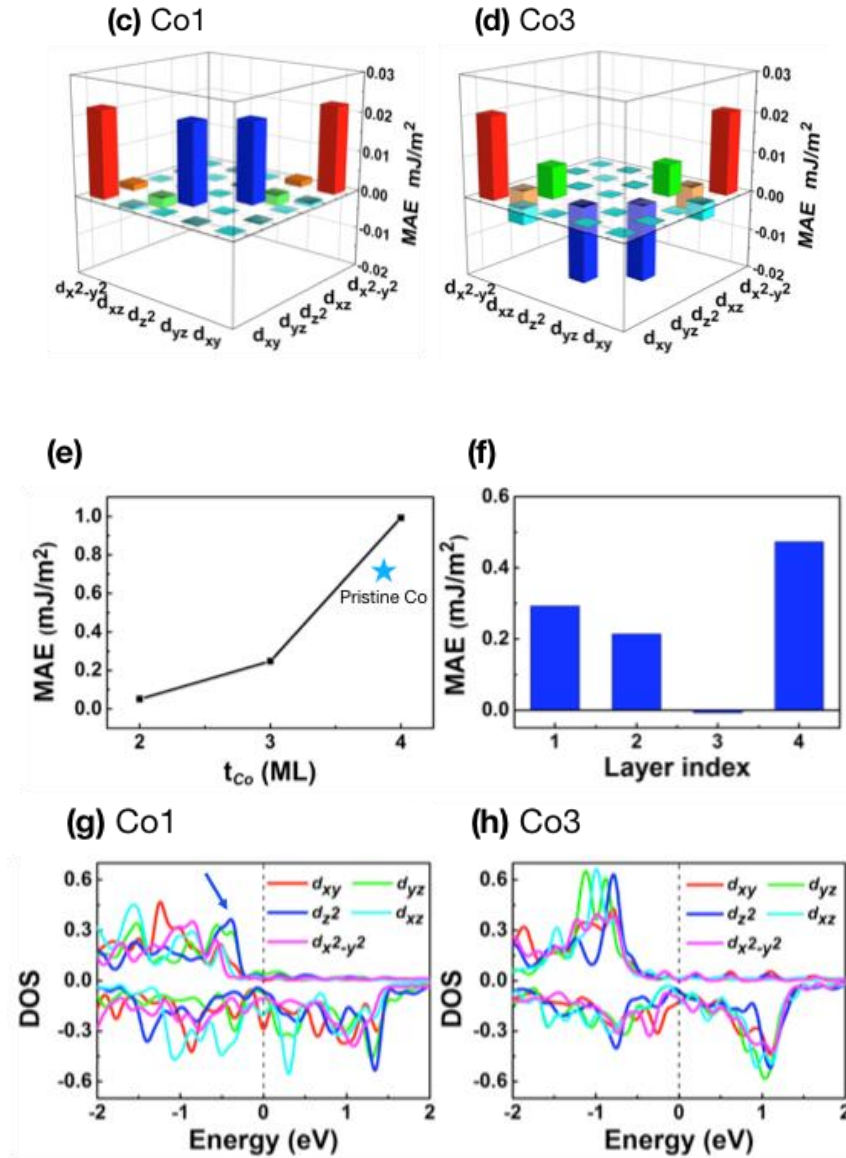


Figure R4.3: (a) Vue latérale de la structure calculée de Co (4ML)/MgO (111). À l'interface Co/MgO, les couleurs jaune et bleu ciel correspondent respectivement aux régions d'accumulation et d'épuisement des charges. (b) Vue de dessus de Co sur la surface de MgO (111). MAE à résolution orbitale de la structure sélectionnée (c) Co1 et (d) Co3 dans la structure Co (4ML)/MgO. (e) MAE calculé en fonction de l'épaisseur de Co. (f) MAE résolue en couche d'hétérostructure Co (4ML)/MgO. Densité projetée d'états des atomes sélectionnés (g) Co1 et (h) Co3 à la structure Co (4ML)/MgO.

Chapitre 5: Contrôle ferroélectrique de la polarisation de

spin dans des jonctions tunnel multiferroïques organiques

Dans ce chapitre, nous avons d'abord passé en revue l'état actuel des recherches sur MFTJ. Nous avons ensuite présenté les résultats obtenus sur des jonctions tunnel multiferroïques utilisant du PVDF dopé avec des nanoparticules de Fe_3O_4 comme barrière, ce qui a démontré des fonctionnalités nouvelles et importantes sur le plan technologique. La Figure R5.1 montre la structure des chaînes de carbone du PVDF avec différentes polarisations. La structure du dispositif LSMO/ PVDF: Fe_3O_4 /Co, fabriqué à IJL, est schématisée à la Figure R5.2. La Figure R5.3 montre la réponse magnéto (résistance par rapport au champ magnétique) du MFTJ LSMO/PVDF: Fe_3O_4 /Co pour deux polarisations ferroélectriques différentes (polarisées à +2,4 et -3,2V, respectivement). En effet, on peut clairement remarquer qu'avec une même tension de polarisation appliquée (10 mV), un TMR positif de + 9,21% ou un TMR négatif de -7% peut être obtenu lorsque le PVDF est polarisé à l'état "bas" ou à la "hausse" état, respectivement. De manière remarquable, le signe TMR peut même être inversé pour un très petit biais appliqué de 100 mV dans l'état initial. Après avoir été polarisée, la TMR la plus grande peut même atteindre -50%, mais des valeurs parfois inférieures telles que -5 à -6% sont obtenues. Ce comportement aléatoire pourrait être lié à l'état de magnétisation de Fe_3O_4 influencé par l'état de polarisation du PVDF. La TMR positive n'est presque pas influencée. La Figure R5.4 montre les boucles TMR et la résistance parallèle en fonction de la tension de polarisation. Le signe de la TMR dépend étroitement de l'état ferroélectrique du PVDF. Une TMR positive est associée à l'état de haute résistance, tandis que la TMR négative est liée à l'état de basse résistance. Entre les deux états de polarisation stables, on observe un régime intermédiaire avec une TMR accordable entre 0 et 4 V. En dopant avec des nanoparticules de Fe_3O_4 , les propriétés ferroélectriques du MFTJ sont améliorées et présentent des valeurs de TER plus élevées, pouvant encore atteindre 100% à température ambiante. La polarisation de spin de la surface de spin organique/ferromagnétique peut non seulement être manipulée par la polarisation ferroélectrique de la barrière organique, mais peut

également être influencée par le dopage avec des nanoparticules magnétiques. Cela pourrait ouvrir de nouvelles fonctionnalités pour contrôler l'injection de polarisation de spin via des barrières organiques ferroélectriques dopées avec des nanoparticules magnétiques.

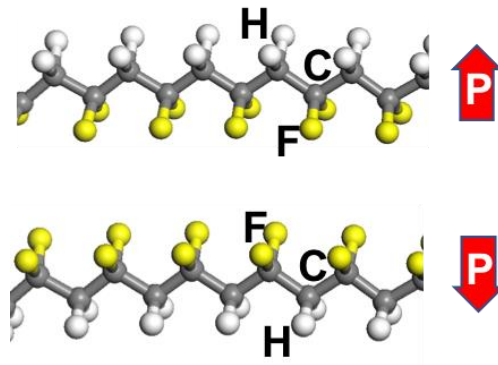


Figure R5.1: Schémas de structure de PVDF avec différentes directions de polarisation ferroélectriques.

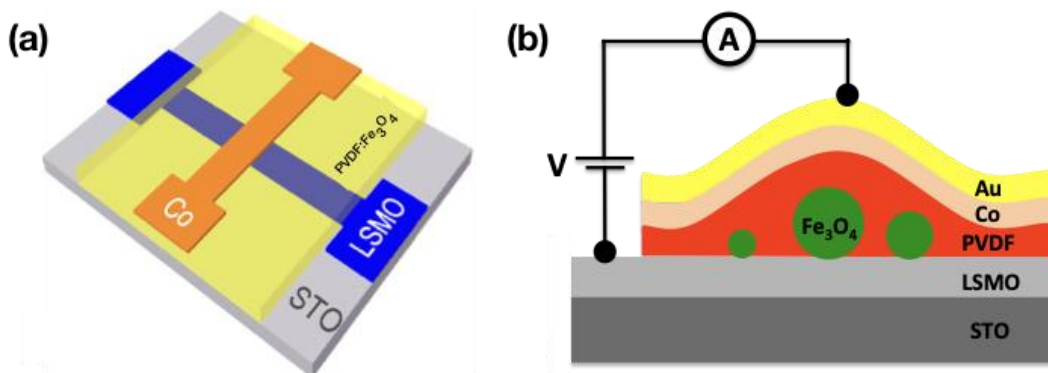


Figure R5.2: (a) Schémas du dispositif LSMO/PVDF:Fe₃O₄/Co. (b) Vue de côté du dispositif LSMO/PVDF:Fe₃O₄/Co.

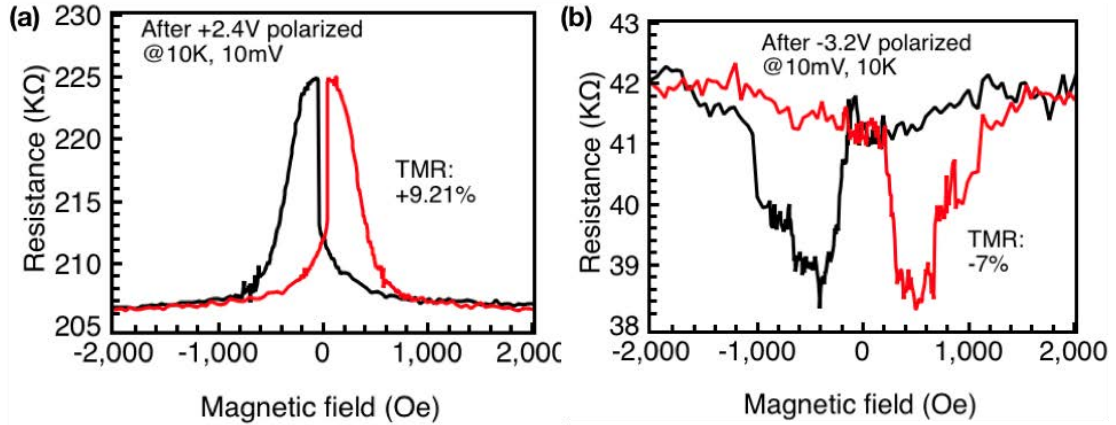


Figure R5.3: Magnétorésistance à effet tunnel mesurée sous 10 mV à 10 K après la tension de polarisation électrique de +2,4 V (a) et -3,2 V (b), respectivement.

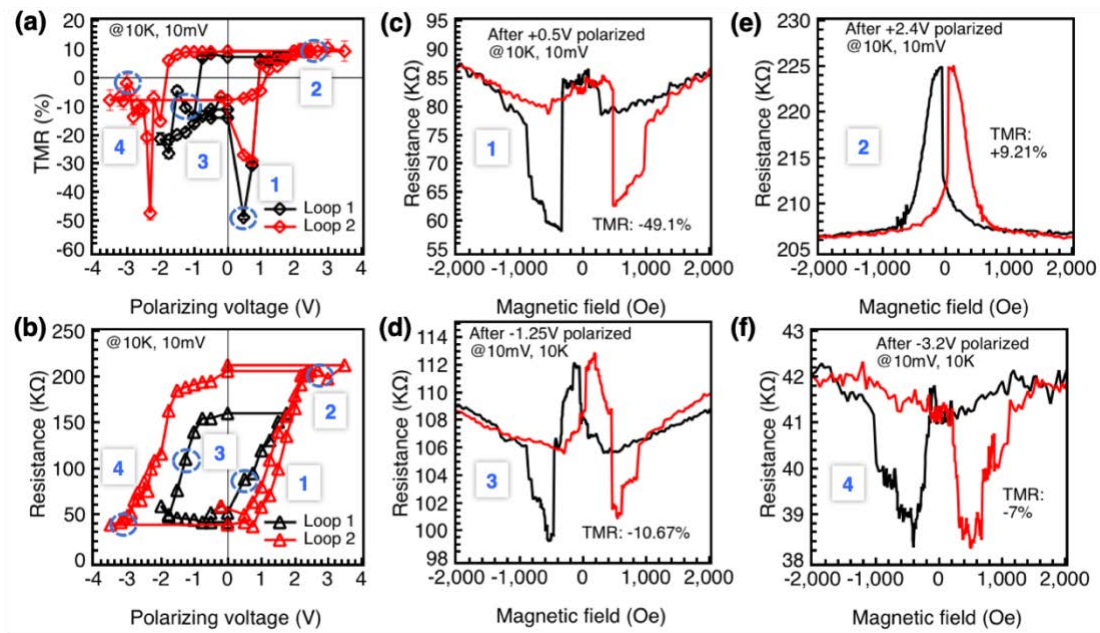


Figure R5.4: Mesures de magnéto-transport effectuées sur des dispositifs LSMO/PVDF: Fe₃O₄/Co. (a) Boucles TMR en fonction de la tension de polarisation. (b) Boucles de résistance parallèles en fonction de la tension de polarisation. (c-f) Magnétorésistance à effet tunnel mesurée sous 10 mV à 10 K pour des tensions de polarisation respectives de +0,5 V, -1,25 V, +2,4 V et -3,2 V, correspondant aux valeurs 1 à 4 indiquées en (a) et (b).

Summary and perspectives:

Nous avons signalé l'émission de lumière polarisée de manière circulaire à partir d'un ensemble de points quantiques InAs / GaAs dopés p incorporés dans une spin-LED à base de GaAs. On constate que le degré de polarisation circulaire PC peut atteindre des valeurs allant jusqu'à 18% sans champ magnétique appliqué extérieur. La corrélation entre le degré de polarisation de la lumière émise et l'aimantation perpendiculaire de la couche d'injection a été établie. Une forte dépendance à la tension de polarisation a révélé un PC maximum à une polarisation optimale de 2,5 V (correspondant à un courant injecté de 6 μ A) à 10K. De plus, la température de mesure montre un fort effet sur PC avec différents comportements à certaines valeurs de température. Des changements remarquables ont été observés avant et après 60-80K. Les mesures de dépendance de courant effectuées à 10K, 60K et 100K ont montré une légère dépendance du PC sur le courant injecté à 60K par rapport à une forte dépendance pour les deux autres températures. L'interprétation de la dépendance du PC en fonction de la polarisation et de la température a été examinée à la lumière de la concurrence entre la durée de vie du spin τ_s et la durée de vie des porteurs de charge τ_r . On pense que ces résultats peuvent aider à une meilleure compréhension du comportement collectif d'un ensemble de QD InAs / GaAs dopés par p.

Deuxièmement, nous avons étudié l'injection de spin dans une LED à base de GaN. En raison de sa faible interaction spin-orbite, de son grand fossé énergétique et de son long temps de relaxation du spin, le GaN est devenu un matériau prometteur pour la spintronique. Très récemment, des résultats de LED à spin visibles et de lasers à spin à base de GaN ont également été rapportés. Cependant, tous les résultats ont été obtenus sous un champ magnétique externe, ce qui est loin d'une application réaliste. En effet, il est nécessaire de réaliser des LED de spin pouvant fonctionner sans champ magnétique et à température ambiante. Par conséquent, des efforts importants ont tout d'abord été consacrés à la réalisation d'un injecteur de spin perpendiculaire sur GaN.

Les injecteurs de spin Fe/MgO et Co/MgO ont été étudiés pour leur possible utilisation en tant qu'injecteurs de spin pour les dispositifs spintroniques à base de GaN. Tout d'abord, des expériences d'optimisation de la croissance des couches de MgO ont été réalisées à différentes températures de croissance sur des matrices de GaN, à l'aide d'analyses RHEED in situ et de mesures AFM ex situ. Nous avons ensuite comparé les injecteurs de spin Fe/MgO et Co/MgO. Nous avons démontré la présence d'un fort PMA pour l'injecteur de spin épitaxial de Co (0001)/MgO (111) développé sur un modèle GaN avec une relation d'orientation cristalline Co (0001) [11-20] // MgO (111) [10-1] // GaN (0002) [11-20]. HRTEM et HR-STEM associés à EELS ont été utilisés pour étudier la structure et la chimie interfaciales. Même après un recuit à 600 ° C, une interface MgO / GaN nette et nette a été trouvée, alors qu'il existait une couche en alliage $Mg_xCo_yO_z$ d'une épaisseur de 2 à 3 ML à l'interface MgO/Co. On constate qu'une Co sur MgO/GaN d'une épaisseur de 4,6 nm présente encore une grande anisotropie magnétique perpendiculaire. Les calculs ab initio sur la structure Co (4ML)/MgO montrent que la surface de MgO (111) peut fortement augmenter la valeur de PMA de 40% par rapport au film vierge de Co hcp de 4ML d'épaisseur. Notre analyse d'anisotropie résolue par couches et par hybridation orbitale a également permis de valider l'origine de l'amélioration du PMA, qui est due à l'hybridation interfaciale d'orbitales 3d O 2p et Co à l'interface Co/MgO. Nous avons ensuite développé l'injecteur de spin Co (0001)/MgO (111) sur une structure à LED GaN de type n-i-p, puis fabriqué des dispositifs à LED de spin GaN. Cependant, aucune émission de lumière polarisée de manière circulaire n'a été détectée dans les mesures EL préliminaires résolues en polarisation. Cela pourrait être dû à la formation d'une couche d'oxyde à l'interface Co/MgO ou à une structure non optimisée de LED GaN.

La dernière partie très importante concerne la spintronique organique. Des résultats concernant les MFTJ basés sur différentes barrières ont été présentés, lesquels ont démontré des fonctionnalités nouvelles et importantes sur le plan technologique. Pour une barrière à base de PVDF: Fe_3O_4 , le signe TMR peut être inversé selon un très faible biais de 100 mV dans l'état initial. Après avoir été polarisée, la TMR la plus

grande peut même atteindre -50%, mais des valeurs inférieures proches de -5 et -6% ont parfois été obtenues. Ce comportement aléatoire pourrait être lié à l'état de magnétisation des nanoparticules de Fe_3O_4 influencées par la polarisation du PVDF. La RTM positive n'a presque pas été influencée. En dopant avec des nanoparticules de Fe_3O_4 , les propriétés ferroélectriques de MFTJ ont été améliorées avec des valeurs de TER plus élevées, pouvant atteindre 100% à température ambiante. Tous ces résultats ont montré que la polarisation de spin de l'interface organique/ferromagnétique peut être manipulée non seulement par la polarisation ferroélectrique de la barrière organique, mais également par dopage avec des nanoparticules magnétiques. Cela pourrait également ouvrir de nouvelles fonctionnalités pour contrôler l'injection de porteurs polarisés en spin via la polarisation ferroélectrique de la barrière de tunneling en spintronique semi-conductrice.

Nous présentons ici quelques perspectives. Pour les LED de spin à base de GaAs, nous allons essayer de déterminer expérimentalement les temps de relaxation de spin en utilisant une mesure EL résolue en temps. Pour étudier plus avant l'injection de spin dans les LED à base de GaN, nous allons essayer de fabriquer une structure n-i-p inverse différente à partir d'une structure p-i-n normale en utilisant la technique de collage de tranche récemment développée. De plus, nous allons également essayer de fabriquer des injecteurs de spin avec des matériaux bidimensionnels comme barrages à effet tunnel, tels que le BN ou le mica. Pour l'étude de la spintronique organique, des calculs ab-initio basés sur la théorie de la densité fonctionnelle seront utilisés pour étudier plus en détail les propriétés des dispositifs MFTJ avec différentes barrières. De plus, nous tenterons également d'obtenir une distribution plus homogène des nanoparticules de Fe_3O_4 .

Abstract

Spintronics with semiconductors is very attractive as it can combine the potential of semiconductors with the potential of the magnetic materials. GaN has a long spin relaxation time, which could be of potential interest for spintronics applications. Organic spintronics is also very appealing because of the long spin lifetime of charge carriers in addition to their relatively low cost, flexibility, and chemical diversity. In this thesis, we investigate spin injection in spin LEDs containing either InAs/GaAs quantum dots or InGaN/GaN quantum wells. Moreover, we further study spin polarized transport in organic multiferroic tunnel junctions (OMFTJs).

Firstly, we will show that the circular polarization of the light emitted by a LED containing a single layer of p-doped InAs/GaAs quantum dots (QDs) can reach about 18% under zero applied magnetic field. A clear correlation is established between the polarization degree of the emitted light and the perpendicular magnetization of the injector layer. The polarization reaches a maximum for an applied bias of 2.5V at 10K, which corresponds to an injected current of 6 μ A. Also, we report a remarkable behavior of the polarization in the temperature region 60-80K. The interpretation of the bias and temperature dependence of the polarization is discussed in light of the competition between radiative recombination time τ_r and the spin relaxation time τ_s .

In addition, significant efforts have been devoted to developing a perpendicular spin injector on GaN based materials to achieve spin injection without applying a magnetic field. Firstly, the growth of MgO has been investigated at various growth temperatures. Then, we studied the growth of either Fe or Co on MgO/GaN. In contrast to Fe/MgO, the Co/MgO spin injector yields a clear perpendicular magnetic anisotropy. In addition, ab-initio calculations have been performed to understand the origin of the perpendicular magnetic anisotropy at the Co/MgO(111) interface.

Finally, we investigate multiferroic tunnel junctions (MFTJs) based on organic PVDF barriers doped with Fe₃O₄ nano particles. The organic MFTJs have recently attracted much attention since they can combine advantages of spintronics, organic and ferroelectric electronics. We report on the successful fabrication of La_{0.6}Sr_{0.4}MnO₃/PVDF:Fe₃O₄/Co OMFTJ, where the poly(vinylidene fluoride) (PVDF)

Abstract

organic barrier has been doped with ferromagnetic Fe₃O₄ nanoparticles. By changing the polarization of the ferroelectric PVDF, the tunneling process in OMFTJ can be switched either through the LSMO/PVDF/Co part (positive polarization) or through the Fe₃O₄/PVDF/Co part (negative polarization). This corresponds to a reversal of tunneling magnetoresistance (TMR) from +10% to -50%, respectively. Our study shows that the doping of OMFTJs with magnetic nanoparticles can create new functionalities of organic spintronic devices by the interplay of nanoparticle magnetism with the ferroelectricity of the organic barrier.

Key words: GaN, Co/MgO spin injector, GaN based spin LED, PVDF: Fe₃O₄ based OMFTJ

Résumé

La spintronique utilisant des matériaux semi-conducteurs est un sujet de recherche très actif. Elle permet de combiner le potentiel des semi-conducteurs avec le potentiel des matériaux magnétiques. Le GaN pourrait être un bon candidat pour des applications en spintronique car le temps de relaxation de spin est très long. La spintronique organique est également un domaine de recherche en plein essor en raison de la longue durée de vie de spin des porteurs de charge ainsi que de leur coût relativement bas, de leur flexibilité et de leur diversité chimique.

Dans un premier temps, nous montrerons que la polarisation circulaire de la lumière émise par une LED contenant une couche unique de points quantiques InAs / GaAs (QD) InAs / GaAs dopés p peut atteindre environ 18% sans champ magnétique extérieur. Une corrélation claire est établie entre le degré de polarisation de la lumière émise et l'aimantation perpendiculaire de l'injecteur. La polarisation atteint un maximum pour une polarisation appliquée de 2.5 V à 10 K, ce qui correspond à un courant injecté de 6 μ A. En outre, nous observons un comportement remarquable de la polarisation pour une température comprise entre 60K et 80K. L'évolution de la polarisation en fonction de la température est discutée à la lumière de la compétition entre le temps de vie de recombinaison radiative τ_r et le temps de relaxation de spin τ_s .

De plus, nous avons développé un injecteur de spin présentant une anisotropie magnétique perpendiculaire sur GaN. Nous avons d'abord optimisé la croissance de MgO pour différentes températures du substrat. Nous avons ensuite étudié la croissance de Fe puis de Co sur MgO/GaN. L'injecteur de spin Co(0001)/MgO(111) a été retenu car celui-ci permet d'obtenir une anisotropie magnétique perpendiculaire. De plus, les calculs ab initio ont également montré que l'interface Co/MgO(111) présente une grande anisotropie magnétique.

Finalement, nous étudions les MFTJ basés sur une barrière de PVDF organique dopée avec des nano-particules de Fe₃O₄. Nous avons fabriqué avec succès une multicouche de La_{0.6}Sr_{0.4}MnO₃/PVDF:Fe₃O₄/Co, dans laquelle la barrière organique en

Résumé

poly (fluorure de vinylidène) (PVDF) a été dopée avec des nanoparticules ferromagnétiques de Fe_3O_4 . En modifiant la polarisation du PVDF, l'effet tunnel dans la jonction multiferroïque peut être commuté via la partie LSMO/PVDF/Co (polarisation positive) ou via la partie Fe_3O_4 /PVDF/Co (polarisation négative). Cela correspond à une inversion de la magnéto-résistance à effet tunnel (TMR) de + 10% à - 50%, respectivement. Notre étude montre que les jonctions tunnel multiferroïques organiques dopées avec des particules magnétiques pourraient créer de nouvelles fonctionnalités en jouant sur l'interaction du magnétisme des nanoparticules avec la ferroélectricité de la barrière organique.

Mots clés: GaN, l'injecteur de spin Co/MgO, LED à base de GaN, OMFTJ basés sur PVDF: Fe_3O_4

Table of contents

Abstract	I
Résumé	III
List of Acronyms	IX
Remerciements.....	XI
General introduction	1
Chapter 1 From metal-based to semiconductor-based spintronics.....	5
1.1 Spintronics with metals.....	5
1.1.1 Giant Magneto Resistance (GMR)	6
1.1.2 Magnetic Tunnel Junctions (MTJs).....	8
1.2 Spintronics with semiconductors	13
1.2.1 The impedance mismatch problem	15
1.2.1.1 Spin accumulation at the FM/NM interface	15
1.2.1.2 Impedance mismatch at the FM/SC interface.....	18
1.2.1.3 The Fert-Jaffrès Model	18
1.2.1.4 Spin injection through a tunnel-barrier	20
1.2.2 Spin injection and detection in semiconductors.....	21
1.2.2.1 All-electrical spin injection and detection	21
1.2.2.1.1 Local geometry.....	21
1.2.2.1.2 Non-local geometry	22
1.2.2.1.3 Hot electron spin injection	25
1.2.2.1.4 Spin pumping injection and ISHE detection	29
1.2.2.2 Electrical spin injection and optical detection.....	32
1.2.2.3 Optical spin injection and electrical detection.....	35
1.3 Summary	37
Chapter 2 Experimental techniques	39
2.1 Molecular beam epitaxy (MBE) growth and in-situ monitoring.....	39
2.1.1 MBE growth.....	39
2.1.2 In-situ monitoring by RHEED	42
2.2 Characterizations of full films.....	46
2.2.1 Transmission Electron Microscopy (TEM).....	47
2.2.2 Atomic Force Microscopy (AFM) and Piezoresponse Force Microscopy (PFM)	48
2.2.3 Vibrating Sample Magnetometry (VSM) and Superconducting QUantum Interference Device (SQUID).....	50
2.3 Device Processing and characterizations	53
2.3.1 Device fabrication.....	53
2.3.1.1 Sample preparation.....	53
2.3.1.2 Photo-lithography	53
2.3.1.3 Ion beam etching (IBE).....	55
2.3.2 Device characterizations	55
2.3.2.1 Electroluminescence (EL) set-up.....	55
2.3.2.2 Magneto-resistance measurement.....	57
Chapter 3 GaAs based Spin LED.....	59

Table of contents

3.1 Spin LED device.....	59
3.1.1 Spin-LED concept and optical selection rules	59
3.1.2 Potential applications of spin-LEDs.....	62
3.2 GaAs based spin LEDs: a review.....	64
3.2.1 In-plane spin injector.....	64
3.2.2 Out-of-plane spin injector	66
3.2.3 CoFeB/MgO spin injector exhibiting PMA on a GaAs LED	67
3.3 Spin injection in a GaAs based spin LED containing a single layer of InAs quantum dots	75
3.3.1 Sample preparation	75
3.3.2 Magnetic field dependence	76
3.3.3 Bias dependence	78
3.3.4 Temperature dependence.....	80
3.4 Summary.....	83
Chapter 4 Towards GaN based Spin LEDs.....	85
4.1 GaN based spin LEDs: state of the art.....	85
4.1.1 Advantage of GaN spin LEDs for applications.....	85
4.1.2 State-of-the-art	86
4.1.2.1 Spin injection into a p-top layer GaN based LED	86
4.1.2.2 Spin injection into GaN by combining a ferromagnetic contact with Fe ₃ O ₄ nanoparticles.....	88
4.1.2.3 Spin injection into n-top GaN based LED and LD by using a FeCo/MgO top contact	92
4.1.3 Limitation of the published work	95
4.2 Development of a spin injector with PMA on GaN.....	96
4.2.1 Motivation.....	96
4.2.2 Characterization of the GaN template	97
4.2.3 Growth of a MgO layer on the GaN template	99
4.2.4 Growth of the Fe/MgO spin injector	101
4.2.5 Development of Co/MgO spin injector with PMA on GaN.....	104
4.2.5.1 Growth of the Co/MgO spin injector.....	104
4.2.5.2 Structural and chemical characterizations of the Co/MgO spin injector.....	105
4.2.5.3 Magnetic properties of the Co/MgO spin injector	111
4.2.5.4 Ab-initio calculations of Co/MgO spin injector	112
4.2.5.5 Discussion.....	115
4.2.5.6 Conclusions.....	116
4.3 Spin injection into a GaN based LED.....	117
4.3.1 The GaN n-i-p inversed structure	117
4.3.2 GaN spin LED device processing and I-V characterization	119
4.3.3 Preliminary polarization resolved EL measurements	121
4.4 Summary	124
Chapter 5 Ferroelectric control of spin polarization in organic multiferroic tunnel junctions	127
5.1 Introduction.....	128
5.1.1 Principle of multiferroic tunnel junctions (MFTJ).....	128
5.1.2 Ferroelectric control of spin polarization.....	129
5.1.3 Organic multiferroic tunnel junctions (OMFTJ).....	130

Table of contents

5.2 MFTJ with PVDF: Fe ₃ O ₄ as barrier.....	135
5.2.1 Motivation of the work.....	135
5.2.2 Device fabrication.....	136
5.2.3 Morphological characterization.....	137
5.2.4 Ferroelectric characterization.....	138
5.2.5 Magnetic characterization.....	139
5.2.6 Magneto-transport characterization.....	141
5.2.6.1 I-V characterization.....	141
5.2.6.2 Ferroelectric control of spin polarization.....	142
5.2.6.3 Bias dependence.....	143
5.2.6.4 Polarization voltage dependence.....	144
5.2.6.5 Temperature dependence.....	146
5.2.7 Discussion.....	147
5.3 Summary.....	148
Summary and perspectives.....	149
Bibliography.....	153

List of Acronyms

A:

- AFM: Atomic Force Microscopy

B:

C:

- CIP: Current in plane
- CPP: Current perpendicular to plane

D:

- DMS: Diluted magnetic semiconductor
- DOS: Density of states
- DMF: Dimethylformamide

E:

- EL: Electroluminescence

F:

- FMR: Ferromagnetic resonance
- FTJ: Ferroelectric tunnel junction

G:

- GMR: Giant Magneto Resistance

H:

I:

- ISHE: Inverse spin hall effect
- IPA: Isopropanol
- IBE: Ion beam etching

J:

K:

L:

- LED: Light emitting diode
- LD: Laser diode

M:

- MTJ: Magnetic Tunnel Junction
- MBE: Molecular beam epitaxy
- MOCVD: Metal-organic chemical vapor deposition
- MRAM: Magnetic random-access memory

List of Acronyms

- MFTJ: Multiferroic tunnel junction

N:

O:

- OMFTJ: Organic multiferroic tunnel junction

P:

- PFM: Piezoresponse force microscopy
- PMA: Perpendicular magnetic anisotropy
- PPMS: Physical property measurement system
- PVDF: Poly (vinylidene fluoride)

Q:

- QW: Quantum well
- QD: Quantum dot

R:

- RHEED: Reflection high-energy electron diffraction

S:

- SDL: Spin diffusion length
- SC: Semiconductor
- STM: Scanning tunneling microscope
- SQUID: Superconducting quantum interference device
- SIMS: Secondary ion mass spectroscopy

T:

- TMR: Tunneling magnetoresistance
- TEM: Transmission electron microscopy
- TER: Tunneling electroresistance

U:

- UHV: Ultra-high vacuum

V:

- VSM: Vibrating-sample magnetometer

W:

X:

Y:

Z

Remerciements

Time flies. It's almost been six years since I started my study after graduating from undergraduate student. This thesis would not have been possible without the help and encouragement of many people. I would like to express deep gratitude to many people who have contributed to the completion of my PhD research.

First and foremost, I must thank my Chinese supervisor Prof. Hui Yang who is really an expert in semiconductor field providing me the opportunity to start a PhD research at SINANO. His continuous support during the entire PhD study, his patience and enthusiasm in semiconductor research, and detailed discussions with students have deeply impressed me. Besides, he also gave me a chance of studying in France as a co-mentorship's student. My deepest gratitude is extended to my French supervisor Prof. Yuan Lu who is a specialist of MBE and the field of semiconductor spintronics. When I arrived at IJL, he even taught me personally how to manipulate MBE and passed on his rich experiences to me. Besides academic research, he also helped me with everything that needs French: apartment, insurance etc. Without his help, I could not accustom myself in Nancy so quickly. I acknowledge my Chinese co-supervisor Prof. Jianping Liu who offered me GaN templates and my French co-supervisor Prof. Mathieu Stoffel giving me a big hand during the double-degree application. All of them spent a lot of precious time discussing with me about my thesis.

Special thanks belong to Prof. Shiheng Liang who showed me a lot of experiments at the very beginning of my study in France. His knowledge and experience are invaluable resource to assist me finish my PhD research. I'm grateful for Crosby Soon Chang's help during magnetic properties' measurements. Thanks to Danielle Pierre for the help on the manipulation of load lock connected to vacuum tube in CC-Daum. I would like to thank my engineer Gwladys Lengaine who had an excellent training for me about the different facilities in the clean room. Apart from this, she also helped me a lot in the process of GaN spin LEDs and MTJs. Thanks to Laurent Badie for solving the problems that I encountered when cutting samples and doing wire-bonding.

Remerciements

Stéphane Suire is always helpful when people are dealing with the problems of magnetic measurements.

I further want to thank Prof. Anthony Ferri and Prof. Rachel Desfeux working in Artois University who offered me assistance in PFM characterization. Even more, I am grateful to Prof. Bérangère Hyot for the aid in TEM characterization. Many thanks to Prof. Pierre Renucci who works in Toulouse University and helped me perform EL measurement of GaN spin LED.

I would like to thank Prof. Sunan Ding working at NANO-X, SINANO who helped me a lot during my CSC application. I need to thank Prof. Stéphane Mangin, Prof. Hervé Rinnert, Prof. Xavier Devaux, Prof. Chunping Jiang, Prof. Zhongming Zeng who have contributed a lot of meaningful discussions to my research results. Many thanks to all the people who work in nanofabrication Facility and Platform for characterizations at SINANO and helped me before. Thanks to all the staff working at students' affair office at SINANO.

Many thanks and best wishes to all my colleagues of Nanoscience group at IJL and GaN based laser group at SINANO. Your support and companionship made my PhD life at SINANO and IJL much more colorful. I'm very lucky that I met so many nice professors, researchers and friends during my PhD study. It's so fantastic that I can learn science, knowledge, life and whatever from each of you.

Last and not least, I would like to thank and dedicate this thesis to my family, especially to my grandparents and parents who trust me, care about me and encourage me all the time. I'm very lucky that I can study in Nancy and I really cherished and enjoyed my life here. The period of pursuing PhD degree will make a difference to the rest of my life.

Xue GAO

April 2019, Nancy, France

General introduction

Spintronics is an emerging multi-disciplinary field, which considers the role played by the electron and the nuclear spin in solid-state physics.¹ The leading goal of these investigations is to develop devices that take advantage of spin instead of, or in addition to, the charge degree of freedom. This could lead towards new multifunctional devices offering non-volatility, higher processing speeds, higher packing densities and reduced power consumption. Spin light emitting diodes (spin-LEDs) and spin-polarized lasers (spin-laser)² are an important class of semiconductor spintronic devices. In these devices, spin-polarized electrons (or holes) are injected into an active region where they recombine radiatively with unpolarized holes (or electrons) to emit preferentially right- or left- circularly polarized light. The direct link between spin injection and emission of circularly polarized light makes spin-polarized light sources particularly suited for many applications. At a very fundamental level, spin-polarized light sources allow for the straightforward detection of spins in semiconductor heterostructures. In addition, spin-LEDs encode the electron spin information into circularly polarized light and show strong potential applications in advanced semiconductor technologies. One can cite the optical transport of information³, quantum cryptography⁴, optical switch by using two circular polarization states² and three-dimensional displays.⁵ Left- and right- circularly polarized light emitted from the light-emitting diode can be switched by spin reversal, which plays a role in binocular vision for stereoscopic imaging by an optical shutter system with polarizer eyewear.

Very recently, highly circularly polarized EL was reported for a device containing a single layer of p-doped InAs/GaAs quantum dots. The spin injection is achieved through a CoFeB electrode. However, this work concentrated mainly on the spin polarization from a single quantum dot, while little attention was paid to the quantum dot ensemble behavior. In this thesis, we investigated carefully the circularly polarized light originating from the ensemble of QDs. The effect of the applied magnetic field, applied bias, and temperature on the circular polarization degree and EL intensity were studied and discussed in light of the concept of competitive spin relaxation and radiative combination rates of the carriers. In addition, we have also developed a fully epitaxial Co (0001)/MgO (111) spin injector with perpendicular magnetic anisotropy on GaN templates. Structural characterizations, magnetic properties measurements and ab-initio calculations have been done for analyzing spin injectors. Hereafter, we also grew the Co (0001)/MgO (111) spin injector on a n-i-p type GaN LED structure and studied polarization-resolved electroluminescence properties.

Compared to inorganic spintronics, organic spintronics is also very appealing because of the long spin lifetime of charge carriers in addition to their relatively low cost, flexibility, and chemical diversity.^{6, 7, 8} The ferroelectric control of spin polarization has been firstly reported in inorganic systems. In 2010, by employing BaTiO₃ (BTO) as ferroelectric tunneling barrier in Fe/BaTiO₃/ La_{0.7}Sr_{0.3}MnO₃ multiferroic tunnel junctions (MFTJ) structure, Garcia *et al.* were the first group to demonstrate a modulation of magnetoresistance from -17% to -3% when BTO was polarized from “up” to “down” states.⁹ Although the modulation was evident, no sign change happened in their experiments. As one of the most typical ferroelectric polymers, poly (vinylidene fluoride) (PVDF) is now widely used in modern electronic systems and devices. The ferroelectric performance relies heavily on its β phase content.¹⁰ Unlike perovskite oxide such as BaTiO₃ where ionic displacement produces polarization, the ferroelectric order of PVDF polymer originates from the permanent dipoles and the cooperative long-range rotation of the molecular chains occurs via the short-range Van der Waals interactions.¹¹ Moreover, PVDF and related copolymers, form high quality ordered layers¹² and exhibit robust ferroelectricity down to the

monolayer thickness.¹³ The electric polarization of PVDF is comparable to that of perovskite oxide ferroelectrics¹⁴, making them favorable for use as barriers in ferroelectric tunnel junctions (FTJs).^{15,16} Recently, our group have for the first time experimentally realized organic MFTJ (OMFTJ) based on $\text{La}_{0.6}\text{Sr}_{0.4}\text{MnO}_3/\text{PVDF}/\text{Co}$ structures by employing PVDF as tunneling barrier.¹⁷ In this work, we have experimentally proved that a TMR effect of 8 to 15% combined with a TER of 75% can be measured at 10K in the organic LSMO/PVDF/Co MFTJs. Magnetite ferroferric oxide (Fe_3O_4) has recently attracted attention because bulk Fe_3O_4 has a high Curie temperature ($T_c \sim 850\text{K}$) and nearly full spin polarization at room temperature. Both properties are of particular interest for applications in giant magneto-electronic and spin-valve devices based on magnetite films.¹⁸ In some previous works, it was proved that the Fe_3O_4 spherical nanoparticles are excellent fillers for high-dielectric-constant polymer composites.^{19,20,21} Some researchers also found an increase in the β phase of PVDF after the addition of Fe_3O_4 nanoparticles.^{22,23,24,25} We have fabricated OMFTJs based on $\text{La}_{0.6}\text{Sr}_{0.4}\text{MnO}_3/\text{PVDF}:\text{Fe}_3\text{O}_4$ nanocomposites/Co structures. The influence of Fe_3O_4 on the properties of the PVDF/Co spinterface was studied.

This manuscript is divided into six chapters.

The first chapter is dedicated to the introduction of the physical concepts and to the background knowledge required for the analysis of the experimental results shown in chapter 3, 4 and 5. In this chapter, the Giant Magneto Resistance (GMR) effect that was considered as the birth of spintronics will be introduced firstly. Then we will present some background about magnetic tunnel junctions (MTJs). At last, we will introduce some basic concepts in semiconductor-based spintronics.

The chapter 2 is dedicated to the experimental techniques used for the realization of this doctoral thesis. Most of the work presented here was done at Institut Jean Lamour (IJL), Nancy, France. GaAs LED wafers were provided by Institute of Semiconductor (IOS), CAS, Beijing, China, grown by Prof. Bo Xu. All the GaN templates used in this thesis were grown by MOCVD at Suzhou Institute of Nano-Tech and Nano-Bionics (SINANO), Suzhou, China, grown by Prof. Jianping Liu. The GaN

LED structures were grown by MOCVD at Peking University, Beijing, China, provided by Prof. Ning Tang.

In chapter 3, we will firstly introduce the state-of-the-art of spin injection into GaAs based structures. Then we will show our very recent work about the circular polarized emission from an ensemble of p-doped InAs/GaAs QDs, which exhibit interesting properties from the low injected current operation point of view.

In chapter 4, we will firstly introduce the state-of-the-art of spin injection into GaN based structures. Then we will show how to develop a Co/MgO spin injector exhibiting PMA property. At last, some preliminary results about spin injection into GaN based LEDs will be presented.

In chapter 5, we will firstly introduce the research state of organic spintronics. Then we will present our recent work on LSMO/PVDF: Fe₃O₄/Co MFTJ.

Finally, we will conclude our work and present some perspectives.

Chapter 1 From metal-based to semiconductor-based spintronics

Spintronics describes a paradigm where the information is carried by the electron spin instead of the charge like in mainstream electronics. This offer opportunities for a new generation of devices combining standard microelectronics with spin-dependent effects arising from the interaction between the electrons spin and the magnetic properties of the material.

In this chapter, the information is presented with respect of the scientific background of the experimental results described later. Firstly, the Giant Magneto Resistance (GMR) effect that was considered as the birth of spintronics will be introduced. Then we will present some background about magnetic tunnel junctions (MTJs). Finally, we will introduce some basic concepts in semiconductor-based spintronics.

1.1 Spintronics with metals

In conventional electronics, passive and active devices use and/or manipulate the charge of the electrons and ignore the existence of the spin of the electron. However, since the pioneering work of Mott in 1930,²⁶ it is known that in magnetic materials the scattering probability of electrons is spin-dependent. This effect has been theoretically and experimentally studied in 1970s. It was found that in ferromagnetic 3d metals, the

conduction can be understood using a two-current model. The conductance of the majority spin channel and of the minority spin channel can be different by more than a factor of ten.²⁷

1.1.1 Giant Magneto Resistance (GMR)

By associating nanometer thick Fe magnetic thin films with antiferromagnetic Cr thin films in multilayer structures grown by MBE, P. Grünberg *et al.*²⁸ and A. Fert *et al.*²⁹ discovered the Giant Magneto Resistance (GMR) effect in 1988, which is shown in Figure 1.1 (a). The discovery of GMR is considered as the beginning of the new, spin-based electronics, which literally means the integration of the spin degree of freedom into traditional electronics. The role of the spin of the electrons has then become a field of high interest for fundamental research as well as for the development of new electronic devices. The combination used of both the charge and the spin of the electrons provided new phenomena, new capabilities and functionalities.³⁰ The Nobel Prize in Physics 2007 was awarded jointly to Albert Fert and Peter Grünberg for the discovery of Giant Magnetoresistance. GMR-based computer hard disk drives became the norm within a few years, dramatically increasing storage density and speed.

The GMR effect has been explained on the basis of the two-current model developed in 1970 and on the fact that the spin of the electron is conserved when it propagates through the non-magnetic layer. The spin-polarized electrons in each channel will experience different scattering potentials in the different magnetic states. As depicted in Figure 1.1(b), in antiparallel (AP) configuration, both spin-up and spin-down electrons undergo collisions in one F layer or the other while in the case of parallel configuration, the spin-up electrons can travel through the spacer layer nearly unscattered, providing a conductivity shortcut and a low resistance. It turns out that changing the configuration of the magnetic layers changes the measured electrical resistance. The magnetoresistance ratio reached 100% in the first publication³¹ while the value of the anisotropic magnetoresistance did not exceed a few percent. For this reason, the effect was described as “giant”.

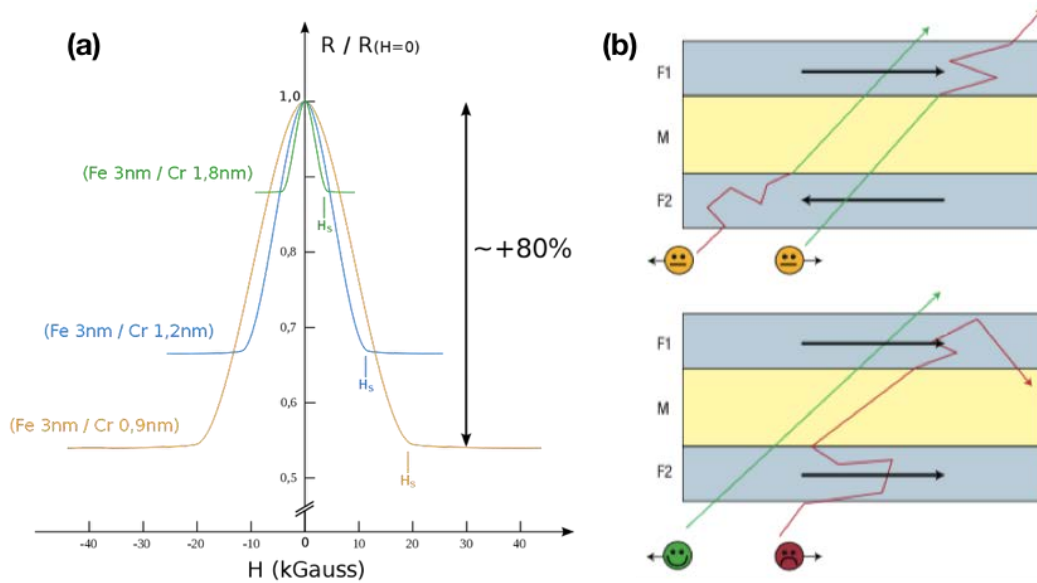


Figure 1.1: (a) The founding results of Albert Fert and Peter Grunberg (1988): change in the resistance of Fe/Cr super lattices at 4.2K in external magnetic field H . The arrow to the right shows maximum resistance change. H_s is the saturation field. (b) Schematic diagram of the scattering processes occurring in the F1/M/F2 layer stack. The triple-layer film consists of two identical ferromagnetic layers F1 and F2 sandwiching a non-magnetic metal spacer layer M, the current circulating in plane. In the parallel configuration (lower scheme), the spin-up electrons (spin parallel to the magnetization) can travel through the sandwich nearly unscattered, providing a conductivity shortcut and a low resistance. On the contrary, in the antiparallel case (top scheme) both spin-up and spin-down electrons undergo collisions in either F1 or F2, giving rise to a higher overall resistance. Adapted from.³⁹

GMR was also shown in multilayers deposited by using sputtering that extended the possibilities of industrial applications. Other materials have been tested like copper for the non-magnetic spacer material because of its high spin diffusion length preserving the spin polarization over several nanometers.³² The spin-valve emerged with the development of exchange biased hard layers.³³ During the first years of the research on GMR, the experiments were performed only with currents flowing along the layer planes, in the geometry called CIP (current in plane). However, the CIP spin valve geometry shown in Figure 1.2 (a) is a limitation to the downscaling. In 1993,

experiments were performed in the geometry called CPP (current perpendicular to plane). This was done first by sandwiching a magnetic multilayer between superconducting electrodes by Bass, Pratt, and Schroeder at Michigan State University^{34,35}. In the CPP geometry, the GMR is not only definitely higher than in CIP geometry, but also subsists in multilayers with relatively thick layers, up to the micron range^{36,37}. Nowadays, most of the read heads in the hard drives are based on the GMR effect by using the CPP geometry. As shown in Figure 1.2 (b), the spin-valve sensor can be directly connected to the magnetic shields in the CPP geometry. More details on the GMR effect can be found in reference.³⁸

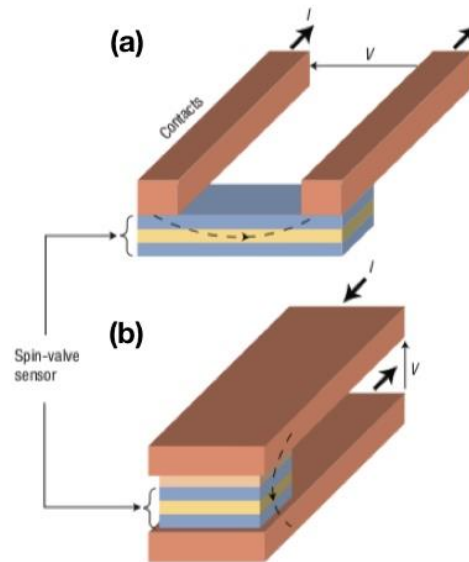


Figure 1.2: (a) Schematic diagram of the CIP spin-valve sensor in a read head. (b) Schematic diagram of the CPP spin-valve sensor in a read head. In both configurations, the recording medium travels parallel to the front face of the sensor. Adapted from.³⁹

1.1.2 Magnetic Tunnel Junctions (MTJs)

By replacing the non-magnetic spacer by an insulator, another important class of spintronic device is obtained: Magnetic Tunnel Junctions. In this structure, a thin electrical insulating layer is sandwiched by two ferromagnetic layers. By applying a voltage across the junction, the electrons can tunnel through the insulating layer from one ferromagnetic layer to the other. The resistance of the device will depend on the

relative orientation of the magnetizations of the magnetic layers in contact with the tunnel barrier, which produces the tunneling magnetoresistance (TMR). More details can be found in reference.⁴⁰ The first report about MTJ dated back to 1975 by Jullière⁴¹ but the community did not pay too much attention because the effect was very small and measured only at low temperature. In fact, the control of the growth of thin insulating layer was the bottleneck for the development of MTJs. In 1995, Moodera *et al.*⁴² was the first to show a relative variation of resistance of more than 10% at room temperature by using alumina oxide (Al_2O_3) tunnel barriers as shown in Figure 1.3.

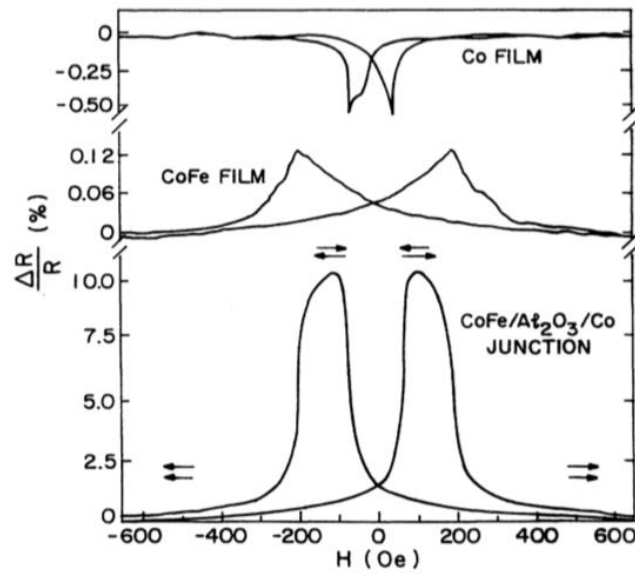


Figure 1.3: Resistance of $\text{CoFe}/\text{Al}_2\text{O}_3/\text{Co}$ junction plotted as a function of H in the film plane, at 295K. Also shown is the variation in the CoFe and Co film resistance. The arrows indicate the direction of M in the two films.⁴²

Jullière's model was based on the concept of spin polarization at the Fermi level defined as:

$$P_i = \frac{N_{M,i} - N_{m,i}}{N_{M,i} + N_{m,i}}$$

where $N_{M,i}$ and $N_{m,i}$ are the densities of states of the electrode number i for the spin majority and spin minority electrons respectively.

As for TMR, the hypothesis considers two conduction channels each one being associated to a spin direction, the spin being conserved during the tunneling process.

Thanks to the Fermi golden rule and considering low applied voltages and low temperatures, the conductance for each spin channel is proportional to the product of the density of states on each side of the barrier. The conductance, which is then the sum of the conductance of the two spin channels, is different in the parallel and antiparallel configurations. As shown in Figure 1.4 where simplified band structures of the ferromagnetic electrodes are sketched, the total conduction can be expressed as:

$$G_P = N_{M1}N_{M2} + N_{m1}N_{m2}, \text{ for parallel configuration,}$$

$$G_{AP} = N_{M1}N_{m2} + N_{m1}N_{M2}, \text{ for antiparallel configuration.}$$

The tunnel magnetoresistance is then defined by:

$$TMR = \frac{R_{AP} - R_P}{R_P} = \frac{G_P - G_{AP}}{G_{AP}} = \frac{2P_1P_2}{1 - P_1P_2}$$

TMR exceeding 70% was expected by using the spin polarization measured on different ferromagnetic materials. In 1989, Slonczewski proposed an analytical model that the tunnel polarization depends on the ferromagnetic/insulator combination.⁴³

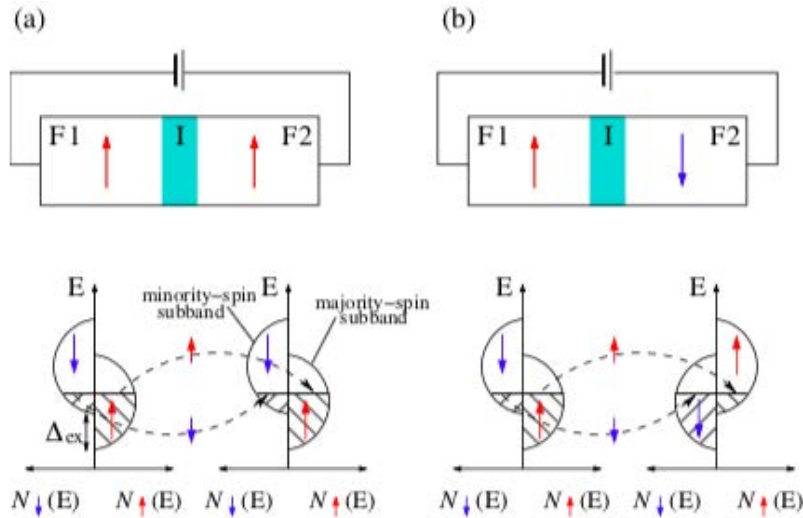


Figure 1.4: Tunneling process in the magnetic tunnel junction. The left part (a) shows the schematic representation of MTJ and schematic of the density of states of electrode 1 and electrode 2 in the parallel magnetization configuration. The right part (b) shows them in the antiparallel magnetization configuration. Adapted from.⁴⁴

Intensive research activities have been triggered due to i) the perspective of high magnetoresistance, ii) low current consumption thanks to the use of an insulator, and iii) high spatial integration thanks to the out-of-plane configuration. Nowadays,

scientists are developing new materials, more accurate theories to explore higher TMR and related new phenomena. Figure 1.5 (a) shows the tunneling magnetoresistance research and development timeline, which includes the development of MTJ with Al_2O_3 tunnel barrier and MgO tunnel barrier. By improving the quality of the Al_2O_3 tunnel barrier, the TMR value could be increased and a TMR of about 70% could be reached by Wang *et al.*⁴⁵ by using annealed CoFeB electrodes. Theoretical developments taking into account the symmetry of the electron Bloch wave functions in the electrodes and the symmetry dependent attenuation length in the insulator were made by Butler *et al.*^{46, 47}. Mathon *et al.*⁴⁸ predicted more than 1000% of TMR in Fe(100)/MgO(100)/Fe(100) epitaxial tunnel barriers. Several years later, 200% of TMR at room temperature was reported by Yuasa *et al.*⁴⁹ and Parkin *et al.*⁵⁰. Ikeda *et al.*⁵¹ reported that the maximum observed TMR value was 604% in a pseudo-spin-valve (PSV) MTJ having a 6.0 nm thick CoFeB electrode annealed at 525°C. Figure 1.5 (b) shows the TMR loop of the sample. In comparison to amorphous Al_2O_3 tunnel barrier, the attenuation length in MgO (100) is strongly symmetry dependent reinforcing the weight of the 100% polarization of the Δ_1 state in the Fe (100) electrode as shown in Figure 1.6.

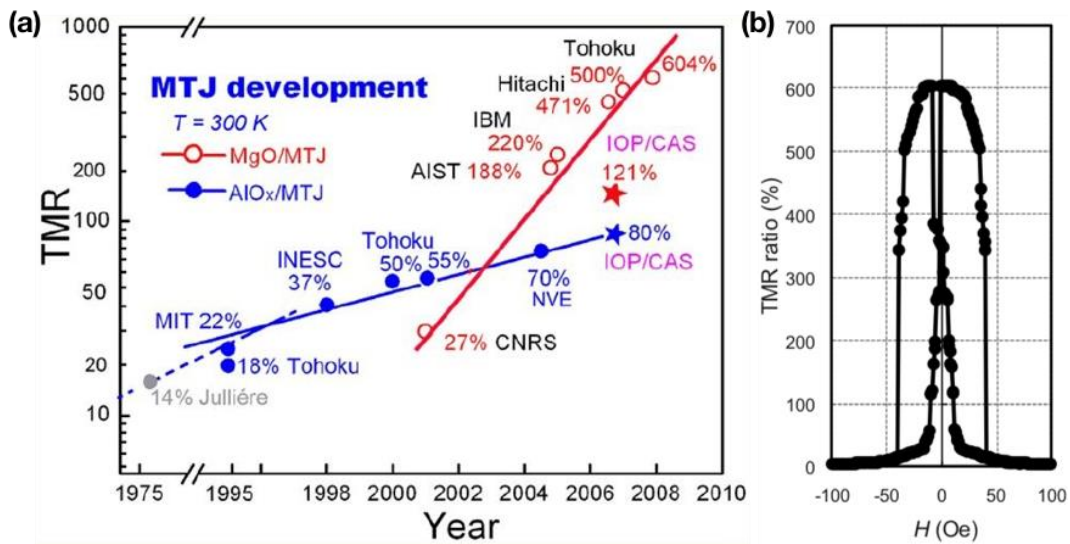


Figure 1.5: (a) Tunneling Magnetoresistance research and development timeline.⁵² (b) Magnetoresistance loop at 300K of the pseudo-spin-valves MTJ annealed at 525°C. TMR ratio is as high as 604% at 300K.⁵¹

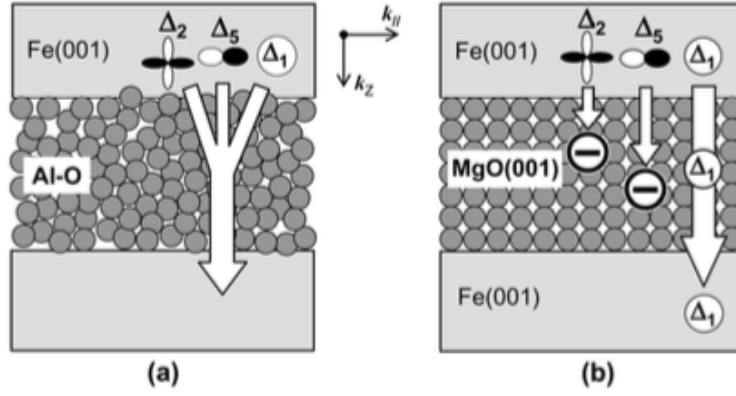


Figure 1.6: Schematic illustrations of electron tunneling. Tunneling processes through (a) an amorphous Al–O barrier and (b) a crystalline MgO (001) barrier are different.⁵³

In addition, the use of half-metallic materials such as Heusler alloys and magnetic oxides as spin injection sources is also a promising way to enhance the efficiency of the spin injection. Due to the existence of an energy gap for one spin band, half-metallic ferromagnets featuring complete spin polarization P at the Fermi level E_F are suitable candidates for spin-polarized current sources. They have gained an increasing interest for spintronic applications such as TMR, current-perpendicular-to-plane giant magnetoresistance (CPP-GMR), lateral spin-valves and spin injectors into semiconductors. Among the various half-metallic materials, Co₂-based ternary Co₂YZ and pseudo-quaternary Co₂Y_{1-x}Y_xZ full Heusler alloys have a special place due to their tunable electronic structure, a Curie temperature T_c that is well above room temperature (RT), and P that is close to unity. High spin polarization (large TMR) for Co₂-based Heusler alloys has been demonstrated in MTJs with an AlO_x barrier. Later, MTJs combining an MgO barrier with Co₂-based Heusler alloy electrodes showing a larger TMR ratio have been investigated. For Co₂MnSi and Co₂Mn_{1-x}Fe_xSi based MTJs as shown in Figure 1.7 (a), the TMR ratio was drastically improved with Mn or Mn-Fe rich compositions, respectively. The record of TMR ratio was 429% at 290K and 2610% at 4.2K as shown in Figure 1.7(b).⁵⁴

In particular, the large magnetoresistance (MR) outputs of CPP-GMR sensors by using Heusler alloy ferromagnetic layers are promising for read sensors of ultrahigh recording density hard disk drives (HDDs). So far, large MR values have been reported

for the CPP-GMR devices using epitaxially grown single-crystalline Heusler alloy films annealed at high temperatures ($\geq 500\text{C}$).^{55,56}

In summary, the MTJ structures possess advantages of large range of resistivity, low energy consumption, and stable magnetic performance, which can be used as read heads, sensors, or in Magnetic Random-Access Memory (MRAM).

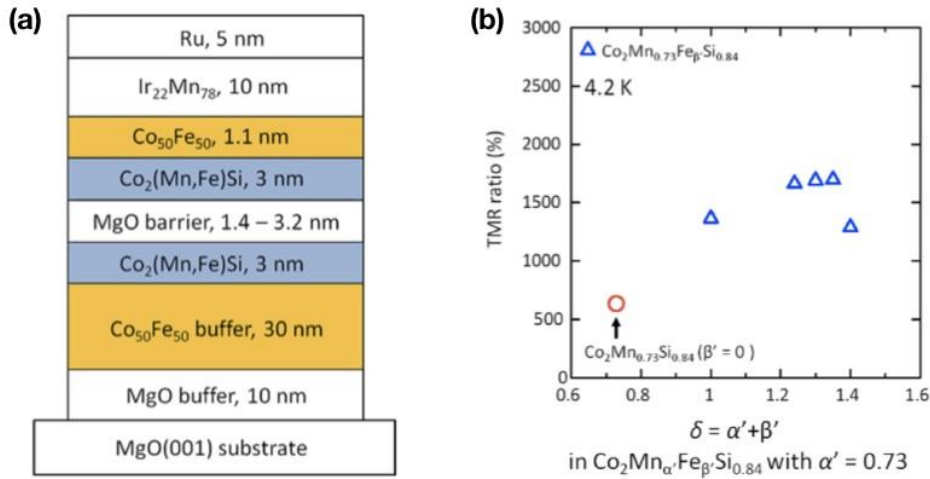


Figure 1.7: (a) Schematic diagram of MTJ layer structure. (b) TMR ratios at 4.2K for CMFS/MgO/CMFS MTJs (CMFS MTJs) as a function of Mn+Fe composition.⁵⁴

1.2 Spintronics with semiconductors

Despite the tremendous progress in micro-fabrication technologies, the size of semiconductor devices will soon encounter fundamental physical limits. Further scale reduction beyond these limits will require an urgent alteration of the concept of functional devices. The control of the spin degree of freedom has brought about a new area of electronics (spintronics). The research in the field of spintronics is currently being pursued extensively due to the potential for the development of a new direction in electronics. The field of spintronics spreads beyond the traditional boundaries among research fields, leading to interdisciplinary research that spans over magnetism, semiconductors, photonics and electronics as shown in Figure 1.8. Since 1990, a number of spin-based device concepts have been proposed. Spin-based transistors^{57,58,59,60}, spin light-emitting diodes (spin-LEDs)^{61,62} and spin transfer torque memories^{63,64} are typical examples.

The Spin-High Electron Mobility field Effect Transistor (HEMFET) proposed by Datta and Das is a great conceptual illustration of what could be achieved with this technology.⁵⁷ Spin-based transistors that do not strictly rely on the raising or lowering of electrostatic barriers can help to overcome scaling limits in charge-based transistors.^{65,66} Spin transport in semiconductors might also lead to dissipation-less information transfer with pure spin currents.⁶⁷ Adding the spin degree of freedom to conventional semiconductor charge-based electronics will add substantially more capabilities and performances to electronic products. The advantages of these new devices would be non-volatility, increased data processing speed and decreased electric power consumption compared with conventional semiconductor devices.⁶⁸

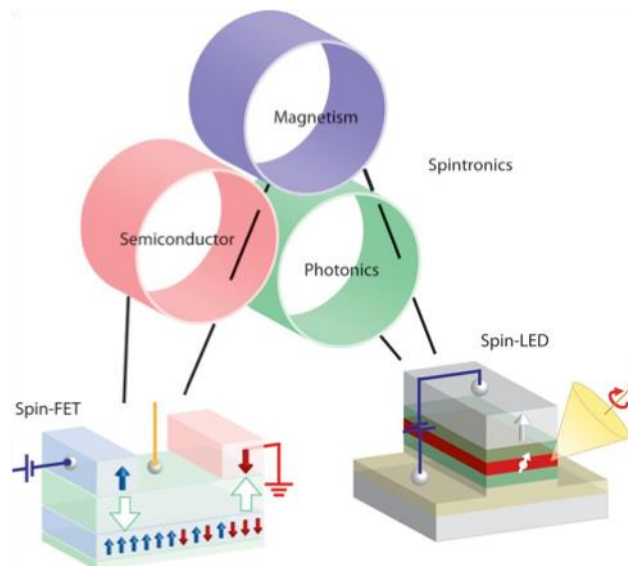


Figure 1.8: A conceptual illustration of spin-based electronic devices. In a spin-FET, spin polarized electrons are injected from a source ferromagnet into a semiconductor and detected using a ferromagnetic drain electrode. In a spin-LED, the spin injection efficiency is probed by measuring the circularly polarized light emission occurring under spin injection. Adapted from.⁶⁹

To operate a spin-based functional semiconductor device, the primary issue is the efficient injection of spin-polarized electrons from the ferromagnet into the semiconductor across the interface. The electron spin is then manipulated by the application of a voltage via the gate electrode, and the spin orientation is detected by

using a ferromagnetic drain electrode in a spin field-effect transistor (FET) or from the circular polarization of the emitted light in a spin LED. The first functional Spin-LED was proposed by Fiederling *et al.* in 1999.⁶¹ This experimental demonstration opened the door to a new field of study: opto-spintronics. More details about the state-of-the-art of spin LEDs will be presented in Chapter 3 (GaAs based spin LEDs) and 4 (GaN based spin LEDs).

1.2.1 The impedance mismatch problem

To manipulate the electron spin in semiconductors, we should firstly efficiently inject a high spin polarized current into the semiconductor. At the earlier stage of research, people developed diluted magnetic semiconductors as spin injectors, but their Curie temperature cannot exceed room temperature. For practical applications, room temperature operation of spin injector is mandatory. Among the possible spin injectors, FM (Ferromagnetic) 3d metals which possess high Curie temperatures have gained much interest, such as Fe, Co or FeCo alloys. However, the resistance mismatch between metal and semiconductor hinders the efficient spin injection into the semiconductor. To understand this problem, we will introduce below the concept of spin accumulation at the FM (Ferromagnetic)/NM (Non-magnetic) interface.

1.2.1.1 Spin accumulation at the FM/NM interface

By introducing the two-spin dependent conduction channel concept in 1936, Mott first proposed that when the band structure of spin-up and spin-down electrons are distinct in ferromagnets below their Curie Temperature ($T < T_c$), their conductivities are not equal. In 1987, van Son *et al.* and Johnson *et al.* independently presented a macroscopic approach describing the electron transport through an interface between ferromagnetic and non-magnetic metals in CPP configuration. They introduced the concepts of spin accumulation generated by conductivity splitting around the interface. When a current is spin-polarized in a ferromagnet, an electrochemical potential on the FM/NM bilayer will create a spin disequilibrium called spin-accumulation $\Delta\mu = \mu_+ - \mu_-$

(electrochemical potential of the spin up μ_+ and electrochemical potential of the spin down μ_-), which is proportional to the current density J across the interface. The concept of spin accumulation is shown in Figure 1.9 (a). When an electron current flows through the interface between a ferromagnetic and a nonmagnetic material, spin accumulation occurs. Far from the interface on the ferromagnetic side, the current is larger in one of the spin channels (spin up in the Figure 1.9 (a)). However, far from the interface on the non-magnetic side, the current is equally distributed in two spin channels. At the interface region, the spin up electrons flip to spin down, creating a zone named as spin accumulation zone. The spin accumulation zone extends on both sides to a distance corresponding to the spin diffusion length (SDL) in FM and NM, respectively. A splitting of chemical potentials ($\Delta\mu$) occurs between the chemical potentials of the spin up and spin down electrons, as shown in Figure 1.9 (b). The steady chemical potential splitting and out-of-equilibrium distribution of spin-polarized electrons result in the spin flips which is needed to adjust the incoming and outgoing fluxes of spin up and spin down electrons. The number of spin flips (n_{flip}) is proportional to $\Delta\mu N L_{\text{sf}} / \tau_{\text{sf}} = \Delta\mu / \rho L_{\text{sf}}$, where N is the density of states (either in FM or NM), L_{sf} is spin diffusion length, τ is spin relaxation time, and ρ is the spin resistivity. In the spin accumulation zone, the current is gradually depolarized by spin flips generated by the spin accumulation.

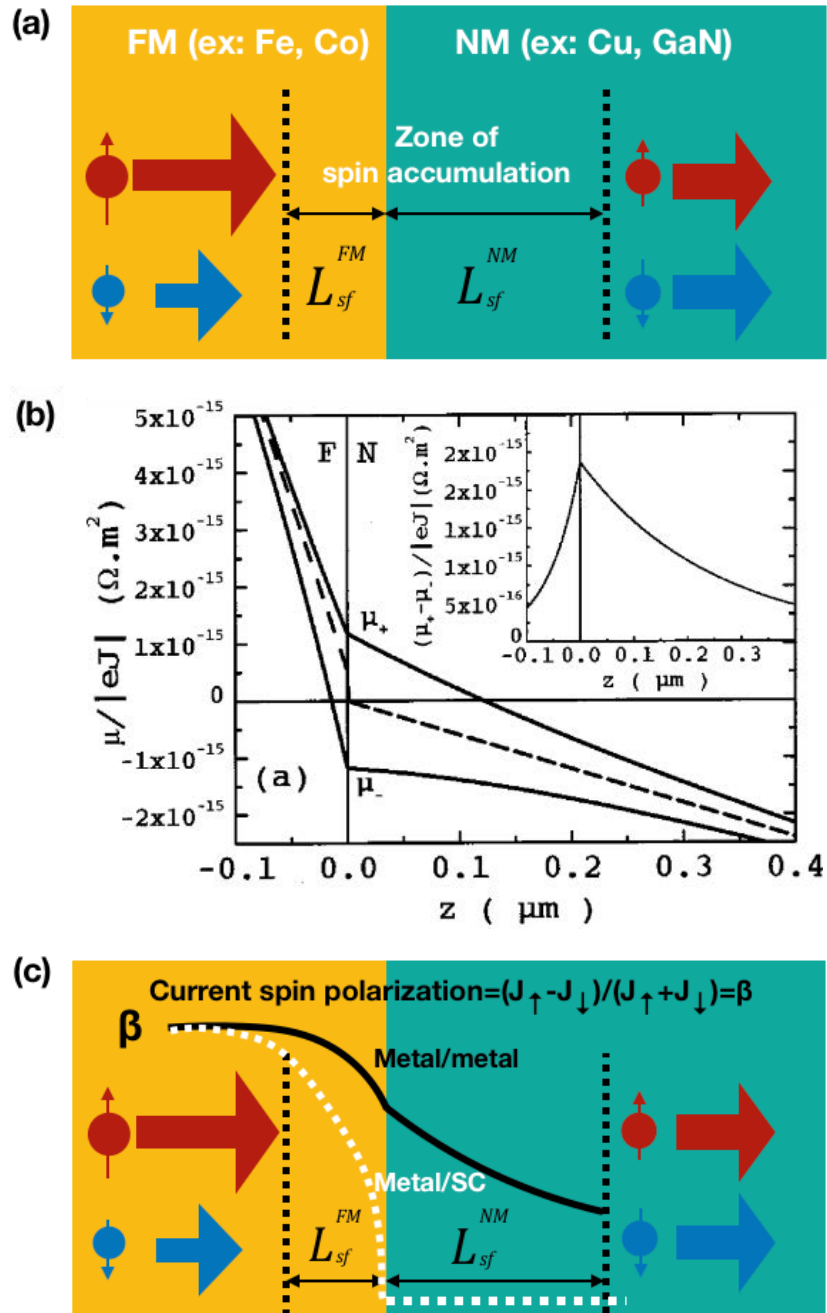


Figure 1.9: Schematic diagram of spin accumulation. (a) Spin-up and spin-down current far from the interface between the ferromagnetic and nonmagnetic conductors. (b) Variation of the electrochemical potentials μ_+ and μ_- as a function of z at a Co /Cu interface. The inset shows the variation of the spin accumulation, $\Delta\mu = \mu_+ - \mu_-$, as a function of z .⁷³ (c) Variation of the current spin polarization.

1.2.1.2 Impedance mismatch at the FM/SC interface

In the case of spin injection from a magnetic metal into a nonmagnetic semiconductor, spin accumulation occurs on the two sides of the interface between FM and SC. However, since the number of spin flips is proportional to $\Delta\mu/\rho L_{sf}$, most of spin flips happen in the FM side due to the much larger resistivity of SC. Therefore, the current is almost fully depolarized at the FM/SC interface before entering the semiconductor, as shown in Figure 1.9 (c). This problem that was first raised by Schmidt *et al.* is termed “conductivity mismatch” or “impedance mismatch” between the FM and the SC.⁷⁰ In 1999, the first spin injection experiments from a FM into a SC have only shown effects less than 1%.^{71,72}

1.2.1.3 The Fert-Jaffrès Model

In 2001, Fert and Jaffrès investigated spin injection from a ferromagnetic metal (FM) into a semiconductor (SC). They studied the perpendicular spin-polarized electronic transport through FM/SC and FM/Tunnel/SC interfaces.⁷³ As shown in Figure 1.10, they extended the Valet-Fert model by introducing a spin-dependent interface resistance r_b , typically by a tunnel junction, to introduce a spin dependent discontinuity of the electron chemical potential $\Delta\mu = \mu_+ - \mu_-$ at the interface which generates a much higher $\Delta\mu$ in the semiconductor side than in the FM side. This increases the proportion of spin flips on the semiconductor side and leads to a more balanced spin-flip ratio between FM and SC and then shifts the depolarization from the metallic to the semiconductor side. It demonstrates an enhancement of the injected current spin polarization in CPP geometry when the interface resistance stands above a threshold value related to the resistivity and the spin diffusion length of the semiconductor.

Rashba simultaneously demonstrated theoretically how the use of tunnel contacts could dramatically increase spin injection in a semiconductor by solving the impedance mismatch problem.⁷⁴ Nevertheless, by neglecting the spin relaxation in the non-

magnetic side, Rashba's approach was not entirely accurate, as the detection condition has been showed experimentally to be essential for the spin information preservation. In contrast, the Fert-Jaffrès model was built from a more complete and rigorous point of view, and it was in agreement with the experimental observations.

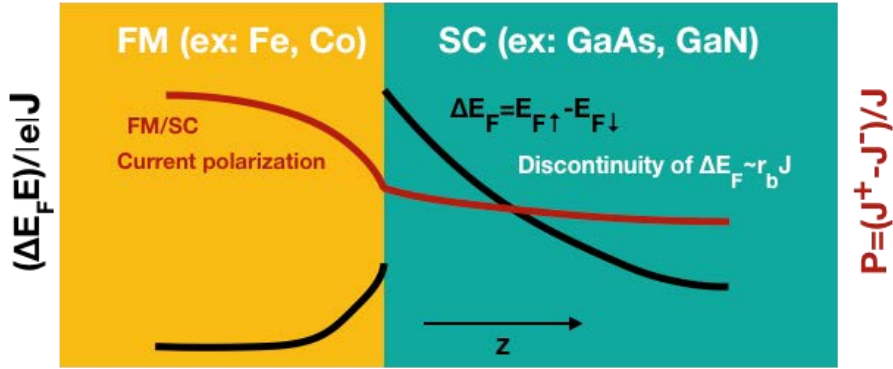


Figure 1.10: Variation of the Fermi level and the current spin polarization as a function of z at the FM/SC interface.

Furthermore, they have modelled a FM/SC/FM structure with insertion of a tunnel barrier to find the optimized thickness for spin injection and detection window as shown in Figure 1.11. For the case of a FM/SC/FM structure with an interface resistance, a significant MR can be obtained when the value of r_b of the tunnel junction is in the range

$$r_N \frac{t_N}{L_{sf}^N} < r_b < r_N \frac{L_{sf}^N}{t_N},$$

which should be relatively narrow. If the resistance r_b is too small, the detection condition can be fulfilled, but the current will be depolarized at the interface. If the resistance r_b is too large, the injection condition can be fulfilled, but the dwell time of electron spins in the SC will be too long. Most of electron spins will be depolarized before it can be detected.

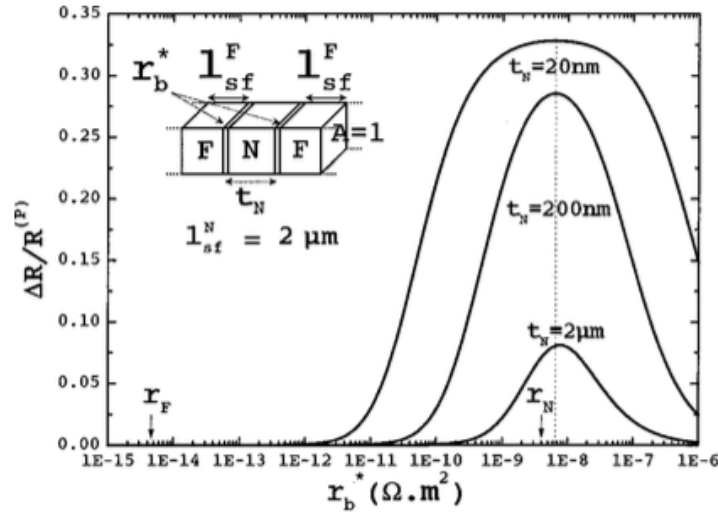


Figure 1.11: Magnetoresistance versus interface resistance r_b^* of a $F_1/N/F_2$ structure where $F_1=F_2=Co$, $N=semiconductor$, with $t_N=20nm, 200nm, 2\mu m$, for the thickness of N and $\gamma=0.5$ for the spin asymmetry coefficient of the interface resistance. The geometry of the structure is shown in the left top of the figure.⁷³

1.2.1.4 Spin injection through a tunnel-barrier

The first experiment of spin injection in a semiconductor using a tunnel barrier was done by Alvarado and Renaud using a Scanning Tunneling Microscope (STM) at IBM Zurich. In 1992 they successfully demonstrated spin-injection in GaAs (110) at room temperature using a Ni probe by using vacuum tunneling barrier.⁷⁵ Amorphous tunnel barriers such as Al_2O_3 or MgO also were demonstrated for significant spin injection in semiconductors.^{76,77,78}

By using a spin-LED configuration, typical injected spin-polarization degree measured with Schottky tunnel barriers were around 30%, but only at low temperatures.⁷⁹ Typical values reached with AlO_x barriers on GaAs were around 25-40% at low temperature (4.2-77 K)⁸⁰ and up to 16% at 300 K. With textured $MgO(001)/CoFeB$ on GaAs spin polarization degrees up to 52% at 100 K and 32% at 300 K were obtained.⁸¹ The textured $MgO(001)/CoFe$ led to an increase of the spin-injection efficiency, which could be due to the symmetry dependent transfer of the tunneling electrons.⁸²

1.2.2 Spin injection and detection in semiconductors

1.2.2.1 All-electrical spin injection and detection

1.2.2.1.1 Local geometry

One way for measuring electron spin injection into semiconductors is to utilize a local geometry structure as shown in Figure 1.12. In the local geometry, the current flows from one FM electrode through the tunnel barrier and the semiconductor to the second FM electrode. The voltage drop between the electrodes is measured simultaneously. The resistance of the two-terminal FM/NM/FM device can be modulated by the relative orientation of the magnetizations of the ferromagnetic contacts.

Sasaki *et al.*⁸³ have reported a local magnetoresistance in Fe/MgO/Si lateral spin valve at room temperature. The magnitude of the local magnetoresistance was estimated to be 0.075Ω at room temperature. A clear rectangular signal was observed in the local magnetoresistance measurement even at room temperature. This result was the first demonstration of magnetoresistance in local geometry in a semiconductor-based spin device. Recently, our group demonstrated the electrical spin injection and detection in the conduction band of a multilayer MoS₂ semiconducting channel by using a two-terminal spin-valve configuration geometry as shown in Figure 1.13 (a). A magnetoresistance around 1% as shown in Figure 1.13 (b) has been observed through a 450 nm long, 6 monolayers thick MoS₂ channel with a Co/MgO tunneling spin injector and detector.⁸⁴

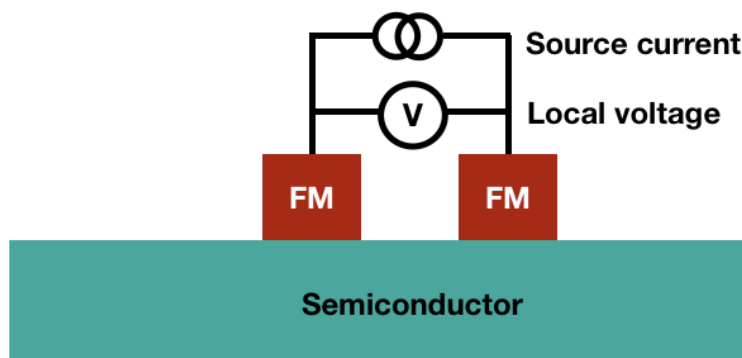


Figure 1.12: Schematic diagram of local geometry measurement.

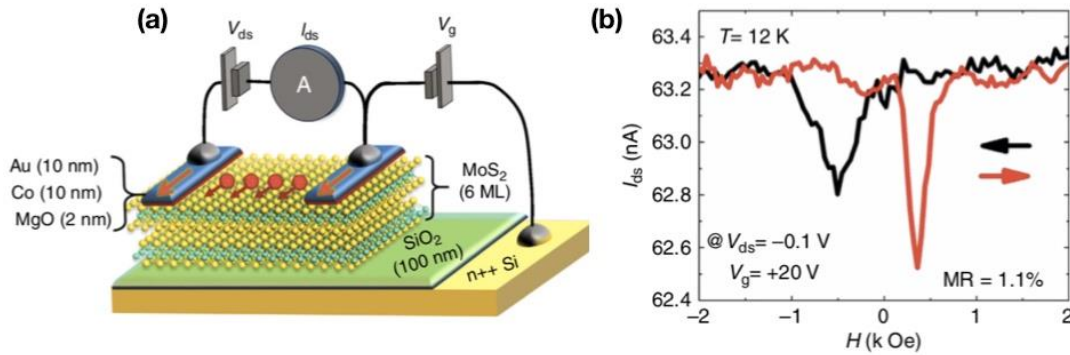


Figure 1.13: (a) Schematic of the lateral spin-valve device. The multilayer MoS₂ serves as spin transport channel, and two Au/Co/MgO electrodes are used to inject spin and measure the current. A back-gate voltage applied between the substrate and one top contact is used to modulate the carrier density in the MoS₂ channel. (b) Magneto-resistance response of the multilayer MoS₂-based lateral spin valve device measured at 12 K with $V_g = +20\text{V}$ and $V_{ds} = -0.1\text{V}$.⁸⁴

1.2.2.1.2 Non-local geometry

Another way for measuring spins injection in semiconductor is to utilize a non-local geometry as depicted in Figure 1.14. In the non-local geometry, the spin and charge currents are separated. The current is injected from left ferromagnetic contact FM1, which results in a spin accumulation under the FM1 contact and a splitting of the electrochemical potential $\Delta\mu$ in the semiconducting channel. The $\Delta\mu$ can be propagated through the SC channel to another FM2 contact. The voltage between the FM2 and a reference NM contact depends on the relative angle of the magnetization of FM2 and the spin injection direction from FM1. This technique allows us to measure the pure spin current (with zero charge current) propagated from FM1 to FM2. The higher spin-polarized current injected from FM1 results in a higher spin signal probed by FM2, which is called as non-local measurement.

When the applied magnetic field ($B_{//}$) is parallel to the magnetization of FM electrodes, the voltage probed on FM2 reaches a maximum when the magnetization of

FM1 is parallel to FM2. However, the voltage reaches a minimum when the magnetization of FM1 is antiparallel to FM2. This is called as a non-local spin valve measurement, as shown in Figure 1.15 (a). One can also apply an out-of-plane magnetic field (B_{\perp}) to measure the Hanle spin precession. In that case, the injected spins in the SC channel precess around the perpendicular magnetic field. Figure 1.15(b) shows a clear spin precession signal for both parallel and antiparallel configurations. The signal decreases (increases) for the parallel (antiparallel) configuration with increasing applied field. One can fit the Hanle curves with the Bloch equation to extract different information:

$$R_{NL} = \int_0^{\infty} \frac{1}{\sqrt{4\pi D_s t}} \exp\left(\frac{-L^2}{4D_s t}\right) \exp\left(\frac{-t}{\tau_s}\right) \cos(W_L t) dt,$$

where R_{NL} is the non-local resistance, L is the separation between the electrodes (center-to-center distance) and W_L is the Larmor frequency. This gives a spin relaxation time τ_s , a spin diffusion constant D_s , and hence, a spin relaxation length λ_s .

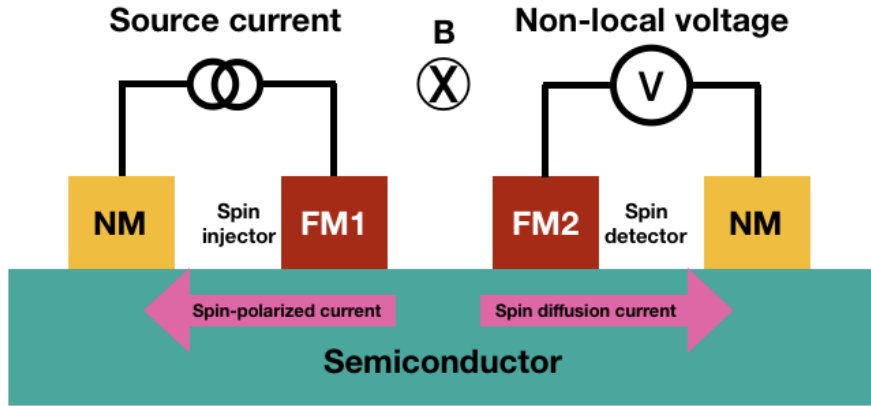


Figure 1.14: Schematic diagram of non-local geometry measurement.

The non-local detection of electron spins was first demonstrated in a metallic lateral spin valve structure by Johnson and Silsbee.⁸⁵ Jedema *et al.*⁸⁶ also used a NiFe/Cu junction structure, where electrons flow from the ferromagnetic NiFe electrode (FM1) into the nonmagnetic copper electrode (NM). The non-local electrical detection technique has also been successfully applied directly to measure spin accumulation in a semiconductor.^{87,88,89,90,91} The non-local electrical detection of spin

accumulation in GaAs was first demonstrated in 2007 by Lou *et al.*⁸⁵ who used a Fe/GaAs (001) heterostructure with a lightly n-doped GaAs epilayer. The spin diffusion length was estimated to be 6 μm at 50K. Sasaki *et al.*⁸³ have reported a non-local magnetoresistance in a Fe/MgO/Si lateral spin valve at room temperature. The magnitude of the non-local magnetoresistance was estimated to be 0.0057Ω at room temperature. Avsar *et al.* have reported a breakthrough towards making two-dimensional semiconductor spin devices. They have fabricated a spin valve based on an ultrathin (~ 5 nm) semiconducting black phosphorus (bP) layer as shown in Figure 1.15 (a). These authors established fundamental spin properties of this spin channel material, which supported all electrical spin injection, transport, precession and detection up to room temperature. Here, a spin-polarized charge current was applied between electrodes 1 and 2 and a non-local voltage was measured between electrodes 3 and 4 as a function of in-plane field B_{\parallel} at a fixed gate voltage.⁹² Figure 1.15 (b) shows a representative non-local spin valve signal measured at $T=100\text{K}$ and $V_{\text{BG}}=30\text{V}$ with in-plane field B_{\parallel} . As the magnetization directions of the ferromagnets were switched, the spin accumulation changed, giving rise to a non-local, bipolar spin signal with a change in the non-local resistance of $\Delta R \approx 15\Omega$ with out-of-plane field B_{\perp} . Hanle spin precession was measured as shown in Figure 1.15 (c) yielding a spin relaxation time of about 4 ns, with a spin relaxation length exceeding 6 μm .

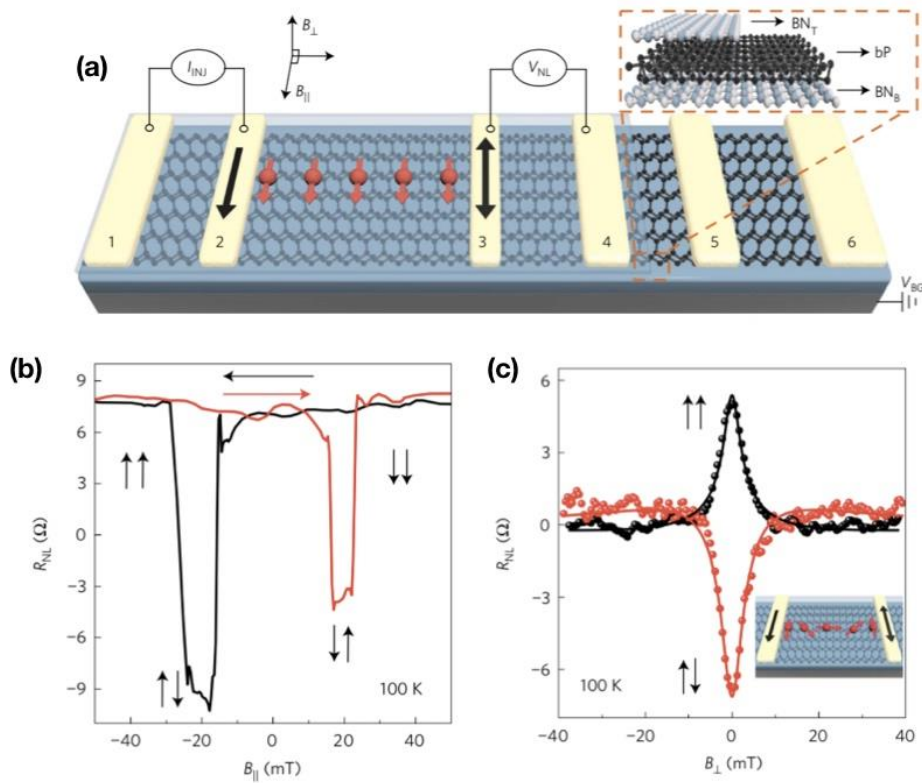


Figure 1.15: (a) Schematics of the device. Electrodes 5 and 6 have direct contact to bP crystal. The red spheres with arrows represent spin diffusion during a non-local spin valve measurement. The inset shows the schematics of the heterostructure. (b) Non-local signal as a function of the in-plane magnetic field. Black and red horizontal arrows represent the sweeping directions of the magnetic field. Vertical arrows represent the directions of the relative magnetization of the injector and detector electrodes. (c) Non-local signal as a function of the perpendicular magnetic field. Measurements are performed with an injected current of $0.5\mu\text{A}$ at 100K and V_{BG} is fixed to 30V. The red spheres with arrows in the schematics represent the precession of spins under the externally applied magnetic field.⁹²

1.2.2.1.3 Hot electron spin injection

A different spin injection technique, which does not necessarily require the impedance mismatch at ferromagnet/semiconductor interface, employs spin-polarized electrons having energies much greater than E_F . This is called “hot electron” spin injection. In this approach, electrons firstly tunnel through a tunnel barrier and are

ballistically injected into a ferromagnetic layer with energies larger than E_F .^{93,94} Since the majority spin and minority spin electrons have very different inelastic mean free paths, the hot electrons passing through the FM layer can be effectively polarized. The polarization can exceed 90% when the FM layer has a thickness more than 3 or 4 nm. The energy of hot electrons can be tuned via the bias across the tunnel junction. If the energy of hot electrons is higher enough to overcome the Schottky barrier height at the FM/SC interface, the highly spin-polarized electrons can be injected into the conduction band of SC. However, the overall efficiency, as defined by the ratio of the spin-polarized current injected into the semiconductor to the tunnel current injected into the FM layer, is low due to the attenuation of the hot electron current during the spin filtering process and to the low ballistic transmissivity at the metal/semiconductor interface.

Figure 1.16 shows the schematic of a tunnel junction used as a source for ballistic hot electron spin injection into a semiconductor conduction band. Spin injection and detection is based on the attenuation of minority-spin hot electrons in ferromagnetic thin films. In step 1, a solid-state tunnel junction injects unpolarized hot electrons from the NM emitter into the ferromagnetic base (FM1), forming emitter current I_e . Spin-dependent hot-electron scattering attenuates minority spin electrons (step 2), so that the electrons transported over the Schottky barrier and into the semiconductor conduction band (forming injected current I_{c1} , the “first collector current”) are polarized, with their spin direction parallel to the magnetization of FM1 (step 3). After transport through the semiconductor collector 1 (step 4), the ballistic hot-electrons are spin-dependent filtered in FM2 and enter into the second SC collector 2 to form the “second collector current” (I_{c2} , step5). This I_{c2} is dependent on the relative direction between the FM2 and the electron spin transported through SC1. Appelbaum *et al.* demonstrated conduction-band spin transport across 10 μm undoped Si by spin-dependent ballistic hot-electron filtering through ferromagnetic thin films for both spin injection and spin detection.⁹⁵ Figure 1.17 (a) displays the micrograph of a wire-bonded Si-based hot electron spin-transport device. In Figure 1.17 (b), in-plane magnetic hysteresis data of I_{c2} at $V_e = -1.8\text{V}$ and 85K are shown. At large magnetic field, the I_{c2} keeps in high current state when the magnetizations of FM1 and FM2 are maintained in a parallel

state. When the magnetic field was swept through zero and changed sign, the magnetization of $\text{Ni}_{80}\text{Fe}_{20}$ was switched to reach an antiparallel state, resulting in a reduction in I_{c2} of approximately 2%.

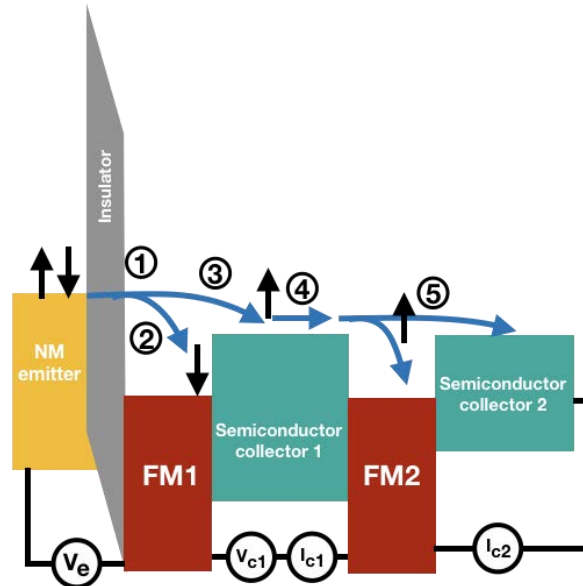


Figure 1.16: Schematic of a tunnel junction used as a source for ballistic hot electron injection into a semiconductor band. At constant emitter voltage (V_e), the “first collector current” (I_{c1}) at the FM1 contact and “second collector current” (I_{c2}) at a contact to substrate are measured, under optional voltage bias (V_{c1}) across the semiconductor drift region.

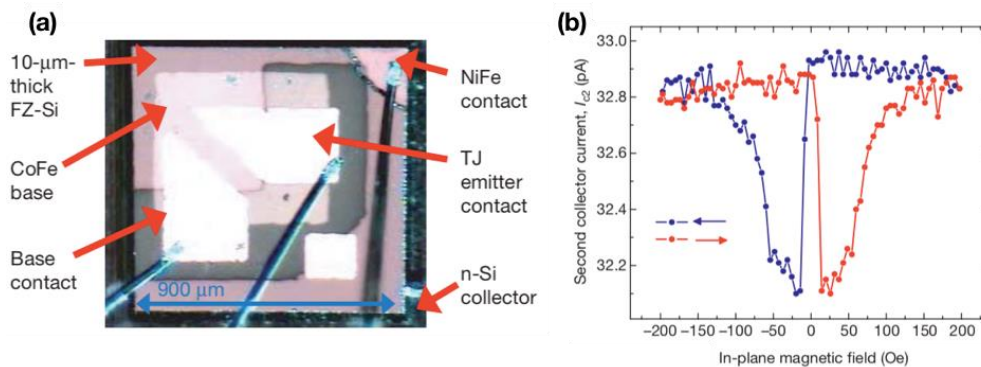


Figure 1.17: Illustration of the Si spin transport device. (a) A top-down micrograph of a representative wire-bonded Si spin-transport device, showing the device structure, contacts to the spin-injection tunnel junction (TJ) base and emitter, and spin-detector buried NiFe layer. (b) In-plane magnetic field dependence at 85K. Second collector current, I_{c2} , at constant emitter bias $V_e = -1.8\text{V}$ and $V_{c1} = 0\text{V}$, showing a clear $\sim 2\%$ spin-valve effect.⁹²

When applying a perpendicular magnetic field, the electron spin will precess in the plane. The amplitude of the second collector current I_{c2} will be modulated depending on the angle of electron spin when it reaches the FM2. Figure 1.18 shows spin precession and dephasing in a perpendicular magnetic field at constant emitter voltage $V_e = -1.8\text{V}$ and 85K . We can find a damped oscillation feature of I_{c2} . The local maximum corresponds to the angle between electron spin and FM2 to be $0, 2\pi, 4\pi \dots$. Because of the random spin diffusion and scattering in Si, spin dephasing was enhanced with higher precession angles, resulting in the damped higher-order oscillations (Hanle effect).⁹⁶ When increasing the voltage V_{c1} across the semiconductor collector 1, the transit time of injected electron was accelerated. As shown in Fig. 1.18, with the same sweeping range of magnet field, the observed period of oscillation was reduced. A useful advantage of the four-terminal design with rectifying Schottky barriers on the both sides of the FZ-Si is that I_{c2} is almost independent of the accelerating voltage V_{c1} . Therefore, the drift electric field in the semiconductor collector 1 can be tuned to change the spin-polarized electron transit time with applied voltage V_{c1} .

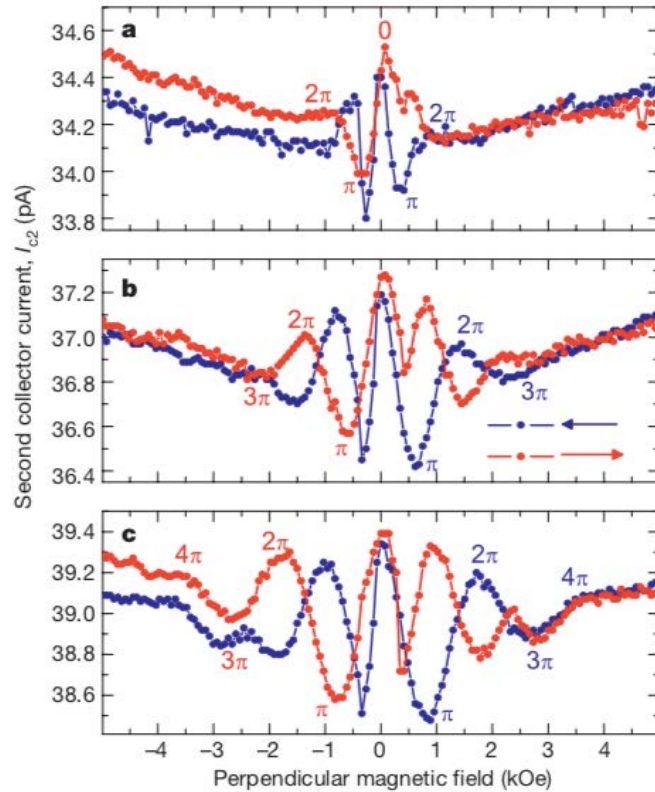


Figure 1.18: Spin precession and dephasing in a perpendicular magnetic field at constant emitter voltage $V_e = -1.8\text{V}$ and 85K . (a) Second collector current, I_{c2} , in zero applied voltage V_{c1} . (b, c) Under an accelerating voltage bias of 0.5V (b) and of 1.0V (c). At higher accelerating voltages, the spin polarized electron transport time is reduced in the increased drift field, so the precession angle at fixed magnetic field is smaller, causing an increased precession period and revealing the presence of precession angles to 4π .

1.2.2.1.4 Spin pumping injection and ISHE detection

In spintronics, pure spin currents play a key role in transmitting, processing and storing information. A pure spin current is a flow of electron spins without a simultaneous flow of charge current. In 2011, Ando *et al.* discovered a new approach to overcome the impedance mismatch at the FM/SC interface: the spin pumping (SP).⁹⁷ This is different from spin-injection by carrier transport through the FM/SC interface. A pure spin current is injected in the SC by Ferromagnetic Resonance (FMR) from the FM layer as shown in Figure 1.19.

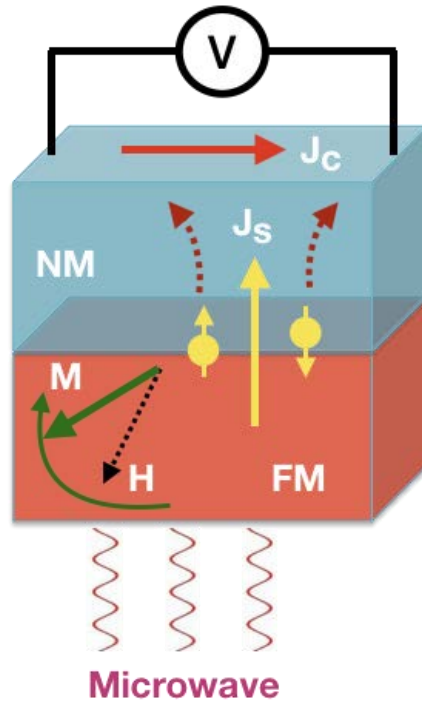


Figure 1.19: Schematic representation of the spin pumping mechanism. A pure spin current is injected in the non-magnetic material by induced Ferromagnetic Resonance of the FM layer. The injected pure spin current is detected as a spin voltage on the sample edges using the inverse spin Hall effect (ISHE).

The concept is based on the use of a FM/NM bilayer immersed in a radiofrequency field in the GHz range. The radio frequency (RF) microwave leads to a ferromagnetic resonance of the FM layer magnetization under a specific DC external magnetic field. The magnetization precession associated with a change of the magnetization longitudinal component is transferred to the electronic bath at the FM/NM interface through dynamical exchange interaction and generates a vertical pure spin current in the non-magnetic metal. The spin accumulation induced by spin pumping in the non-magnetic metal is detected as a voltage using the inverse spin Hall effect (ISHE). Furthermore, by applying a bias voltage at the FM/NM interface, the spin pumping can be tuned by controlling the level of the exchange interaction.

Spin pumping has also been proven to be an efficient method of creating a pure spin current for spin injection from FM to SC. Combined with a heavy metal (such as Pt, W, or Pd) for the spin to charge conversion by ISHE, the spin-current can be

electrically probed in metals, semiconductors, organic materials, or, more recently, in topological insulators. Shikoh *et al.* reported dynamical generation of pure spin current and spin transport in p-type silicon (p-Si).⁹⁸ Watanabe *et al.* used ferromagnetic resonance spin pumping in a ferromagnet/conjugated polymer/nonmagnetic spin-sink trilayers to demonstrate the ability of polarons to carry pure spin currents over hundreds of nanometers with long spin relaxation times of up to a millisecond and to exhibit Hanle precession.⁹⁹ Dushenko *et al.*¹⁰⁰ reported an experimental demonstration of room-temperature spin transport in n-type Ge epilayers grown on a Si (001) substrate. By utilizing spin pumping under ferromagnetic resonance, a pure spin current was generated in n-Ge at room temperature. The pure spin current was detected by using the inverse spin-Hall effect of either a Pt or Pd electrode on n-Ge. Recently, our group has demonstrated the establishment of a pure spin-current over micrometric distance in n-Si at room temperature in CoFeB/MgO/Si/Pt hybrid vertical structures as shown in Figure 1.20 (a).¹⁰¹ In this experiments, a pure propagating spin current was generated via ferromagnetic resonance spin pumping and converted into a measurable voltage by using the inverse spin Hall effect occurring in the top Pt layer. Figure 1.20 (b) shows that the spin current generated by spin pumping can be electrically detected.

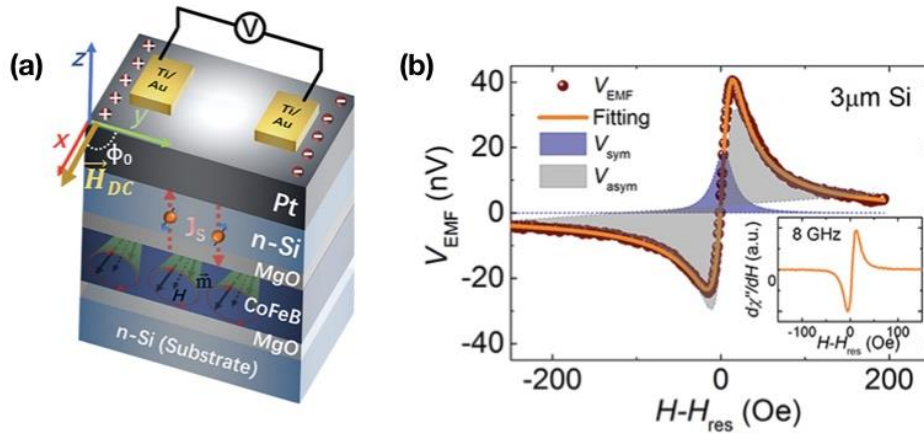


Figure 1.20: (a) Schematic drawing of the vertical metal-Si-metal heterostructure used for FMR and electromotive force (EMF) voltage measurements. It also illustrates the process of spin current (J_s) injection/conversion by spin pumping of the CoFeB layer and ISHE of the top Pt layer, respectively. (b) EMF voltage measured with spin-pumping excitation in the CoFeB (5.2nm)/MgO (2.2nm)/Si (3 μ m)/Pt (6nm) sample. The symmetric and asymmetric components are separated with Lorentzian and anti-Lorentzian fitting of the spectrum, respectively. Inset: FMR spectra of the same sample with the same spin-pumping condition (8GHz).

1.2.2.2 Electrical spin injection and optical detection

The optical detection of an electrically injected spin polarization in a semiconductor was first demonstrated in 1999 independently by Fiederling *et al.*⁶¹ and Ohno *et al.*⁶² These authors used LED structures with InGaAs or GaAs QWs and analyzed the optical polarization of the emitted light. Figure 1.21 shows the schematic diagram of a spin LED used for electrical spin injection and optical detection. Fiederling *et al.* used the paramagnetic semiconductor $\text{Be}_x\text{Mn}_y\text{Zn}_{1-x-y}\text{Se}$ as a spin aligner and achieved an injection efficiency of 90% of spin-polarized current into a GaAs based spin LED at low temperature as shown in Figure 1.22 (a) and (b).⁶¹ A large magnetic field (1.5T) has been applied to orientate the magnetization of spin injector to out-of-plane, and the optical detection was from the surface emission. Ohno *et al.* utilized the ferromagnetic semiconductor $\text{Ga}_x\text{Mn}_{1-x}\text{As}$ to align the electron spin orientation and obtained spin injection into GaAs with efficiency of the order of 1% at

low temperatures as shown in Figure 1.22 (c) and (d).⁶² In their experiments, the magnetization of spin-injector was in-plane, and the optical detection was from the edge emission. Since the first demonstrations, numerous studies on similar systems have been reported, in which either the QW structures were modified or different spin injector layers were used. To achieve high spin efficiencies at room temperature, ferromagnetic injectors with a Curie temperature far above room temperature are necessary. The research in this area has therefore focused on the use of ferromagnetic metals such as 3d transition metals (Fe, Co, CoNi, CoFe, CoFeB...) and Heusler alloys rather than using ferromagnetic semiconductors.

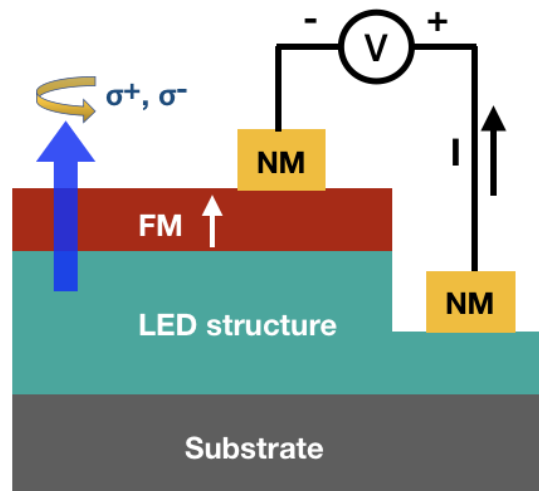


Figure 1.21: Schematic diagram of spin LED for electrical spin injection and optical detection.

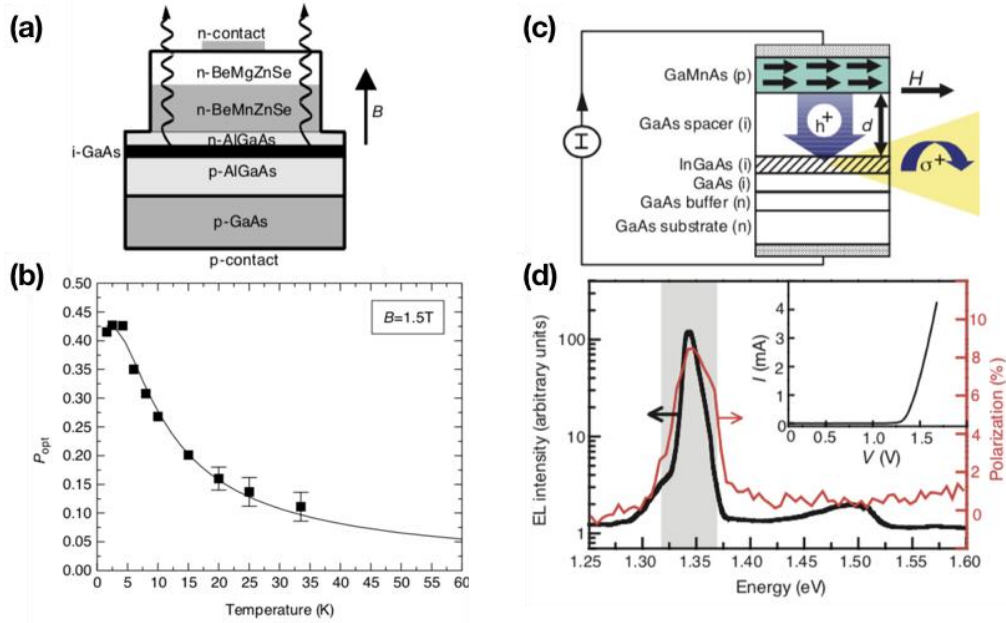


Figure 1.22: (a) Side view of the device showing the direction of the magnetic field and the emitted light. (b) Temperature dependence of the degree of circular polarization of the electroluminescence. The line represents a fit using the splitting and occupation of the spin levels. (c) A spin LED device structure. (d) Total electroluminescence (EL) intensity of the spin-LED device measured at 6K. Adapted from.^{61,62}

As the optical detection of electron spins is based on the conversion of out-of-plane electron spins into the photon helicity of emitted light, the magnetization of spin injector should be saturated normal to the sample plane. This generally requires the application of a high magnetic field of over 2T, which is not possible for real application. Perpendicularly magnetized spin injectors are then required for the optical detection of spin polarization at zero applied magnetic field. By using perpendicularly magnetized CoFeB/MgO spin injector, our group has recently reported an unprecedentedly high circular polarization degree up to 35% at zero applied magnetic field from single GaAs quantum dot (QD) based LED¹⁰². More importantly, this study showed a signature of dynamic polarization of the nuclear spins in the quantum dot induced by the hyperfine interaction with the electrically injected electron spins. This study paves the way for the electrical control of nuclear spin polarization in a single quantum dot without any external magnetic field.

1.2.2.3 Optical spin injection and electrical detection

Besides electrical spin injection, an optical approach based on optical spin orientation is also employed to generate spin-polarized electrons in semiconductors. Optical spin orientation was first demonstrated in 1968 by Lampel¹⁰³. Pierce and Meier¹⁰⁴ subsequently developed an approach by using photoemission for optically detecting spin-oriented electrons emitted from GaAs using a Mott detector. The fundamental mechanism for optical spin orientation is based on the inverse electron transition process to that for the radiative recombination of electrons and holes in III-V semiconductors. For practical applications, electrical detection of spin-polarized carriers generated by circularly polarized light is more important. Figure 1.23 shows the schematic diagram of the semiconductor structure used for optical spin injection and electrical detection. When the semiconductor is irradiated with right- or left-handed circularly polarized light at the band gap energy, spin-polarized electrons and holes with a maximum spin polarization of 50% are generated according to the optical selection rules in the bulk materials. As spin-polarized carriers are generated in a SC embedded in an FM/SC heterostructure, the spin-polarized carriers travel towards the FM/SC Schottky interface under the bias across the interface (forward bias for electrons and inverse bias for holes). As the transmission probability depends on the electron spin orientation due to spin filtering effects, the measurement of spin-dependent photocurrent (the difference ΔI between the photocurrents for excitations by right- and left-handed circularly polarized light) provides information about spin-dependent transport from the SC into the FM across the interface.

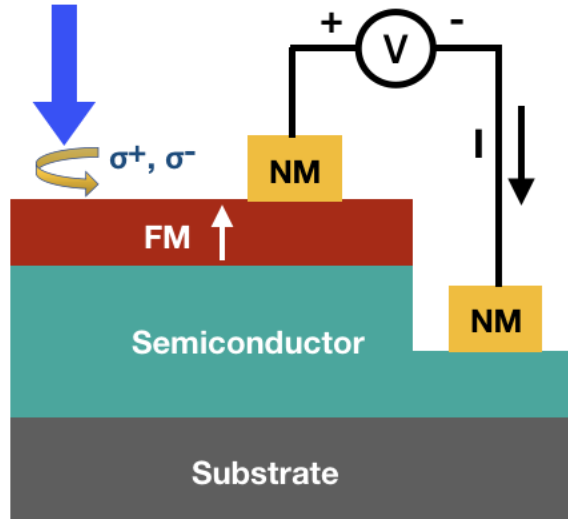


Figure 1.23: Schematic diagram of the semiconductor structure used for optical spin injection and electrical detection.

Recently, our group reported on the growth of CoFeB/MgO/Ge (001) spin photodiodes as shown in Figure 1.24 (a) by using a combination of both molecular beam epitaxy (MBE) and sputtering methods. These heterostructures demonstrated a photocurrent helicity asymmetry of about 0.9% at 9K and 0.1% at RT at the telecommunication wavelength of 1310 nm without any applied magnetic field (Figures 1.24 (b) and (c)).¹⁰⁵

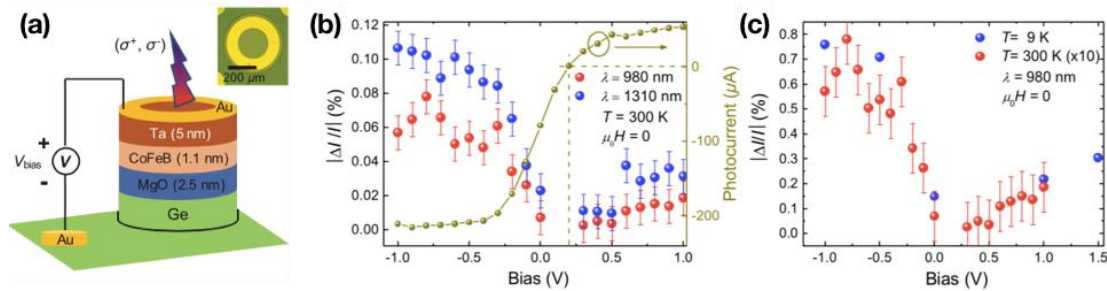


Figure 1.24: (a) Schematics of the Ge-based spin photodiode with the top and bottom contacts. Inset: a typical mesa with a diameter of about 400 μm . (b) $|\Delta I/I|$ measured as a function of the applied bias for two different excitation wavelengths (980 and 1310 nm) at RT without any applied magnetic field. The bias-dependent photocurrent with 980 nm excitation at RT is also shown. At a bias of 0.2V (dashed line), the zero photocurrent indicates a flat band condition. (c) $|\Delta I/I|$ as a function of the applied bias measured at 9 and 300K at zero magnetic field. The excitation wavelength is kept at

980nm. For comparison with the low temperature measurements, the data measured at RT (shown as red circles) is multiplied by 10^{105}

1.3 Summary

In this chapter, we briefly reviewed some basic concepts of metal-based spintronics and semiconductor spintronics. Great progresses have been made in the field of semiconductor spintronics since the discovery of the GMR effect. The efficient spin injection into semiconductor device, together with the subsequent manipulation and detection of the injected spin polarization, is essential to the development of advanced semiconductor spintronics devices. The pioneering experiments have shown different possibilities to study spin injection and detection into semiconductors, which will be helpful for understanding the following studies of spin injection and detection in GaAs and GaN based spin LEDs in this thesis.

Chapter 2 Experimental techniques

This chapter is dedicated to the experimental techniques used for the realization of this doctoral thesis. Most of the work presented here was done at Institut Jean Lamour (IJL), Nancy, France. All the GaN templates used in this thesis were grown by MOCVD in SINANO, Suzhou, China. The GaN LED structures were grown by MOCVD in Peking University, Beijing, China.

2.1 Molecular beam epitaxy (MBE) growth and in-situ monitoring

2.1.1 MBE growth

In this thesis, a MECA 2000 MBE system as shown in Figure 2.1 was used for the fabrication of all the samples. The advantage of MBE lies in its great capability to deposit of ultra-thin layers (up to monolayer thickness) with precise composition and abrupt interfaces. In this section, the MBE system is briefly described, as well as the standard procedure used to grow the spin injector.



Figure 2.1: Photo of the MECA 2000 MBE system.

A schematic of the MBE system is shown in Figure 2.2. Only the components relevant for this work are depicted for the sake of simplicity. Fundamentally, a typical MBE system is equipped with at least two chambers: introduction (load-lock) and growth ones. Prior to growth, the substrate is chemically cleaned in isopropanol and acetone under ultra-sonication to remove any dirt or organic residues from the surface. After simple surface treatments, the substrate is then mounted on a sample holder and put into the load-lock chamber, which is closed and pumped to a rough vacuum by a primary pump. Subsequently, the load-lock chamber is further pumped with a turbo pump to reach a pressure in the order of 10^{-8} Torr in approximately 1 hour. The sample can then be transferred to the growth chamber where they are outgassed under high vacuum (pressure $\sim 10^{-10}$ Torr) at certain temperature to remove water vapor and organic contaminants. The sample is attached to the manipulator, which can be rotated to orient the sample in transfer position (facing the load lock) or in growth position (facing the e-beam source). Then according to what we need, both high temperature growth and low temperature growth can be carried out in our MBE system.

Experimental techniques

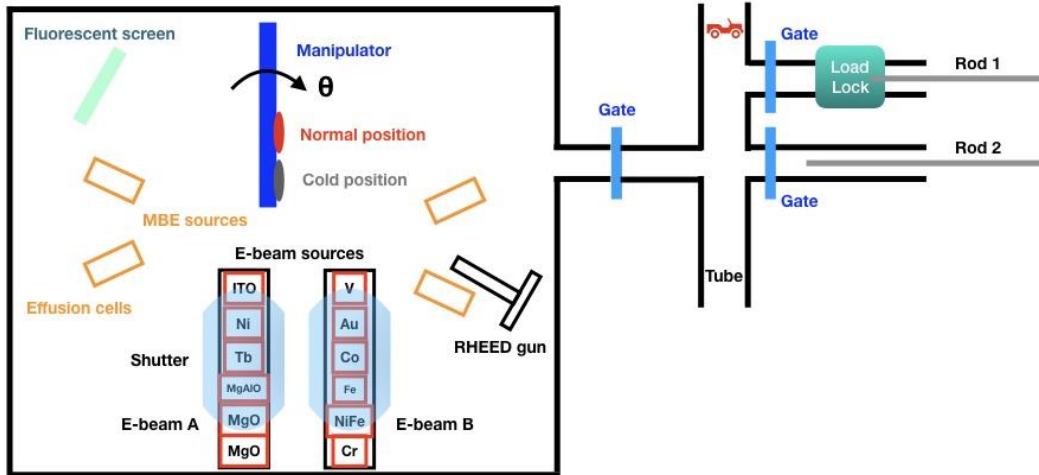


Figure 2.2: A top view of the MECA 2000 MBE system connected with the tube.

All the spin injectors (chapter 4) were grown at normal position. To minimize the metal diffusion into the organic barrier, the deposition temperature of Au/Co was maintained at around 80K by cooling the sample with injection of liquid-N₂ through the sample holder, as shown in Figure 2.3 (a). Figure 2.3 (b) shows cold position and heat position of our MBE system.

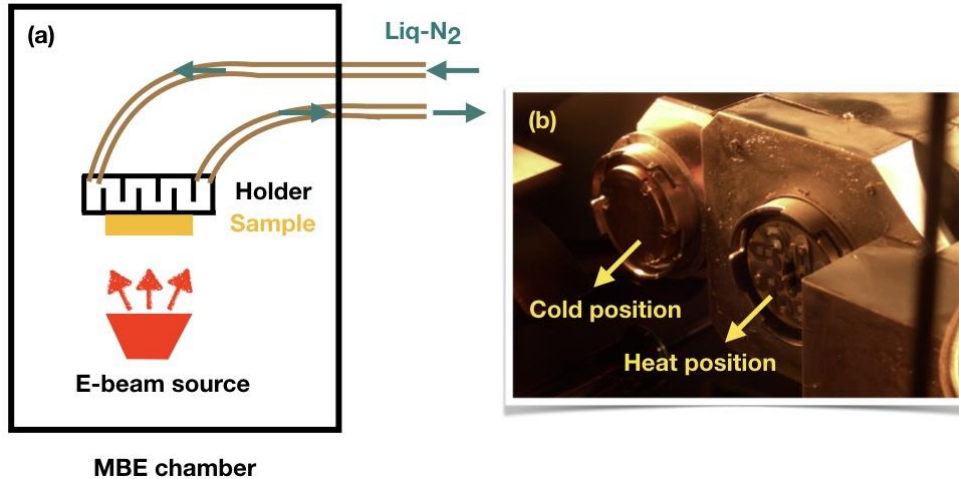


Figure 2.3: (a) Schematic of MBE deposition while keeping the sample temperature at ~80K. This is obtained by injection of liquid-N₂ into the holder that is in close contact with the sample. (b) Photo of cold and heat positions of the MBE system.

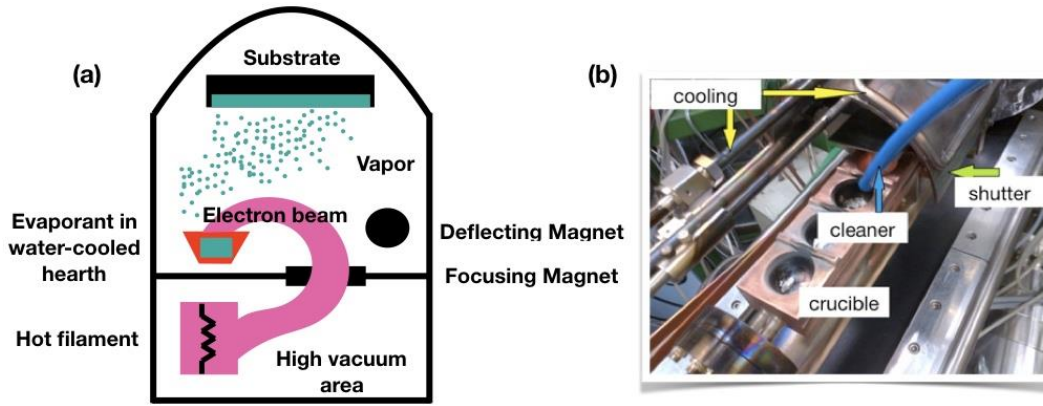


Figure 2.4: (a) Configuration of the electron beam evaporator system. (b) Photo of the e-beam evaporator.

In e-beam evaporation, the source material is bombarded with an e-beam given off a tungsten filament and deflected with magnets in high vacuum. The electron beam leads to the local evaporation or sublimation of the target surface. Depending on the temperature and vacuum level, the target material then evaporates. The vacuum chamber is then coated with a thin solid film formed by the deposition of evaporated atoms. The schematic illustration of e-beam system is provided in Figure 2.4 (a). The source materials we used are put in crucibles, as shown in Figure 2.4 (b). The evaporation rate is monitored by a quartz microbalance system. The growth process is controlled by WINEVAP software.

2.1.2 In-situ monitoring by RHEED

Reflection High-Energy Electron Diffraction (RHEED) is a very important technique for in-situ and real time characterization of growing films. Due to the low penetration of the electron beam and the distinct interactions between the electron beam and the encountered atoms, RHEED is a technique used to characterize the surface of crystalline materials. A typical RHEED system is shown in Figure 2.5. In our MBE system, an electron beam with energy of 30 KV is incident onto a surface at a glancing angle of $1-5^\circ$. The incident electrons diffract at atomic planes close to the surface and a small fraction of the scattered electrons interfere constructively at specific angles (Bragg condition) to form regular patterns on the fluorescent screen. The resultant

visible fluorescent pattern corresponds to the crystal structure of the surface. By analyzing the separation between streaks observed in RHEED patterns, one can get information of the in-plane lattice parameter evolution during growth.

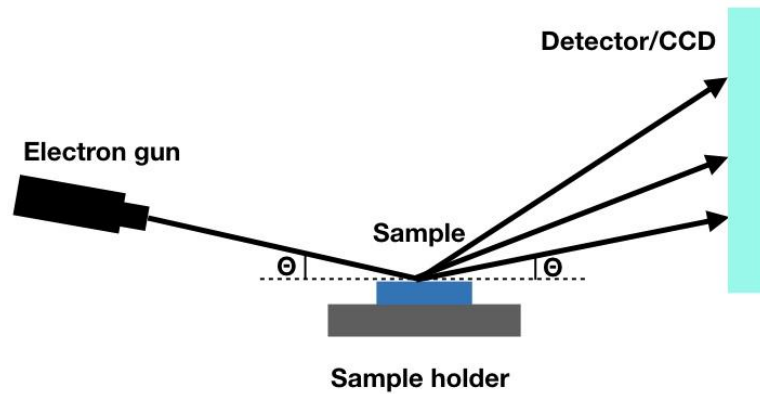


Figure 2.5: Components of a RHEED system.

The basic principle of RHEED is based on the construction of the Ewald sphere. Since the incoming electrons have a high energy, the curvature of the Ewald sphere is low. The intersection between the Ewald sphere and the nodes of the reciprocal surface lattice thus leads to the observation of streaks. Ewald's spheres show the allowed diffraction conditions for kinematically scattered electrons in a given RHEED setup. The diffraction pattern at the screen relates to the Ewald's sphere geometry, so RHEED users can directly calculate the reciprocal lattice of the sample with a RHEED pattern, the energy of the incident electrons and the distance from the detector to the sample. The user must relate the geometry and spacing of the spots of a perfect pattern to the Ewald's sphere in order to determine the reciprocal of the sample surface. Figure 2.6 shows schematically the relation between the geometrical arrangement in RHEED and the reciprocal space (momentum space). K_{in} is wave vector of the incident electron wave. Since we restrict ourselves to elastic scattering only, the diffracted waves K_{out} have the same magnitude of wave vectors as K_{in} . Therefore, when these vectors are drawn from the common origin with that of K_{in} , their end points are on a sphere with its radius K_{in} . This is called as an Ewald sphere. When the sample is assumed, as shown in Figure 2.6, to be atoms arranged equidistantly on a line along the incident beam, the Fourier transform of this atom row is a series of equidistant planes (reciprocal lattice

planes) perpendicular to the atom row. Intersections between the Ewald sphere and the reciprocal lattice planes are a series of circles. The vectors from the center of Ewald, which is the common origin of the wave vectors, to the circles are wave vectors of the diffracted waves. This process for constructing the figure ensures both of the elastic scattering and diffraction conditions fulfilled simultaneously. The circles are actually observed on the fluorescence screen as concentric circles (though only the half of circles above the shadow edge is observed on the screen).

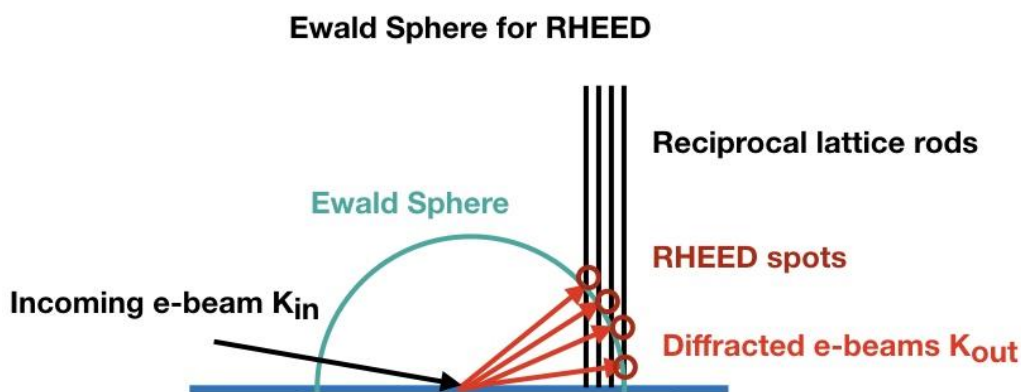


Figure 2.6: Physical principle of the RHEED pattern formation.

RHEED patterns display surface specificity very clearly after the incidence of electron beam in a proper glancing angle ($1-5^\circ$). For an amorphous/polycrystalline surface, the RHEED pattern is made of concentric ring structures (Figure 2.7 (a)). The streaky RHEED patterns shown in Figure 2.7 (b) indicate an atomically flat surface corresponding to planar growth. The RHEED pattern shown in Figure 2.7 (c) is typical of the surface reconstruction of GaAs. The surface reconstruction can depend on the annealing temperature. Therefore, it is possible to effectively evaluate the growth temperature upon change of the surface reconstruction. For instance, GaAs has 2×4 surface reconstruction under a typical of arsenic overpressure at 580°C .^{106,107}

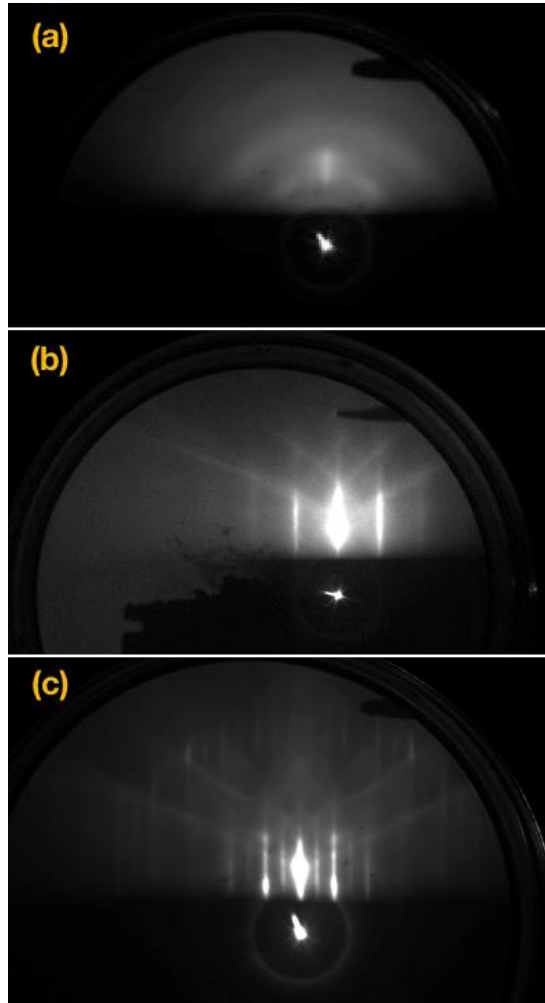


Figure 2.7: RHEED patterns obtained on (a) an amorphous/polycrystalline surface of MgO, (b) a monocrystalline surface of c-plane GaN, (c) a smooth surface of GaAs. Images were taken under a 30KV electron beam with a glancing angle between 1-5° in different azimuths.

RHEED is commonly utilized to evaluate the surface of the sample prior to growth and during the growth. It helps to verify that the substrate is smooth and contaminant free, which is crucial for the overgrowth of high-quality epilayers. In addition, growth parameters such as the growth mode and growth rate are evaluated during the growth by monitoring RHEED intensity oscillations. A smooth surface provides an intense, coherent primary spot, while a rough surface provides a weak, primary spot. Each fraction of a ML growth leads to an increased roughness up to the deposition of 0.5 ML

corresponding to a lower diffracted intensity. For higher coverages up to 1ML, the roughness decreases and hence leads to a higher diffracted intensity. This is shown diagrammatically in Figure 2.8 (a). The number of monolayers can thus be deduced from the number of oscillations (1 oscillation=1 ML). By averaging them over time (in seconds), it becomes possible to determine the growth rate in ML/s. The oscillations will eventually damp out. The reason for the damping is due to the fact that the 2nd ML starts on the wide islands before the 1st ML is fully formed and so on for the 3rd and 4th MLs; hence the system is moving toward some equilibrium surface roughness.

Figure 2.8 (b) displays the intensity oscillations recorded on the specular spot during the growth of 12ML MgAlO_x and MgO barrier on Fe. The clear oscillations of the RHEED intensity demonstrate a two-dimensional layer-by-layer growth.

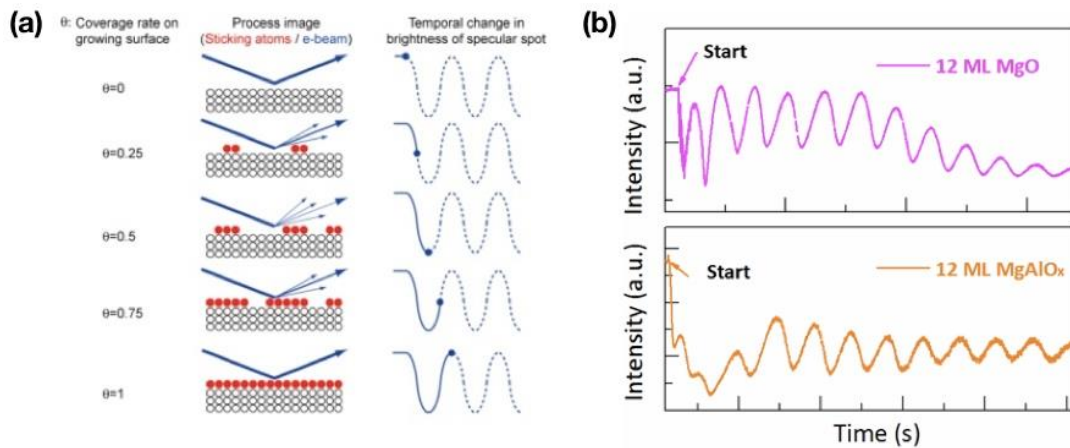


Figure 2.8: (a) RHEED oscillation diagram taken from Neave *et al.* 1983.¹⁰⁸ (b) Oscillations of RHEED intensity recorded during growth of 12ML of MgO and MgAlO_x barriers on Fe.

2.2 Characterizations of full films

Apart from in-situ monitoring during deposition, other ex-situ characterization techniques after deposition (i.e. structural, morphological and electrical) have been used in this thesis.

2.2.1 Transmission Electron Microscopy (TEM)

Transmission electron microscopy (TEM) enables the observation of dislocations and crystal defects inside the bulk of crystals. The electron column shown in Figure 2.9 consists of an electron gun and set of 5 or more electromagnetic lenses operating in vacuum. It is convenient to divide up the TEM into three components: the illumination system, the objective lens/stage, and the imaging system.

Sample preparation is a critical step in TEM characterization. The sample must be thinned to transmit electrons (< 100 nm). Moreover, the sample must be stable under a high-energy electron beam in vacuum.

In the diffraction mode, the pattern comprises an array of spots that corresponds to a particular diffraction vector. In order to facilitate the selection and index the diffraction spots, the diffraction mode is used prior to imaging mode to ultimately form an image.

In the imaging mode, the aperture at the back of the objective lens is used to collect the electron beam to form the image. For the bright field imaging, images are taken from the transmission electrons along the direction of the incident electron beam. The dark field image is collected from the electrons that are scattered off the direction of the incident electron beam, which means the dark field image is created from the diffracted beam.

A perfect crystal will form an image with uniform diffraction intensity while crystal imperfections such as variations in composition, changes in thickness and structural defects will produce image contrast. Dislocations may displace the diffracted planes by altering the separation and orientations. In this thesis, TEM was used to characterize the crystal structure of the spin injector described in chapter 4.

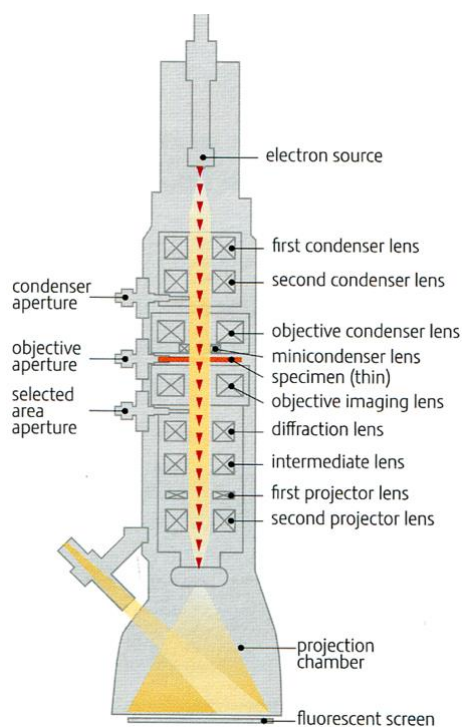


Figure 2.9: Schematic of a TEM column.

Electron energy loss spectroscopy (EELS) typically incorporated into a scanning TEM (STEM) is the analysis of the energy distribution of electrons that pass through a thin sample to analyze the chemical content of the sample. Spectrum imaging (SI) is a method that generates a spatially resolved distribution of EELS data, which was used in our work to do chemical analysis of interface.

All the TEM measurements were done at Institut Jean Lamour, Nancy and CEA LETI, Grenoble.

2.2.2 Atomic Force Microscopy (AFM) and Piezoresponse Force Microscopy (PFM)

Since the first AFM was proposed by G. Binnig and Ch. Gerber in 1986, it has become one of the most commonly used tools for scanning probe microscopy. AFM with the MFP-3D apparatus is used in this study. Detailed information of surface morphology such as mounds, 3D islands, or quantum dots as well as surface defects can be observed directly.

Experimental techniques

AFM allows three-dimensional topographical imaging. It is used to analyze the sample surface and determine the surface roughness. In this technique, a sharp tip mounted on a flexible cantilever scans across the sample surface by maintaining a constant force. A piezoelectric tube scanner derives the scanning motion. The tip-sample interaction is detected by the reflection of a focused laser diode on the back of the cantilever. Cantilever's deflection or oscillation amplitude changes are obtained through a photo detector simply by measuring the difference in output voltages. Systems can be operated in three different modes such as contact, non-contact and tapping. In this work, tapping mode was used. The tip slightly touches the surface and deflection of the cantilever is detected via the position of the laser spot on the photo detector as shown in Figure 2.10.

In this thesis, AFM was done at Institut Jean Lamour, Nancy, France.

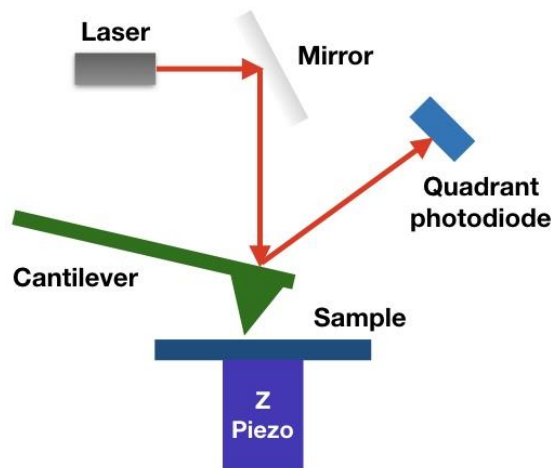


Figure 2.10: A schematic diagram of a typical AFM instrument.

Common AFM provides an ideal platform for local piezoelectric effect study due to the high vertical resolution and high localization of electric field at the junction between the metallized tip and surface. Hence, PFM is a contact-mode AFM in which an electrically biased conductive AFM tip is used as a probe of local electromechanically coupling via the piezoelectric effect. The PFM approach for probing piezoelectric and ferroelectric properties at the nano scale is based on the strong coupling between polarization and mechanical displacement. The coupling can be probed by applying a highly localized electric field to the material and probing the

resultant minute surface displacements with a picometer precision as shown in Figure 2.11. Remarkably, the basic image formation mechanism in PFM is complementary to force-based AFM methods (force is applied and the tip deflection is measured). In this PhD work, PFM done at Artois University, Lille was used to characterize the ferroelectric properties of organic ferroelectric materials.

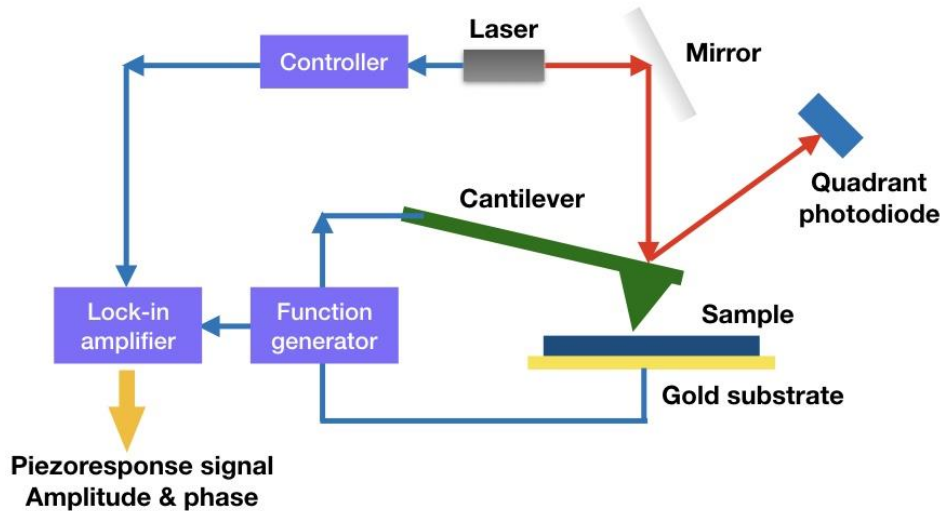


Figure 2.11: Schematic of the PFM arrangement where both AC and DC voltages are applied to the metallized tip and mechanical displacement is measured via conventional AFM method.

2.2.3 Vibrating Sample Magnetometry (VSM) and Superconducting QUantum Interference Device (SQUID)

Vibrating Sample Magnetometry (VSM) is a measurement technique, which allows determining the magnetic moment of a sample with high precision. VSM is based on Faraday's law that states that an electromagnetic force is generated in a coil when there is a change in magnetic flux through the coil. In the measurement setup, a magnetic sample is moving in the proximity of two pickup coils as indicated in Figure 2.12. The oscillator provides a sinusoidal signal that is translated by the transducer assembly into a vertical vibration. The sample which is fixed to the sample rod vibrates with a given frequency and amplitude. If the sample is placed within a uniform magnetic field H , a magnetization M will be induced in the sample. In a VSM, the

sample is placed within suitably placed sensing coils, also held at the desired angle. The vibrating sample component undergoes sinusoidal motion. A magnetic field H appears around the sample and once the vibration begins, and then the magnetization of the sample can be analyzed as changes occur in relation to the timing of movement. A magnetic flux change induces a voltage in the sensing coils that is proportional to the magnetization of the sample. The detected signal changes are converted by the software to the graph magnetization M versus the magnetic field H strength, often referred to as a hysteresis loop as shown in Figure 2.14. The hysteresis loop shows the “history dependent” nature of the magnetization of a ferromagnetic material. Once the material has been driven to saturation, the magnetizing field can then be dropped to zero and the material will retain partly its magnetization.

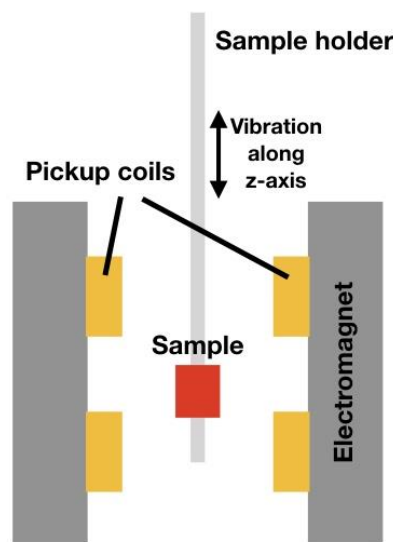


Figure 2.12: Schematic representation of a VSM.

SQUID magnetometers use a superconducting ring with Josephson junctions to measure changes in magnetic field that can be sensitive to a single magnetic flux quantum ($\Phi_0 = 2 \times 10^{-15}$ Wb).¹⁰⁹ The Josephson junctions consist of insulating or non-superconducting material, which separate the superconducting regions of the SQUID as shown in Figure 2.13. If a constant biasing current is maintained in the SQUID, the measured voltage oscillates with the changes in phase at the two junctions, which depend upon the change in the magnetic flux. For conventional VSM, a changing flux

Experimental techniques

is required to generate signal by using vibration. However, for SQUID VSM, thanks to the Josephson Macroscopic Quantum Effect, the flux itself generates a signal and there is no need for changing the flux. Vibration mode is used to speed up data acquisition and filter out noise using lock-in modulation. A Quantum Design Magnetic Properties Measurement System was used for magnetic property measurement carried out in this thesis.

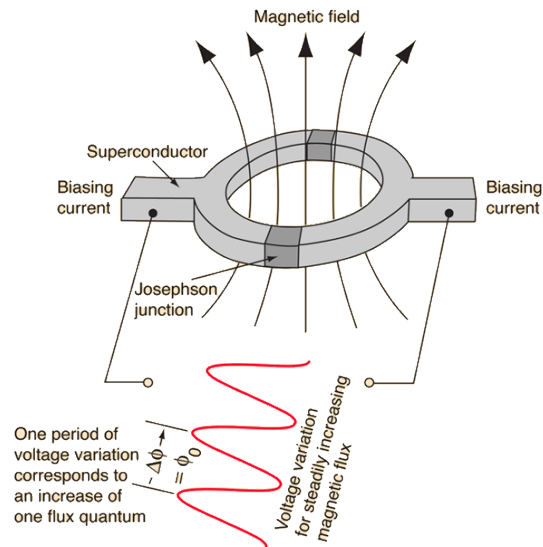


Figure 2.13: Schematic representation of a SQUID magnetometers.

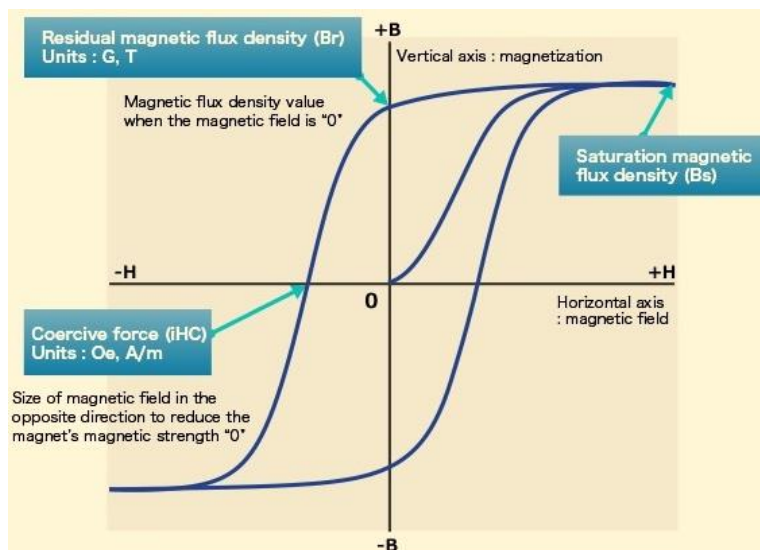


Figure 2.14: A typical hysteresis loop.

2.3 Device Processing and characterizations

In this section, several techniques about fabrication processes and characterizations of the spin light emitting diodes (spin-LED) will be presented.

2.3.1 Device fabrication

2.3.1.1 Sample preparation

The device fabrication starts with the preparation of the samples. First of all, it is necessary to remove the contaminants coming from ambient. The standard cleaning procedure includes dipping the sample in acetone followed by isopropanol (IPA) for 1min by using spin-coater. The samples are then dried by blowing nitrogen gas (N_2).

2.3.1.2 Photo-lithography

Lithography is one of the basic steps in the processing of any semiconductor device. The aim is the transfer of patterns from a mask to a photoresist. The photolithography system we used is MJB4 mask aligner from SUSS MicroTec.

Optical lithography necessitates ultraviolet (UV) light sensitive polymers called photoresists. The process steps right after substrate cleaning contains photoresist coating, soft baking, UV exposure and development. A thin layer of photoresist is deposited onto the cleaned samples using spin coating. The thickness of the resist is determined by the spinning speed and time. A uniform resist layer is necessary for a good quality lithography. Right after, the sample is baked to remove the solvent from the resist and increase its adhesion to the substrate. The mask is then aligned using a mask aligner system. The configuration is presented in Figure 2.15. The aligned sample is exposed to the UV light for a certain amount of time depending on the type of the photoresist. Finally, the patterns are developed using proper developer. The removal of resists is performed with a procedure called lift-off. Different type of resists can be used depending on the application. The photoresists can be divided into two categories as

Experimental techniques

positive or negative. For positive photoresists, the exposed areas are removed during the development stage, whereas for negative ones, regions behind the masks are removed. The exact patterns in the mask are transferred to the substrate upon the use of positive photoresists. The reverse image is obtained upon the use of negative photoresist as shown in Figure 2.16. Positive photoresists were used in our device processes.

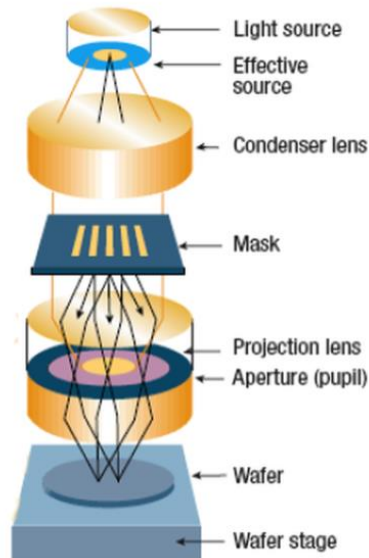


Figure 2.15: Configuration of the mask aligner system.

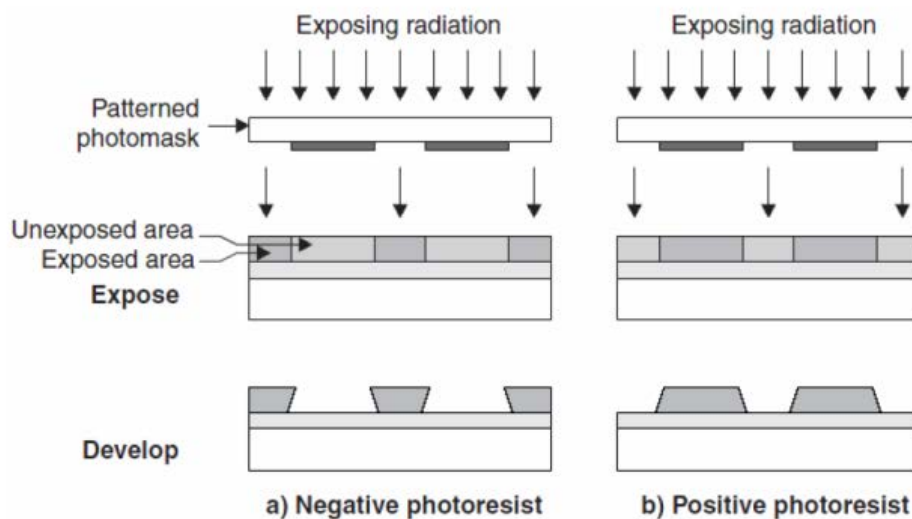


Figure 2.16: Pattering using (a) positive and (b) negative photoresist.

2.3.1.3 Ion beam etching (IBE)

The etching system we used is ion beam etching (IBE) from 4 WAVE. IBE uses an energetic, broad beam collimated and highly directional ion source to physically mill material from a substrate mounted on a rotating holder with adjustable tilt angle. Figure 2.17 shows the schematic diagram of our IBE system. The ion sources used are gridded ion sources of the Kaufman type and are typically neutralized with an independent electron source. The highly collimated, directional ion flux allows for anisotropic etching of any material. The ability to modify the angle of the substrate allows the creation of processes that result in tailored sidewall profiles with minimal sputtered redeposition on overlying masks.

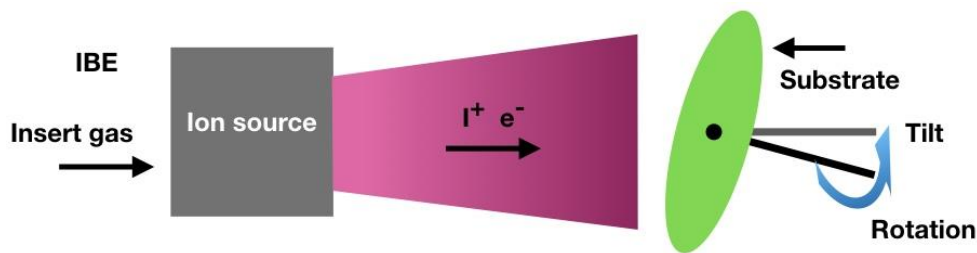


Figure 2.17: Schematic diagram of IBE system.

To fabricate the mesas, the top layers should be etched down to p-type GaN layer (LED structures we used are reversed and n-type GaN layer is on the top, see chapter 4). Since the bond energies in III-nitrides are very strong, wet etching results in small etching rates, rough surface and sidewalls, inhomogeneous depth and negative slope. Thus, dry etching is preferred. During etching process, SIMS analysis was used to monitor the process and to define the depth at which the etching is stopped.

2.3.2 Device characterizations

2.3.2.1 Electroluminescence (EL) set-up

After finishing the fabrication of spin LED devices, we have to do EL measurements. Spin injection is characterized by an intensity difference between left

Experimental techniques

and right circularly polarized emitted light. The detection scheme is rather simple. The emitted light passes through a $\lambda/4$ plate and a linear polarizer. The $\lambda/4$ plate changes the circularly polarized light to linearly polarized light, which is then analyzed with a linear polarizer. After transmission of the $\lambda/4$ plate, right-handed circular polarized light is linear polarized $+45^\circ$ and left-handed circular polarized light is linear polarized -45° with respect to the neutral axis of the quarter wave plate. The following linear polarizer has to be placed with an angle of $+45^\circ$ with respect to the neutral axis in order to measure the intensity of the right-handed circular polarization light I^{σ^+} . To measure the intensity of the left-handed circular polarized light I^{σ^-} , the quarter wave plate has to be turned by 90° (or -45° starting from the neutral axis). Figure 2.18 shows the general setup. The optics has to be adapted for the wavelength of the emitted light. The sample was glued onto a chip carrier that was mounted on a sample holder with electrical connections. For our polarization-resolved electroluminescence (EL) measurements, the spin-LED was placed into an electromagnet, providing a maximum magnetic field (B) of 1.5T normal to the sample plane. The EL signal was detected in the Faraday geometry where the light is collected in the direction of the external applied magnetic field. The circular polarization P_c of the EL is defined as $P_c = (I^{\sigma^+} - I^{\sigma^-}) / (I^{\sigma^+} + I^{\sigma^-})$ where I^{σ^+} and I^{σ^-} are the intensities of the right and left circularly polarized components of the luminescence, respectively.

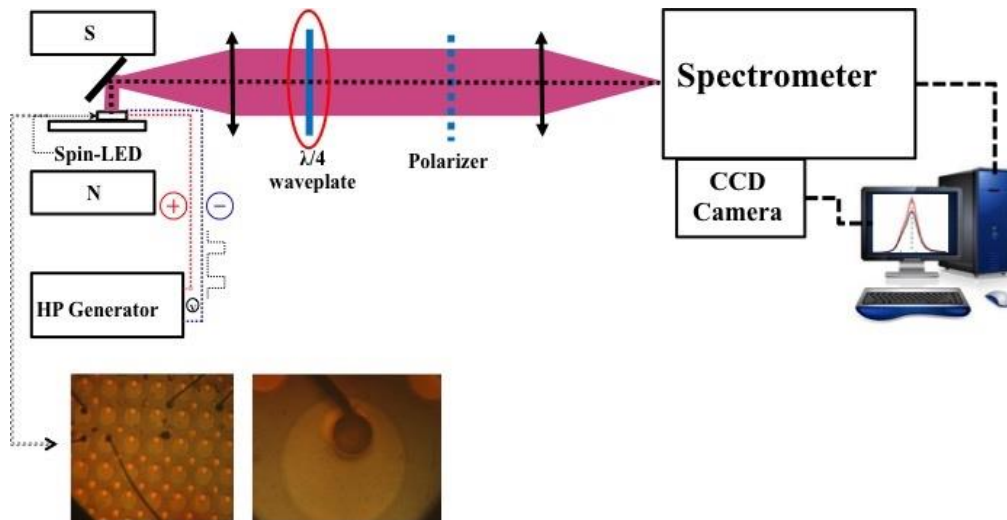


Figure 2.18: Setup developed for polarization-resolved EL measurement. The optical components are placed close to an intermediate focus to gather all the light with the optics. In the experiment, the quarter wave plate is turned by $\pm 45^\circ$, while maintaining fixed the linear polarizer.

2.3.2.2 Magneto-resistance measurement

Magneto-transport measurements are very important for the characterization of organic multiferroic tunnel junctions (OMFTJs). The measurements were performed in a close cycle cryostat by varying the temperature from 10 to 300K with a magnetic field up to 4kOe. I-V measurements were performed in two-terminal geometry by using a Keithley 2400 as a voltage source and a Keithley 6487 picoamperometer to measure the current. To polarize the PVDF barrier, electric voltage pulses with a ramp of 0.1V/s and a duration of 1s were applied to the junction at various voltages. Figure 2.19 shows the configuration of the magneto-transport measurement system.

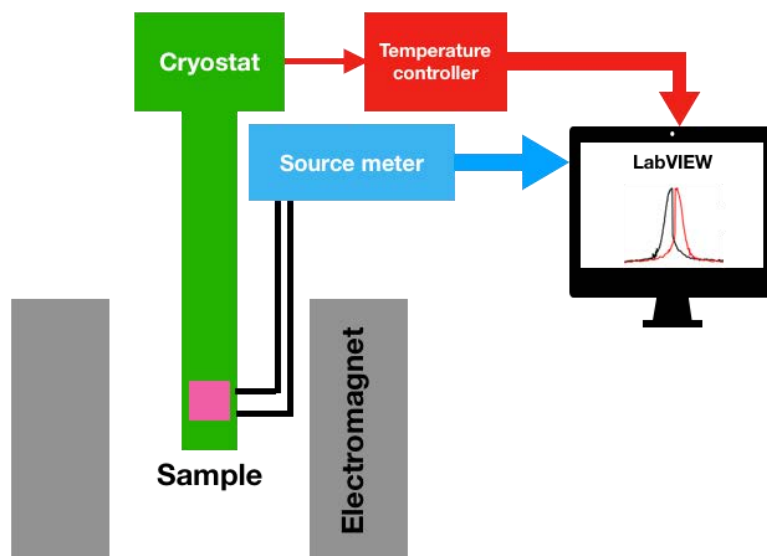


Figure 2.19: Configuration of magneto-transport measurement system.

Chapter 3 GaAs based Spin LED

In this chapter, we will firstly introduce the state-of-the-art of the research on GaAs based spin-LEDs. Then we will show our very recent work about polarization-resolved EL measurements from an ensemble of p-doped InAs/GaAs QDs embedded in a GaAs based spin-LED.

3.1 Spin LED device

3.1.1 Spin-LED concept and optical selection rules

A Spin-LED is a Light Emitting Diode structure capped with a ferromagnetic spin injector used to spin-polarize the carriers before their injection into the active region of the LED structure. Figure 3.1 shows the schematic band structure of a n-i-p spin-LED. The LED structure is typically a semiconductor heterostructure including an electron reservoir (n-doped region) and a hole reservoir (p-doped region) separated by a nearly intrinsic semiconductor region. The radiative recombination of spin-polarized electrons with unpolarized holes leads to the emission of circularly polarized light. Depending on the spin polarization, right or left circularly polarized light will be emitted. The first significant spin injection into a LED structure was realized by Fiederling *et al.* by using a II-VI Diluted Magnetic Semiconductor (DMS) injector on top of an AlGaAs/GaAs QW LED structure.⁵⁸

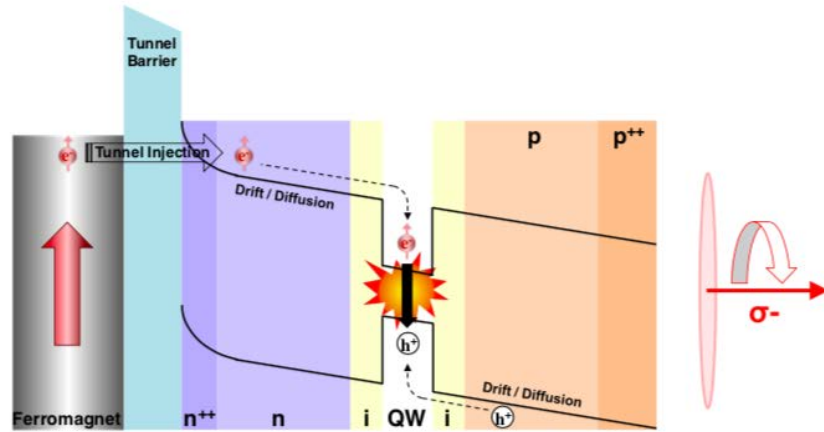


Figure 3.1: Schematic band structure of a n-i-p spin LED.

To study the spin injection across a ferromagnet/semiconductor interface, the development of appropriate techniques for detecting electron spin polarization in a semiconductor is essential. The basic concept underlying the optical approach is the analysis of the circular polarization of the electroluminescence when spin-polarized electrons are injected into III-V semiconductor quantum wells (QWs) such as GaAs. In the direct band gap semiconductor GaAs, the conduction band (s-character) is two-fold spin degenerated, whereas the valence band (p-character) is four-fold degenerated (heavy- and light-hole spin). The situation is schematically depicted in Figure 3.2. In bulk GaAs, the hh and lh states are degenerated at the Γ -point. The spin degeneracy can be lifted by applying a magnetic field, and the light-hole (lh)/ heavy-hole (hh) degeneracy can be lifted by, for instance, by biaxial strain or confinement. When the conduction-band states are occupied with carriers of one spin orientation only, for instance by injecting spin $-1/2$ electrons from a ferromagnetic contact, then according to the selection rule for the magnetic quantum number m_j ($m_j = \pm 1$), only two transitions are possible: one heavy-hole transition (from $-1/2$ to $-3/2$) and one light-hole transition (from $-1/2$ to $+1/2$). While the heavy-hole transition is circularly polarized in one direction (called σ^+ circular right polarization), the light-hole transition is polarized in the opposite direction (σ^- circular left polarization). The transition probabilities to the heavy-hole subband and the light-hole subband are different; the transition probability to the heavy-hole subband is a factor of three larger than that of the light-hole transition,

leading to light with a maximum circular polarization of 50% given an injection of fully spin-polarized electrons. The electron spin polarization is defined as:

$$P_s = \frac{n_+ - n_-}{n_+ + n_-}.$$

Here, n_{\pm} are the densities of electrons in the $+1/2$ and $-1/2$ electron states, respectively. If $I(\sigma^+)$ and $I(\sigma^-)$ are the intensities for the right and left circularly polarized light, the circular polarization degree can be described as:

$$P_{circ} = \frac{I(\sigma^+) - I(\sigma^-)}{I(\sigma^+) + I(\sigma^-)}.$$

Then we assume that each hole state is sufficiently populated and thus the electron densities are the only limiting factors for optical transitions. Then the equation can be reformed to:

$$P_{circ} = \frac{I(\sigma^+) - I(\sigma^-)}{I(\sigma^+) + I(\sigma^-)} = \frac{(n_+ + 3n_-) - (3n_+ + n_-)}{(n_+ + 3n_-) + (3n_+ + n_-)} = -\frac{P_s}{2}.$$

This shows that the circular polarization degree (CPD) of the light emitted from a QW is always 50% of the electron spin-polarization degree. This correlation is valid as long as we consider both lh and hh transitions. However, the energetic separation of hh and lh states even allows for higher polarization degrees: if the emission is energy selective, that is, if only the hh-electron transition takes place, a CPD of up to 100% can be obtained for an electron spin-polarization degree of -1. As mentioned above, these selection rules directly link the spin polarization of the carriers and the polarization of the emitted light. This approach can be used to quantify the efficiency of spin injection across the FM/SC interface. For the surface detection geometry, a spin injector with perpendicular magnetic anisotropy is needed. In contrast, for the edge detection geometry, an in-plane spin injector is needed. Figure 3.3 shows different detection geometries used for spin-LEDs.

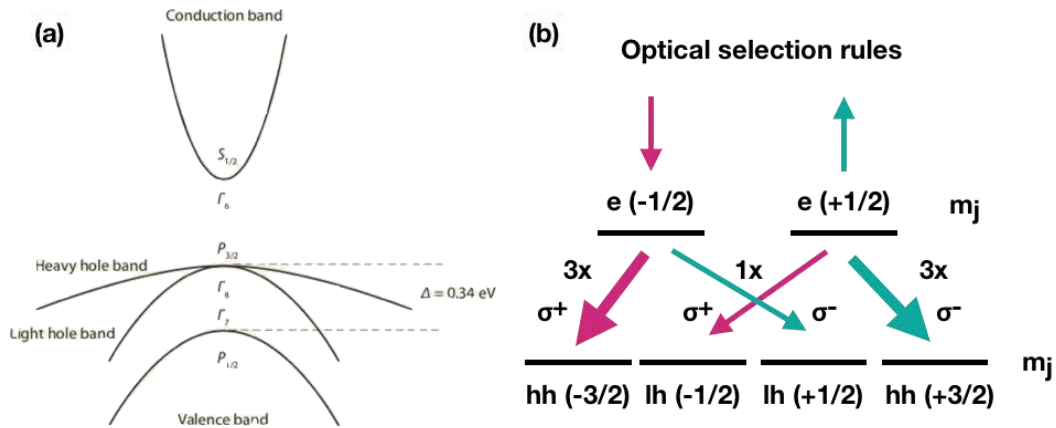


Figure 3.2: Selection rules for optical transitions in GaAs. (a) Band diagram for GaAs. (b) The quantum numbers m_j , which correspond to the z-projections of the total angular momentum of each Bloch state are printed in brackets. The transition rates and the associated circular polarization states are plotted next to the transition. The transition matrix element for heavy-hole transitions is a factor of 3 larger than for light-hole transitions.

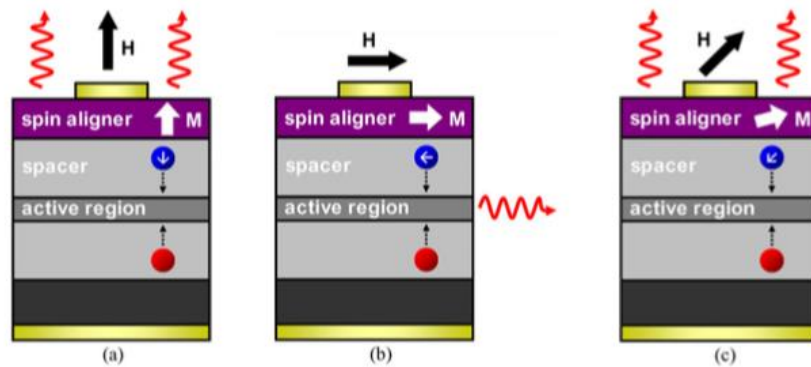


Figure 3.3: Schematic representation of a spin-LED under the (a) Faraday, (b) quasi-Voigt and (c) oblique Hanle effect geometries.²

3.1.2 Potential applications of spin-LEDs

Spintronics is an emerging multi-disciplinary field, which investigates the role played by both electron and nuclear spins in solid-state physics.¹ The dominant goal of these investigations is to develop devices that exploit spin instead of, or in addition to, the charge degree of freedom, which would lead to new multifunctional devices providing non-volatility, higher processing speeds, higher packing densities and

reduced power consumption. Spin light emitting diodes (spin-LEDs) and spin-polarized lasers (spin-laser)² are an important class of semiconductor spintronic devices.

In these devices, spin-polarized electrons (or holes) are injected into an active region of a LED where they recombine radiatively with unpolarized holes (or electrons) to emit preferentially right- or left-circularly polarized light. The direct link between the spin and the optical polarizations makes spin-polarized light sources uniquely suited for a number of applications.

At a very fundamental level, spin-polarized light sources allow for the straightforward detection of spins in semiconductor heterostructures. In addition, spin-LEDs encode the electron spin information into circular polarized light and show strong potential applications in advanced semiconductor technologies. For example,

- ◇ Optical transport of information³, which is necessary for the full implementation of spintronic circuits to transmit spin information from one device to another separated by a long distance. The information can be stored in a magnetic memory and read out with light emission.
- ◇ Spin-LED can be used as advanced optical switches. Switching through the circular polarization instead of on/off states, which is expected to be much faster.
- ◇ It can also be used for quantum cryptography⁴ for optical telecommunication by using two circular polarization states.
- ◇ Spin-LED can also be used to examine DNA chirality.
- ◇ It can also be used for three-dimensional displays⁵. Left- and right-circularly polarized light emitted from the light-emitting diode can be switched by spin reversal, playing a role in binocular vision for stereoscopic imaging by an optical shutter system with polarizer eyewear. This kind of new display system is expected to have many advantages including high spatial resolution, feasibility of a large-scale stereoscopic display panel in the open air, and so on.

Spin LEDs could be the first application of semiconductor spintronics. All of these applications require that devices could work at zero magnetic field and at room

temperature. The development of a perpendicular spin-injector, allowing to work in remanent conditions, is therefore of paramount importance.

3.2 GaAs based spin LEDs: a review

3.2.1 In-plane spin injector

In 1999, the concept of a spin light emitting diode (spin-LED) was first introduced. The degree of spin injection from a magnetic injector into the underlying GaAs based LED structure is determined by measuring the degree of circular polarization of the emitted light. Fiederling *et al.* used the paramagnetic semiconductor $\text{Be}_x\text{Mn}_y\text{Zn}_{1-x-y}\text{Se}$ as a spin aligner and achieved an injection efficiency of 90% spin-polarized current into a GaAs based spin LED at low temperature.⁶¹ Ohno *et al.* utilized the ferromagnetic semiconductor $\text{Ga}_x\text{Mn}_{1-x}\text{As}$ to align the electron spins and to obtain spin injection into GaAs with efficiency of the order of 1% at low temperatures.⁶² Subsequently, many kinds of spin-injectors employing common ferromagnetic (FM) 3d-transition metals, such as Fe^{78,110,111,112,113,114,115}, Co^{74,116}, CoFe^{75,79,117}, and CoFeB^{118,119}, were developed to obtain circularly polarized light at room temperature. Zhu *et al.* demonstrated spin injection from a Fe film grown on a GaAs/InGaAs based structure leading to a spin injection efficiency of 2% from polarization resolved EL measurements.¹⁰⁷ However, even if one forgets the technical difficulties due to the reactivity of the transition metals with most semiconductors, there are fundamental problems that strongly limit the spin-polarization of the injected electrons, as this has been clearly shown by Schmidt *et al.* By solving the spin transport equations at a ferromagnetic (FM)/Semiconductor (SC) interface, Schmidt *et al.* found that the spin-polarization of the current in the semiconductor became very small when the resistivity of the SC was much higher than that of the FM metal. It has been shown that the conductance mismatch between FM and semiconductors⁶⁷ can be solved by inserting either a tunnel barrier layer or a Schottky barrier^{107,108,109,110,111,113} AlO_x ^{109,112} and MgO ^{114,115,116} between the injector and the semiconductor.^{70,71} A high circular polarization P_c of about 30% at room

temperature has been reported by using a CoFe/MgO (100) tunnel injector.¹¹⁴ Figure 3.4 shows a high-resolution transmission electron microscopy image of the CoFe/MgO spin injector. Both the MgO and CoFe layers are very smooth and polycrystalline with a strong (100) texture along the growth direction.¹¹⁴ Ferromagnetic contacts usually exhibit in-plane magnetization because of the shape anisotropy. Thus, an external magnetic field of about 2T or more is needed to turn the magnetization into the perpendicular direction. This is a major problem for future applications, and effects induced by the magnetic field superimpose with the effects related to pure spin injection. A comparative summary of spin-injection efficiencies is given in Table 3.1 (for in-plane spin injectors).

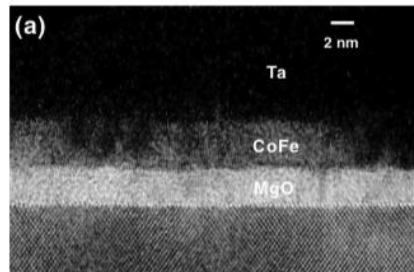


Figure 3.4: Cross sectional TEM image of the CoFe/MgO spin injector.¹¹⁴

GaAs based spin LED

In-plane spin-injector	Interface contacts	Semiconductor detector	Circular polarization (%)	Ref.
MnAs	Schottky barrier	GaAs/InGaAs/GaAs QW	1	Ramsteiner 2002 ¹²⁰
Co ₂ MnGe	Schottky barrier	AlGaAs/GaAs/AlGaAs QW	13	Dong 2005 ¹²¹
Co ₂ FeSi	Schottky barrier	AlGaAs/GaAs/AlGaAs QW	17	Ramsteiner 2008 ¹²²
Fe	Schottky barrier	GaAs/InGaAs/GaAs QW	2	Zhu 2001 ¹¹⁰
Fe	Schottky barrier	AlGaAs/GaAs/AlGaAs QW	32	Hanbicki 2003 ¹¹¹
Fe	Schottky barrier	GaAs/InAs/GaAs QW	27	Li 2007 ¹²³
Co	Schottky barrier	AlGaAs/GaAs/AlGaAs QW	4	Liu 2003 ¹¹⁶
CoFe	Al ₂ O ₃ tunnel barrier	AlGaAs/GaAs/AlGaAs QW	21	Motsnyi 2003 ¹²⁴
CoFe	MgO tunnel barrier	AlGaAs/GaAs/AlGaAs QW	57(5T)	Jiang 2005 ⁸¹
CoFeB	MgO tunnel barrier	AlGaAs/GaAs/AlGaAs QW	32(0.8T)	Lu 2008 ¹¹⁸
NiFe	CoFe/Al ₂ O ₃ /CoFe/NiFe hot electron injection	GaAs/InGaAs/GaAs QW	13	Jiang 2003 ¹²⁵
Fe	Schottky barrier	GaAs/InAs/GaAs QD	5	Li 2005 ¹²⁶
Co	Al ₂ O ₃ tunnel barrier	GaAs/InAs/GaAs QD	15	Lombez 2007 ¹²⁷

Table 3.1: Summary of circular polarization degree obtained for various in-plane spin-injectors.

3.2.2 Out-of-plane spin injector

According to the optical selection rules,^{128,129} the magnetization of the spin injector has to be maintained perpendicular to the LED surface in order to emit circularly polarized light using the surface emission geometry. As mentioned before, this usually requires a strong external magnetic field up to several Tesla to keep the perpendicular magnetization. For practical applications, it is important to realize remanent spin injection at zero or small magnetic field. This requires the development of spin injectors with perpendicular magnetic anisotropy (PMA) to overcome the

demagnetization field, which tend to maintain the magnetization in plane. Results involving several kinds of spin injectors with PMA including Fe/Tb,^{130,131} Co/Pt,^{132,133} FePt¹³⁴ and δ -MnGa¹³⁵ with either Schottky or MgO barriers have been reported. However, the remanent Pc was limited to only 3%-4% due to the low spin polarization at the FM/semiconductor interface. One of the best results has been obtained by using a 7 nm thick δ -MnGa layer.¹²⁴ A comparative summary of circular polarization degree for various out-of-plane spin injectors is given in Table 3.2.

Out-of-plane spin injector	Interface contact	Semiconductor detector	Circular polarization (%)	Ref.
Fe/Tb	Schottky barrier	GaAs/InGaAs/GaAs QW	0.4	Gerhardt 2005 ¹³⁰
FePt	MgO tunnel barrier	AlGaAs/GaAs/AlGaAs QW	1.5	Sinsarp 2007 ¹³⁴
δ -MnGa	Schottky barrier	AlGaAs/GaAs/AlGaAs QW	3.5	Adelmann 2006 ¹³⁵
Fe/Tb	Schottky and MgO	AlGaAs/GaAs/AlGaAs QW	3	Hovel 2008B ¹³¹
Co/Ni	MgO tunnel barrier	AlGaAs/GaAs/AlGaAs QW	3	Zarpellon 2012 ¹³³

Table 3.2: Summary of circular polarization degree obtained for various out-of-plane spin injectors.

3.2.3 CoFeB/MgO spin injector exhibiting PMA on a GaAs LED

In our group's previous work,^{136,137} we have demonstrated large and robust remanent spin injection into a GaAs based LEDs by using Ta/CoFeB/MgO spin injectors with strong PMA thanks to the interfacial anisotropy at the FM/oxide interface.¹³⁸ Large values of circular polarization degree reaching 20% at 25 K and 8% at 300 K were measured under zero applied field. Figure 3.4 (a) shows the whole structure of the sample, where the spin injector consists of a 1.2 nm thick CoFeB layer annealed at 300°C. The low magnification image shown in the inset of Figure 3.5 (b) indicates a good homogeneity and a sharp MgO/GaAs interface. The HRTEM image

shown in Figure 3.5 (b) reveals a MgO (001) texture with an abrupt interface to both CoFeB and GaAs layers.

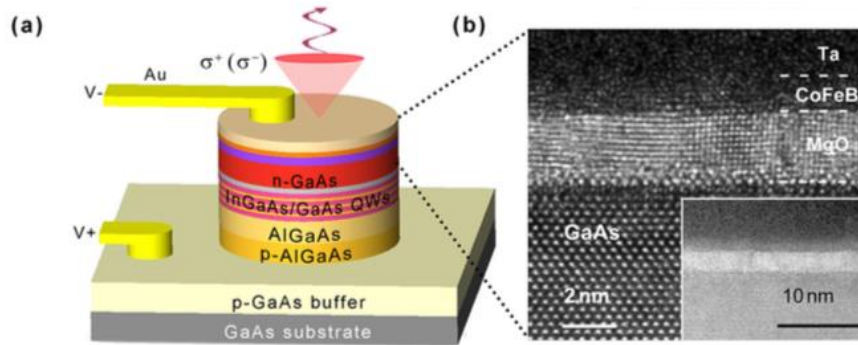


Figure 3.5: (a) Schematic diagram of the spin-LED device structure. (b) HRTEM images of the CoFeB/MgO PMA injector. Inset: low magnification image showing excellent homogeneity and low interface roughness.¹³⁶

Figure 3.6 (a) displays the out-of-plane magnetization (M) vs external magnetic field (H) curves for spin injectors with different CoFeB thicknesses annealed at 250°C. When the thickness is lower than 1.2nm, the CoFeB possesses a remanent out-of-plane magnetization indicating the occurrence of PMA. This can be easily understood from the competition between the bulk in-plane shape anisotropy (K_b) and the interface anisotropy (K_i) which is inversely proportional to the layer thickness. From the analysis of saturation magnetization (M_s) vs CoFeB thickness and the loss of M_s for small layer thicknesses (Figure 3.6 (b)), we can determine a CoFeB magnetic dead layer thickness of about $t_d=(0.5\pm 0.2)\text{nm}$, which can be attributed to intermixing at the top Ta/CoFeB interface during either deposition or during annealing. The PMA energy density per unit volume (K_{eff}) varies with the effective CoFeB thickness ($t_{\text{eff}}=t_{\text{CoFeB}}-t_d$) (Figure 3.6 (c)) and can be obtained from the integrated difference between the out-of-plane and the in-plane M-H curves. When $K_{\text{eff}}>0$, the CoFeB is characterized by a perpendicular easy axis of magnetization, and K_i can be obtained from the intercept of $K_{\text{eff}}\cdot t_{\text{eff}}$ vs t_{eff} . The value found from our group's result is about $0.63\pm 0.10 \text{ mJ/m}^2$. The annealing temperature is critical for obtaining a good PMA. The optimized annealing temperature

was found to be around 250°C. Below or above this temperature, the PMA is much reduced, and the magnetization rotates back along the in-plane direction. As already investigated theoretically by Yang *et al.*,¹³⁹ the PMA is very sensitive to the Fe(Co)/MgO interface chemical structure. The improvement of PMA at T_{an} up to 250°C can be attributed to an optimization of the chemical structure at the CoFeB/MgO interface.

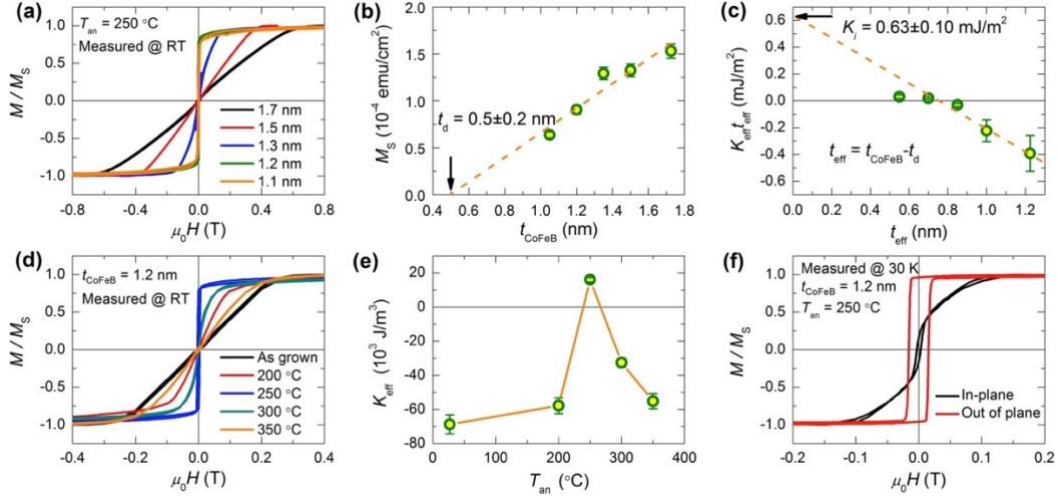


Figure 3.6: (a) RT out-of-plane M-H curves for spin injectors with different CoFeB thicknesses annealed at 250°C. (b) Extrapolation of CoFeB magnetic dead layer t_d from the CoFeB thickness-dependent saturation magnetization M_s . (c) t_{eff} dependence of the $K_{eff} t_{eff}$ product. The intercept to the vertical axis of the linear extrapolation corresponds to K_i . (d) RT out-of-plane M-H curves for spin injectors with 1.2 nm thick CoFeB before and after annealing at various temperatures. (e) K_{eff} as a function of annealing temperature. (f) M-H curves at 30K for a 1.2 nm thick CoFeB layer annealed at 250°C for both in-plane and out-of-plane configurations.¹³⁶

To get a better understanding of the origin of the PMA, ab initio calculations have been performed. The slab used for the calculations was composed of three MgO layers sandwiched between five Fe layers at both sides as shown in Figure 3.7 (a) (middle). A $19 \times 19 \times 3$ k-point mesh was used in the calculations. In bulk Fe with bcc structure, the charge distribution in the 3d shell is almost isotropic, as well as the resulting average orbital moment. The orbital moment acquired in the plane of the layer exactly

compensates that acquired along the out-of-plane direction by equal filling of the corresponding orbitals. In contrast to a bulk Fe film, the Fe/MgO interface exhibits a strong uniaxial character. The out-of-plane Fe $3d_z^2$ orbital strongly bonds to the O $2p_z$ orbital, which introduces a significant charge transfer from Fe to O orbitals (see the inset of Figure 3.7 (a) on the left). This results in a lack of electrons within the Fe $3d_z^2$, $3dxz$, and $3dyz$ out-of-plane orbitals compared to the Fe in-plane orbitals ($3dx^2-y^2$ and $3dxy$). An enhanced out-of-plane orbital moment occurs from the uncompensated in-plane orbitals and generates a sizeable PMA once the spin-orbit coupling (SOC) is introduced. As shown on the right in Figure 3.7 (a), from the integration of the occupied states below the Fermi level (E_F), we found a difference of about 3% between out-of-plane and in-plane orbitals for Fe atoms bound to O atoms at the interface (Fe5), while almost no difference appears for Fe in the bulk (Fe3). This yields an unbalanced orbital moment anisotropy ($\Delta\mu\approx 0.03\mu_B$) associated with the magnetization or spins in the out-of-plane direction from the interfacial atom Fe5 (and Fe1). Consequently, the PMA originates from a net uncompensated out-of-plane orbital moment at the Fe(Co)/MgO interface. Such a sizable anisotropy of orbital moment is expected to be very sensitive to the interface atomic configuration and bonding. For the overoxidized Fe/MgO interface, since the bonding mechanism with O species occurs now along both out-of-plane and in-plane directions, the stronger bonding along the in-plane direction results in a higher out-of-plane orbital occupation. This completely changes the interface anisotropy and promotes an in-plane magnetization orientation at the interface. Concerning the underoxidized interface, a lack of bonding with O species makes an almost equivalent orbital occupation for in-plane and out-of-plane orbitals, which also reduces the PMA.

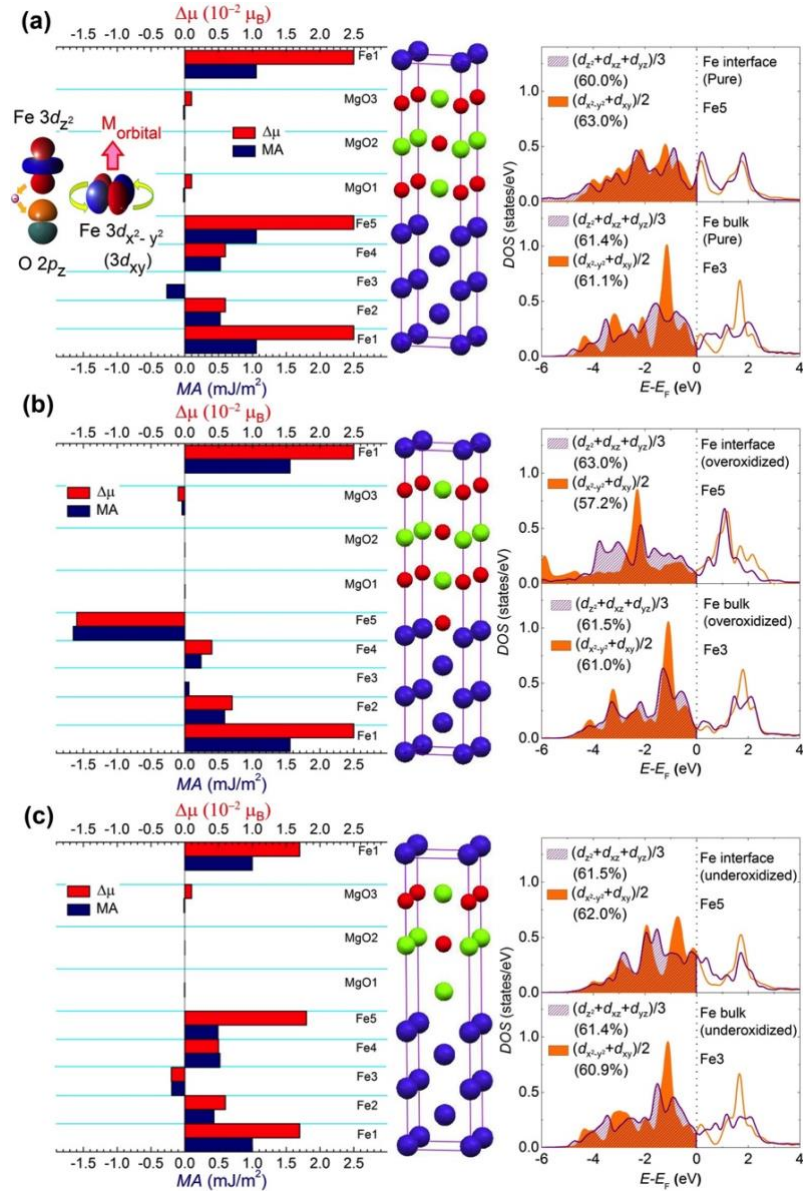


Figure 3.7: (a) Left: layer-resolved orbital moment anisotropy along with magnetic anisotropy (MA) energy. Middle: schematics of the calculated crystalline structures. Fe, Mg and O are represented by blue, green and red balls, respectively. Right: DOS with SOC for averaged Fe 3d out-of-plane and in-plane orbitals with Fe both at the interface (Fe5) and in the bulk (Fe3). Inset: a simple picture showing that the origin of PMA comes from the hybridization of Fe out-of-plane orbitals and O $2p_z$ orbitals, which leads to an uncompensated charge occupation in Fe in-plane orbitals and results in an enhanced out-of-plane orbital moment for PMA. Two other different interfaces structures: (b) overoxidized and (c) underoxidized geometries.¹³⁶

Furthermore, a perpendicular magnetic tunnel junction (MTJ) type spin-injector has also been developed for the future electrical control of the spin-injection direction¹⁴⁰. In addition, strong circularly polarized electroluminescence of a single InGaAs quantum dot embedded in GaAs was reported by using an ultrathin CoFeB electrode.¹⁴¹ A polarization degree of up to 35% (20%) was observed for single dots (dot ensembles) in the absence of an external magnetic field. This demonstrates that very efficient electrical spin injection and optical read-out of spin-polarized electrons are possible in a single quantum dot without the need of an external magnetic field. The key role of the Ta layer to absorb boron (B) and to establish the PMA property has been demonstrated. However, the PMA of Ta/CoFeB/MgO system suffers from insufficient thermal stability at annealing temperatures higher than 300°C^{142,143}, which limits the achievement of even higher spin-injection efficiencies.

Several alternative capping layers have been explored to improve the thermal stability, among which Mo shows good stability with thermal treatment up to 425°C. Our group employed Mo as the capping layer to develop perpendicular Mo/CoFeB/MgO¹⁴⁴ spin injectors and studied systematically their characteristics in comparison with the Ta/CoFeB/MgO spin injector. Figure 3.8 shows the structure of the spin-LED. The perpendicular magnetic anisotropy (PMA) of the Mo/CoFeB/MgO injector shows more advanced thermal stability than that of the Ta/CoFeB/MgO injector and robust PMA can be maintained up to 400°C annealing. Figure 3.9 shows the EELS mapping and profile of the different elements for both Ta and Mo injectors annealed at 400°C. In the case of the Ta injector, the B concentration is too low to be detectable. As shown in the element mapping in Figure 3.9 (a), there is significant Ta diffusion through the CoFeB into the MgO layer. It is interesting to note that the concentration of Ta is higher in the MgO layer than in the CoFeB layer. This eventually leads to formation of a $Mg_xTa_yO_z$ oxide. However, no Ta can be found in the GaAs layer. More remarkably, the Mo spin injector displays few Mo diffusion during annealing at $T_{an}=400^\circ C$. As shown in Figure 3.9 (b), although some Mo atoms are detectable close to the Mo/CoFeB interface, Mo cannot fully penetrate into the CoFeB layer to reach the CoFeB/MgO interface. Moreover, no Mo can be detected either in the MgO or in the GaAs layers.

The remanent circular polarization (P_c) of the EL from the Mo capped spin-LED reaches a maximum value of 10% after 300°C annealing, and even remains at 4% after 400°C annealing. In contrast, for the Ta capped spin-LED, the circular polarization is almost zero under 400°C annealing. These findings offer a comprehensive perspective for using the highly thermally stable Mo/CoFeB/MgO spin injector for efficient electrical spin injection under zero applied field. This type of spin injectors not only has great potential for future spin-LED and spin-laser applications, but also can be widely applied for electrical spin-injection into different kinds of semiconductors and 2D material systems.

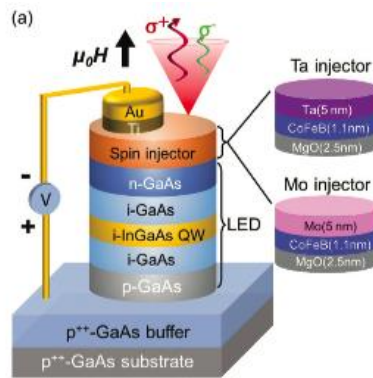


Figure 3.8: Schematic diagram of the spin-LED structure with a Ta or Mo capped spin-injector.¹⁴⁴

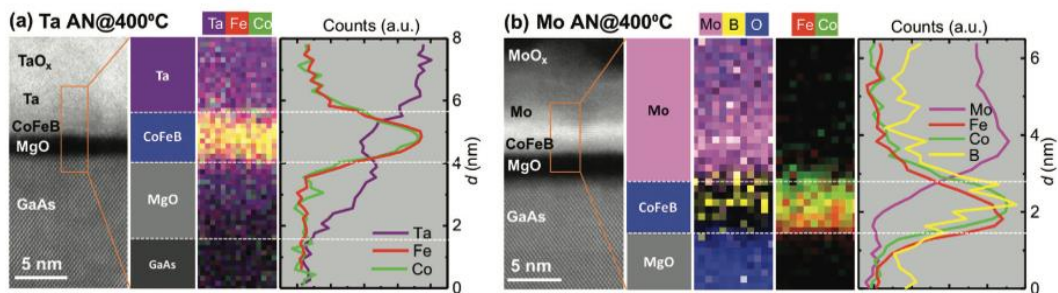


Figure 3.9: Chemical characterization of spin-injectors annealed at 400°C. Dark field HR-STEM images and the corresponding EELS mappings and profiles for (a) Ta and (b) Mo injectors annealed at 400°C. The profiles are constructed from the integration of the element signal in the EELS mapping from an area of 1 pixel in height and 8 pixels in width, corresponding to an area of 0.2 nm in height and 1.6 nm in width.¹⁴⁴

To further enhance the circular polarization degree of the emitted light, our group has recently designed a spin-LED containing a single layer of InAs/GaAs quantum dots (QDs). InAs/GaAs quantum dots are promising candidates for efficient circular polarized light emitters thanks to their strong quantum confinement and the high quality of crystal fabrication that can be reached. In addition, neutral, negatively (n-), and positively (p-) doped InAs/GaAs QDs have attracted significant attention due to the effect of the charged excitons on the spin dynamics. It has been reported that p-doped InAs/GaAs QDs have favorable electron spin polarization features, by forming positively charged excitons (trion X^+), compared to the neutral and negatively charged excitons. The electroluminescence (EL) from one single QD shows an unprecedentedly high circular polarization degree up to 35% at zero applied magnetic field.¹³⁰ The injection of spin-polarized electrons is achieved by combining ultrathin CoFeB electrodes on top of a spin-LED device with p-type InAs/InGaAs quantum dots in the active region. More importantly, this study shows a signature of dynamic polarization of the nuclear spins in the quantum dot induced by the hyperfine interaction with the electrically injected electron spin. This study paves the way for electrical control of nuclear spin polarization in a single quantum dot without any external magnetic field.

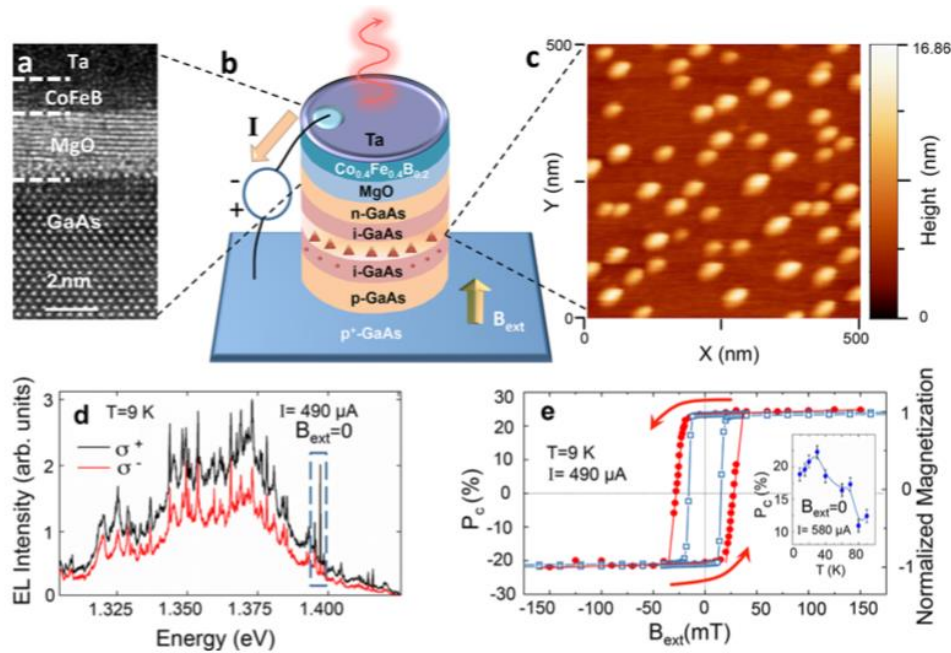


Figure 3.10: Spin LED device with p-doped InAs/GaAs quantum dots and polarization resolved electroluminescence of an ensemble of quantum dots. (a) High-resolution

TEM image of the injector Ta/CoFeB/MgO/GaAs. (b) Schematic structure of the spin-LED device. A single layer of InAs QDs is embedded in the intrinsic region of the p-i-n junction of the LED. (c) AFM image of InAs QDs with a density of $1.6 \times 10^{14} \text{ m}^{-2}$. The average lateral dot diameter is about 30 nm and their height is about 9 nm. (d) Electroluminescence from the device shows spectrally narrow emission lines stemming from an ensemble of semiconductor quantum dots. (e) The circular polarization degree of the EL (red circles) is plotted as a function of the applied magnetic field B_{ext} for the ensemble emission of panel (d). Hysteresis loop of the normalized magnetization of the CoFeB electrode measured by SQUID at $T=30\text{K}$ (blue squares). The inset shows the evolution of P_c with temperature at $B_{\text{ext}}=0$.

3.3 Spin injection in a GaAs based spin LED containing a single layer of InAs quantum dots

The previous study was mainly focused on the emission of circularly polarized light stemming from a single InAs/GaAs QDs embedded in a GaAs based spin-LED. Much less attention was, however, devoted to the behavior of the quantum dot ensemble. This system is of great interest from the low injected current point of view. The effect of the applied magnetic field, biasing voltage, and temperature on the circular polarization degree and EL intensity were studied and discussed in light of competitive spin relaxation time and radiative recombination rates of the charge carriers.

3.3.1 Sample preparation

The p-i-n LED sample, with a single layer of InAs/GaAs QDs embedded in the active region, has been grown by MBE. The complete layers structure and the doping concentrations are indicated in Figure 3.11. Then, a 2.5 nm thick MgO layer followed by a 1.1 nm thick $\text{Co}_{0.4}\text{Fe}_{0.4}\text{B}_{0.2}$ spin injector layer has been deposited by sputtering technique. Circular mesas with 300 μm diameter were processed and realized by UV

photolithography and etching techniques. The sample has been cut into pieces, which underwent rapid thermal annealing (RTA) at 300 °C for 3 min. For the optical characterizations, the sample has been mounted on a cryostat allowing to reach 10K for low temperature electroluminescence measurement. The cryostat is placed between polar pieces of an electromagnet so that the magnetic field can be applied perpendicularly to the surface. A function generator has been used to apply pulse bias to avoid/reduce thermal effects on the sample at high biases. The EL signals are collected and focused by using a set of lenses, then dispersed by an *i*HR 320 spectrometer with 300 grooves/mm grating and finally detected by a Si-based CCD camera. In the case of polarization resolved EL, a quarter wave-plate followed by a linear polarizer were involved in the optical path.

In the following sections, we will investigate the EL circular polarized emission degree and the EL intensity as a function of the magnetic field, applied voltage, and temperature.

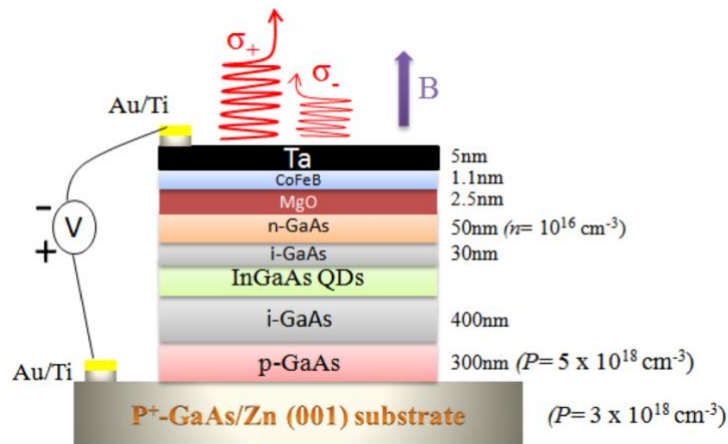


Figure 3.11: Schematic diagram representing the layer structure of the spin-LED.

3.3.2 Magnetic field dependence

Figure 3.12 (a) shows the polarization-resolved electroluminescence (PR-EL) spectra of the spin LED described in Figure 3.11 measured at low temperature (10K) without any applied magnetic field. The PR-EL spectra, top (bottom) panel have been measured after sample pre-saturation with a magnetic field ~ 0.35 T at negative (positive) values then returned to zero prior to each measurement. The EL spectra are

characterized by a band centered at ~ 905 nm corresponding to the emission of a structure ensemble of InAs/GaAs quantum dots. Due to the limited resolution of our setup, we cannot observe individual emission peaks originating from single QDs. Obviously, there is a clear intensity difference between the circularly right (σ_+) and circularly left (σ_-) components of the polarized emission. The degree of the circular polarization is estimated using the relation, $P_c(\%) = \frac{I(\sigma_+) - I(\sigma_-)}{I(\sigma_+) + I(\sigma_-)}$. We found that P_c reaches +17.4% and -18.5% for the two magnetization directions. The sign reversal when the magnetization is changed directly points out the role of the spin injector.

This large P_c , at zero applied magnetic field and low injected current, 6 μA , indicates the high efficiency of the spin injection at low power operation conditions. The correlation between the circularly polarized emission of the QDs and the perpendicular magnetization of the spin injector layer can be probed by measuring P_c as a function of applied magnetic field being swept between positive and negative values. Figure 3.12 (b) displays the P_c -B loop which is compared to the measured M-B loop. The similarity between the hysteresis behavior of the P_c -B loop and the M-B loop proves that the circularly polarized EL is related to the perpendicular magnetization of the spin injector.

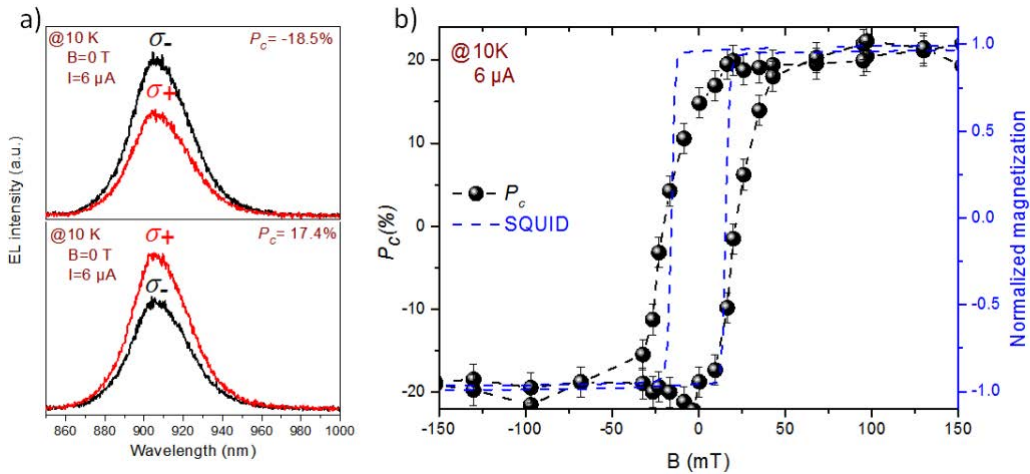


Figure 3.12: (a) EL spectra with polarization resolved components (σ_+ and σ_-) measured at 10K and zero applied magnetic field, after pre-saturation from negative to zero (top panel) and from positive to zero (bottom). (b) Circular polarization degree of the EL as a function of magnetic field swept from negative to positive direction and vice versa.

3.3.3 Bias dependence

In the following, we will investigate the bias dependence on the EL intensity in order to determine the optimum operation conditions. The evolution of both P_C and EL intensity as a function of the applied bias at 10 K in remanent condition is shown in Figure 3.13.

P_C exhibits strong dependence on the bias voltage by showing a maximum value around (~17%) at 2.5 V within the investigated range (2-3.8 V). A similar bias dependence behavior has been reported in our previous work on InGaAs/GaAs quantum wells and attributed to a complex relative behavior between the radiative recombination lifetime (τ_r) and the spin relaxation lifetime (τ_s) of the charge carriers. The circular polarization P_C is related to the dynamics of the injected charge carriers by the following relation: $P_C \propto \frac{1}{1+(\tau_r/\tau_s)}$. The variation of P_C is then essentially governed by the τ_r/τ_s ratio.

In general, relatively long τ_s compared to short τ_r is favorable to the emission of circularly polarized light. The change in τ_s , is determined by a fluctuation of the effective intrinsic magnetic field originating from spin relaxation mechanisms. The change in τ_r is linked to a modification in the band structure of the semiconductors. For the same device, both lifetimes can be affected by the application of an external magnetic field, bias, and/or operating temperature. Because of the complex interactions of both lifetimes with the external effects, the behavior of the P_C is determined by the dominance of different mechanisms at different ranges of the applied bias, magnetic fields and temperatures.

The first increase in P_C with the applied bias, at fixed temperature (10K), could be referred to a slight increase in the radiative recombination rate of the charge carriers, i.e. to a slow decrease in τ_r . This is supported by the exponential increase of the EL intensity with applied bias as shown in Figure 3.13 (b). Due to the application of an electric field, the electron-hole wave function overlapping is reduced thus leading to a

decrease of τ_s . Hence, P_C rapidly increases when the applied bias increases from 0 to 2.5 V.

For applied biases higher than 2.5 V, the kinetic energy of the injected charge carriers increases. In addition, under biasing, bending of the tunnel barrier and alignment of the semiconductor conduction band to the Fermi level of the ferromagnetic-metal can occur. To simulate the band energy of the spin-LED device, "1D Poisson" program is used. The used layers thicknesses and dopant concentrations in the program are the same as in the real sample. Figure 3.14 shows the simulation of the band energy diagram for different applied biases. As the voltage increases, the bias drops on the MgO/semiconductor interface and results in bending of the tunnel barrier and alignment of the semiconductor conduction band. This will efficiently increase the injection of energetic electrons that encounter a spin relaxation owing to the Dyakonov-Perel mechanism (DP) thus resulting in a strong decrease of τ_s . However, the recombination rate of the non-polarized charge carriers increased significantly, (Figure 3.13 (b)). Consequently, the competition between the shorter spin relaxation time and the increasing radiative recombination rate results in a reduced P_C for applied biases larger than 2.5V. Moreover, we cannot exclude possible thermal effects at high applied biases.

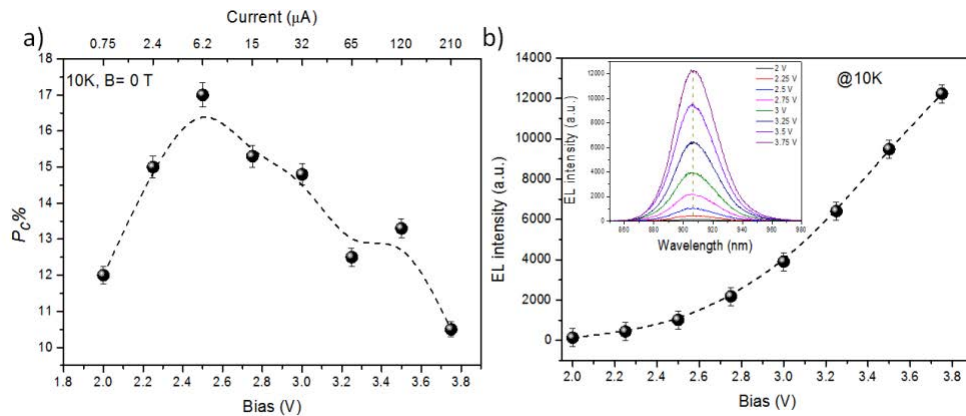


Figure 3.13: Evolution of P_C (a) and EL intensity (b) as a function of bias. The inset of (b) shows EL spectra measured at different applied biases.

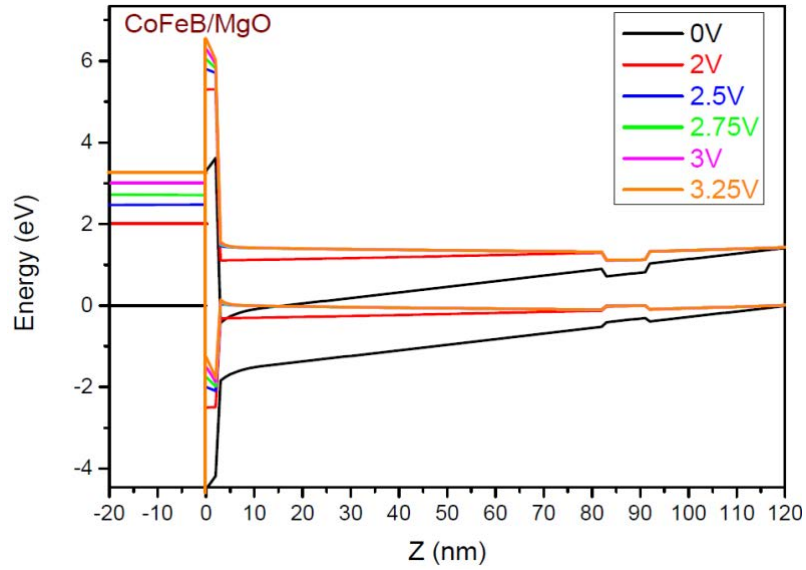


Figure 3.14: Simulation of the energy band diagram of the spin-LED device shown in Figure 3.11 (a) using the “1D-Poisson” program.

3.3.4 Temperature dependence

In the following, we will investigate the temperature dependence of the EL intensity. The polarization resolved EL has been measured as a function of temperature in the range from 10K to 100K. Two injection current regimes, low current regime $\sim 6\mu\text{A}$ (at the optimum bias) and high current regime at $30\mu\text{A}$, have been considered for this study. The measurements were conducted under an applied magnetic field (saturation condition, 0.35 T) and without magnetic field (remanent condition, 0 T).

Figure 3.15 (a) shows the evolution of P_C with the temperature. At a given current, P_C exhibits a similar trend independently of the magnetic properties (saturation or remanent). For instance, in the low current regime, P_C decreases monotonically with increasing the temperature, while a non-monotonic variation is observed for the high current regime. In the latter case, P_C decreases until 80 K and then starts to increase again. This non-monotonic behavior is reported frequently either in GaAs QWs or QDs based spin-LEDs. Interestingly, the minimum value of P_C is found, in independent studies, in the same temperature range 60-80 K. However, a careful look at the P_C for the low current regime at temperatures higher than 80K, under an applied magnetic field, suggests a further increase. The latter seems to be more pronounced after 100 K.

This confirms the suggested reason reported in, about this temperature dependence of the P_C . As discussed above, the competition between the two lifetimes, τ_r and τ_s , under bias voltage and/or temperature will control the behavior of P_C . Referring to literature, it is established that the DP spin relaxation rate for quantum well based devices is given by $\frac{1}{\tau_s} \propto t_p T$, where t_p is the momentum scattering time and T is the temperature. At low temperatures i.e. below $\sim 70\text{K}$, t_p is independent of the temperature. This leads to a rapid increase of the spin relaxation rate, i.e. to a decrease of τ_s , which is consistent with our previous work. Moreover, an increase of τ_r has also been reported in the same temperature range. In our present case, the increase of τ_r can be deduced from the strong decrease in the EL intensity (as shown in Figure 3.15 (b)). The thermal quenching of the EL intensity (Figure 3.15 (b)) is attributed to an increase of the nonradiative recombination rate owing to spreading (or even escape) of the confined carriers over the adjacent energy states hence modifying the value of τ_r . Combining both modifications in τ_s and τ_r , results in a significant decrease of P_C . At higher temperatures, thanks to the dominance of the momentum scattering due to the polar optical phonons, the increase in the spin relaxation rate became slower than the rate at low temperatures (i.e. longer τ_s), as reported elsewhere. In addition, τ_r exhibits little change at higher temperatures. This is responsible for increasing of P_C and points to strong and significant competition between the charge carrier dynamics.

Interestingly, at 60 K, P_C does not depend on the injected current either at saturation or in remnant conditions. In addition, for temperatures larger than 60K and for the high injected current regime, P_C turns to be larger than the corresponding values obtained for the low current regime. This observation is in contrast with the situation for temperatures lower than 60 K. The reason for that is not yet clear, but further investigations of both τ_r and τ_s values in different temperature ranges are essential to draw a complete picture about the relevant mechanisms of the EL and polarization resolved EL features. We then investigate the influence of the injected current on the behavior of P_C at three temperatures, 10K, 60K, and 100K. Figure 3.16 shows the dependence of P_C on the injected current. P_C at 10K and 100K exhibits strong

dependence on the injected current and shows almost the same behavior. P_C first increases until an optimum value and then decreases. The optimum P_C value at 100K is obtained for a higher injection current, 64 μA , compared to 6 μA at 10K. At higher temperatures, the thermal quenching of the EL leads to a loss of most of the injected carriers (both polarized and un-polarized) via non-radiative recombination pathways. This can explain the shift in the optimum P_C value to higher injection currents in order to compensate the loss of polarized spins. In contrast, at 60K, P_C depends only slightly on the injected current, which confirms our previous observation (as shown in Figure 3.15 (a)). This raises the question about the particular value of this temperature, which is close to the onset of the optical phonon scattering temperature in GaAs.

Finally, one can also observe a shift of the EL peak to longer wavelengths, accompanied by broadening in the bandwidth with temperature, (inset of Figure 3.16 (b)). The shift of the EL peak is due to the band gap shrinking of GaAs as the temperature increases. The EL bandwidth broadening is accounted for by the optical phonon scattering as reported elsewhere. Such changes in the EL spectra further reflect the modification in the band structure.

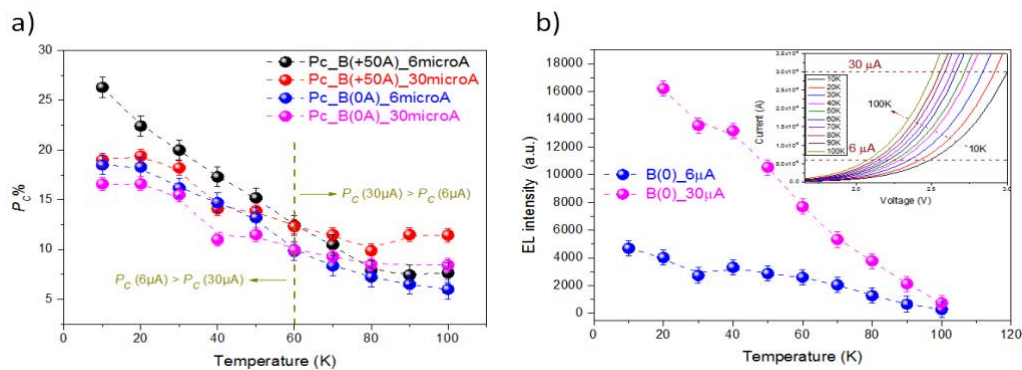


Figure 3.15: P_C (a) and EL intensity (b) as a function of temperature for injected currents of 6 μA and 30 μA . Inset of (b): I-V curves measured at each corresponding temperature values.

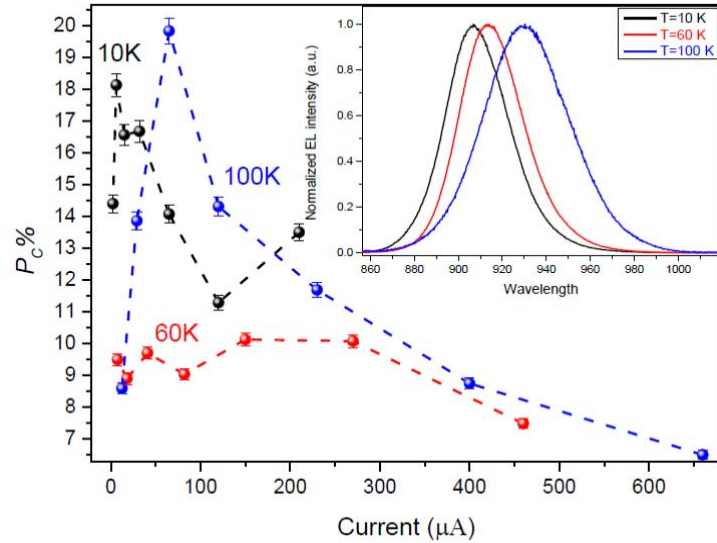


Figure 3.16: P_c as a function of injected current at zero magnetic field at 10K, 60K, and 100K. The inset shows the EL spectra at each corresponding temperature and at fixed current.

3.4 Summary

In this chapter, we firstly introduced the concept of a spin LED and their potential applications. Then we reviewed the state-of-the-art of spin-LED based on GaAs structures, which contains research work about both in plane and out-of-plane spin injectors. In addition, we also presented our previous research work about CoFeB/MgO PMA spin injector. Then we showed our very recent work about the polarization resolved electroluminescence from an ensemble of p-doped InAs/GaAs QDs, which exhibits interesting properties from the low injected current operation point of view. We found that P_c reaches a value as high as 18% under zero applied magnetic field at 10K. A clear correlation has been established between the circular polarization degree of the emitted light and the perpendicular magnetization of the injector layer. A strong dependence on the bias voltage revealed a maximum P_c at optimum bias 2.5 V (6 μ A) at 10K. In addition, the operating temperature shows strong effect on the P_c with different behavior at certain temperature values. The behavior of P_c exhibits remarkable change before and after 60-80K. The current dependence measurements performed at temperature values 10K, 60K, and 100K shows slight dependence of the P_c on the

injected current at 60K compared to the strong dependence in the two other temperatures. The interpretation of the bias and temperature dependence of the P_C has been discussed in light of the competition between the spin relaxation time τ_s and the charge carrier recombination rate. It is believed that these findings can help for better understanding the collective behavior from an ensemble of p-doped InAs/GaAs QDs under different operation conditions.

Chapter 4 Towards GaN based Spin LEDs

In this chapter, we will firstly introduce the state-of-the-art of spin-LED based on GaN structures. Then we will show how to develop an efficient spin injector on GaN exhibiting perpendicular magnetic anisotropy. Finally, we will present some preliminary results about spin injection into GaN based spin-LEDs.

4.1 GaN based spin LEDs: state of the art

4.1.1 Advantage of GaN spin LEDs for applications

A Spin-LED is an important device for spin-optoelectronic applications since it can convert spin information stored in the magnetic injector to optical circular polarization information. However, most of these devices require the application of a high magnetic field. Moreover, low temperatures are required to obtain an appreciable spin polarization. The band gap of GaAs is 1.35 eV, which can only provide infrared or red LEDs. In light of great brightness of InGaN/GaN MQW LEDs for commercial solid-state lighting, backlight modules of flat panel and GaN-based field effect transistors, the extension of nitride-based semiconductors to spintronic devices has triggered substantial efforts.^{145,146,147,148,149}

GaN is a wide bandgap semiconductor with a high thermal stability.¹⁵⁰ It is often used in optoelectronics, high frequency and high-power microelectronics.¹⁵¹ For spintronic applications, GaN is also an attractive candidate because it has a weak spin-

orbit interaction ($\Delta_{so} \approx 15$ meV). In combination with a wide energy gap (~ 3.4 eV) at 300K, this leads to a long spin relaxation time (~ 20 ns at $T=5$ K¹⁵² and a few hundred ns at room temperature (RT)), which are two orders¹⁵³ of magnitude larger than the spin lifetimes in GaAs (about 500ps). This is an important advantage of GaN since spintronic devices usually require long spin coherence times. For optical applications, a GaN LED is generally characterized by the p-type layer on the top of the structure. However, for investigating the spin injection into a GaN based spin-LED, we need a n-type top GaN LED structure (n-i-p type structure), which is difficult to grow. Several problems about growing a n-i-p structure will be presented later.

4.1.2 State-of-the-art

4.1.2.1 Spin injection into a p-top layer GaN based LED

In 2004, Buyanova *et al.* investigated a wurtzite GaMnN/InGaN/AlGaIn spin-LED grown by molecular beam epitaxy (MBE). However, no spin polarization was detected within the active region through characterization of the polarization resolved electroluminescence.^{154, 155, 156, 157, 158} Similar results were found for wurtzite ZnMnO/ZnMgO/ZnO/AlGaIn/GaN spin-LEDs where the n-type ferromagnetic ZnMnO spin-aligner layer was grown by pulsed-laser deposition.¹⁵⁹ Optical orientation experiments failed to create any spin or optical polarization at zero magnetic field. This could be due to two main reasons: (1) limited optical polarization due to the valence band (VB) structure of the InGaIn QW, (2) fast spin relaxation within the InGaIn QW. A spin relaxation process in InGaIn QW with a characteristic relaxation time of about 50 ps which arose from spin flips of individual carriers near $K=0$ was obtained. Such fast spin relaxation is rather unexpected if one simply considers a weak S-O interaction in InGaIn. However, it can be attributed to a strong Rashba effect due to structural inversion asymmetry in the presence of a large piezoelectric field inherent to InGaIn QWs (D'yakonov-Perel' (DP) mechanism). Elliott-Yafet (EY) mechanism may also play an important role due to strong compositional and structural nonuniformity and a

high density of defects in InGaN. These processes can be greatly promoted during momentum and energy relaxation at high K vectors.¹⁵⁰ In 2006, Ham *et al.* investigated the electrical spin injection from the room-temperature ferromagnet (Ga, Mn)N in a GaN based spin-LED. The electroluminescence spectra indicated the existence of a spin polarization via optical polarization of the emitted light up to room temperature. The EL polarization saturated around 8 T at 150 and 300 K and reached maximum values of approximately 1.3% and 0.8% at 150 and 300 K, respectively.¹⁶² The spin-LED heterostructure was prepared through a combination of metal-organic chemical vapor deposition (MOCVD) and plasma-enhanced molecular beam epitaxy (PEMBE) methods on (0001) sapphire substrates. The EL results suggest that (Ga, Mn) N is an appropriate material for spin injection in a room-temperature operating semiconductor spintronic device. Low spin injection efficiencies have been reported, which might be attributed to cancellation of the optical polarization due to the overlap of heavy-hole and light-hole transitions with opposite signs for circular polarization. In 2011, Chen *et al.* investigated the spin relaxation in GaN-based light-emitting diodes with an MnZnO film formed by spray pyrolysis.¹⁶⁰ The PL polarization reached 3.6% under a 0.5T applied magnetic field. The photo-ionized lifetime and spin-polarization lifetime values were approximately 13.64 and 54.54 ns, respectively. The right- and left-circular-spin-polarization lifetimes were about 39.09 and 40.01 ns, respectively. In 2013, Banerjee *et al.* demonstrated electrical spin-injection from a GaCrN dilute magnetic semiconductor (DMS) in a GaN-based light emitting diode (spin-LED).¹⁷⁰ The spin-LED structure is shown in Figure 4.1 (a). The remanent in-plane magnetization of the semiconducting ferromagnet has been used to introduce the spin-polarized electrons into the non-magnetic InGaN quantum wells. The output circular polarization obtained from the spin-LED closely follows the normalized in-plane magnetization curve of the DMS. A saturation circular polarization of ~2.5% is obtained at 200K as shown in Figure 4.1 (c). Room temperature polarization was not obtained owing to relaxation of the injected spin population over the significantly long transport length.¹⁶¹

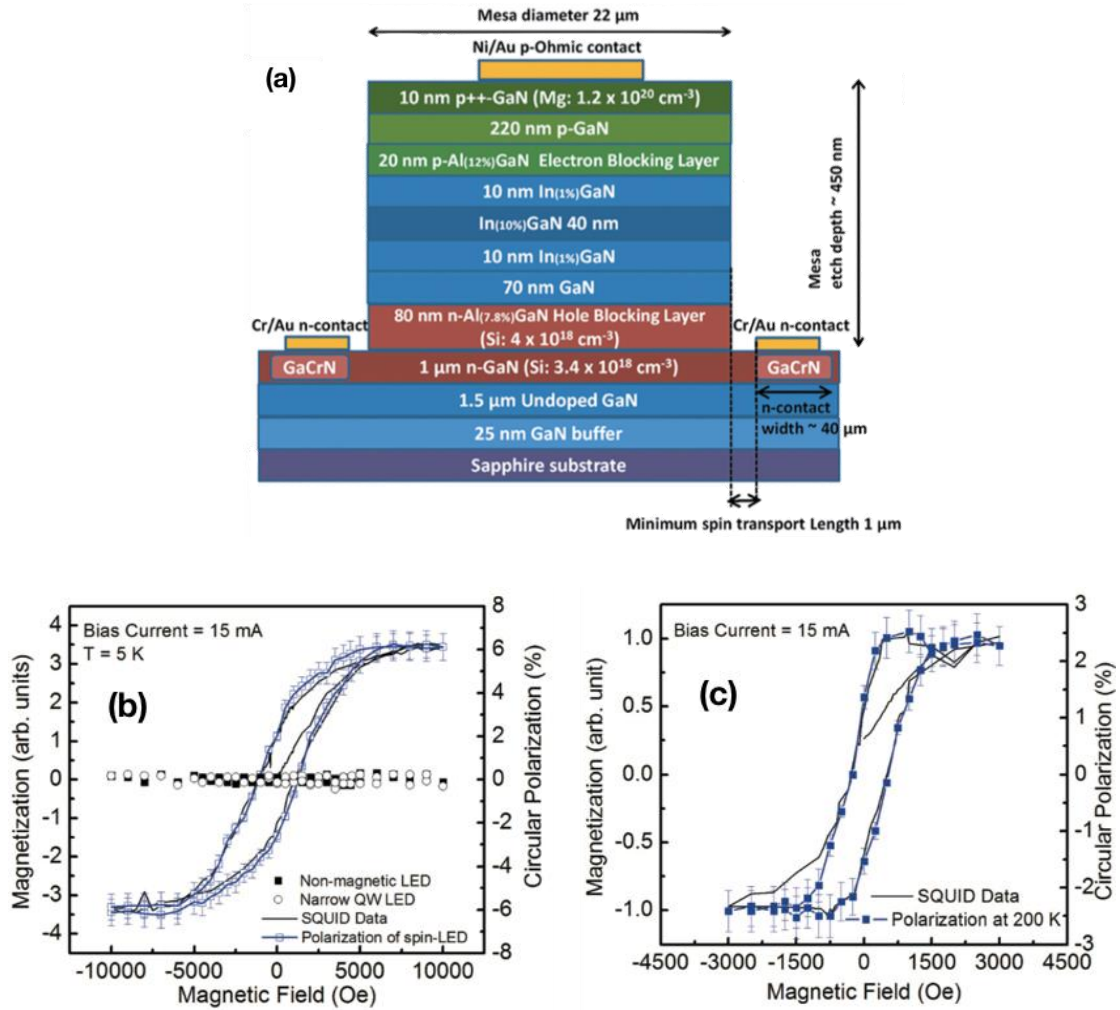


Figure 4.1: (a) Schematic of a GaN based spin-LED device. The device dimensions are also mentioned alongside. The top p-contact is non-magnetic and the bottom GaCrN n-contact is ferromagnetic in nature. Output circular polarization from the spin-LED as a function of the in-plane magnetic field at (b) 5K and (c) 200K. The output circular polarization follows the in-plane magnetic field confirming the electrical spin injection and optical detection in these devices.

4.1.2.2 Spin injection into GaN by combining a ferromagnetic contact with Fe₃O₄ nanoparticles

In 2014, Chen *et al.* found that the circular polarization degree of the electroluminescence (EL) from a spin LED could reach 10.9% at room temperature in a low magnetic field of 0.35T.¹⁷¹ This result is much larger than the usual very low

degree of spin polarization reached in nitride semiconductors. The authors used InGaN/GaN multiple quantum disks (MQD) as the central element of the spin-LED as shown in Figure 4.2. The internal strain in planar InGaN/GaN multi quantum wells can be relaxed during the nanodisk formation, which leads to the disappearance of the Rashba term in the Hamiltonian and eventually results in a larger spin relaxation time. The device is composed of InGaN/GaN MQD LED, ferromagnetic contact and Fe₃O₄ nanoparticles. The sample was grown by metal-organic chemical vapor deposition (MOCVD). An inductively coupled plasma reactive-ion etching (ICP-RIE) process was then used to turn the InGaN/GaN MQWs into MQD nanorods, which had an average diameter of 300 nm and an average height of 1.2 μm. The InGaN/GaN MQD nanorods were then coated with a 3.5nm thick Ni film, which served as the metal contact for both hole and electron injection layers. The vacancies between nanorods were filled with 10 nm Fe₃O₄ nanoparticles. Finally, the structures were coated by photoresist to avoid short circuit.

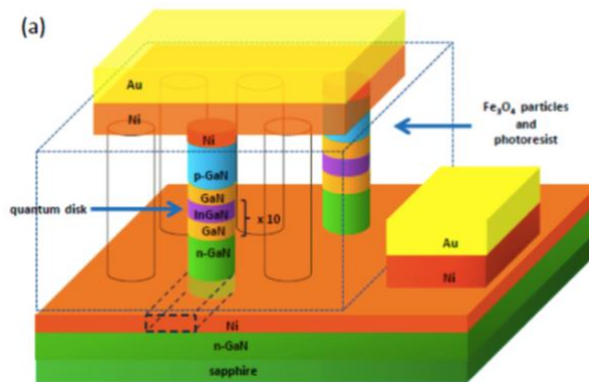


Figure 4.2: Schematic structure of the InGaN/GaN MQD LED.

The Fe₃O₄ magnetic nanoparticles possess a different band alignment for electrons with spin-up and spin-down as shown in Figure 4.3, which enables the selective transfer of spin polarized electrons between nanodisks and nanoparticles and thus leads to an enhanced output spin polarization of the LED. Based on the unique band structure of Fe₃O₄, for spin-down electrons, Fe₃O₄ acts as a conductor, while for spin-up electrons, it acts as an insulator.^{162,163} Therefore, according to the band alignment between Fe₃O₄

nanoparticles and InGaN/GaN MQDs,^{155,156,164} when there are extra electrons in InGaN/GaN MQDs due to an injected current or to the light excitation source, spin-down electrons can pass through a monolayer of oleylamine and flow into Fe₃O₄ nanoparticles, while spin-up electrons remain in the InGaN/GaN MQDs. As a result, Fe₃O₄ nanoparticles can be used to increase the percentage of spin-up electrons in MQDs and enhance the degree of the circular polarization of MQDs. For the holes, because the effective mass of heavy holes is much larger than that of light holes perpendicular to the c axis of the wurtzite structure, the magnetic nanoparticles with suitable energy band alignment can cause the transfer of light holes from nanodisks to nanoparticles much easier. Thus, the population difference between heavy holes and light holes is increased in MQDs, where electroluminescence (EL) is emitted.

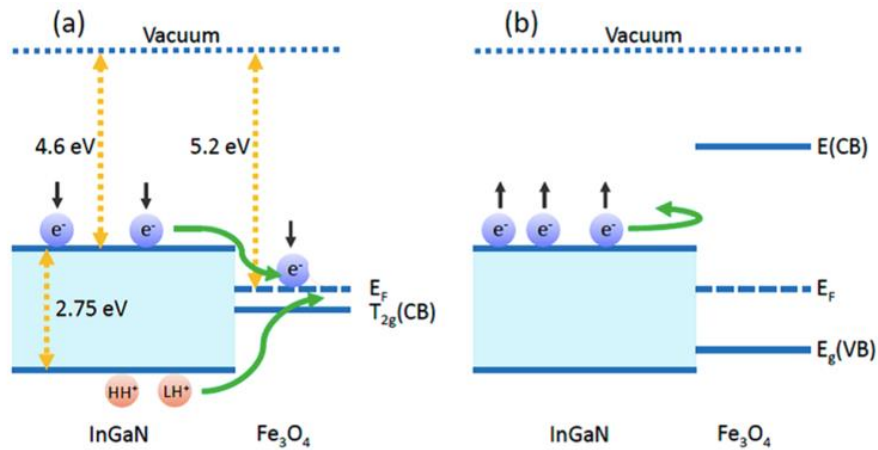


Figure 4.3: Band diagram of (a) spin-down and (b) spin-up electrons in InGaN and Fe₃O₄.

Laser emission from GaN nanorods coupled with Fe₃O₄ nanoparticles was also achieved yielding spin polarization up to 28.2% at room temperature under a low magnetic field of 0.35T.¹⁷⁴ The nanoscale hexagonal cross-section of GaN nanorods, as shown in Figure 4.4, serves as a natural laser cavity for the creation of ultraviolet whispering gallery modes (WGMs).¹⁶⁵ Periodic GaN nanorod arrays were obtained by using a nanoimprint technique on a 2 μm-thick GaN template, which was grown by MOCVD on a c-plane sapphire substrate. The nanorods were estimated to have an average diameter of 250 nm and an average length of 1 μm. The vacancies between the

GaN nanorods were filled with Fe₃O₄ nanoparticles. Figure 4.5 (a) shows a schematic of the PL measurement for GaN nanorod arrays filled with Fe₃O₄ nanoparticles. Figure 4.5 (b) shows the PL spectra under different applied biases. It is clear that the intensity of PL can be controlled by an external bias. With a positive bias, the PL intensity increases, but then decreases under a negative bias. The external bias can thus be used to tune the band bending upwards or downwards across the interface between the GaN nanorods and the Fe₃O₄ nanoparticles. The electron flow can then be controlled, and the emission intensity can be manipulated. Due to the spin selectivity, the polarization of the PL spectra can also be manipulated. When an external bias of -10V is provided to bend the bands, the degree of circular polarization can reach 28.2%. Both the output spin polarization and intensity are tunable by the external bias thus providing an excellent route to control and modulate the characteristics of spin-lasers. This offers a very attractive feature that makes the developed spin-lasers more feasible for several practical applications, such as secure communications, high-speed modulators and chiroptical spectroscopies,¹⁶⁶ when compared with those derived from electrical or optical spin injections. In addition, the tunable feature of the output spin polarization by an external bias can also be used to rule out that the magnetic circular dichroism of Fe₃O₄ nanoparticles is responsible for the observed spin effect.

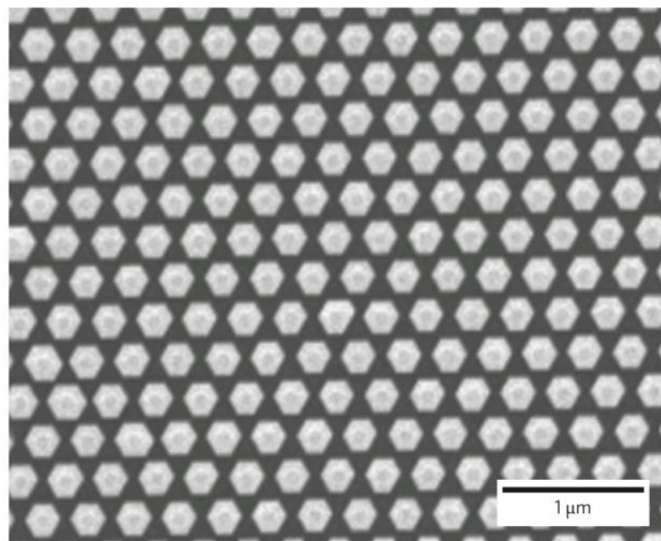


Figure 4.4: Scanning electron microscopy image of the top view of the GaN nanorod arrays.

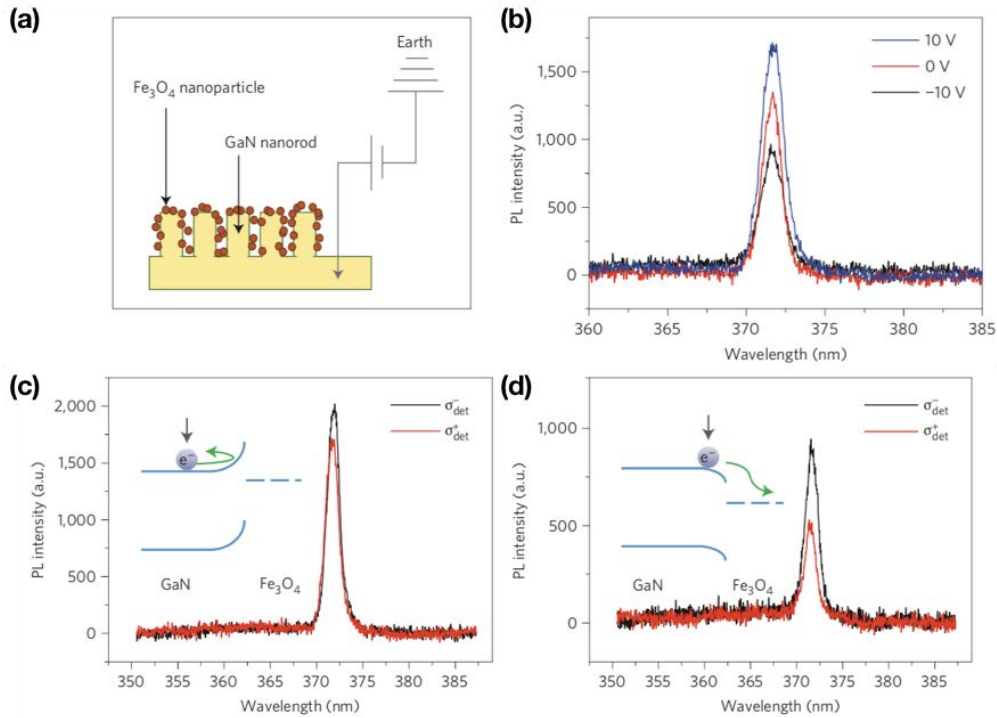


Figure 4.5: Spin-polarized emission spectra under different external biases. (a) Schematic of the applied bias for the measurement of PL spectra of GaN nanorod arrays filled with Fe₃O₄ nanoparticles. (b) PL spectra under different external biases and a magnetic field of 0.35T. (c, d) PL spectra and the band bending (inset) of GaN nanorod arrays filled with Fe₃O₄ nanoparticles under +10V (c) and -10V (d) and a magnetic field of 0.35T. The obtained spin polarizations are 8.66% in (c) and 28.2% in (d).

4.1.2.3 Spin injection into n-top GaN based LED and LD by using a FeCo/MgO top contact

In 2017, Bhattacharya *et al.* observed room temperature circularly polarized electroluminescence from bulk GaN-based double-heterostructure edge-emitting LEDs. An output circular polarization of ~6% was obtained at 300K for the spin LED.¹⁷² The device heterostructure, schematically depicted in Figure 4.6 (a) and the edge-emitting spin LED (Figure 4.6 (b)) was grown by plasma-assisted molecular beam epitaxy on wurtzite c-plane, p-type (Mg-doped) epitaxial GaN (0001)-on-sapphire template. The energy band-diagram of the device heterostructure is shown alongside

Figure 4.6 (a). The n-type $\text{In}_{0.18}\text{Al}_{0.82}\text{N}$ layer serves the dual function of an optical cladding as well as a charge carrier confinement layer. The active region of these devices is bulk GaN and thus the generation of edge-emitting circularly polarized electroluminescence originating from radiative recombination of spin-polarized carriers is quantum-mechanically allowed. As shown in Figure 4.6 (c), the degree of circular polarization of the edge-emitting LED, biased at a constant injected current strength of $\sim 640 \mu\text{A}$, is seen to closely follow the in-plane magnetization of a 80 nm-thick FeCo layer, which demonstrates that the measured polarization originates from spin injection by the ferromagnetic FeCo/MgO contact. The degree of circular polarization saturates at $\sim 5\%$ for applied magnetic fields greater than the in-plane saturation field for FeCo.

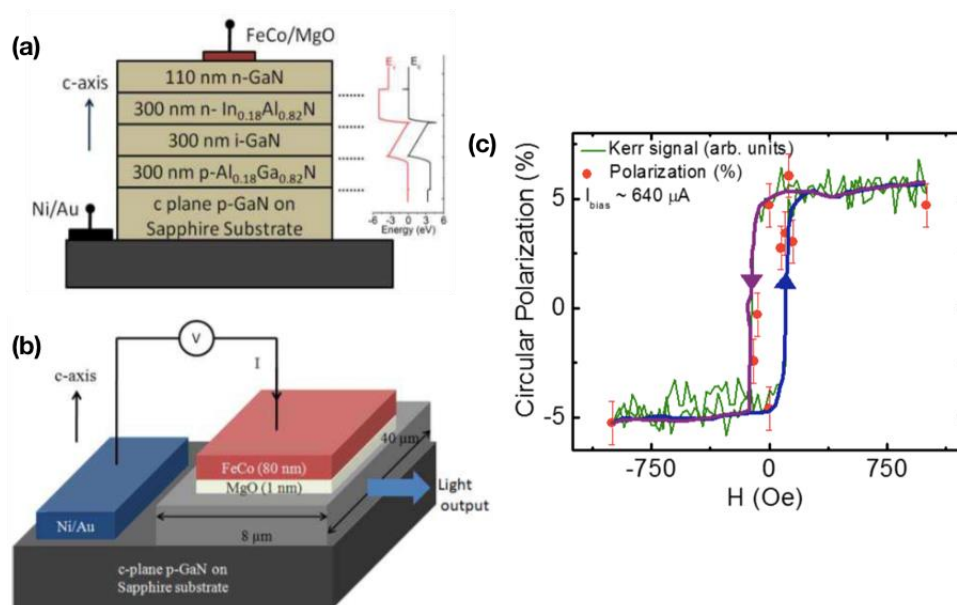


Figure 4.6: (a) Schematic representation of the double heterostructure GaN-based spin LED. The energy band-diagram of the device heterostructure is shown alongside. (b) Schematic diagram of the edge emission geometry of the spin-polarized LED. (c) Degree of circular polarization of the spin-polarized LED measured as a function of the in-plane magnetic field. The normalized in-plane magnetization curve determined from hysteresis measurements is shown for comparison. The solid lines are guides to the eye representing increasing and decreasing magnetic field sweeps respectively.

These authors also investigated the output polarization characteristics of a bulk GaN-based microcavity polariton diode laser at room temperature with electrical injection of spin-polarized electrons via a FeCo/MgO spin injector. An output circular polarization degree of $\sim 25\%$ was obtained under remanent magnetization at 300K for the spin polariton diode laser.¹⁷³ A schematic of the GaN-based microcavity polariton laser diode fabricated from a single epitaxially grown heterostructure is shown in Figure 4.7 (a). The regular n-type ohmic contact was replaced by a n-type FeCo/MgO spin injector to introduce a net electron spin imbalance in the laser diode. Moreover, the diode heterostructure was grown on a p-type substrate so that the FeCo/MgO spin contact can be formed on the n-GaN layer on top. This reduces the transport length of the spin-polarized electrons to the active recombination region. Figure 4.7 (b) depicts the measured steady state circular polarization of the electroluminescence of the same device as a function of the injected current. There is a nonlinear increase of the polarization at threshold and a maximum value of output circular polarization of $\sim 25\%$ was observed above the nonlinear threshold. The device represents a bias-tunable low energy coherent polarized light source operating at room temperature.

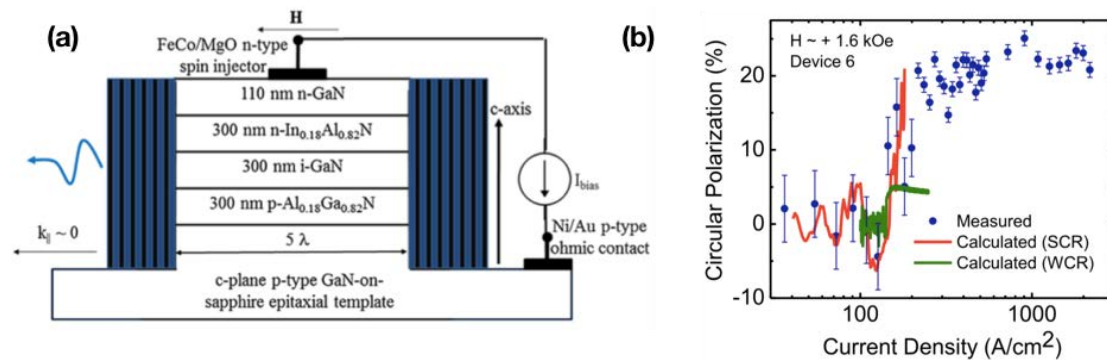


Figure 4.7: (a) Schematic diagram of the spin-polarized double heterostructure GaN-based microcavity diode. (b) Measured steady state degree of circular polarization as a function of injected current density recorded after in-plane magnetization of ferromagnetic contacts with $H \sim +1.6$ KOe.

As mentioned before, the transitions meeting the requirement of the optical selection rules lead to emission of circularly polarized light. A conventional spin

injector with in-plane magnetization cannot satisfy the practical application for quantum well based spin-LEDs because a strong external magnetic field in the range of up to a few Tesla is required to rotate the magnetization into the perpendicular direction. A prerequisite to obtain optimized device functionalities is to promote a robust perpendicular magnetic anisotropy (PMA) medium up to room temperature (RT) to be used as a solid-state FM injector electrode. A comparative summary of spin-injection into GaN based structures is given in Table 4.1.

Magnetic injector	Semiconductor detector	Circular polarization (%)	Ref.
GaMnN (MBE)	InGaN(3nm)/GaN(10nm) [~40% In, MOCVD]	Very low	Buyanova et al. APL 2004, JEM 2004, JVSTB 2004, APL 2005 ^{154, 155, 156, 157}
GaMnN (PEMBE)	InGaN(4nm)/GaN(10nm) [~10% In, MOCVD]	1.3%@150K 0.8%@300K(B=8T)	Ham et al. JPCM 2006 ¹⁶⁹
MnZnO (spray pyrolysis)	InGaN(25nm)/GaN(4nm) [MOCVD]	3.6%@300K(B=0.5T)	Chen et al. TSF 2011 ¹⁶⁰
GaCrN	In _{0.1} Ga _{0.9} N(40nm)/ In _{0.01} Ga _{0.99} N (10nm) [MOCVD]	2.5%@200K(B=0.5T)	Banerjee et al. APL 2013 ¹⁷⁰
Ni film +Fe ₃ O ₄ particles	In _{0.22} Ga _{0.78} N(2nm)/ GaN (9nm) [MOCVD]	10.9%@300K(B=0.35T) (LED) 28.2%@300K(B=0.35T) (LD)	Chen et al. Nano letters 2014, Nature nanotechnology ^{171, 174}
FeCo/MgO	n-In _{0.18} Al _{0.82} N/ i-GaN/p- Al _{0.18} Ga _{0.82} N [MBE]	6%@300K (LED) 25%@300K (LD)	Bhattacharya et al. IEEE PTL 2017, PRL 2017 ^{172, 173}

Table 4.1: Summary of spin injection into GaN based structures (in-plane magnetization anisotropy).

4.1.3 Limitation of the published work

To conclude, lots of researches on spin LEDs and even spin LDs have been reported.^{167, 168, 169, 170, 171, 172, 173, 174} For p-top GaN based structures, the injection efficiency was too low to be detected. Although Chen *et al.* obtained high spin polarizations (28.2%), the device process was quite sophisticated. By injecting spin-polarized electrons into the n-top GaN layer, higher spin polarizations should be

expected. Moreover, all the results are obtained under an external applied magnetic field, limiting potential applications. For practical applications, it is necessary to realize spin LEDs that can operate at room temperature without any external magnetic field. Therefore, significant efforts have been devoted firstly to achieve a perpendicular magnetic spin injector on GaN, which will be presented in the following section.

4.2 Development of a spin injector with PMA on GaN

4.2.1 Motivation

The perpendicular magnetic anisotropy (PMA) arising at the interface between ferromagnetic transition metals and metallic oxides has been investigated and very large values of PMA up to 3 erg/cm^2 at Fe/MgO interfaces were reported.¹²⁸ The origin of the PMA is attributed to the overlap between O- p_z and transition metal d_z^2 orbitals hybridized with $d_{xy(yz)}$ orbitals exhibiting a stronger spin-orbit coupling-induced splitting around the Fermi level for perpendicular magnetization orientation. Yang *et al.*¹⁷⁵ also reported strongly enhanced perpendicular magnetic anisotropy (PMA) of Co films coated by graphene from both first-principles calculation and experiments. Their calculations showed that graphene can dramatically boost the surface anisotropy of Co films up to twice the value of its pristine counterpart and can extend the out-of-plane effective anisotropy up to an unprecedented thickness of 25 \AA . They proposed super exchange stabilized Co-graphene heterostructures with a robust constant effective PMA and linearly increasing interfacial anisotropy as a function of film thickness.

Co and Co-based alloy multilayer films combined with thin MgO layers have been investigated for magnetic applications like tunneling magnetoresistance (TMR) heads and magnetic random-access memory (MRAM) devices^{176, 177, 178}. For such applications, high-quality epitaxial thin films are strong candidates since the magnetic anisotropy and the film uniformity are well controlled. Theoretical calculations show that the TMR ratio of a magnetic sensor prepared using an epitaxial film is one order

of magnitude greater than that obtainable with an amorphous film^{45, 179}. The crystallographic property of Co or Co-alloy/MgO structure strongly influences the TMR value. Large TMR ratios have been reported at room temperature for Co/MgO/Co (410%)¹⁸⁰ and CoFeB/MgO/CoFeB (604%)⁴⁸ MTJs. Even though we have achieved a lot of remarkable results using a CoFeB/MgO spin injector exhibiting PMA, fully epitaxial Co/MgO spin injectors are very attractive.

First of all, we develop a spin injector exhibiting PMA on a GaN template, and then we will transfer the optimized spin injector on a GaN LED structure.

4.2.2 Characterization of the GaN template

Before optimizing the growth of the spin injector, we first studied the property of the GaN template we were going to use. The template consists of an epitaxial 2 μm -thick GaN (0001) layer grown directly on c-plane sapphire (Al_2O_3) substrates by metal-organic chemical vapor deposition (MOCVD) in SINANO, Suzhou. Figure 4.8 shows an AFM image ($2 \times 2 \mu\text{m}^2$) of the surface of the GaN (0001) template. One can identify different features such as atomic terraces and steps. This is the consequence of the step-flow growth mode occurring at 1000°C . The measured RMS value is about 1\AA for the $2 \times 2 \mu\text{m}^2$ area.

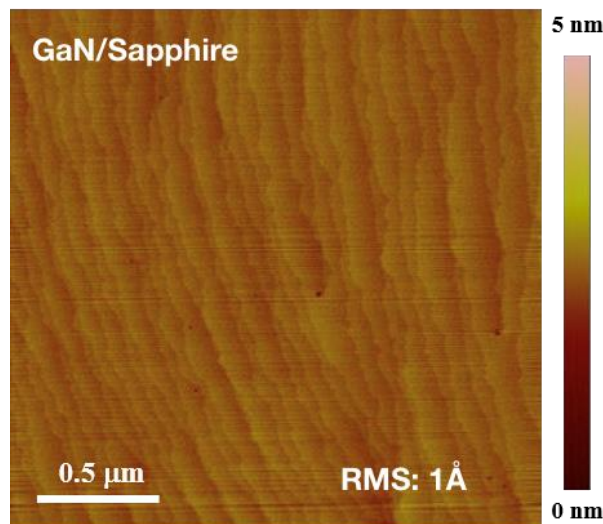


Figure 4.8: AFM image ($2 \times 2 \mu\text{m}^2$) of the GaN (0001) template. Black spots indicate dislocations. The bar on the right indicates the contrast scale.

We further investigate the vibrational and the optical properties by both Raman and photoluminescence spectroscopy. Figure 4.9 shows the Raman spectrum measured on the GaN template. A laser diode operating at 532 nm was used as excitation source. At least four peaks can be identified corresponding to the E₂ mode (at 142 and 569 cm⁻¹) and the A₁ mode (at 735 cm⁻¹). In addition, a rather broad and weak band at around 416 cm⁻¹ seems to be due to the E_g modes of the sapphire substrate. Figure 4.10 shows photoluminescence (PL) measurements of the GaN template grown on sapphire substrate. The PL was excited by a 325nm He-Cd laser at room temperature. Two main bands can be observed: firstly, a strong near band-gap-edge emission (NBE) at a wavelength of 360nm and secondly, a broad yellow luminescence band (YL) centered at about 570nm. The latter may be due to the presence of Ga and N vacancies, oxygen or deep level impurities, and possibly amorphous phases.

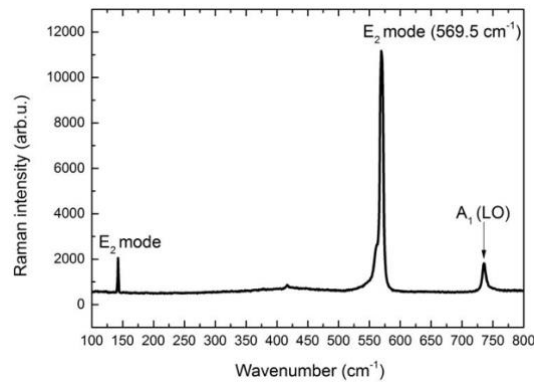


Figure 4.9: Raman spectrum measured on the GaN template at RT. The excitation is provided by a 532nm laser diode.

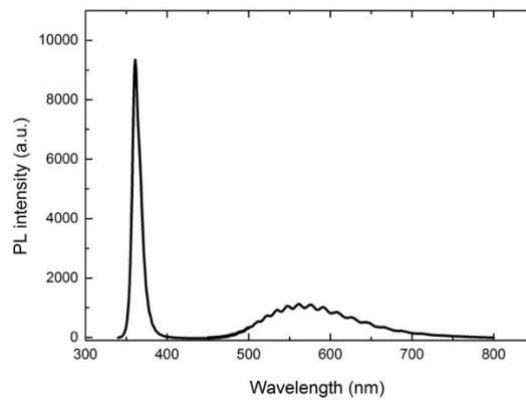


Figure 4.10: PL spectrum of a GaN template grown on sapphire substrate excited by a 325 nm He-Cd laser at room temperature.

4.2.3 Growth of a MgO layer on the GaN template

The epitaxial growth of a MgO layer is a first step for the realization of a spin injector on GaN. The structural quality of the MgO layer is essential to ensure efficient spin injection. The growth of MgO layer on the GaN template was carried out in an ultra-high vacuum (UHV) molecular beam epitaxy (MBE) chamber. Before being introduced into the MBE chamber, the GaN (0001) surface was firstly cleaned ex-situ with acetone and isopropanol in an ultrasonic bath for 5 min in each solvent. The GaN template was then dipped in a 10% HCl solution for 2 min to remove the native oxide layer and possible surface contaminants. Gallium (III) oxide react with hydrogen chloride to produce gallium (III) chloride and water. Finally, the GaN template was cleaned with isopropanol again for 1 min and subsequently dried with N₂ gas. After loading the GaN substrate in the MBE chamber, an in-situ deoxidation is further performed by heating the template to 600°C for 30 min in order to obtain a clean and well-ordered surface. The surface evolution was monitored by in situ reflection high-energy electron diffraction (RHEED). Figure 4.11 shows RHEED patterns taken from the GaN surface along the [11-20] and [10-10] azimuthal directions. The incident electron beam was parallel to the [11-20] azimuthal direction. One can distinguish faint Kikuchi lines from the GaN (0001) surface, as shown in Figure 4.11, indicating that a high quality, smooth, and long range ordered single crystalline surface is obtained. The substrates were then cooled down to the temperature used for the growth of MgO. Subsequently, we grew a 3 nm thick MgO layer at various temperatures (room temperature, 200°C and 400°C) by evaporating directly MgO from a high-purity (99.999%) single MgO crystal. The base pressure of the chamber was around 2×10^{-10} Torr. The MgO layer serves as a tunneling barrier to overcome the impedance mismatch problem for spin injection from a ferromagnetic metal to a semiconductor. When the growth was finished, we firstly checked the RHEED patterns to determine whether the film is single-crystalline or not. Once taken from the MBE chamber, ex-situ AFM measurements were conducted. Figure 4.12 (a), (b) and (c) show the RHEED patterns obtained after growth of MgO on GaN at various temperatures. Figure 4.12 (d), (e) and

(f) show the corresponding AFM images. By combining the RHEED patterns with the AFM results, we found that the growth conditions are optimized for a growth at 200°C with a roughness of 2.41 Å over an area of 1×1 μm². By using these conditions, a flat and smooth surface can be obtained.

MgO can thus be grown epitaxially on the GaN template. According to Craft *et al.*¹⁸¹, there are two possible orientations for the growth of the rock salt structure MgO on the wurtzite GaN. Figure 4.13 shows the in-plane epitaxial relationship between (111)-oriented MgO thin films on (0001) wurtzite GaN. The first possibility is that the MgO [10-1] direction, is parallel to the GaN [11-20] direction. The second possibility is that the MgO [10-1] direction is parallel to the GaN [10-10] direction. The two orientations are nearly degenerate from a lattice mismatch perspective with 6.9% tensile against 7.4% compressive strain, respectively. We obtained the epitaxial relationship (111) [10-1] MgO// (0001) [11-20] GaN with a 6.9% tensile strain. From our RHEED patterns, the spacing between the diffraction streaks of MgO is slightly larger than that of GaN (see blue dashed lines in Figure 4.17 (c)), indicating a smaller lattice constant of MgO, which corresponds well to the orientation relationship MgO(111) [10-1]//GaN(0001) [11-20].

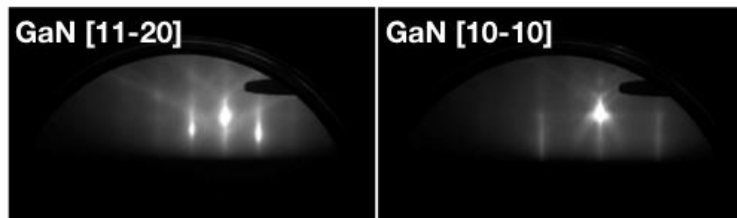


Figure 4.11: RHEED patterns of GaN template after 600C annealing for 30 mins.

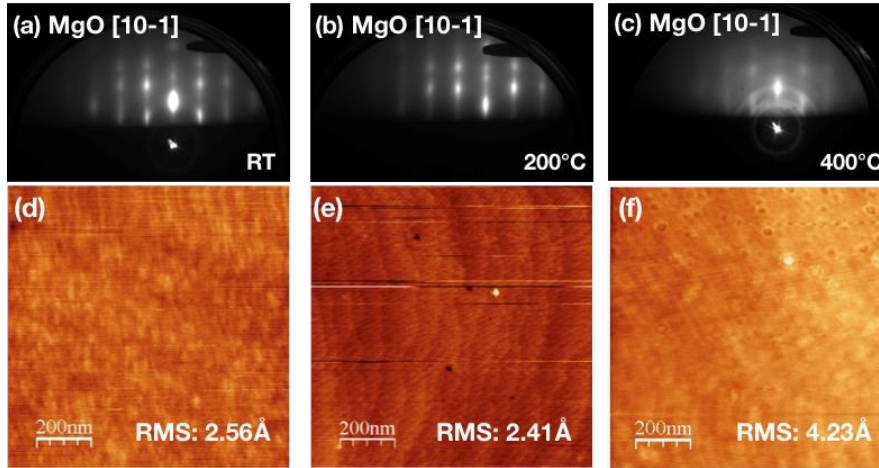


Figure 4.12: RHEED patterns obtained after growth of a 3nm-thick MgO layer at RT (a), 200°C (b) and 400°C (c). (d-f) Corresponding AFM images.

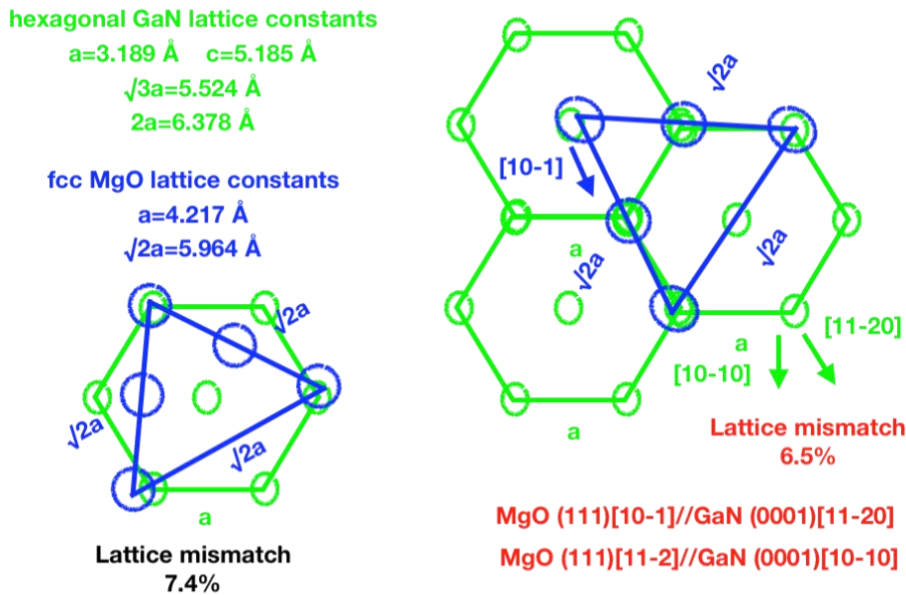


Figure 4.13: Schematic diagram showing the in-plane epitaxial relationship between (111)-oriented MgO thin films on (0001) wurtzite GaN.

4.2.4 Growth of the Fe/MgO spin injector

After obtaining an epitaxial MgO layer on the GaN template, we further grow the ferromagnetic layer consisting of a 10 nm thick Fe layer while the substrate temperature was kept at around 79°C. The Fe/MgO spin injector is finally capped by a 5 nm thick Au film to prevent any oxidation of the Fe layer. The sample was then annealed at different temperatures. The base pressure of the chamber was around 2×10^{-10} Torr.

During the growth, we used in-situ RHEED to monitor the surface change. Ex-situ characterization of the surface morphology was conducted by Atomic force microscope (AFM). A schematic of the layer stack is shown in Figure 4.14 (a).

Figure 4.14 (b) shows the RHEED patterns of both as-grown Fe films and Fe films annealed at different temperatures during Fe/MgO growth on GaN. For as grown films, the RHEED patterns appear spotty indicating a rough surface. With increasing annealing temperature, the RHEED patterns became more and more streaky indicating that the surface is progressively smoothed. The incident electron beam was parallel to the [11-20] azimuthal direction of GaN (0001). Figure 4.15 shows the epitaxial relationships of Fe/MgO/GaN. The proposed growth of this heterostructure¹⁷⁷, including the observed cyclic twinned (triplets) Fe crystal domains (green) on MgO (111) (red), is shown on the GaN (0001) lattice (black circles). In our case, the epitaxial relationships can be defined as (110) <001>Fe//((111)<1-10>MgO. Hauch *et al.*¹⁸², Lazarov *et al.*¹⁸³ and Khalid *et al.*¹⁸⁴ studied the growth of Fe (110) films on MgO (111) and reported the same epitaxial relations.

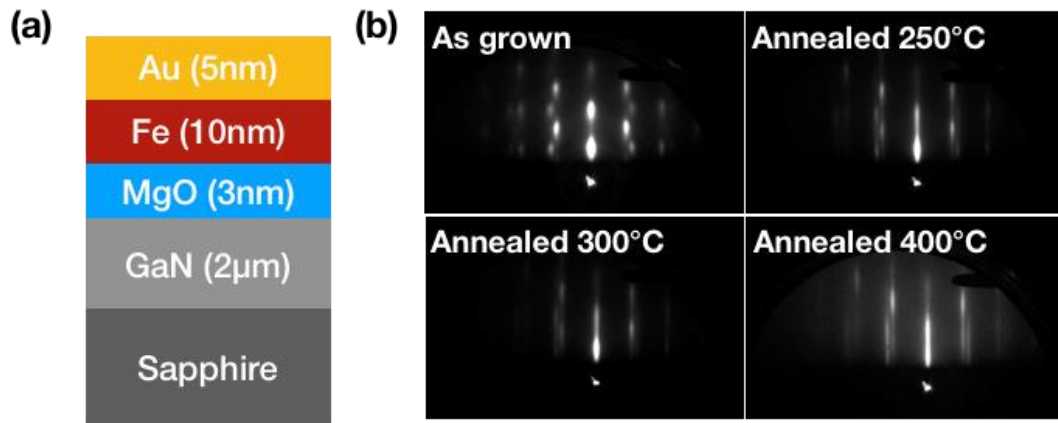


Figure 4.14: (a) Schematic structure of the Fe/MgO spin injector. (b) RHEED patterns of Fe film as grown and annealed at different temperatures (250°C, 300°C and 400°C) taken along the [11-20] azimuthal direction of the GaN (0001) surface.

Figure 4.16 shows the AFM images of Fe/MgO spin injector. As we can see, the RMS is about 3.28 Å when the Fe/MgO spin injector is measured over an area of 1×1

μm^2 . However, similar measurements performed over an area of $5 \times 5 \mu\text{m}^2$ show that the Fe/MgO spin injector is rough, with a RMS value of 7.2 \AA .

RHEED patterns show that Fe films on MgO (111)/GaN (0001) are reconstructed but the surface appears to be rough. Moreover, since the magnetization is expected to be in-plane (not shown here) for a 10 nm thick Fe thin film, the Fe/MgO spin injector seems not to be of great interest to obtain the desired PMA. For all these reasons, we then investigate the growth of a Co/MgO spin injector on GaN.

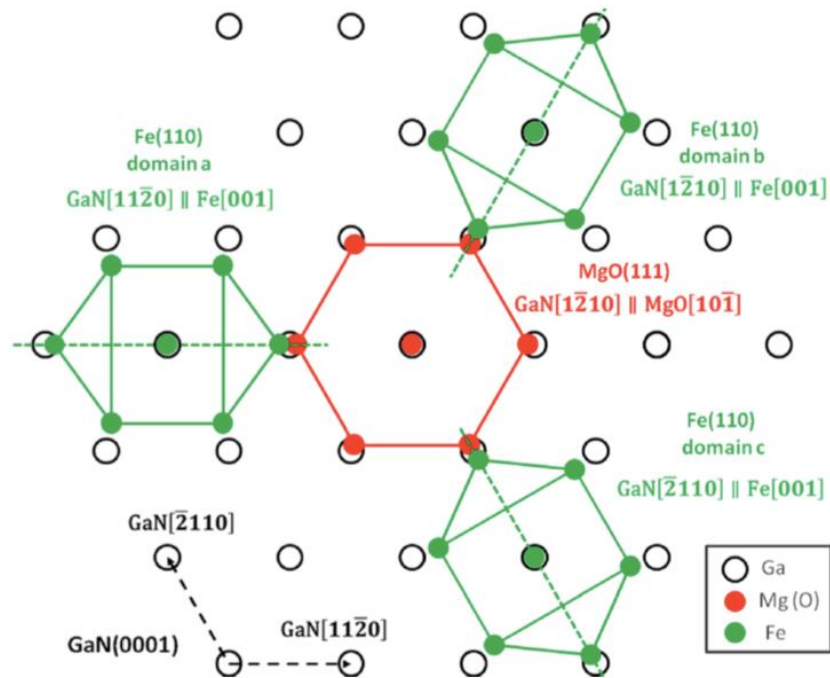


Figure 4.15: Schematic diagram of three Fe lattices (green) on MgO (111) lattice planes (red) overlaid on a c-plane GaN lattice (black).

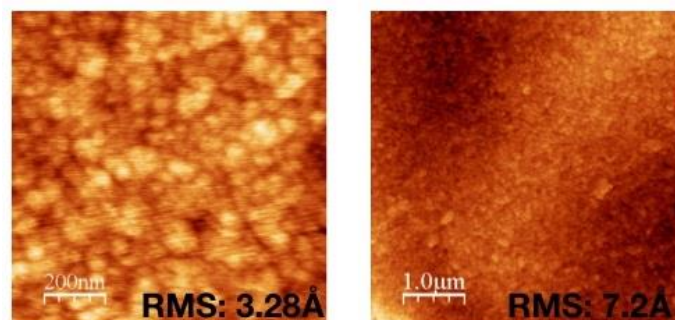


Figure 4.16: AFM measurements of the Fe/MgO spin injector.

4.2.5 Development of Co/MgO spin injector with PMA on GaN

4.2.5.1 Growth of the Co/MgO spin injector

As mentioned before, a 3nm thick MgO layer was first deposited on the GaN surface at 200°C by using e-beam evaporation. Then the growth of a 5nm thick Co layer on MgO was performed at RT, following by an annealing at 250°C for 20mins to improve the crystalline quality. Finally, a 5nm thick Au layer was deposited to protect the sample from oxidation. A schematic of the layer structure is shown in Figure 4.17 (a).

High-resolution transmission electron microscopy (HR-TEM) and high-resolution scanning transmission electron microscopy (HR-STEM) and spatially resolved EELS were performed by using a probe-corrected FEI TITAN and a probe-corrected microscope JEOL ARM200F equipped with a GATAN GIF quantum energy filter to reveal the structure and element distribution in the Co/MgO/GaN structure. The microscope was operated at 200kV. High angle annular dark-field (HAADF), annular dark-field (ADF) and bright-field (BF) images were simultaneously recorded for the structural study, while only the HAADF and ADF signals were recorded during the EELS chemical analysis. Two EELS spectrum images were simultaneously recorded with energy dispersion of 0.5eV, one containing the zero and low loss peaks and the other one containing the high loss peaks. EELS spectrum images were denoised using a principal component analysis procedure¹⁸⁵ before their processing to draw the chemical maps. Thin lamellae for STEM investigations were prepared by focused ion beam milling. During this procedure the sample is capped by a Pt-C layer on the area of lift out. This layer appears on TEM or STEM micrographs as granular Pt-C deposited on the Au layer. Ex-situ magnetic measurements were performed by superconducting quantum interference device (SQUID) and vibrating sample magnetometer (VSM) magnetometry measurements.

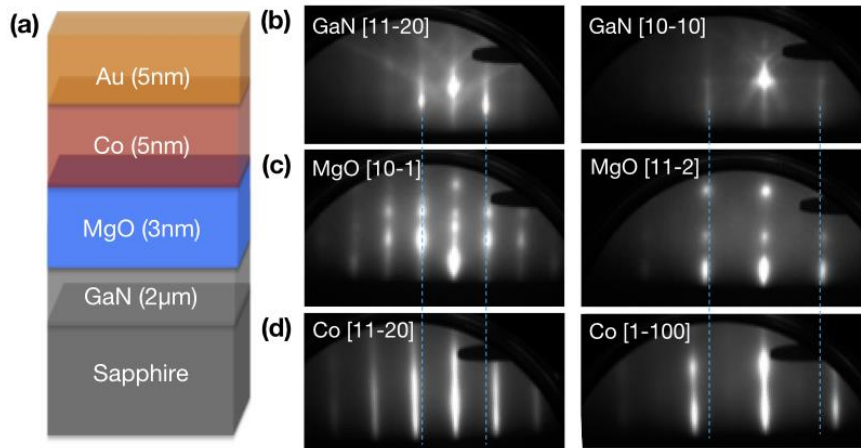


Figure 4.17: (a) Schematic diagram of the multilayer stack. RHEED patterns taken at 30 KV along the [11-20] and [10-10] azimuths of (b) the GaN (0001) surface before deposition, (c) after 3 nm MgO deposition and (d) subsequent 5 nm Co film followed by annealing at 250°C for 20 minutes.

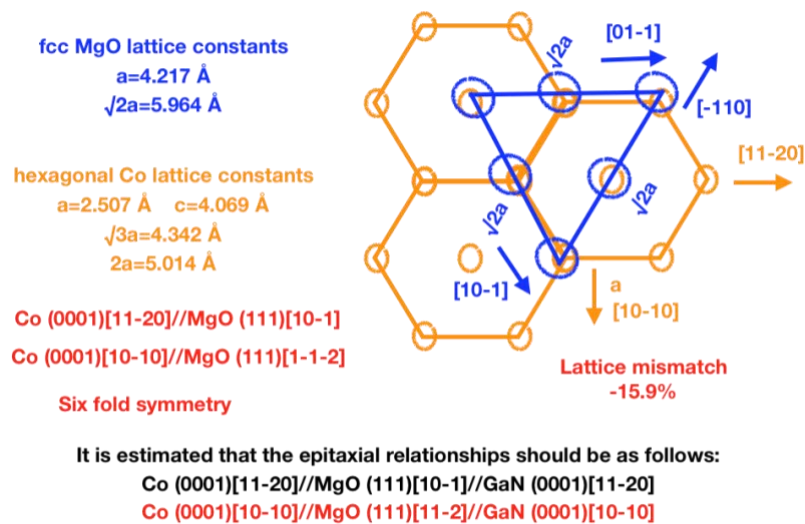


Figure 4.18: Schematic diagram showing the in-plane epitaxial relationship between (111)-oriented MgO thin films on (0001) Co.

4.2.5.2 Structural and chemical characterizations of the Co/MgO spin injector

In situ reflection high energy electron diffraction (RHEED) was used to monitor the surface crystallinity during the growth of MgO and Co in the MBE chamber. Figure 4.17 (b) show the RHEED patterns from the GaN surface along both [11-20] and [10-10] azimuthal directions after the deoxidation procedure at 600°C. We then deposit a

3nm thick MgO layer at 200°C on the GaN surface. This growth temperature has been optimized to get the best crystallinity and lowest surface roughness. Although the RHEED patterns obtained after MgO growth become spotty (Figure 4.17 (c)), they are compatible with the patterns obtained after GaN deoxidation in both azimuthal directions. Moreover, they appear after each 60° rotation thus indicating an epitaxial growth relationship between MgO and GaN.

The growth of the Co film on MgO is performed at RT to ensure a full coverage of Co on MgO due to the well-known wetting problem of metals on oxide. The as-grown Co film is characterized by an elongated spot-like RHEED pattern (not shown). However, the pattern becomes streaky after annealing at 250°C for 20mins, indicating an improvement of both surface roughness and crystallinity (Figure 4.17(d)). As marked by the blue dashed lines in Fig. 4.17 (d), the separation between the diffraction streaks is larger for Co than for MgO thus indicating that Co has a smaller lattice constant. From the RHEED observations, we can thus deduce the epitaxial orientation relationship which is given by $\text{Co}(0001)[11\text{-}20]/\text{MgO}(111)[10\text{-}1]$. This is quite surprising since the lattice mismatch corresponding to this epitaxial relationship is as large as 16%. Nevertheless, our finding is consistent with the reported epitaxial relationship by Nukaga *et al.*¹⁸⁶.

Figure 4.19 shows AFM measurements of the Co/MgO spin injector. As we can see, the measurements performed over an area of $5 \times 5 \mu\text{m}^2$ show that the surface of the Co/MgO spin injector is much smoother (RMS is about 3.96 Å) than the surface of the Fe/MgO spin injector, (RMS of which is 7.2 Å).

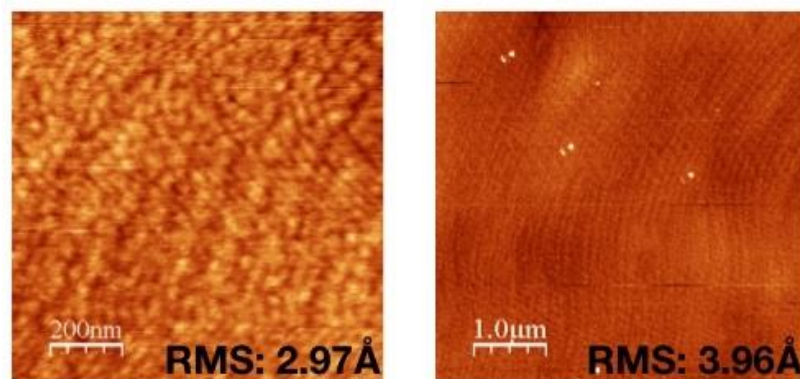


Figure 4.19: AFM measurements of Co/MgO spin injector.

HR-STEM has been used to investigate the interfacial structure of the Co/MgO/GaN heterostructure. In Figure 4.20 (a), the low magnification bright-field STEM image reveals a good homogeneity and low roughness of the heterostructure. From the high magnification STEM image of the cross-section (Figure 4.20 (b)), the real thickness of MgO and Co can be measured to be 2.9 nm and 4.6 nm, respectively. MgO appears well crystalline and with an epitaxial relationship with GaN. This confirms what was observed by RHEED during the sample growth. The analysis of the patterns obtained by Fast Fourier transform (FFT) of the HR-STEM images further confirm the orientation relationship between MgO and GaN and between Co and MgO that were already described in the above RHEED analysis. Because of the strong difference of mean atomic numbers between the layers, there are large differences of electron diffusion between the different layers. It is thus difficult to show atomic arrangements of all layers in one STEM image due to the limited contrast. To more easily display the atomic planes spacing in all the layers and precisely define the interfaces, the contrast between layers was equalized and an intensity profile crossing perpendicularly the interfaces was drawn from a HAADF micrograph (Figure 4.20 (c)). Each peak corresponds to one atomic plane. From the left to the right, GaN, MgO, Co and Au can be easily identified. The GaN/MgO interface is found to be very sharp. However, the interface between MgO and Co seems to be more difficult to define from the d spacing and from the contrast variation in the HAADF image. Red dotted lines on Figure 4.20 (c) show the location of this interface where the phase is not clear on 2 or 3 atomic planes (thickness between 0.5 and 0.7 nm). Two possibilities could explain this observation. The first could have its origin in the roughness of the surface of the MgO layer. Since the TEM lamella has a certain thickness, a small interface roughness can result in the superposition of MgO and Co without any break in the epitaxial relationship. However, this possibility can be excluded from the measurement of MgO surface roughness, which shows an atomic step feature with room mean square roughness of about 2.4 Å. The other reason could be due to the reaction between MgO and Co at the interface, resulting in the oxidation of Co or in the formation of a mixed oxide at the interface.

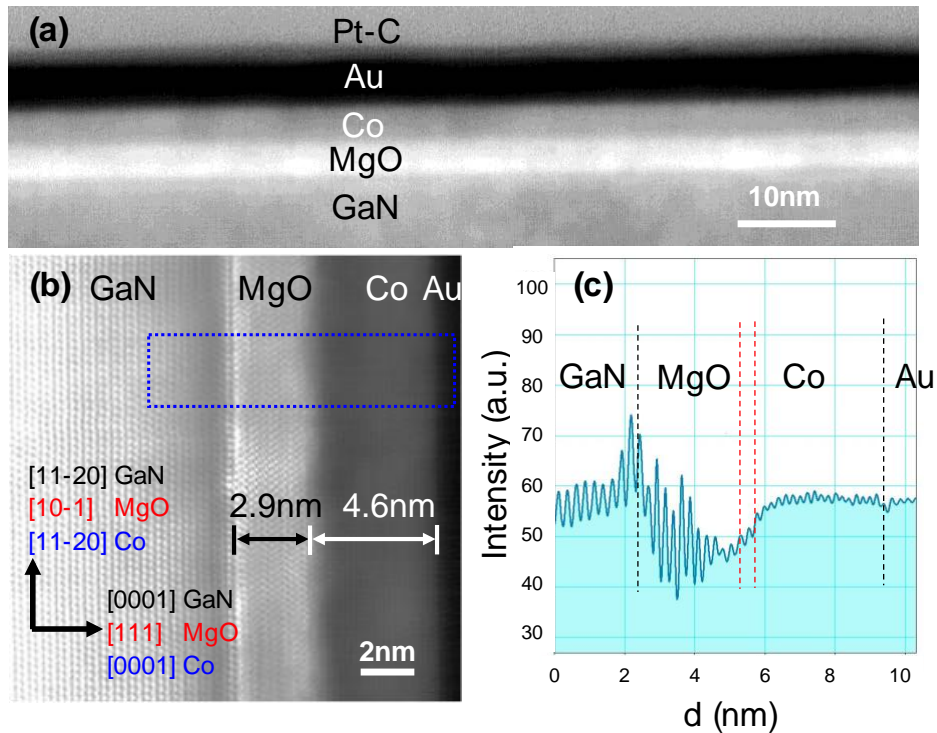


Figure 4.20: (a) Large-scale cross-sectional HR-STEM dark field image of Au/Co/MgO/GaN interface. PtC capping was deposited during the lamella processing by FIB. (b) Magnified HR-STEM bright field image shows the detailed structure of the GaN/MgO/Co interface. (c) Intensity profile drawn from equalized HAADF image recorded in the rectangular area (marked with blue dashed lines in panel (b)). The peaks indicated the position of atom planes, showing from left to right GaN (0002)//MgO(111)//Co(0002)//Au(111). The two red lines indicate where a “gray” contrast at the MgO-Co interface reveals a possible chemical reaction between MgO and Co.

To understand the structure of this interface, spatially resolved STEM-EELS analyses were performed. Figure 4.21 (a) shows a HAADF image of the area where EELS spectrum images were recorded. Figure 4.21 (b) shows elemental maps extracted from the semi-quantitative analysis of the EELS spectrum image. The maps drawn respectively for N_K , Mg_{L23} , O_K , Co_{L3} , Au_{N45} edges clearly display the distribution of the different elements in the GaN/MgO/Co/Au heterostructure. To qualitatively identify the interface diffusion, semi-quantitative profiles of the elements were plotted Figure 4.21 (c), by integrating the elemental signals of the EELS maps from an area of 0.2 nm

in height (about 1 atomic column) and 10 nm in width parallel to the interfaces. Some information can be obtained from these profiles. Firstly, at the Co/Au interface, the overlap of Co and Au is restricted to about 2 nm, indicating a small inter-diffusion of Co and Au at this interface. This agrees with the inter-diffusion between Co and Au that has been observed in organic spin valve structures grown at room temperature.¹⁸⁷ Secondly, a separation of about 0.4 nm between the slopes of Mg and O signals at the MgO/Co interface is observed. This slope separation and the small overlapping of the Co signal to Mg and O signals indicates the oxidation of cobalt at the interface and the possible formation of a $Mg_xCo_yO_z$ mixed oxide layer with a thickness of 2-3 atomic layers. This explains the reason why a diffusive contrast is observed at the MgO/Co interface in HR-TEM or HR-STEM images. Thirdly, a structurally sharp and chemically clean GaN/MgO interface is confirmed even after annealing treatment at 600°C.

EELS spectrum images were recorded in STEM mode at 200kV with a probe current of 50 pA, a semi angle of convergence 24 mrad and a semi angle of collection angle of 83 mrad. Two spectrum images have been recorded simultaneously with a dispersion of 0.5 eV, one containing the zero-loss peak, the second starting from a loss of 80 eV. Spatial drift control and correction was applied at the end of each line of spectra. The energy drift was corrected in the both spectrum images using the position of the zero-loss signal of each pixel. Then the spectrum images were denoised using a principal component analysis (PCA). After background subtraction and plural scattering correction, elemental maps were drawn from semi-quantitative analysis of the spectra.

Figure 4.22 shows typical spectra after PCA processing and before the background subtraction. The spectra were extracted from the high-loss spectrum image in the zones indicated by the rectangular area labelled on the HAADF image. The HAADF image was recorded simultaneously with the two spectrum images. The positions of edges are indicated on the figure. One can note that even if the Au_{N3-2} is a minor edge, the signal is strong enough and typical to be used for gold identification and mapping.

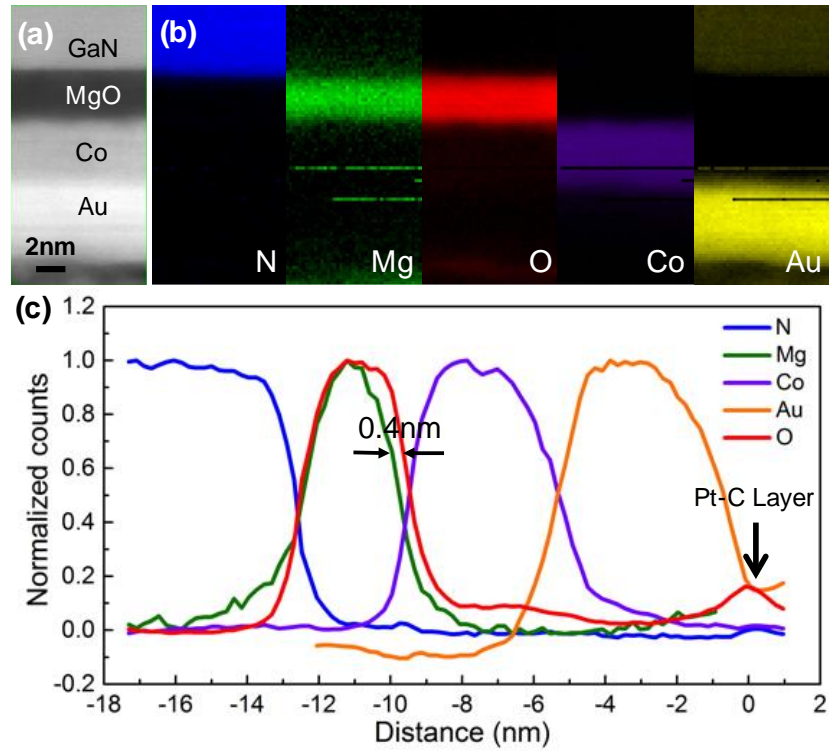


Figure 4.21: (a) HAADF image recorded simultaneously with the EELS spectrum images. The GaN substrate is presented on the top of the images. (b) Individual element maps drawn with N_k , Mg_{L23} , O_K , Co_{L3} , Au_{N45} signals extracted from processed EELS spectrum images. (c) The normalized profiles of elements were extracted from the maps of elements.

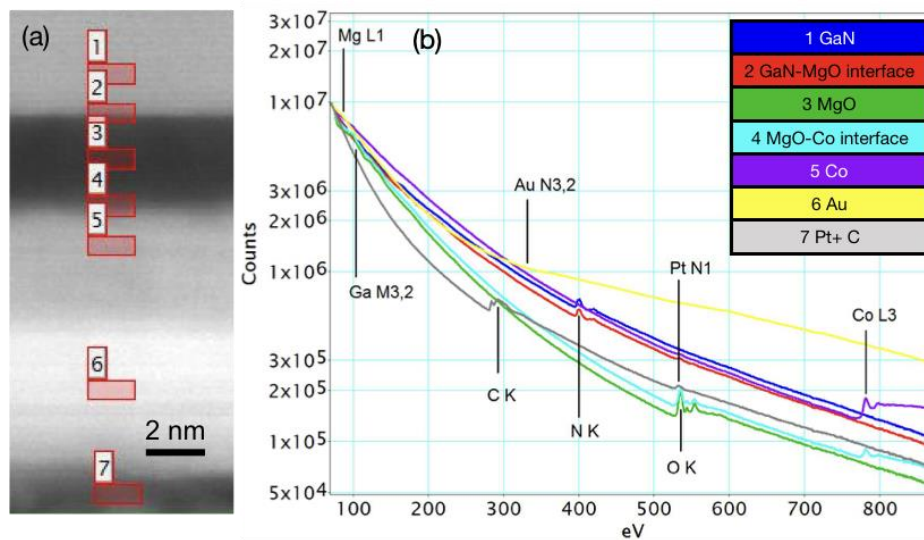


Figure 4.22: (a) HAADF image where the EELS spectrum image was recorded. (b) EELS spectra extracted from the spectrum images after PCA denoising in the area marked on the HAADF image. The positions of the edges are indicated on the figure.

4.2.5.3 Magnetic properties of the Co/MgO spin injector

The magnetic properties of the Co(4.6nm)/MgO(2.9nm)/GaN sample has been measured by SQUID and VSM. Figure 4.23 (a) shows the magnetic hysteresis loops acquired at 300K with both in-plane (IP) and out-of-plane (OOP) magnetic field. A clear perpendicular magnetic anisotropy can be observed since the remnant magnetization at zero field in out-of-plane measurement is much larger than that obtained for the in-plane measurement. The ratio of perpendicular remnant magnetization to the saturation magnetization (M_r/M_s) reaches about 0.8 at room temperature. To confirm that the in-plane measurement is not influenced by the in-plane magnetic hard axis, we have performed a measurement of remnant magnetization as a function of in-plane angle, as shown in Figure 4.23 (b). We have observed a uniaxial behavior with the maximum of M_r/M_s not exceeding 0.2. This confirms the large perpendicular magnetic anisotropy (PMA) in our sample. We can further extract the effective anisotropy constant (K_{eff}) by calculating the difference in area between the magnetization loops measured when the magnetic field is applied perpendicular and parallel to the layers. The K_{eff} is extracted to be $2.2 \times 10^5 \text{ J/m}^3$ at RT. The inset of Figure 4.23 (a) shows the hysteresis loops measured at different temperatures with out-of-plane field. The coercivity and M_r/M_s increases with decreasing temperature, which indicates an improvement of PMA at low temperatures.

This large PMA is quite surprising for such thick Co layer (4.6nm) since the bulk in-plane anisotropy and demagnetization always tend to keep the magnetization in the plane. This thickness is much larger than that of the intensively studied Fe/MgO structure (1.2nm)^{188,189}, and also two times larger than the recently reported Co thickness (2.5nm) on graphene¹⁹⁰. To understand the interface contribution to the establishment of PMA, we have prepared several Co/MgO/GaN samples with different thickness of Co ranging from 1 to 3nm. Figure 4.23 (c) shows the hysteresis loops measured at RT with out-of-plane magnetic field. It is found that the PMA cannot be established for Co thicknesses less than 3 nm, and the ratio M_r/M_s shown in Figure 4.23 (d) increases with the increasing of Co thickness. This can be understood by the

incomplete coverage of Co layer on the MgO surface when the Co layer is too thin. For the growth of Co on MgO (100) surface, it is reported that a 2nm thick Co exhibits the morphology of separated islands with 3D growth mode, while a 5nm thick Co is a continuous 2D film.¹⁹¹ Therefore, the magnetic properties of Co for thicknesses less than 3 nm is dominated by the superparamagnetic behavior of Co islands. For Co thicknesses larger than 3 nm, the film becomes continuous and ferromagnetic.

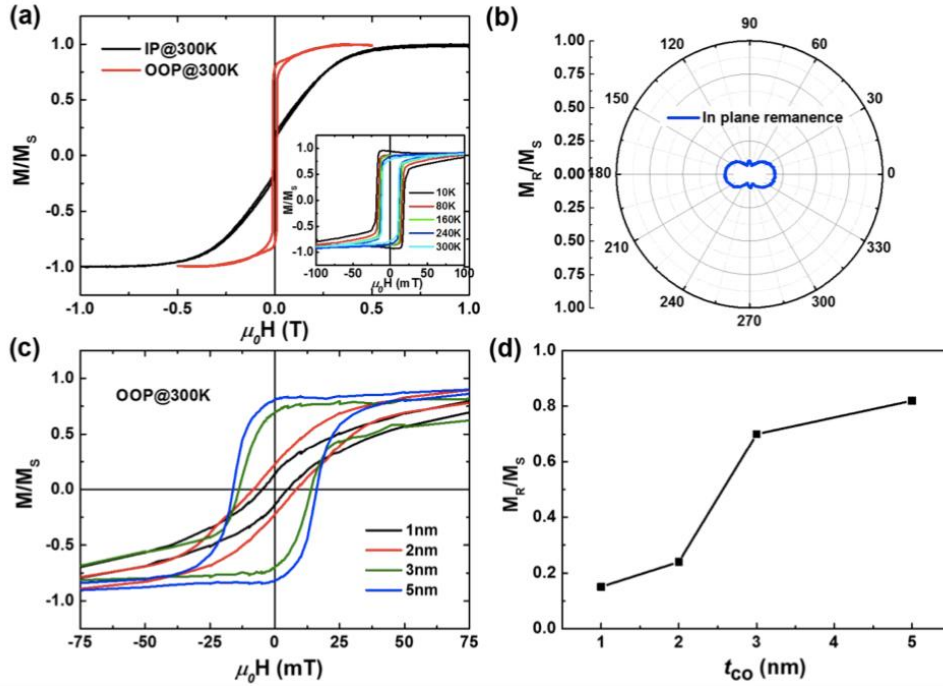


Figure 4.23: (a) M-H curves measured at RT by SQUID for Co (4.6nm)/MgO/GaN structure with applied in-plane (IP) and out-of-plane (OOP) magnetic fields. Inset: M-H curves at different temperatures with OOP field. (b) Normalized in-plane remnant magnetization as a function of in-plane angle with magnetic field. (c) RT out-of-plane M-H curves for Co/MgO/GaN with different Co thicknesses. (d) Normalized perpendicular remnant magnetization as a function of different Co thicknesses.

4.2.5.4 Ab-initio calculations of Co/MgO spin injector

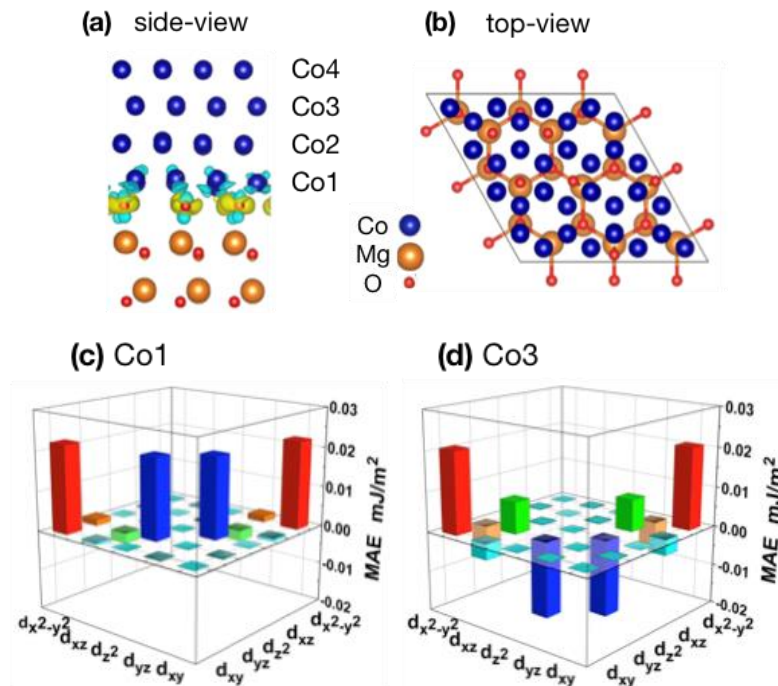
To further shed light on the origin of the magnetic anisotropy in Co/MgO/GaN heterostructure, we performed first principle calculations using the Vienna ab-initio simulation package (VASP).^{192,193,194} In all the calculations, the exchange-correlation potential was treated within the generalized gradient approximation (GGA) using the

Perdew-Burke-Ernzerhof (PBE)¹⁹⁵ functional. The cutoff energy is 420 eV and a $9 \times 9 \times 1$ k-mesh was used in the calculations. The convergence energy and force of the heterostructure are 10^{-7} eV and 0.001 eV/Å, respectively. The optimized 4 monolayer (ML) Co(0001)/MgO(111) structure is shown in Figure 4.24 (a) for the side view and in Figure 4.24 (b) for the top view (only the first Co layer is shown). The magnetic anisotropy energy (MAE) was defined as $MAE = E_x - E_z$, where E_x and E_z are the energies corresponding to magnetic moment aligning along in-plane and out-of-plane directions, respectively. Therefore, a positive value of MAE corresponds to a perpendicular magnetic anisotropy (PMA).

The calculated MAE as a function of Co thickness ranging from 2 to 4 monolayers (ML) is shown in Figure 4.24 (e). One can find that the MAE increases as the Co thickness increases. For Co(4ML)/MgO, the PMA can reach 0.99 mJ/m². For comparison, we have also calculated the MAE of a pristine Co 4ML to be 0.71 mJ/m². Therefore, the growth of Co on MgO (111) leads a 40% enhancement of PMA compared to the pristine Co. The contribution of PMA is further analyzed from the layer-resolved MAE for the Co(4ML)/MgO structure, as shown in Figure 4.24 (f). Similar to Fe/MgO heterostructure¹⁹⁶, the interfacial and surface Co atoms dominate the PMA, while the MAE of interfacial third layer Co atoms is negative, which indicates an in-plane anisotropy. The increase of MAE for the surface Co atoms is due to the contact with vacuum. To comprehensively understand the enhancement of MAE for the interfacial Co, we have performed a comparative analysis between Co atoms at the interface (Co1) and Co in the third layer (Co3) in the aspect of orbital resolved MAE, as shown in Figure 4.24 (c) and (d), respectively. One can see that the matrix element of $(d_{xy}, d_{x^2-y^2})$ (labeled as red bars in Figure 4.24 (c) and (d)) gives rise to the largest positive contribution to the PMA both in Co1 and Co3. The matrix element of (d_{yz}, d_{z^2}) (blue bars) in Co3 is negative and the absolute value of this matrix element is larger than $(d_{xy}, d_{x^2-y^2})$, which can explain why Co3 shows an in-plane magnetic anisotropy. However, different from Co3, (d_{yz}, d_{z^2}) in Co1 still maintains a large positive contribution to the PMA leading to the overall contribution of PMA much larger than

that of Co3. Therefore, the matrix element of (d_{yz} , d_{z^2}) is the main origin responsible for the different MAE observed in the two Co layers.

Considering that the largely enhanced MAE comes from the Co1 at the Co/MgO (111) interface, the hybridization between Co- d and O- p orbitals may have a large influence on the MAE. Therefore, to further understand the electronic state changes at the interface, we plot the projected density of states (pDOS) of Co1 and Co3 as shown in Figure 4.24 (g) and (h), respectively. It can be seen that the interfacial oxygen atoms strongly influence the energy levels of Co1- d orbitals. One of the most important changes comes from the majority occupied d_{yz} and d_{z^2} states. In particular, it is found that the d_{yz} and d_{z^2} states of interfacial Co1 atoms (blue arrow in Figure 4.24 (g)) are closer to the Fermi level compared to those of Co3. This is because that the Co atom at the interface has large hybridization with MgO layer underneath. A direct view of this hybridization can be seen in the differential charge density plotted in Figure 4.24 (a), where the yellow and sky blue color represent for charge accumulation and depletion regions, respectively. As demonstrated from the second perturbation theory by Wang et al., the electronic states in the vicinity of the Fermi level give the largest contribution to the MAE¹⁹⁷. Therefore, the d_{yz} and d_{z^2} states closer to the Fermi level strongly enhance the MAE of Co1 at the interface.



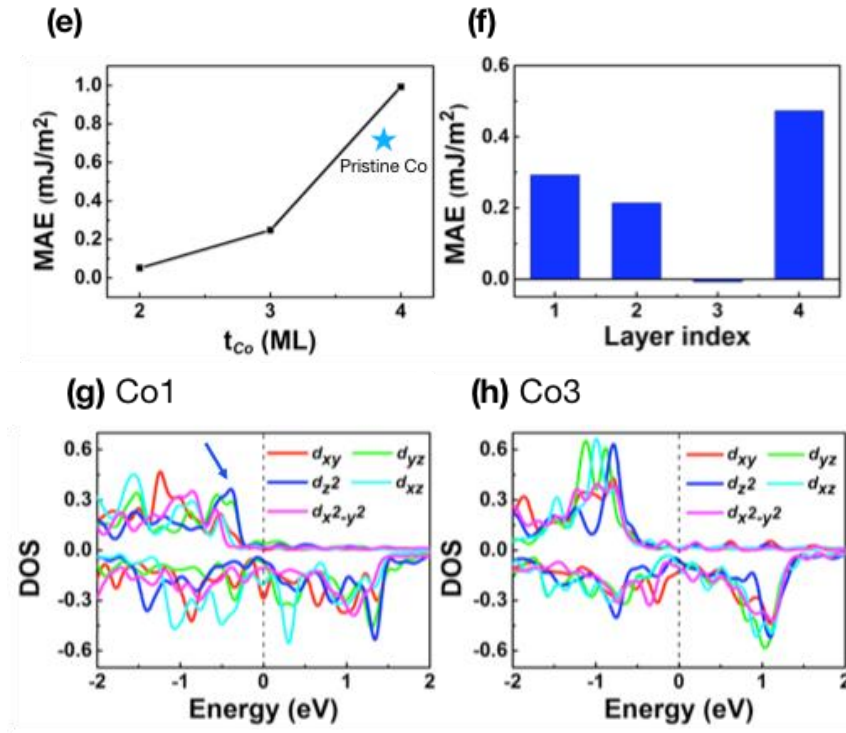


Figure 4.24: (a) Side view of calculated Co (4ML)/MgO (111) structure. At the Co/MgO interface, the yellow and sky blue color correspond to charge accumulation and depletion regions, respectively. The isosurface charge density is $0.01 \text{ e}/\text{\AA}^3$. (b) Top view of Co on MgO (111) surface. Orbital-resolved MAE of selected (c) Co1 and (d) Co3 in Co (4ML)/MgO structure. (e) Calculated MAE as a function of Co thickness. (f) Layer resolved MAE of Co(4ML)/MgO heterostructure. Projected density of states of selected (g) Co1 and (h) Co3 atoms at the Co (4ML)/MgO structure.

4.2.5.5 Discussion

The interfacial chemical analysis indicates that a 0.4nm thick $\text{Co}_x\text{Mg}_y\text{O}_z$ alloy could exist at the MgO/Co interface. This alloy could have a cubic spinel structure (MgCo_2O_4 ¹⁹⁸), which is probably formed during the annealing of the Co layer at 250°C . However, in the case of Co or Fe growth on MgO (001) surface, clean and sharp interfaces are observed even after 400°C annealing. This could be due to the different chemical reactivity on the non-polar surface MgO (001) and on the polar surface MgO (111)¹⁹⁹. Since MgO (111) has an oxygen terminated surface, Co could be easily oxidized during the annealing. However, in ab-initio calculations, for the reason of

simplification, we have not taken account this interfacial oxidation layer. To understand how it influences on the PMA, we have calculated the surface anisotropy K_s via the extracted K_{eff} by the formula: $K_s=(K_{\text{eff}}-E_{\text{demag}}-K_b)\times t_{\text{Co}}$, where E_{demag} is the demagnetization field energy, which can be calculated from $-Ms^2/2\mu_0$, is about $1.33\times 10^6\text{J/m}^3$. K_b is magnetic crystalline anisotropy which is $0.53\times 10^6\text{J/m}^3$ for hcp Co(0001)^{200,201}. With the extracted $K_{\text{eff}}=2.2\times 10^5\text{J/m}^3$ and the Co thickness t_{Co} of 4.6nm, we can obtain $K_s=4.5\text{mJ/m}^2$, which is larger than the estimated MAE for the same thickness of Co on MgO (111) by ab-initio calculation (about 2mJ/m^2). This could suggest that this oxidation layer may also play an important role to enhance the PMA. Further calculation with a refined structure could be necessary to investigate the influence by the oxidation layer.

Since we found an increase of PMA with increasing Co thickness, it could be interesting to determine the critical thickness at which the magnetic anisotropy becomes in plane. With the estimated $K_s=4.5\text{mJ/m}^2$, the critical thickness t_{cri} can be calculated when $K_{\text{eff}}=0$. Therefore, we can estimate $t_{\text{cri}}=5.9\text{nm}$. Experimentally, we have found that a 10nm thick Co film on MgO/GaN has an in-plane magnetic anisotropy. More samples with Co thicknesses between 5 and 10nm would be necessary to confirm the estimated critical thickness. Since the total metallic layer thickness in the spin-injector for spin-LED should not exceed 10nm due to the strong light absorption of metals (50% with 10nm thickness), the thickness of Co should be as thin as possible. Therefore, the thickness in this study (4.6nm) is a good compromise to achieve good PMA, acceptable light absorption ratio and high spin injection efficiency.

4.2.5.6 Conclusions

We have demonstrated strongly enhanced perpendicular magnetic anisotropy of Co films in Co/MgO/GaN heterostructures both experimentally and theoretically using ab-initio calculations. The Co/MgO heterostructures have been grown by MBE on GaN/sapphire substrate, exhibiting an epitaxial structure with crystalline orientation relationships Co(0001)[1-100]/MgO(111)[11-2]/GaN(0002)[11-20]. HRTEM and HR-

STEM combined with EELS have been used to investigate the interfacial structure and chemistry. A sharp and clean MgO/GaN interface is found even after 600°C annealing, while a 2-3ML thick $\text{Mg}_x\text{Co}_y\text{O}_z$ alloy layer exists at the MgO/Co interface. It is found that a 4.6nm thick Co layer on MgO/GaN still exhibits large perpendicular magnetic anisotropy. Ab-initio calculations on the Co (4ML)/MgO structure shows that the MgO (111) surface can strongly enhance the PMA value by 40% compared to the pristine 4ML thick Co hcp film. Our layer-resolved and orbital-hybridization resolved anisotropy analysis further validate the origin of the PMA enhancement which is due to the interfacial hybridization of O $2p$ and Co $3d$ orbitals at the Co/MgO interface. The perpendicularly magnetized Co/MgO/GaN heterostructure is promising for efficient spin injection and detection in GaN without any external magnetic field.

4.3 Spin injection into a GaN based LED

4.3.1 The GaN n-i-p inversed structure

A Spin-LED is a spin-optoelectronic device converting a spin-polarized carrier population into circularly polarized light through the optical quantum selection rules for dipole radiation. In practice it is usually employed as a detection tool for the study of electrical spin-injection in semiconductors as it offers a fairly direct readout of the spin-polarization injected in the device. After developing a spin injector exhibiting perpendicular magnetic anisotropy, we tried to grow the spin injector on a GaN based LED structure to study the spin injection into the LED. It is well known that a normal GaN LED structure contains a p-type GaN layer on the top (p-i-n type structure). However, for spin injection, what we need is a n-type top GaN LED structure (n-i-p type structure), which is difficult to grow. For a n-i-p type LED structure, during p-type growth, normally we use Mg as p-type dopant. Due to a large amount of hydrogen in the MOCVD growth chamber, Mg doping requires a post-growth annealing in an N_2 atmosphere to remove hydrogen, which then forms passivated Mg-H complexes. For achieving a higher hole concentration, we need a larger doping concentration.

Therefore, after p-type GaN growth, there is a large amount of remaining Mg in the MOCVD growth chamber, which will lead to a memory effect for the following layer growth. A Mg-rich film can form in the subsequent layers after the Mg source is switched off. Alternatively, Mg atoms can even propagate into n-type GaN layer to compensate the n-type doping. In addition, the growth temperature of the n-type GaN is higher than that of the p-type GaN, which probably influences the quality of the quantum wells. Eventually, the threshold voltage of the LED may be higher than that of the normal LED structure. To solve this problem, D.J.H. Lambert et al.²⁰² used a gas without Mg atoms to blow the growth chamber holders for a long time to decrease the concentration of remaining Mg. Lee S. McCarthy et al.²⁰³ combined MBE and MOCVD together to grow heterojunction bipolar transistors (HBT). They took out samples after p-type growth and put the samples in another chamber without Mg atoms to grow the n-type GaN layers.

In this work, all the p-i-n GaN based LED heterostructures as shown in Figure 4.25 were grown by Metal-organic chemical vapor deposition (MOCVD) at Peking University. The spin-injectors deposited on top of the GaN based LED structures were grown by MBE at IJL. The GaN LED structure we used is a blue LED structure grown on sapphire substrate, which contains 5 periods of InGaN/GaN multi-quantum wells (MQWs). In the n-region, the layer that contacts with the spin-injector is significantly doped compared to the active region. The doping profile at the interface is tuned to adjust the Fermi level pinning near the tunnel barrier region and to optimize the spin-injection efficiency in the LED. Here is a detailed description of the LED structure used in this work: c-plane sapphire substrate // 30 nm buffer layer GaN// 2 μm GaN// 600 nm p-type GaN doped with Mg ($p = 10^{17} \text{ cm}^{-3}$)// 20 nm p-type $\text{Al}_{0.18}\text{Ga}_{0.82}\text{N}$ doped with Mg ($p = 10^{17} \text{ cm}^{-3}$)// 5 periods InGaN/GaN MQWs// 200nm n-type GaN doped with Si ($n = 1 \times 10^{18} \text{ cm}^{-3}$).

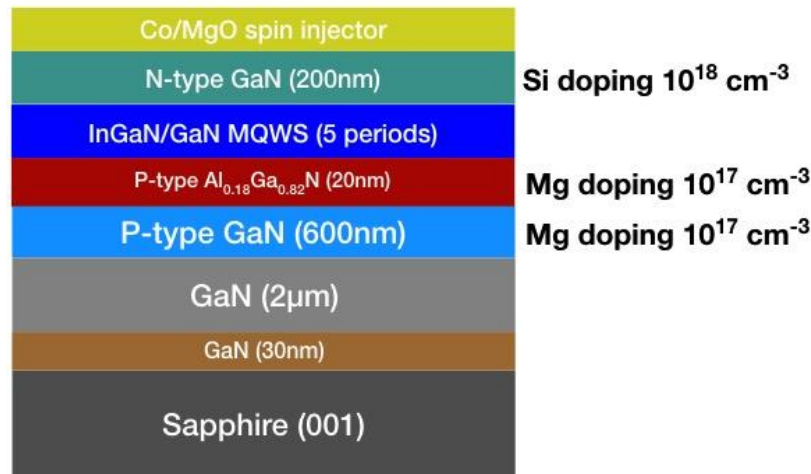


Figure 4.25: A schematic of the GaN based Spin LED.

4.3.2 GaN spin LED device processing and I-V characterization

All the LED devices were fabricated using the same micro-pillar photolithography processes at IJL's clean room (CC-MiNaLor). The lithography processes were based on the classic 2-contacts junction architecture with a top-contact located on the spin-injector and a bottom contact located on the semiconductor substrate. Thus, when reverse biasing the junction; the carriers injected through the spin-injector are being spin-polarized before reaching the active region of the LED. Two main stages can be identified in the fabrication process: (i) first the patterning of micro-pillar-shaped LED junctions with a diameter of $500 \mu\text{m}$ using Ion Beam Etching (During etching, in-situ SIMS was used to monitor the process). The p-i-n sample is usually IBE-etched down to the bottom p-type GaN substrate in order to ensure an ohmic contact between the doped semiconductor and the Ti/Au metals. (ii) formation of the pattern for the electrodes and then deposition of (10nm) Ti/(150nm) Au metal contacts followed by a standard Lift-Off technique. For the contact, the Au layer is taken thick enough (150 nm) in order to protect the fragile spin-injector during the Au-wire bonding using a bonding-machine. The 10 nm Ti layer is used as an anchor layer for Au. Figure 4.26 shows the essential steps of device processings. After finishing the LED process, we firstly carried out I-V measurements on a simple probe station. Figure 4.27 shows the

I-V characteristic of a GaN spin LED. The inset is a photo of the emitted light. Although the spin LED could be lit up, the current is too low at low voltage. Then we did wire-bonding and performed electroluminescence measurements, which will be presented in the paragraph 4.3.3.

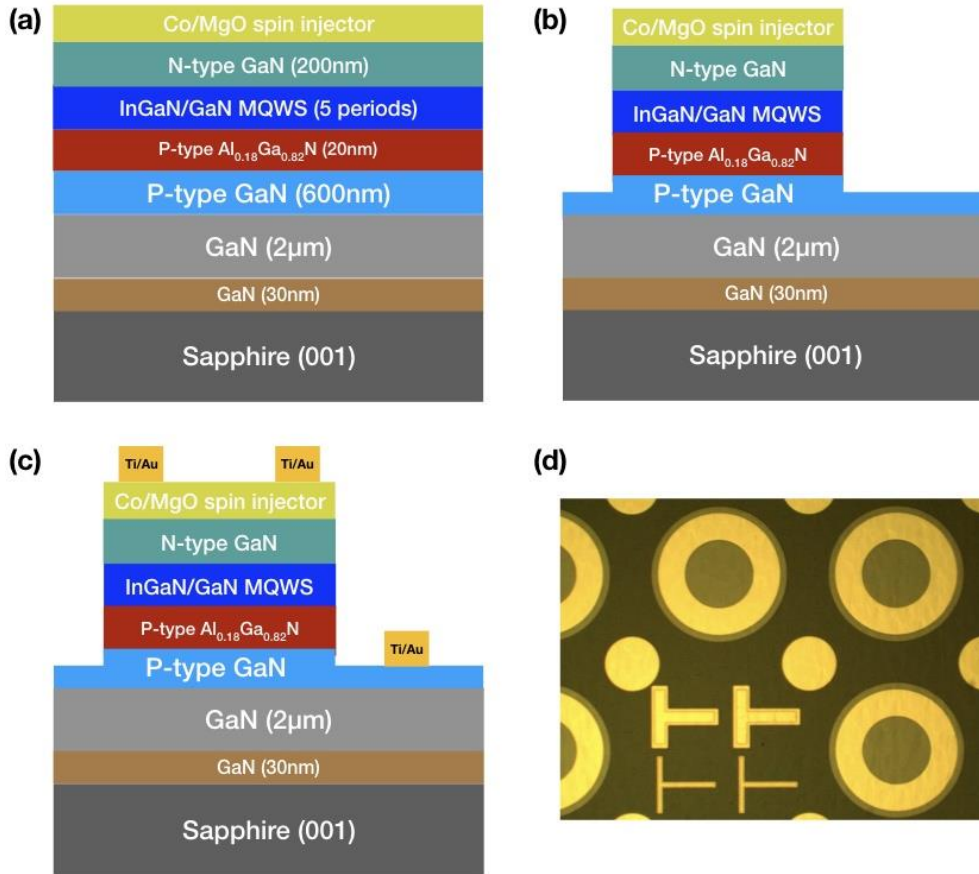


Figure 4.26: Schematic diagram of the spin LED device fabrication process. (a) (b) (c) Side views of the spin LED process. (d) Sample surface after Ti/Au electrode deposition.

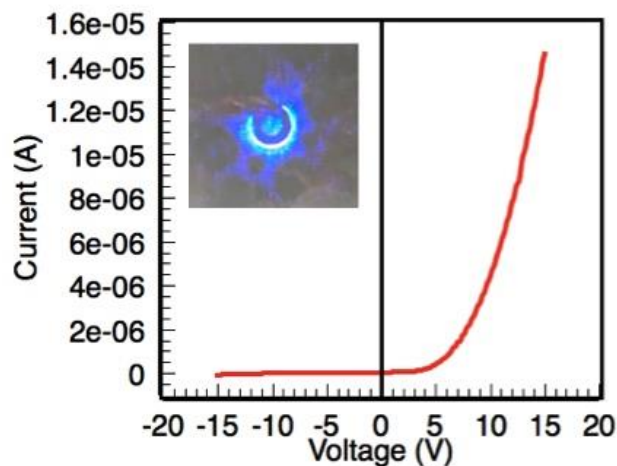


Figure 4.27: I-V curve of the GaN spin-LED measured at RT. (The inset shows a photo of the blue emitted light).

4.3.3 Preliminary polarization resolved EL measurements

All the EL measurements presented below were done by Professor Pierre Renucci at the Laboratoire de Physique et Chimie des Nano-objets (LPCNO), Toulouse. The EL measurement setup is similar to the one described in chapter 2.

Firstly, the sample was mounted onto a cryostat as shown in Figure 4.28 (a). By applying 60V on the sample at low temperature, we can observe the emission from localized spots as shown in Figure 4.28 (b). When the LED was biased, several bright spots appeared on the spin-LED surface.

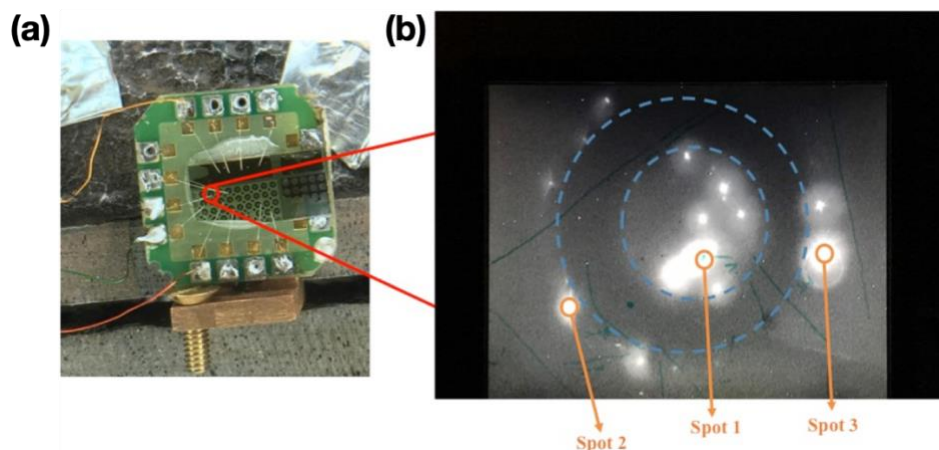


Figure 4.28: (a) Photo of the sample used for the EL measurements. (b) The dashed lines correspond to the electrode ring.

Then detailed EL measurements were performed on these three spots. Figure 4.29 shows EL measurement of spot 1 (Localized inside the electrode ring) biased at 60V at 14K by applying different magnetic fields varying from 0T up to 0.35T. We did not observe any difference between $I(\sigma^+)$ and $I(\sigma^-)$. Therefore, no circularly polarized light could be detected for the different magnetic fields. Similar results were obtained for light applied magnetic field up to 1T.

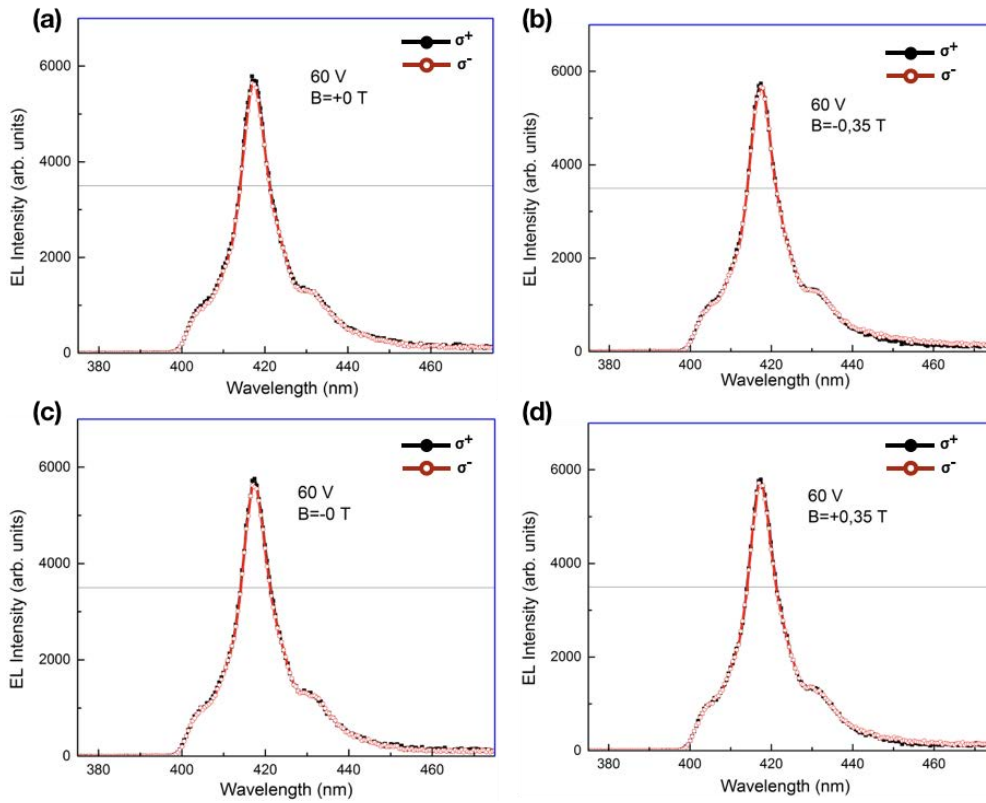


Figure 4.29: EL measurement of spot 1 (inside the electrode ring) biased at 60V at 14K by applying different magnetic fields (a) +0T, (b) -0.35T, (c) -0T, (d) +0.35T.

Figure 4.30 shows the EL measurement of spot 3 biased at 60V at 9K by applying different magnetic fields (a) 0T, (b) +0.5T, (c) -0.5T. In this case, a small intensity appears between the right and left circularly polarized light. In this case, the emitted light originates from radiative recombination occurring in the GaN layer. This is not surprising since spot 3 is located next to a pillar. However, the intensity difference is same when the sign of the applied magnetic field changes. The intensity difference is not due to the magnetization of the spin injector. Figure 4.31 shows EL measurement of spot 2 biased at 50V at 7K by applying different magnetic fields (a) 0T, (b) +0.5T, (c) 1T, (d) 0T. The circular polarization analysis also shows that polarization results are independent of the applied magnetic field thus excluding any role of the spin injector. To continue the study, we will try to improve the quality of the inversed LED structure grown by MOCVD. Moreover, we will also grow the normal GaN LED structure and

then try to use the recently developed wafer-bonding technique to obtain high quality GaN LED structures.

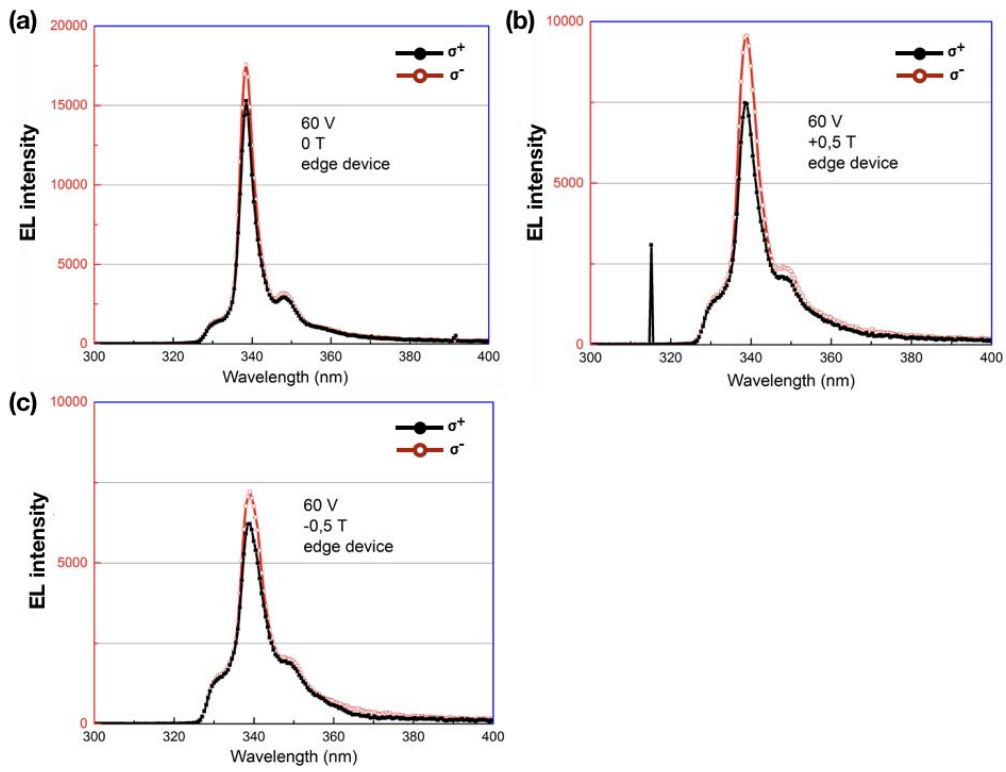


Figure 4.30: EL measurement of spot 3 biased at 60V at 9K by applying different magnetic field (a) 0T, (b) +0.5T, (c) -0.5T.

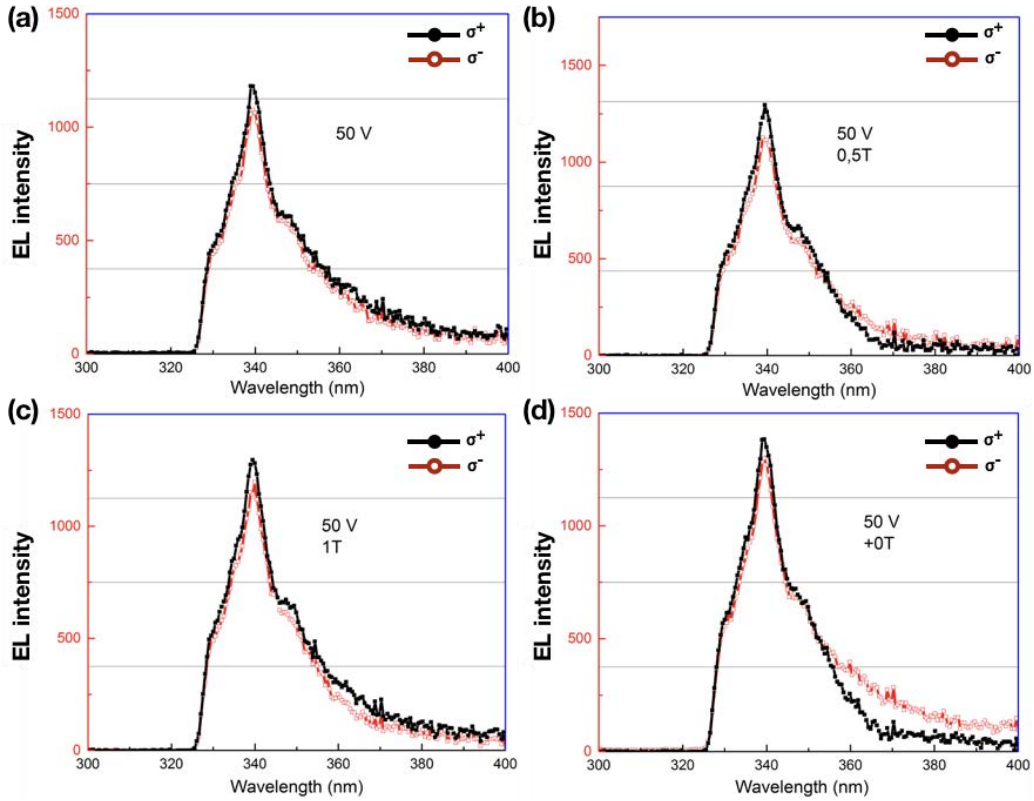


Figure 4.31: EL measurement of spot 2 biased at 50V at 7K by applying different magnetic fields (a) 0T, (b) +0.5T, (c) 1T, (d) 0T.

4.4 Summary

In this chapter, we reviewed the previous research concerning spin injection into GaN based materials. GaN is a wide band gap semiconductor ($\sim 3.4\text{eV}$) which is expected to be a good candidate for spintronics applications since it has a weak spin-orbit interaction ($\Delta_{\text{so}} \approx 15\text{ meV}$) and a long spin relaxation time ($\sim 20\text{ ns}$ at $T=5\text{K}$ and a few hundred ns at room temperature (RT)). The latter are two orders of magnitude larger than the spin lifetimes in GaAs (about 500ps). This is an important advantage of GaN since spintronic devices usually require a long spin coherence time. More recently, results from GaN-based visible spin LEDs and spin lasers have also been reported. However, all the results are obtained under a certain magnetic field, which is far from realistic applications. For applications, it is necessary to realize spin LEDs that can operate without any applied magnetic field and at room temperature. Therefore, significant efforts have been devoted firstly to achieve a perpendicular spin injector on

a GaN template. We compared both Fe/MgO and Co/MgO spin injectors. We demonstrate strong PMA by investigating a Co (0001)/MgO (111) epitaxial spin injector on a GaN template. Structural characterizations and magnetic measurements have been done. In addition, ab-initio calculations also showed that the Co/MgO interface has a large magnetic anisotropy. Hereafter, we grew a Co (0001)/MgO (111) spin injector on a n-i-p type GaN LED structure. However, no spin polarization could be detected in the polarization resolved EL measurements. This could be due either to the formation of an oxide layer formed at the Co/MgO interface or to an un-optimized GaN LED structure. Although no circularly polarized light emission could be detected, we suggest to use the wafer bonding technique to realize a n-i-p structure starting from a normal p-i-n structure.

Chapter 5 Ferroelectric control of spin polarization in organic multiferroic tunnel junctions

Spin-polarized transport in ferromagnetic tunnel junctions, characterized by tunneling magneto-resistance²⁰⁴, has already been proven to have great potential for application in the field of spintronics⁶⁵ and in magnetic random-access memories²⁰⁵. Compared to inorganic spintronics, organic spintronics is also very appealing because of the long spin lifetime of the charge carriers in addition to their relatively low cost, flexibility, and chemical diversity^{206,207,8}. In this chapter, we will focus on the study of spin-polarized transport in organic multiferroic tunnel junctions (OMFTJ) based on the ferroelectric organic material PVDF. In this kind of OMFTJ, we have found that by switching the ferroelectric polarization of PVDF, it becomes possible to reverse the spin-polarization at the Co/PVDF interface. In this thesis, we will intentionally dope the PVDF barrier with Fe₃O₄ magnetic nanoparticles. We expect that the interplay between magnetic nanoparticles and the ferroelectric barrier can lead to new phenomena for the spin-polarized transport.

5.1 Introduction

5.1.1 Principle of multiferroic tunnel junctions (MFTJ)

A junction consisting of an ultrathin insulating layer between two conducting electrodes is known as a tunnel junction as shown in Figure 5.1 (a). However, the junction made of a FE tunnel barrier sandwiched between two metallic electrodes is called FTJs as shown in Figure 5.1 (b). The important characteristic of bulk FE materials is the spontaneous electrical polarization, which can be switched between at least two stable orientations by applying an external electric field. By switching the polarization direction of the FE barrier, a notable change in the resistance of the junction occurs, which is known as the TER effect.

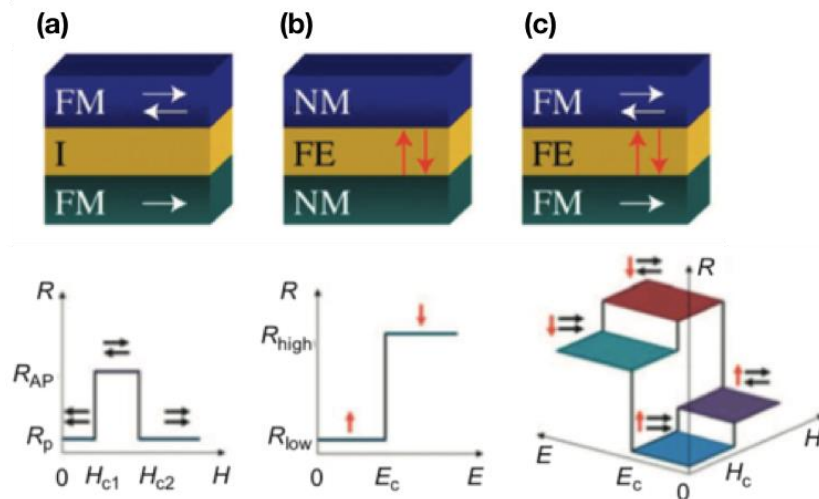


Figure 5.1: Schematic view of different types of tunnel junctions: (a) magnetic tunnel junction (MTJ), (b) ferroelectric tunnel junction (FTJ), and (c) multiferroic tunnel junction (MFTJ), Ferromagnetic (FM), ferroelectric (FE), normal metal (NM), and insulating (I) layers are indicated where appropriate. Bottom panels show the resistance response of these junctions to magnetic (H) and electric (E) fields. Horizontal and vertical arrows indicate the orientations of the magnetization and electric polarization, respectively. Adapted from.²⁰⁸

Recently, a tremendous amount of research has been focused on multiferroic

Ferroelectric control of spin polarization in organic multiferroic tunnel junctions

heterostructures that combines both ferroic order and magnetism. The latter are expected to create new functionalities. Multiferroic heterostructures are receiving an increasing interest in the community due to the search for strong and enhanced coupling between these two properties. These heterostructures have been fueled by the dream of magnetically readable and electrically writable data storage. Multiferroic heterostructures-based tunnel junctions refer to MTJs with FE barriers or FTJs with ferromagnetic electrodes. MFTJs are expected to be characterized by the TMR and TER simultaneously and exhibit four resistance states in a single memory unit cell, which is promising for the next generation of information storage devices.

5.1.2 Ferroelectric control of spin polarization

The ferroelectric control of spin polarization has been firstly reported in inorganic systems. In 2010, by employing BaTiO₃ as ferroelectric tunneling barrier in Fe/BaTiO₃/La_{0.7}Sr_{0.3}MnO₃ MFTJ structure, Garcia *et al.* were the first group to demonstrate a modulation of magnetoresistance from -17% to -3% when BTO is polarized from “up” to “down” states.²⁰⁹ Although the modulation is evident, the sign of the magnetization did not change in their experiments. Two years later, Pantel *et al.* reported a more exciting modulation of TMR by using another ferroelectric perovskite oxide PbZr_{0.2}Ti_{0.8}O₃ (PZT). In their Co/PZT/LSMO MFTJ, they realized a robust switching of TMR from +5% to -7% when switching the polarization of PZT.²¹⁰ They explained the change of spin-polarization at the PZT/LSMO interface by the induced magnetic moment on the interfacial Ti, which is aligned antiparallel to the Co magnetic moment after ferroelectric displacement of the position of oxygen atoms.

In 2014, by using a combination of PZT and an organic tunneling barrier Alq₃, Sun *et al.* reported an active control of magnetoresistance in organic spin valves.²⁰¹ By switching the ferroelectricity of the PZT layer, the MR can be tuned from +50% to -15%. They explained this phenomenon by the adjustment of the energy levels at the PZT/Alq₃ interface, so that either spin-injection of holes from the majority band or from the minority band of LSMO can be realized. Compared to their sample structure, our

Ferroelectric control of spin polarization in organic multiferroic tunnel junctions

approach based on the use of ferroelectric organic material is much simpler for the structure design.

5.1.3 Organic multiferroic tunnel junctions (OMFTJ)

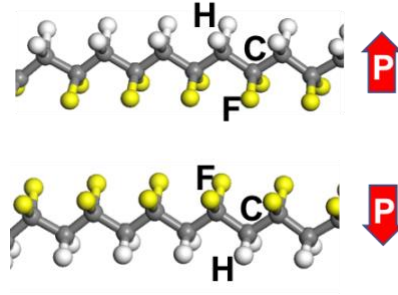


Figure 5.2: Schematics of PVDF structure with different ferroelectric polarization directions.

In this study, we use one of the most typical ferroelectric polymers, poly (vinylidene fluoride) (PVDF). This organic material has been widely used in modern electronic systems and devices. The ferroelectric performance relies mostly on the β phase content²¹¹. Figure 5.2 shows the structure of PVDF carbon chains with different polarizations. Unlike perovskite oxide such as BaTiO_3 where the ionic displacement produces the polarization, the ferroelectric order of PVDF originates from the permanent dipoles and the cooperative long-range rotation of the molecular chains via the short-range Van der Waals interactions.¹¹ Moreover, PVDF and related copolymers, form high quality ordered layers¹² and exhibit robust ferroelectricity down to the thickness of one monolayer¹³. The electric polarization of PVDF is comparable to that of perovskite oxide ferroelectrics¹⁴, making them favorable for use as barriers in ferroelectric tunnel junctions^{15,16} (FTJs). In 2012, Kusuma *et al.* have firstly reported the successful fabrication of PVDF based organic ferroelectric tunnel junction devices. The presence of conductance bistability within a biasing voltage of $\pm 0.5\text{V}$ and stable memory retention after 10^4 cycles was confirmed. This material then boosted an intensive research in the field of organic ferroelectricity. In 2016, by using a nano-structured bottom electrode with 190nm size, Tian *et al.* have reported a tunnel

Ferroelectric control of spin polarization in organic multiferroic tunnel junctions

electroresistance reaching 1000% at room temperature in Au/PVDF (2ML)/W tunnel junctions.²¹² This finding proves the excellent ferroelectric properties of PVDF and paves the way for future applications using low-cost, large-scale arrays of organic ferroelectric tunnel junctions.

In 2011 Lopez-Encarnacion *et al.* have firstly proposed theoretically to study MFTJ with PVDF barriers.¹⁵ Using *ab-initio* calculations, they showed that a sizeable TER (-80%) and TMR could be obtained in Co/PVDF/Fe/Co structures. The TMR could be modulated from +17% to +35%, while no change of sign happens.

Recently, we have for the first time experimentally realized organic MFTJs based on $\text{La}_{0.6}\text{Sr}_{0.4}\text{MnO}_3/\text{PVDF}/\text{Co}$ structures by employing PVDF as tunneling barrier.¹⁷ In this work, we have experimentally proved that a TMR effect of 8 to 15% combined with a TER of 75% can be measured at 10K in the organic LSMO/PVDF/Co MFTJs. Furthermore, we demonstrated that the TMR sign can be changed when the PVDF polarization is reversed and proved that the spin-polarization at the PVDF/Co interface can be engineered by controlling the ferroelectric polarization of PVDF. This study confirms the critical role of the spinterface on altering the spin polarization at the organic/ferromagnetic interface. This opens new functionalities in controlling the spin injection into organic materials via the ferroelectric polarization of the barrier. The OMFTJ structure of the LSMO/PVDF/Co device, which was fabricated at IJL is schematically shown in Figure 5.3 (a). The PVDF film, which acts as a tunneling barrier, was spin-coated. The PVDF barrier thickness checked by atomic force microscopy (AFM) is about 26nm. Finally, 10nm Co/10nm Au were deposited in a molecular beam epitaxy (MBE) system at 80K to minimize the metal diffusion into organic materials. The surface morphology of the PVDF barrier is investigated by AFM. A smooth surface with a RMS roughness of 3.12 nm was observed over an area of $1 \times 1 \mu\text{m}^2$ (Figure 5.3 (b)). The ferroelectric properties of the PVDF barrier have been characterized by piezo response force microscopy (PFM). In the PFM results shown in Figure 4.3 (c) and (d), the two opposite polarization states and the clear hysteresis loop reveal the local switching behavior.

Ferroelectric control of spin polarization in organic multiferroic tunnel junctions

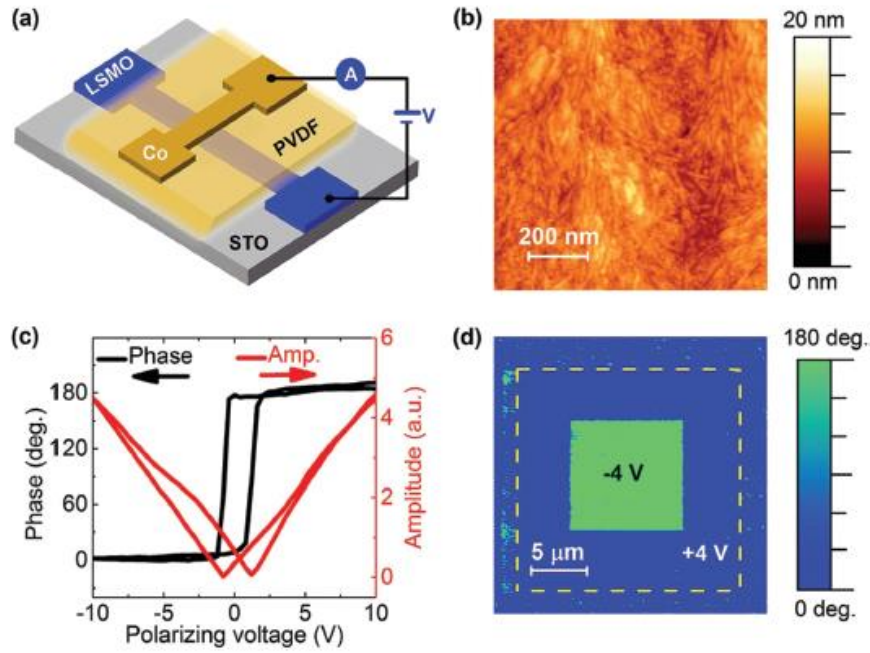


Figure 5.3: (a) Schematics of the LSMO/PVDF/Co device. (b) AFM topography measurement of the PVDF barrier surface over an area of $1 \times 1 \mu\text{m}^2$. (c) Local PFM hysteresis phase and amplitude loops measured on the PVDF surface. (d) PFM phase image recorded on the PVDF surface. The contrasts showing the ferroelectric switching are obtained after application of a +4V DC bias on the tip over an area of $20 \times 20 \mu\text{m}^2$ (dashed square) and subsequently -4V over an area of $10 \times 10 \mu\text{m}^2$ area. The total image size is $25 \times 25 \mu\text{m}^2$.

The magneto-transport measurements as the most important finding are shown in Figure 5.4. Figure 5.4 (a) shows the magneto-response (resistance vs. magnetic field) of the LSMO/PVDF/Co MFTJ for two different ferroelectric polarizations (polarized using +1.2V and -1.5V, respectively). Indeed, one can clearly notice that for a same bias voltage (10mV), a positive +8% TMR or a negative -15% TMR can be achieved when the PVDF is polarized to either “down” state or “up” state, respectively. By considering the resistance in the “up” state and the resistance in the “down” state, we can define the TER as follows: $\text{TER} = \frac{R_P^{\text{Down}} - R_P^{\text{Up}}}{R_P^{\text{Up}}} \times 100\%$, where R_P^{Down} and R_P^{Up} are the parallel resistances in PVDF “down” and “up” polarization states, respectively. In our case, we found a TER as high as 75%. The four resistance states associated with

Ferroelectric control of spin polarization in organic multiferroic tunnel junctions

different magnetization and ferroelectric configurations are identified in the inset of Figure 5.4 (a). This is the first time that an MFTJ junction can be realized by employing a ferroelectric organic barrier, which is particularly interesting for developing applications such as multi-level data storage devices^{213,214} with organic materials. Moreover, we have clearly observed a significant change of TMR sign when the PVDF ferroelectric polarization is reversed. Figure 5.4 (b) and (c) show the resistance and corresponding TMR loops with different polarizing voltages. The sign of the TMR closely depends on the ferroelectric state of PVDF. The positive TMR is associated with the high resistance state, while the negative TMR is linked to the low resistance state. Between the two stable polarization states, intermediate states show a tunable TMR for a polarizing voltage varying between 0-1.5V. This result provides a strong argument that TMR can be controlled by the ferroelectric polarization of the PVDF barrier.

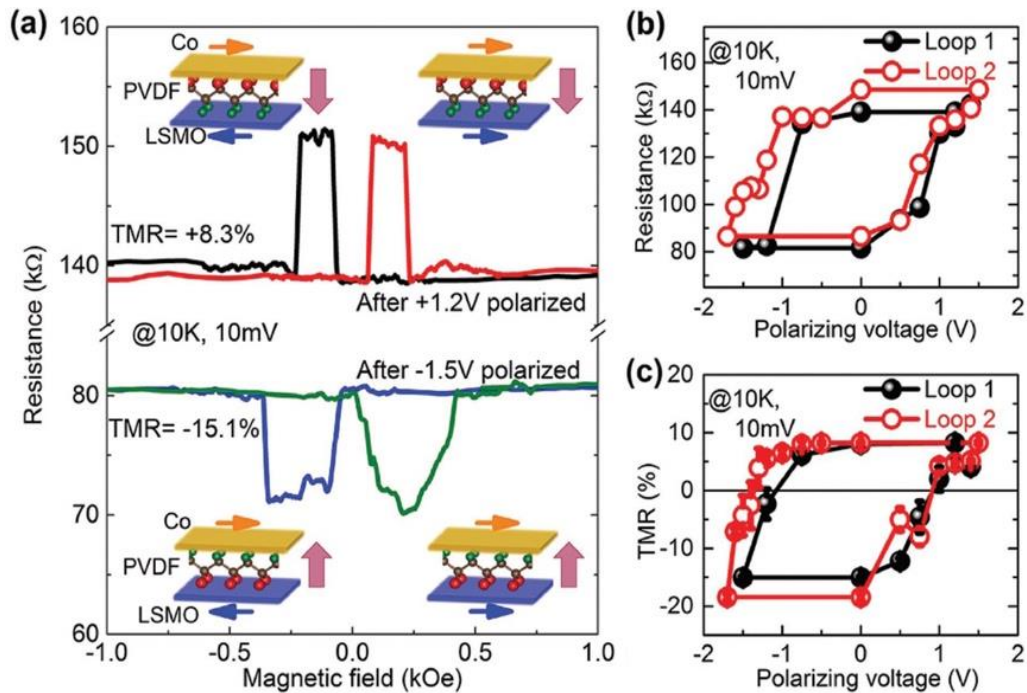


Figure 5.4: (a) Tunneling magnetoresistance measured under 10mV at 10K after polarizing the device at +1.2V and -1.5V. The insets show four resistance states associated with different polarization and magnetization orientations. (b) Two successive loops for parallel resistance versus polarizing voltage. (c) Two successive loops for TMR versus polarizing voltage.

Ferroelectric control of spin polarization in organic multiferroic tunnel junctions

To understand the change of the TMR sign with the polarization, we have performed *ab-initio* calculations by considering three PVDF layers contacted with four Co layers. These calculated structures with two PVDF polarization states are schematically shown in Figure 5.5 (a) and (d). Figure 5.5 (b, c) and (e, f) display the spin-resolved density of states (DOS) and the spin-polarization of DOS on the first and second carbon layers adjacent to Co for both PVDF polarizations. As shown in Figure 5.5, although the spin-polarization at E_F keeps the same sign in the first C layer for both polarizations (-23% to -26%), the sign is indeed found to be opposite in the second C layer with +44% for H-C-F/Co and -47% for F-C-H/Co interfaces. Therefore, the change of TMR sign with different PVDF polarizations could be explained by the change of the sign in the spin-polarization of the second C layer, which acts as a final spin-filter for electrons tunneling through the PVDF barrier according to Jullière's model.¹⁹⁸ This magneto-electric coupling mechanism is different from those found in inorganic systems. The spin-polarization change at the PVDF/Co interface occurs in the second PVDF layer adjacent to the Co layer, which justifies the importance of the organic/ferromagnetic spinterface.

These preliminary results not only demonstrate that the organic MFTJ can be fabricated, but also show that the spin-polarization of the organic/ferromagnetic spinterface can be manipulated by the ferroelectric polarization of the organic barrier. This opens up new functionalities in controlling the injection of spin polarization via the ferroelectric polarization of the tunneling barrier.

Ferroelectric control of spin polarization in organic multiferroic tunnel junctions

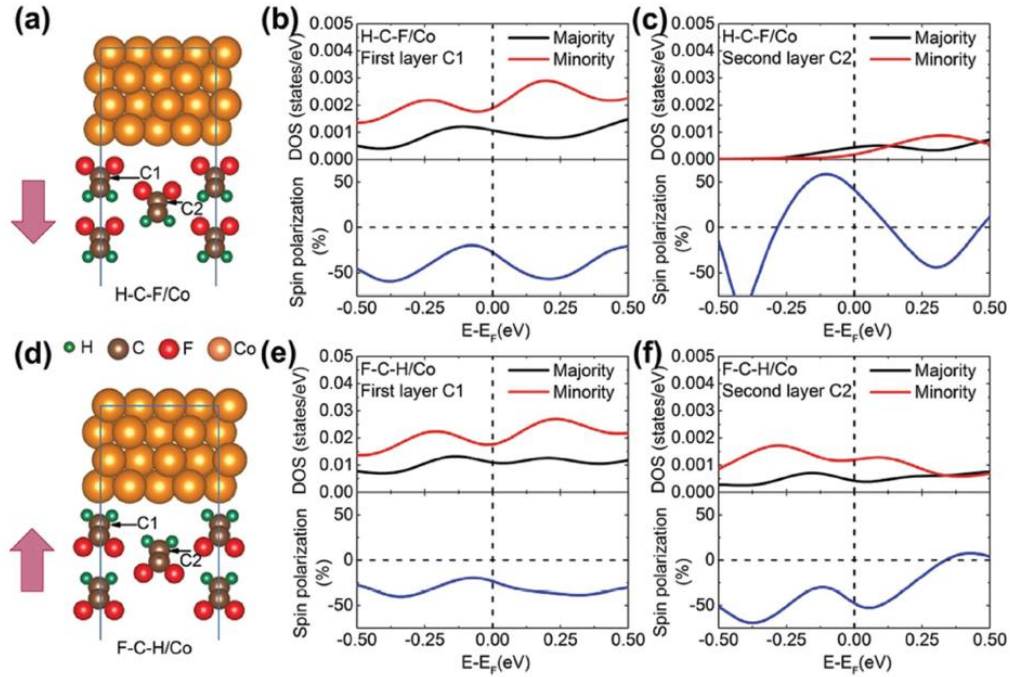


Figure 5.5: Ab-initio calculations of PVDF/Co structures. Calculated structures of $[\text{PVDF}]_3\text{Co}_4$ with (a) H-C-F/Co configuration, corresponding to ferroelectric polarization “down” state and (d) F-C-H/Co configuration, corresponding to ferroelectric polarization “up” state. Density of states and spin-polarization of C atoms (marked with black arrows) on the first and second interfacial PVDF layers (b-c) at the H-C-F/Co interface and (e-f) at the F-C-H/Co interface.

5.2 MFTJ with PVDF: Fe_3O_4 as barrier

5.2.1 Motivation of the work

Magnetite Fe_3O_4 has recently attracted attention because bulk Fe_3O_4 has a high Curie temperature ($T_c \sim 850\text{K}$) and nearly full spin polarization at room temperature. Both properties are of great potential for applications in giant magneto-electronic and spin-valve devices based on magnetite films²¹⁵. In some previous work, it was proved that ferromagnetic oxide (Fe_3O_4) spherical nanoparticles were excellent fillers for high-dielectric-constant polymer composites.^{19,20,21} Some researchers also found that the addition of Fe_3O_4 leads to an increase of the β phase of PVDF.^{22,23,24,25} Jayakumar et al. found an increase in polarization values of PVDF: Fe_3O_4 composite films, which can

Ferroelectric control of spin polarization in organic multiferroic tunnel junctions

be due to the accumulation of charges at the interface of the conducting and dielectric Fe_3O_4 , which facilitates the heterogeneous polarization in the systems and enhances the ferroelectric behavior of the sample. In this work, we fabricated organic multiferroic tunnel junctions (MFTJs) based on $\text{La}_{0.6}\text{Sr}_{0.4}\text{MnO}_3/\text{PVDF}:\text{Fe}_3\text{O}_4$ nanocomposites/Co structures. The influence of Fe_3O_4 on the properties of the PVDF/Co spinterface will be studied.

5.2.2 Device fabrication

$\text{La}_{0.6}\text{Sr}_{0.4}\text{MnO}_3$ films with thickness of ≈ 50 nm were epitaxially grown on $\langle 100 \rangle$ oriented SrTiO_3 substrates at 750°C using DC magnetron sputtering at the University of Science and Technology of China. The films were subsequently annealed at 800°C for 2h in O_2 atmosphere before being slowly cooled down to room temperature. PVDF: Fe_3O_4 nanocomposite films were prepared by the spin-coating method. The PVDF solution was first obtained by dissolving PVDF powders (Sigma-Aldrich) into dimethylformamide (DMF) with magnetic stirring overnight. Then, the Fe_3O_4 nanoparticles (Sigma-Aldrich) diluted in toluene with a concentration of 5mg/mL were added into the PVDF solution with a ratio 1:1. The mixtures were sonicated (bath-type sonication) for 5h. The mixed solution was then spin-coated onto pre-etched LSMO/STO (001) substrates with a speed of 3000 RPM for 1 min. Subsequently the as-coated film was annealed at 150°C in air for 2h to improve the crystallinity of the ferroelectric β phase. The MFTJ has a PVDF thickness of about 26 nm prepared with a concentration of 20 mg/mL. The MFTJ structure of LSMO/PVDF: Fe_3O_4 /Co/Au device is schematically shown in Figure 5.6. The LSMO layer was etched by hydrogen chloride (37%) to pattern 200 μm width bars as the bottom electrodes. The PVDF: Fe_3O_4 nanocomposite film was then spin-coated on the whole sample surface. Finally, 10nm Co/10nm Au were deposited in a molecular beam epitaxy (MBE) system with a shadow mask to form the top electrode. The final junction size is $200 \times 200 \mu\text{m}^2$. To minimize the metal diffusion into organic materials^{216,217}, the temperature during the growth of the top electrode was maintained at around 90K.

Ferroelectric control of spin polarization in organic multiferroic tunnel junctions

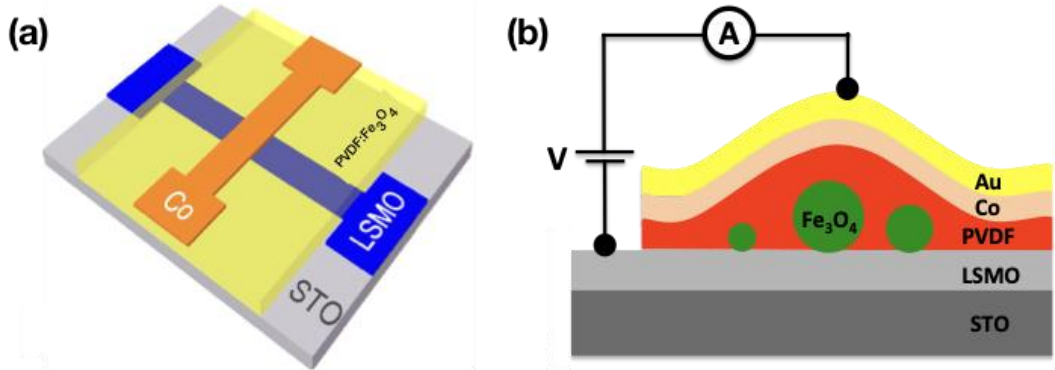


Figure 5.6: (a) Schematics of the LSMO/PVDF/Co device. (b) Side-view of the LSMO/PVDF/Co device.

5.2.3 Morphological characterization

The surface morphology of pure PVDF films and PVDF: Fe₃O₄ nanocomposite films was investigated by AFM (figure 5.7). The roughness of the nanocomposite film (i.e. RMS roughness 7.1 nm) is much larger than that of the pure PVDF film (RMS roughness of 3.2 nm). The AFM images also show that the size of the nanoparticles is larger than 5 nm, which is due to aggregation. From the surface observations, it is known that Fe₃O₄ particles embedded in nanocomposite films are not homogeneous. The PVDF: Fe₃O₄ nanocomposite film contains not only small particles, but also larger ones.

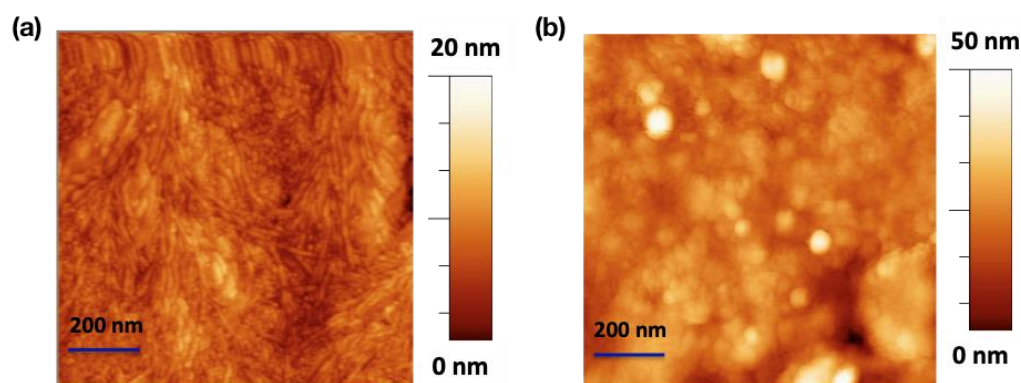


Figure 5.7: Morphology characterization of pure PVDF film (a) and PVDF: Fe₃O₄ nanocomposite film (b).

5.2.4 Ferroelectric characterization

To check the ferroelectric properties of the PVDF: Fe₃O₄ nanocomposite film with PFM, the film was spin-coated on a thermally oxidized SiO₂/n-Si substrate covered with 100nm Au. For the measurement, the surface morphology was studied using an AFM (Asylum Research, MFP-3D, USA) working in contact mode under environmental conditions. Local electrical experiments were performed on a dual AC resonance tracking PFM. Pt/Ir conductive coating tips (Nanosensors PPP-EFM probes, $k \approx 2.5$ N/m) and ground conductive bottom electrodes were used.

The ferroelectric properties of the PVDF: Fe₃O₄ barrier have been characterized by piezo-response force microscopy (PFM). In the PFM image shown in Figure 5.8 (c), the film was first polarized with a tip biased at +3 V over an area indicated with the dark square, then an opposite poling bias of -3 V was subsequently applied over a bright area within the previous area. As observed, the polarization of the as-grown domains is almost the same as the area that has been positively polarized, while clear reversal of the polarization was obtained by applying a negative bias voltage. Representative local PFM phase and amplitude hysteresis loops are shown in Figure 5.8 (d). The coercive voltage is just 0.2 V, which is smaller than that of a pure PVDF barrier (1.2V) as shown in Figure 5.8 (b). This means that the ferroelectric properties of PVDF: Fe₃O₄ nanocomposite films are improved compared to pure PVDF barriers.

Ferroelectric control of spin polarization in organic multiferroic tunnel junctions

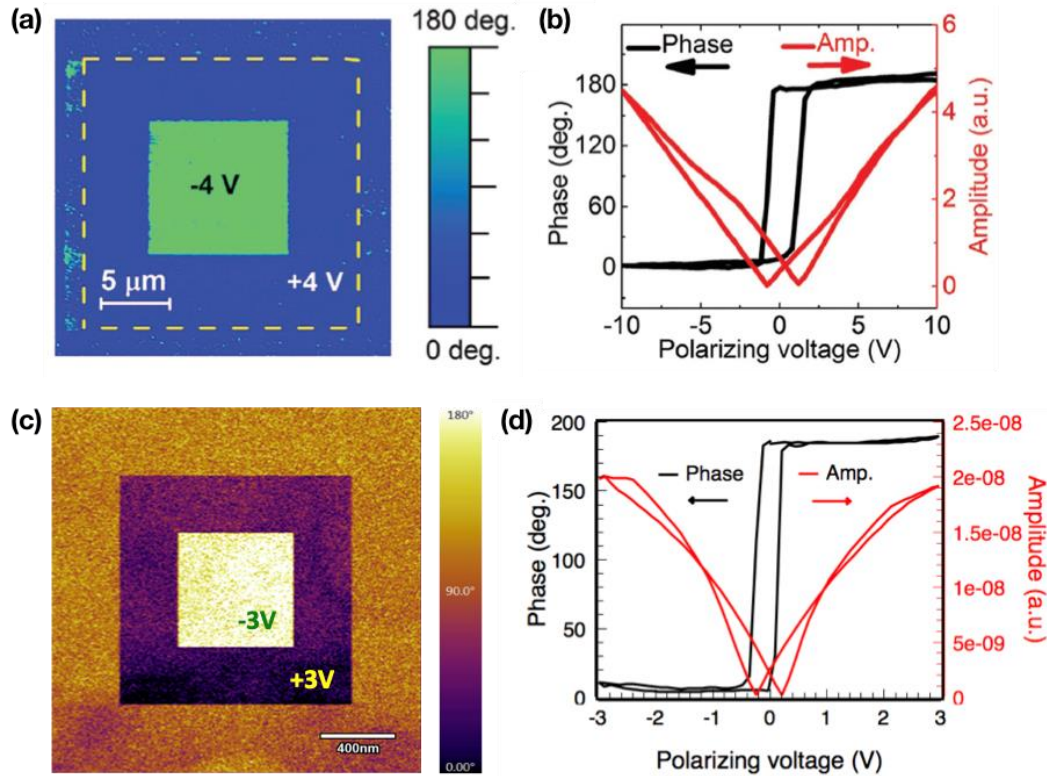


Figure 5.8: Piezoelectric characterization of pure PVDF film and PVDF: Fe₃O₄ nanocomposite film. (a) PFM phase image recorded on the PVDF surface. Contrasts showing the ferroelectric switching were obtained after application of +4 V DC bias on the tip over a 20×20 μm² area (dashed square) and subsequently -4 V over a 10×10 μm² area. The total image was acquired over a 25×25 μm² area. (b) Local PFM hysteresis phase and amplitude loops measured on the PVDF surface. (c) PFM phase image recorded on the PVDF: Fe₃O₄ surface. Contrasts showing the ferroelectric switching were obtained after application of a +3 V DC bias on the tip over the dark square and subsequently -3 V over the bright area. The total image was acquired over a 2×2 μm² area. (d) Local PFM hysteresis phase and amplitude loops measured on the PVDF: Fe₃O₄ surface.

5.2.5 Magnetic characterization

Magnetic moment versus magnetic field (M vs H) curves and magnetic moment versus temperature (M vs T) curves were measured in a commercial superconducting quantum interference device (SQUID) magnetometer (Quantum Design). Zero-field-

Ferroelectric control of spin polarization in organic multiferroic tunnel junctions

cooled (ZFC) and field-cooled (FC) curves were taken between 10 and 400K with a magnetic field 5T. The data were obtained by first cooling the sample from room temperature in zero applied field (ZFC process) to low temperature (10K). Then, a small magnetic field was applied, and the variation of magnetization was measured with increasing temperature up to $T = 400\text{K}$. After the last point was measured, the sample was cooled again to low temperature while keeping a field of 5T (FC process); then, the M vs T data were measured for increasing temperatures.

Figure 5.9 shows the temperature dependent magnetic hysteresis loops measured by SQUID for a PVDF: Fe_3O_4 nanocomposite film spin-coated on a Si/Au substrate. The saturation of the magnetization is observed at around 2kOe for 10 K and 7kOe for 300 K, which indicates a paramagnetic behavior of Fe_3O_4 . From zero-field cooling down curve in Figure 5.9 (b), the blocking temperature can be obtained at around 15 K, which is in good agreement with the size of the Fe_3O_4 nanoparticles (i.e. 5 nm). Figure 5.9 (c) and (d) show the temperature dependent magnetic hysteresis loops measured by SQUID for $\text{La}_{0.6}\text{Sr}_{0.4}\text{MnO}_3(50\text{nm})/\text{SrTiO}_3$ and $\text{Au}(10\text{nm})/\text{Co}(10\text{nm})/\text{PVDF}/\text{SiO}_2$ full film samples, respectively. It is found that the coercivities of LSMO and Co decreased with the increasing temperature. It is clear that the coercivity of LSMO is always smaller than that of Co on PVDF.

Ferroelectric control of spin polarization in organic multiferroic tunnel junctions

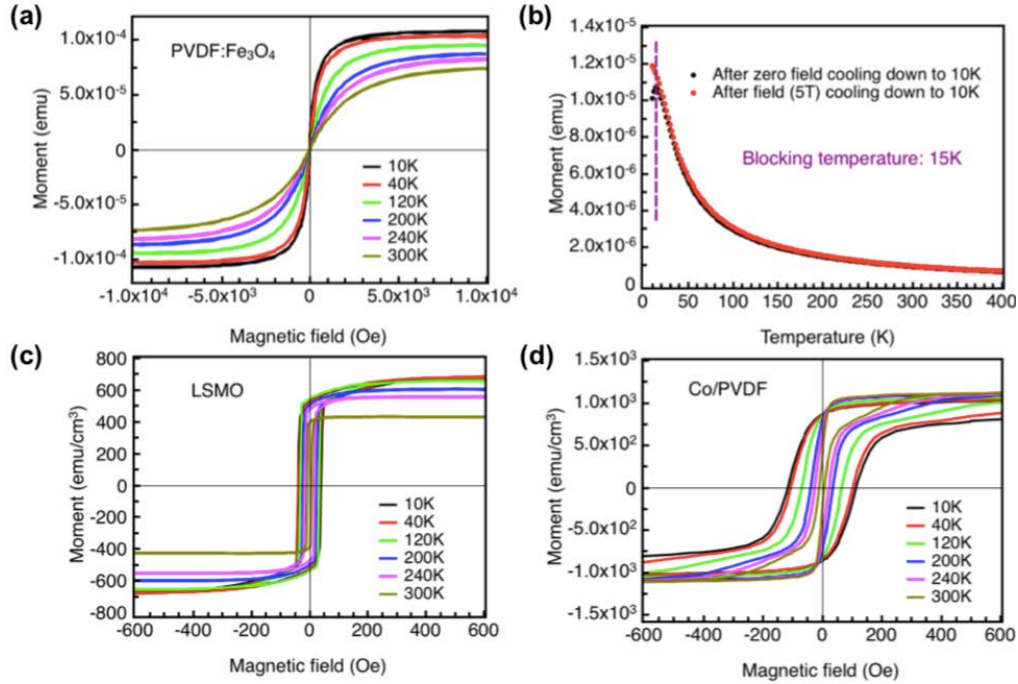


Figure 5.9: Magnetic properties of PVDF: Fe₃O₄ nanocomposite film. (a) SQUID measurement of M-H curves at different temperature for Si/Au/PVDF: Fe₃O₄ sample. (b) M-T measurement for Si/Au/PVDF: Fe₃O₄ sample. SQUID measurement of M-H curves at different temperatures for (c) LSMO (50nm)/STO and (d) Au(10nm)/Co(10nm)/PVDF/SiO₂ full film samples, respectively.

5.2.6 Magneto-transport characterization

The setup used for magneto-transport measurements is described in chapter 2. The

TMR is defined as: $TMR = \frac{R_{AP}-R_P}{R_P} \times 100\%$, for positive TMR, and

$TMR = \frac{R_{AP}-R_P}{R_{AP}} \times 100\%$, for negative TMR,

where R_P and R_{AP} are the junction resistance when the magnetizations of two electrodes are parallel and antiparallel, respectively.

5.2.6.1 I-V characterization

Figure 5.10 shows the I-V curves measured at RT after polarization by both -2.5 V and + 2.4 V. for the PVDF: Fe₃O₄ nanocomposite film. One can clearly recognize a

Ferroelectric control of spin polarization in organic multiferroic tunnel junctions

non-linear variation indicating good tunneling properties. Obviously, no metallic behavior is observed.

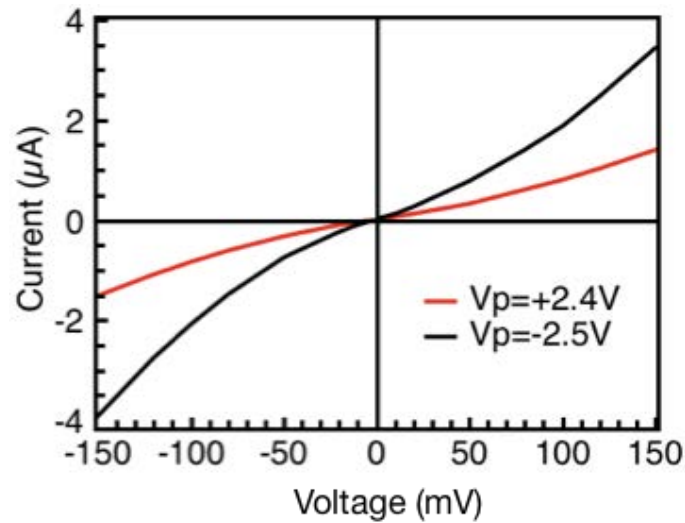


Figure 5.10: I-V characteristics after polarization by -2.5 V and +2.4V in the range between -150mV and +150mV.

5.2.6.2 Ferroelectric control of spin polarization

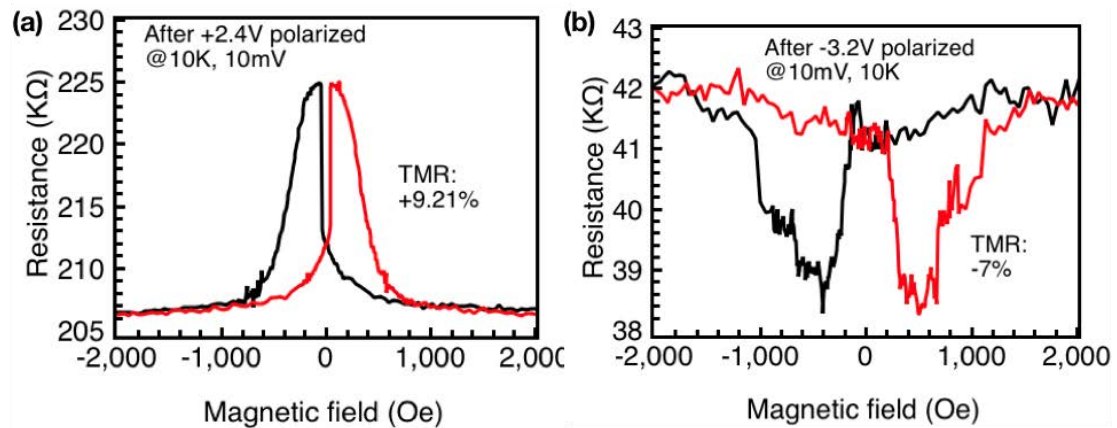


Figure 5.11: Tunneling magneto-resistance measured under 10mV at 10K after the electric polarizing voltage of +2.4 V (a) and -3.2 V (b), respectively.

In the following, we will consider the ferroelectric properties of the PVDF: Fe_3O_4 MFTJ. Figure 5.11 shows the magneto-response (resistance vs. magnetic field) of the LSMO/PVDF/Co MFTJ for two different ferroelectric polarizations (polarized at +2.4 and -3.2V, respectively). Indeed, one can clearly notice that with a same applied bias

Ferroelectric control of spin polarization in organic multiferroic tunnel junctions

voltage (10 mV), a positive +9.21% TMR or a negative -7% TMR can be achieved when the PVDF is polarized in the “down” state or in the “up” state, respectively.

5.2.6.3 Bias dependence

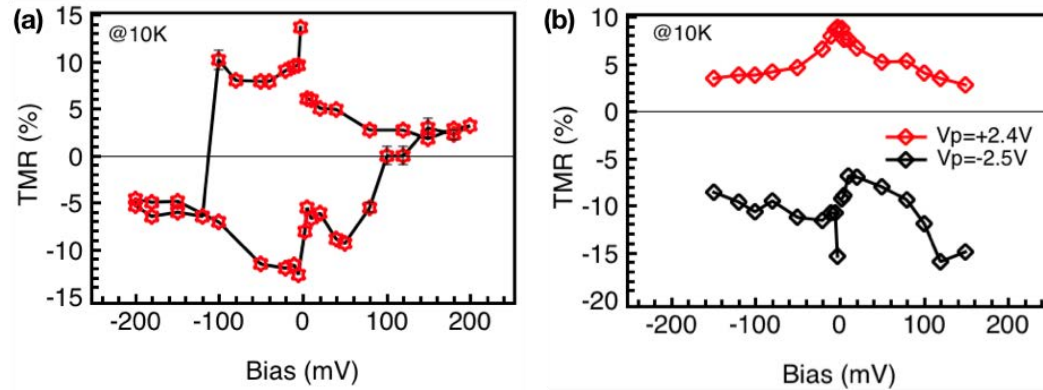


Figure 5.12: Magneto-transport measurements on LSMO/PVDF: $\text{Fe}_3\text{O}_4/\text{Co}$ devices. (a) Initial state loop for TMR versus bias. (b) Bias dependence of TMR at 10K with polarizing voltage $V_p = +2.4$ V and -2.5 V for the two PVDF polarization states.

Figure 5.12 (a) shows the initial state loop for TMR versus bias. It is clearly shown that the TMR sign can be reversed even at very small bias of 100 mV in the initial state. Figure 5.12 (b) presents the bias dependence of TMR for the device based on PVDF: Fe_3O_4 barrier. Compared with the device based on the pure PVDF barrier, it is found that the positive TMR shows the same tendency, but the negative TMR is completely different.

5.2.6.4 Polarization voltage dependence

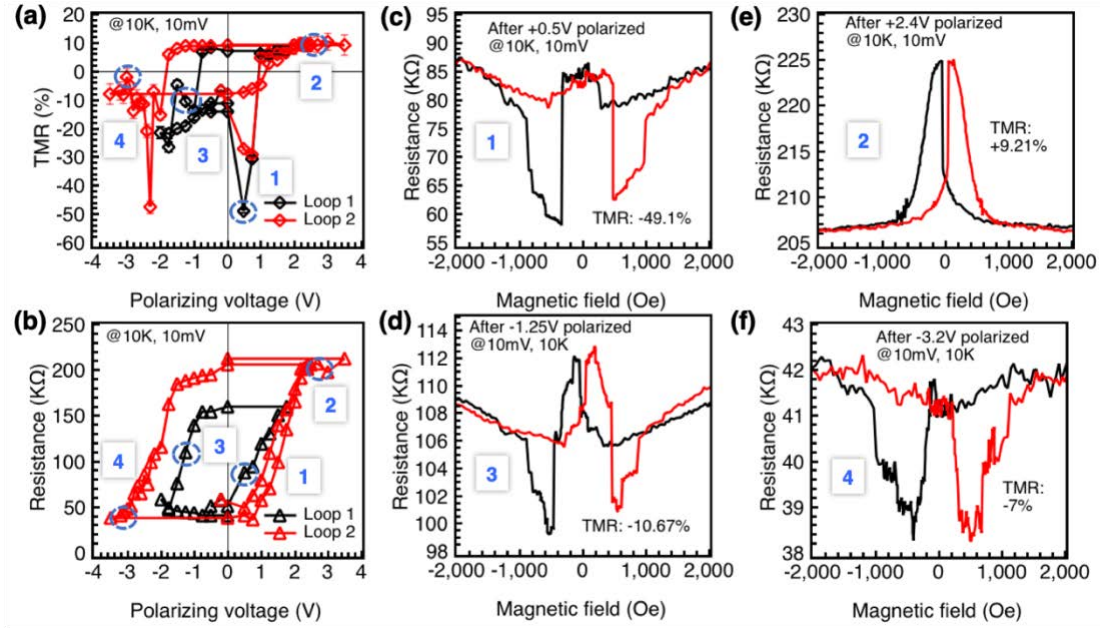


Figure 5.13: Magneto-transport measurements performed on LSMO/PVDF: $\text{Fe}_3\text{O}_4/\text{Co}$ devices. (a) TMR loops versus polarizing voltage. (b) Parallel resistance loops versus polarizing voltage. (c-f) Tunneling magneto-resistance measured under 10mV at 10K for polarization voltages of +0.5 V, -1.25V, +2.4 V and -3.2 V, respectively, corresponding to the numbers 1 to 4 marked in (a) and (b).

Figure 5.13 (a) shows the TMR loops as a function of the polarizing voltage. The sign of TMR closely depends on the ferroelectric state of PVDF. A positive TMR is associated with the high resistance state, while the negative TMR is linked to the low resistance state. Between the two stable polarization states, we observe an intermediate regime with a tunable TMR between 0 and 4 V. Figure 5.13 (b) shows the change of the parallel resistance R_P as a function of the polarizing voltage applied on the junction. The resistance clearly shows a hysteresis loop behavior. The switching voltage is larger than that measured by PFM on the full PVDF: Fe_3O_4 films at room temperature (0.2 V). These results provide a strong argument that TMR can be controlled by the ferroelectric polarization of the PVDF: Fe_3O_4 barrier. Figure 5.13 (c), (e), (d) and (f) show the magneto-response (resistance vs. magnetic field) of the LSMO/PVDF:

Ferroelectric control of spin polarization in organic multiferroic tunnel junctions

$\text{Fe}_3\text{O}_4/\text{Co}$ MFTJ for four different polarizing voltages (i.e. +0.5 V, +2.4 V, -1.25V and -3.2 V, respectively). For pure PVDF MFTJ and MFTJ doped with Fe_3O_4 nanoparticles, positive TMR are almost the same. However, the sample based on the PVDF: Fe_3O_4 barrier is characterized by random negative TMR values, which are varying after each polarizing step. The largest TMR can even reach -50%, but sometimes lower values ranging from -5 to -6% can be reached. This random behavior could be related to the magnetization state of Fe_3O_4 influenced by the PVDF polarization. When the magnetization of the Fe_3O_4 particles are all aligned, they could enhance the spin polarization of electrons injected from the Co electrode. However, if the Fe_3O_4 particles have a random magnetization, they will probably depolarize the spins, thus resulting in a smaller TMR. Interestingly, we found that the positive TMR values are almost not influenced. The latter is mainly due to the positive spin-polarization of the H-C-F/Co spinterface with PVDF, with a reduced influence of the Fe_3O_4 magnetization state.

Besides the TMR sign change, one can also notice that the width of the antiparallel plateau in the TMR curves is different for the two polarization states. This could be due to a change in the interfacial magnetic anisotropy. The modification of the width of the antiparallel plateau is mainly due to the change of coercivity at the PVDF: $\text{Fe}_3\text{O}_4/\text{Co}$ interface. Moreover, it was found that the shape of the antiparallel plateau for devices based on PVDF: Fe_3O_4 barrier is different than for devices based on a pure PVDF barrier. This is due to the paramagnetism of the Fe_3O_4 nanoparticles.

5.2.6.5 Temperature dependence

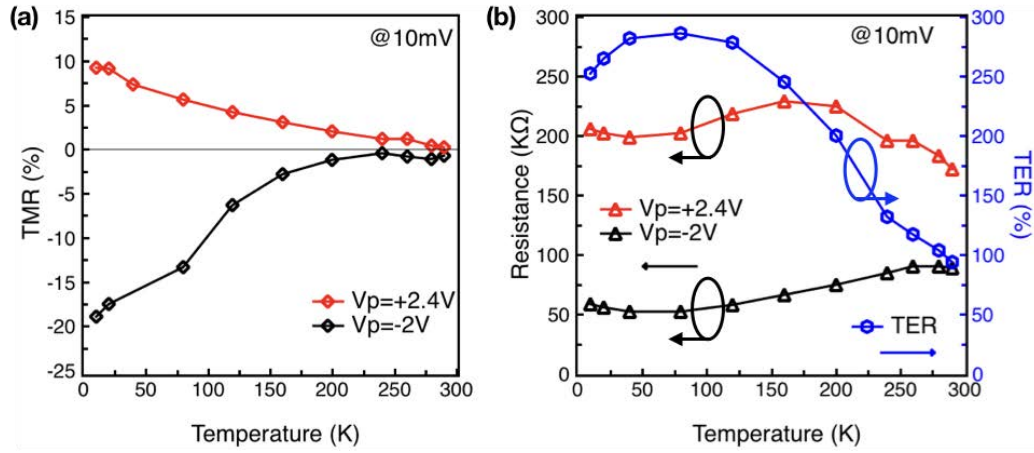


Figure 5.14: (a) Temperature dependence of TMR at 10K with polarizing voltage $V_p = +2.4V$ and $-2V$ for the two PVDF polarization states. The polarizing voltage is only applied at 10K before increasing the temperature. (b) Temperature dependence of R_P and TER for both polarization states.

The temperature dependence of the TMR is shown in Figure 5.14 (a). The device based on the PVDF: Fe_3O_4 barrier can keep positive TMR values up to 200K. The same behavior is observed for negative TMR, which can be explained by the loss of LSMO surface magnetization at high temperatures.²¹⁸ Figure 5.14 (b) shows the variation of TER and parallel resistance (R_P) for both polarizations with temperature. The TER displays a quite complicated temperature dependent behavior. Firstly, the TER increases from 250% to 280% at 80K and then decreases with the increasing temperature. It is easy to see that the sample based on the PVDF: Fe_3O_4 barrier has a better TER at low temperatures. It decreases slower with the increasing temperature and can still reach 100% at room temperature. The change of R_P can be divided into two temperature regions. For Region-1 (0K to 160K), R_P increases for both polarizations with the increasing temperature. This is the signature of a metallic behavior. For Region-2 (160K to 300K), the resistance for positive polarization decreases while that for negative polarization continue to increase when the temperature increases. It is well known that PVDF is characterized by the coexistence

Ferroelectric control of spin polarization in organic multiferroic tunnel junctions

of an amorphous phase and a ferroelectric crystalline phase.²¹⁹ When the temperature increases, the thermal energy can cause a structural disorder in the PVDF film. This has been demonstrated in some organic superconductors, the structural transition occurring at around 80K.²²⁰ The thermal activation of structural disorder could induce an increase of electron scattering and result in the increase of the resistance in Region-1 for both polarization states.²²¹ When the thermal energy is high enough to overcome the energy barrier between the two polarization states, the molecular chain starts to rotate to the other polarization state. The temperature dependence of R_P indicates the disappearance of the polarization contrast due to the thermal fluctuation of the ferroelectric domains.²⁰⁶

5.2.7 Discussion

		PVDF up	PVDF down			PVDF up	PVDF down
Co/PVDF/LSMO	Co/PVDF	+	-	Co/PVDF/Fe ₃ O ₄	Co/PVDF	+	-
	LSMO/PVDF	+	+		Fe ₃ O ₄ /PVDF	+	+
TMR (%)		+	-	TMR (%)		+	-
Resistance		R1	R2	Resistance		R3	R4

TABLE 5.1. TMRs for two tunneling models (Co/PVDF/LSMO and Co/PVDF/Fe₃O₄) are shown with two different PVDF polarization states.

Since both LSMO and Fe₃O₄ are half-metals at low temperatures, a +100% spin polarization is expected^{222,223}. In addition, the TMR sign is a product of the spin-polarizations at the Co/PVDF, LSMO/PVDF or Fe₃O₄/PVDF interfaces. Therefore, as seen from Table 5.1, one can conclude that the positive TMR measured in our PVDF: Fe₃O₄ MFTJ is associated with both positive spin polarization at the H-C-F/Co and LSMO/PVDF interfaces. The negative TMR is associated with a negative spin polarization at the F-C-H/Co interface and a positive spin polarization at the Fe₃O₄/PVDF interface. When the PVDF is in the up state, and if $R_1 < R_3$, tunneling

Ferroelectric control of spin polarization in organic multiferroic tunnel junctions

occurs through the Co/PVDF/LSMO. However, when PVDF is in the down state, and if $R_4 < R_2$, tunneling occurs through the Co/PVDF/Fe₃O₄. This is consistent with the negative TMR curves. Theoretical calculations are further required to get a better understanding.

5.3 Summary

In this chapter, we firstly reviewed the state of the art of the research on MFTJ. Then, we presented results on multiferroic tunnel junctions using PVDF doped with Fe₃O₄ nanoparticles as barrier, which demonstrated new and technologically important functionalities. Remarkably, the TMR sign can even be reversed for a very small applied bias of 100mV in the initial state. After being polarized, the largest TMR can even reach -50%, but sometimes lower values such as -5 to -6% are obtained. This random behavior could be related to the magnetization state of Fe₃O₄ influenced by the PVDF polarization state. The positive TMR is almost not influenced. By doping with Fe₃O₄ nanoparticles, the ferroelectric properties of MFTJ are improved exhibiting higher TER values, which still can reach 100% at room temperature. Spin-polarization of organic/ferromagnetic spinterface not only can be manipulated by the ferroelectric polarization of the organic barrier, but also can be influenced by the doping with magnetic nanoparticles. This could open up new functionalities on controlling the injection of spin polarization via ferroelectric organic barriers doped with magnetic nanoparticles.

Summary and perspectives

We have reported the emission of circularly polarized light from an ensemble of p-doped InAs/GaAs quantum dots (QDs) embedded in a GaAs-based spin-LED. It is found that the circular polarization degree P_C can reach values up to 18% without any external applied magnetic field. The correlation between the polarization degree of the emitted light and the perpendicular magnetization of the injector layer has been established. A strong dependence on the bias voltage revealed a maximum P_C at an optimum bias of 2.5 V (corresponding to an injected current of 6 μ A) at 10K. In addition, the measurement temperature shows a strong effect on P_C with different behaviors at certain temperature values. Remarkable changes were observed before and after 60-80K. The current dependence measurements performed at 10K, 60K, and 100K have shown slight dependence of P_C on the injected current at 60K compared to a strong dependence for the two other temperatures. The interpretation of the bias and temperature dependence of P_C has been discussed in light of the competition between the spin lifetime τ_s and the charge carrier lifetime τ_r . It is believed that these findings can help for a better understanding of the collective behavior from an ensemble of p-doped InAs/GaAs QDs.

Secondly, we investigated the spin injection into a GaN based LED. Due to its weak spin-orbit interaction, its wide energy gap and its long spin relaxation time, GaN has emerged as a promising material for spintronics. Very recently, results from GaN-based visible spin LEDs and spin lasers have also been reported. However, all the

results were obtained under an external magnetic field, which is far from realistic applications. Indeed, it is necessary to realize spin LEDs that can operate with no magnetic field and at room temperature. Therefore, significant efforts have been devoted firstly to achieve a perpendicular spin injector on GaN. Fe/MgO and Co/MgO spin injectors have been investigated for their possible use as spin injectors for GaN based spintronic devices. Firstly, growth optimization experiments of MgO layers have been done at various growth temperatures on GaN templates with the help of both in-situ RHEED analysis and ex-situ AFM measurements. Then we compared both Fe/MgO and Co/MgO spin injectors. We demonstrated the occurrence of a strong PMA for the epitaxial Co (0001)/MgO (111) spin injector grown on GaN template with crystalline orientation relationship Co (0001)[11-20]//MgO (111)[10-1]//GaN (0002)[11-20]. HRTEM and HR-STEM combined with EELS have been used to investigate the interfacial structure and chemistry. A sharp and clean MgO/GaN interface was found even after 600°C annealing, while a 2-3MLs thick $Mg_xCo_yO_z$ alloy layer existed at the MgO/Co interface. It is found that a 4.6nm thick Co on MgO/GaN still exhibits large perpendicular magnetic anisotropy. Ab-initio calculations on the Co (4ML)/MgO structure shows that the MgO (111) surface can strongly enhance the PMA value by 40% compared to the pristine 4ML thick Co hcp film. Our layer-resolved and orbital-hybridization resolved anisotropy analysis further validate the origin of the PMA enhancement which is due to the interfacial hybridization of O 2*p* and Co 3*d* orbitals at the Co/MgO interface. Hereafter, we grew the Co (0001)/MgO (111) spin injector on a n-i-p type GaN LED structure and then fabricated GaN spin LED devices. However, no circularly polarized light emission was detected in preliminary polarization resolved EL measurements. This could be due either to the formation of an oxide layer at the Co/MgO interface or to an un-optimized GaN LED structure.

The last very important part is concerned with organic spintronics. Results about MFTJs based on different barriers were presented, which demonstrated new and technologically important functionalities. For a PVDF: Fe₃O₄ based barrier, the TMR sign can be reversed at a very small bias of 100mV in the initial state. After being polarized, the largest TMR can even reach -50%, but sometimes lower values close to

-5 and -6% were obtained. This random behavior could be related to the magnetization state of the Fe_3O_4 nanoparticles influenced by the PVDF polarization. The positive TMR was almost not influenced. By doping with Fe_3O_4 nanoparticles, the ferroelectric properties of MFTJ were improved with higher TER values, which still can reach 100% at room temperature. All these results showed that the spin-polarization of the organic/ferromagnetic spinterface can be manipulated not only by the ferroelectric polarization of the organic barrier, but also by doping with magnetic nanoparticles. This could also open new functionalities in controlling the injection of spin polarized carriers via the ferroelectric polarization of the tunneling barrier in semiconductor spintronics.

Here we present some perspectives. For GaAs based spin LED, we will try to experimentally determine spin relaxation time τ_s by using time-resolved EL measurement. For further investigating spin injection into GaN based LEDs, we will try to fabricate a different reversed n-i-p structures starting from a normal p-i-n structure by using the recently developed wafer bonding technique. Moreover, we will also try to fabricate spin injectors with two-dimensional materials as tunnel barriers, such as BN or mica. For the organic spintronics study, ab-initio calculations based on the density functional theory will be used to further investigate the properties of MFTJ devices with different barriers. In addition, we will also try to obtain a more homogenous distribution of Fe_3O_4 nanoparticles.

Bibliography

- ¹ D. D. Awschalom, D. Loss, N. Samarth, 2002, *Semiconductor Spintronics and Quantum Computation* (Berlin: Springer).
- ² M. Holub and P. Bhattacharya. Spin-polarized light-emitting diodes and lasers. *J. Phys. D: Appl. Phys.*, 2007, 40, R179–R203.
- ³ R. Farshchi, M. Ramsteiner, J. Herfort et al. Optical communication of spin information between light emitting diodes. *Appl. Phys. Lett.*, 2011, 98, 162508.
- ⁴ P. Asshoff, A. Merz, H. Kalt et al. A spintronic source of circularly polarized single photons. *Appl. Phys. Lett.*, 2011, 98, 112106.
- ⁵ D. Y. Kim, Potential application of spintronic light-emitting diode to binocular vision for three-dimensional display technology. *J. Korean Phys. Soc.*, 2006, 49, S505–S508.
- ⁶ V. A. Dediu, L. E. Hueso, I. Bergenti et al. Spin routes in organic semiconductors. *Nat. Mater.* 2009, 8, 707.
- ⁷ D. Sun, M. Fang, X. Xu et al. Active control of magnetoresistance of organic spin valves using ferroelectricity. *Nature communications*, 2014, 5.
- ⁸ G. Szulczewski, S. Sanvito, J. M. D. Coey, A spin of their own. *Nat. Mater.* 2009, 8, 693.
- ⁹ V. Garcia, M. Bibes, L. Bocher et al. Ferroelectric control of spin polarization. *Science* 327, 1106 (2010).
- ¹⁰ Jiang S, Wan H, Liu H, et al. High β phase content in PVDF/CoFe₂O₄ nanocomposites induced by DC magnetic fields. *Applied Physics Letters*, 2016, 109(10), 102904.
- ¹¹ W. J. Hu, D. M. Juo, L. You et al. Universal ferroelectric switching dynamics of vinylidene fluoride-trifluoroethylene copolymer films, *Sci. Rep.* 4, 4772 (2014).
- ¹² A. J. Lovinger, Ferroelectric polymers. *Science* 1983, 220, 1115–1121.
- ¹³ A. V. Bune, V. M. Fridkin, S. Ducharme et al. Two-dimensional ferroelectric films. *Nature* 1998, 391, 874–877.
- ¹⁴ S. M. Nakhmanson, M. B. Nardelli, J. Bernholc. Collective Polarization Effects in β -Polyvinylidene Fluoride and its Copolymers with Tri- And Tetrafluoroethylene. *Phys. Rev. B*, 2005, 72, 115210.
- ¹⁵ J. M. López-Encarnación, J. D. Burton, E. Y. Tsymbal et al. Organic Multiferroic Tunnel Junctions with Ferroelectric Poly(Vinylidene Fluoride) Barriers. *Nano Lett.* 2011, 11, 599–603.
- ¹⁶ J. P. Velev, J. M. López-Encarnación, J. D. Burton et al. Multiferroic Tunnel Junctions with Poly(Vinylidene Fluoride). *Phys. Rev. B* 2012, 85, 125103.
- ¹⁷ Liang. S, Yang. H, Tao. B et al. Ferroelectric control of organic/ferromagnetic spinterface. *Advanced Materials*, 2016, 28(46), 10204-10210.
- ¹⁸ Goya, G. F., Berquo, T. S., Fonseca, F. C. et al. Static and dynamic magnetic properties of spherical magnetite nanoparticles. *Journal of Applied Physics*, 2003, 94(5), 3520-3528.

Bibliography

- ¹⁹ T. T. Wang, W. P. Li, L. H. Luo et al. Ultrahigh dielectric constant composites based on the oleic acid modified ferroferric oxide nanoparticles and polyvinylidene fluoride, *Appl. Phys. Lett.* 102, 092904 (2013).
- ²⁰ X. Y. Huo, W. P. Li, J. J. Zhu et al. Composite based on Fe₃O₄ at BaTiO₃ particles and polyvinylidene fluoride with excellent dielectric properties and high energy density. *J. Phys. Chem. C* 119, 25786 (2015).
- ²¹ J. J. Zhu, W. P. Li, X. Y. Huo et al. An ultrahigh dielectric constant composite based on polyvinylidene fluoride and polyethylene glycol modified ferroferric oxide. *J. Phys. D: Appl. Phys.* 48, 355301 (2015).
- ²² Wang, H., Fu, Q., Luo, J., Zhao, D., Luo, L., & Li, W. (2017). Three-phase Fe₃O₄/MWNT/PVDF nanocomposites with high dielectric constant for embedded capacitor. *Applied Physics Letters*, 110(24), 242902.
- ²³ O. D. Jayakumar, Ehab H. Abdelhamid, Vasundhara Kotari et al. Fabrication of flexible and self-standing inorganic-organic three phase magneto-dielectric PVDF based multiferroic nanocomposite films through a small loading of graphene oxide (GO) and Fe₃O₄ nanoparticles. *Dalton Trans.*, 2015, 44, 15872–15881.
- ²⁴ T. Prabhakaran, J. Hemalatha. Ferroelectric and magnetic studies on unpoled Poly (vinylidene Fluoride)/ Fe₃O₄ magnetolectric nanocomposite structures. *Materials Chemistry and Physics* 137 (2013) 781-787.
- ²⁵ W. Li, H. Li, Y.M. Zhang. Preparation and investigation of PVDF/PMMA/TiO₂ composite film. *J. Mater. sci* 44 (2009) 2977-2984.
- ²⁶ N. F. Mott. The resistance and thermoelectric properties of the transition metals. *Proc. R. Soc. Lond. Ser. Math. Phys. Sci.* 156, 368 (1936).
- ²⁷ A. Fert and I. A. Campbell. Two-current conduction in nickel. *Phys. Rev. Lett.* 21, 1190 (1968).
- ²⁸ G. Binash et al., Enhanced magnetoresistance in layered magnetic structures with antiferromagnetic interlayer exchange, *Phys. Rev. B* 39, 4828 (1989).
- ²⁹ M. N. Baibich et al., Giant Magnetoresistance of (001)Fe/(001)Cr Magnetic Superlattices, *Phys. Rev. Lett.* 61, 2472 (1988).
- ³⁰ N. Locatelli et al., Spin-torque building blocks, *Nat. Mater.* 13, 11 (2014).
- ³¹ S. S. P. Parkin et al., Giant magnetoresistance in antiferromagnetic Co/Cu multilayers, *Appl. Phys. Lett.* 58, 2710 (1991).
- ³² B. Dieny et al, Spin-valve effect in soft ferromagnetic sandwiches, *J. Magn. Magn. Mater.* 93, 101 (1991).
- ³³ B. Dieny et al., Magnetotransport properties of magnetically soft spin-valve structures (invited), *J. Appl. Phys.* 69, 4774 (1991).
- ³⁴ J. Bass, W.P. Pratt, Current-perpendicular (CPP) magnetoresistance in magnetic metallic multilayers. *J. Magn. Magn. Mater.* 200 (1999) 274–289.
- ³⁵ W. P. Pratt, Jr., S.-F. Lee, J. M. Slaughter et al. Perpendicular giant magnetoresistances of Ag/Co multilayers. *Phys. Rev. Lett.* 1991, 66, 3060.

Bibliography

- ³⁶ L. Piraux, J. M. George, J. F. Despres et al., Giant magnetoresistance in magnetic multilayered nanowires. *Appl. Phys. Lett.* 65, 2484 (1994).
- ³⁷ A. Fert and L. Piraux. Magnetic nanowires. *J. Magn. Magn. Mater.* 200 (1999) 338–358.
- ³⁸ D. L. L. Mills and J. A. C. Bland, *Nanomagnetism: Ultrathin Films, Multilayers and Nanostructures* (Elsevier, 2006).
- ³⁹ C. Chappert, A. Fert, and F. N. Van Dau, The emergence of spin electronics in data storage, *Nat. Mater.* 6, 813 (2007).
- ⁴⁰ K. H. J. Buschow, *Handbook of Magnetic Materials* (Elsevier, 2003).
- ⁴¹ M. Julliere, Tunneling between ferromagnetic films, *Phys. Lett. A* 54, 225 (1975).
- ⁴² J. S. Moodera et al., Large magnetoresistance at room temperature in ferromagnetic thin film tunnel junctions, *Phys. Rev. Lett.* 74, 3273 (1995).
- ⁴³ J. C. Slonczewski, Conductance and exchange coupling of two ferromagnets separated by a tunneling barrier, *Phys. Rev. B* 39, 6995 (1989).
- ⁴⁴ I. Žutić, J. Fabian, and S. Das Sarma, Spintronics: fundamentals and applications, *Rev. Mod. Phys.* 76, 323 (2004).
- ⁴⁵ D. Wang et al. 70% TMR at room temperature for SDT sandwich junctions with CoFeB as free and reference layers, *IEEE Trans. Magn.* 40, 2269 (2004).
- ⁴⁶ W. H. Butler et al., Spin-dependent tunneling conductance of Fe/MgO/Fe sandwiches, *Phys. Rev. B* 63, 054416 (2001).
- ⁴⁷ J. M. MacLaren et al., Layer KKR approach to Bloch-wave transmission and reflection: application to spin-dependent tunneling, *Phys. Rev. B* 59, 5470 (1999).
- ⁴⁸ J. Mathon and A. Umerski. Theory of tunneling magnetoresistance of an epitaxial Fe/MgO/Fe (001) junction. *Phys. Rev. B* 63, 220403 (2001).
- ⁴⁹ S. Yuasa, T. Nagahama, A. Fukushima et al. Giant room-temperature magnetoresistance in single-crystal Fe/MgO/Fe magnetic tunnel junctions. *Nat. Mater.* 3, 868 (2004).
- ⁵⁰ S. S. P. Parkin, C. Kaiser, A. Panchula et al. Giant tunneling magnetoresistance at room temperature with MgO (100) tunnel barriers. *Nat. Mater.* 3, 862 (2004).
- ⁵¹ S. Ikeda, J. Hayakawa, Y. Ashizawa et al. Tunnel magnetoresistance of 604% at 300K by suppression of Ta diffusion in CoFeB/MgO/CoFeB pseudo-spin-valves annealed at high temperature. *Appl. Phys. Lett.* 93, 082508 (2008)
- ⁵² <http://www.dowaytech.com/en/1778.html>.
- ⁵³ S. Yuasa and D. D. Djayaprawira. Giant tunnel magnetoresistance in magnetic tunnel junctions with a crystalline MgO (001) barrier. *J. Phys. Appl. Phys.* 40, R337 (2007).
- ⁵⁴ H. Liu, T. Kawami, K. Moges et al. Influence of film composition in quaternary Heusler alloy Co₂(Mn,Fe)Si thin films on tunneling magnetoresistance of Co₂(Mn,Fe)Si/MgO-based magnetic tunnel junctions. *J. Phys. D: Appl. Phys.* 48 (2015) 164001 (9pp)
- ⁵⁵ Y. Sakuraba, M. Ueda, Y. Miura, K. Sato, S. Bosu, K. Saito, M. Shirai, T.J. Konno, K. Takanashi,

- Extensive study of giant magnetoresistance properties in half-metallic $\text{Co}_2(\text{Fe,Mn})\text{Si}$ -based devices. *Appl. Phys. Lett.* 101 (2012), 252408,
- ⁵⁶ S. Li, Y.K. Takahashi, T. Furubayashi et al. Enhancement of giant magnetoresistance by L21 ordering in $\text{Co}_2\text{Fe}(\text{Ge}_{0.5}\text{Ga}_{0.5})$ Heusler alloy current-perpendicular-to-plane pseudo spin valves, *Appl. Phys. Lett.* 103 (2013), 042405,
- ⁵⁷ S. Datta, B. Das. Electronic analog of the electro-optic modulator. *Appl. Phys. Lett.* 56, 665 (1990)
- ⁵⁸ M. Johnson. Spin injection in metals: the bipolar spin transistor. *J. Magn. Magn. Mater.* 156, 321 (1996).
- ⁵⁹ S. Sugahara, M. Tanaka. A spin metal-oxide-semiconductor field-effect transistor using half-metallic ferromagnet contacts for the source and drain. *Appl. Phys. Lett.* 84, 2307 (2004).
- ⁶⁰ H. C. Koo, J. Y. Kwon, J. Eom et al. Control of spin precession in a spin-injected field effect transistor. *Science* 325, 1515 (2009).
- ⁶¹ R. Fiederling, M. Keim, G. Reuser et al. Injection and detection of a spin-polarized current in a light-emitting diode. *Nature* 402, 787 (1999).
- ⁶² Y. Ohno, D. K. Young, B. Beschoten et al., Electrical spin injection in a ferromagnetic semiconductor heterostructure. *Nature* 1999, 402, 790.
- ⁶³ J. C. Slonczewski, Current-driven excitation of magnetic multilayers. *J. Magn. Magn. Mater.* 1996, 159, L1.
- ⁶⁴ E. Chen, D. Apalkov, Z. Diao et al. Advances and future prospects of spin-transfer torque random access memory. *IEEE Trans. Magn.* 2010, 46, 1873.
- ⁶⁵ C. M. Jaworski, J. Yang, S. Mack et al. Observation of the spin-Seebeck effect in a ferromagnetic semiconductor. *Nature Materials* 2010, 9, 898.
- ⁶⁶ K. C. Hall and M. E. Flatte. Performance and a spin-based insulated gate field effect transistor. *Applied Physics Letters* 2006, 88, 162503.
- ⁶⁷ S. Murakami, N. Nagaosa, S. C. Zhang. Dissipationless quantum spin current at room temperature. *Science* 2003, 301, 1348.
- ⁶⁸ S. A. Wolf. Spintronics: a spin-based electronics vision for the future. *Science* 2001, 294, 1488.
- ⁶⁹ T. Taniyama, E. Wada, M. Itoh et al. Electrical and optical spin injection in ferromagnet/semiconductor heterostructures. *NPG Asia Mater.* 2011, 3, 65–73.
- ⁷⁰ G. Schmidt, D. Ferrand, L. W. Molenkamp et al. Fundamental obstacle for electrical spin injection from a ferromagnetic metal into a diffusive semiconductor. *Physical Review B* 2000, 62, R4790.
- ⁷¹ P. R. Hammar, B. R. Bennett, M. J. Yang et al. Observation of spin injection at a ferromagnet-semiconductor interface. *Physical Review Letters* 1999, 83, 203.
- ⁷² W. Y. Lee, S. Gardelis, B. C. Choi et al. Magnetic reversal and magnetoresistance in a lateral spin-injection device. *Journal of Applied Physics* 1999, 85, 6682.
- ⁷³ A. Fert and H. Jaffrès, Conditions for efficient spin injection from a ferromagnet metal into a semiconductor. *Physical Review B* 2001, 64, 184420.

Bibliography

- ⁷⁴ E. I. Rashba. Theory of electrical spin injection: tunnel contacts as a solution of the conductivity mismatch problem. *Physical Review B* 2000, 62, R16267.
- ⁷⁵ S. F. Alvarado and P. Renaud. Observation of spin-polarized-electron tunneling from a ferromagnet into GaAs. *Physical Review Letters* 1992, 68, 1387.
- ⁷⁶ W. Van Roy, P. Van Dorpe, R. Vanheertum et al. Spin injection and detection in semiconductors. *IEEE Transactions on Electron Devices* 2007, 54, 933.
- ⁷⁷ L. Lombez, P. Renucci, P. F. Braun et al. Electrical spin injection into p-doped quantum dots through a tunnel barrier. *Applied Physics Letters* 2007, 90, 081111.
- ⁷⁸ V. F. Motsnyi, P. V. Dorpe, W. V. Roy et al. Optical investigation of electrical spin injection into semiconductors. *Physical Review B* 2003, 68, 245319.
- ⁷⁹ A. T. Hanbicki, O.M.J. Van't Erve, R. Magno et al. Analysis of the transport process providing spin injection through an Fe/AlGaAs Schottky barrier. *Applied Physics Letters* 2003, 82, 4092.
- ⁸⁰ V. F. Motsnyi, J. De. Boeck, J. Das et al. Electrical spin injection in a ferromagnet/ tunnel barrier/semiconductor heterostructure. *Applied Physics Letters* 2002, 81, 265.
- ⁸¹ X. Jiang, R. Wang, R. M. Shelby et al., Highly Spin-Polarized Room-Temperature Tunnel Injector for Semiconductor Spintronics using MgO(100). *Phys. Rev. Lett.* 94, 056601 (2005).
- ⁸² W. H. Butler, X.G. Zhang et al., Spin-dependent tunneling conductance of Fe//MgO//Fe sandwiches. *Phys. Rev. B* 63, 054416, 2001.
- ⁸³ T. Sasaki, T. Suzuki, Y. Ando et al. Local magnetoresistance in Fe/MgO/Si lateral spin valve at room temperature. *Applied Physics Letters*, 2014, 104, 052404.
- ⁸⁴ S. H. Liang, H. W. Yang, P. Renucci et al. Electrical spin injection and detection in molybdenum disulfide multilayer channel. *Nature Communications* 2017, 8, 14947.
- ⁸⁵ M. Johnson, R. H. Silsbee, Interfacial charge-spin coupling: injection and detection of spin magnetization in metals. *Phys. Rev. Lett.* 1985, 55, 1790.
- ⁸⁶ F. J. Jedema, A. T. Filip, B. J. van Wees. Electrical spin injection and accumulation at room temperature in an all-metal mesoscopic spin valve. *Nature* 2001, 410, 345.
- ⁸⁷ T. Inouchi, T. Marukame, M. Ishikawa et al. Electrical spin injection into n-GaAs channels and detection through MgO/CoFeB electrodes. *Appl. Phys. Exp.* 2009, 2, 023006.
- ⁸⁸ X. Lou, C. Adelman, S.A. Crooker et al. Electrical detection of spin transport in lateral ferromagnet-semiconductor devices. *Nature Phys.* 2007, 3, 197.
- ⁸⁹ I. Appelbaum, B. Huang, D. J. Monsma. Electronic measurement and control of spin transport in silicon. *Nature* 2007, 447, 295.
- ⁹⁰ O. M. J. van't Erve, A.T. Hanbicki, M. Holub et al. Electrical injection and detection of spin-polarized carriers in silicon in a lateral transport geometry. *Appl. Phys. Lett.* 2007, 91, 212109.
- ⁹¹ S. P. Dash, S. Sharma, R. S. Patel et al. Electrical creation of spin polarization in silicon at room temperature. *Nature* 2009, 462, 491.
- ⁹² A. Avsar, J. Y. Tan, M. Kurpas et al. Gate-tunable black phosphorus spin valve with nanosecond spin

Bibliography

- lifetimes. *Nature Physics* 2017, 13, 888–893.
- ⁹³ D. J. Monsma, J. C. Lodder, Th. J. A. Popma et al. Perpendicular hot electron spin-valve effect in a new magnetic field sensor: the spin-valve transistor. *Phys. Rev. Lett.* 1995, 74, 5260.
- ⁹⁴ W. H. Rippard, and R.A. Buhrman. Spin-dependent hot electron transport in Co/Cu thin films. *Phys. Rev. Lett.* 2000, 84, 971.
- ⁹⁵ I. Appelbaum, B. Q. Huang, D. J. Monsma. Electronic measurement and control of spin transport in silicon, *Nature* 2007, 447, 295–298.
- ⁹⁶ M. Johnson, R. H. Silsbee. Interfacial charge-spin coupling: Injection and detection of spin magnetization in metals. *Phys. Rev. Lett.* 1985, 55, 1790–1793.
- ⁹⁷ K. Ando, S. Takahashi, J. Ieda et al. Electrically tunable spin injector free from the impedance mismatch problem. *Nature Materials* 2011, 10, 655.
- ⁹⁸ E. Shikoh, K. Ando, K. Kubo et al. Spin-pump-induced spin transport in p-type Si at room temperature. *Phys. Rev. Lett.* 2013, 110, 127201.
- ⁹⁹ S. Watanabe, K. Ando, K. Kang et al. Polaron spin current transport in organic semiconductors. *Nat. Phys.* 2014, 10, 308.
- ¹⁰⁰ S. Dushenko, m. Koike, Y. Ando et al. Experimental demonstration of room temperature spin transport in n-type germanium epilayers. *Phys. Rev. Lett.* 2015, 114, 196602.
- ¹⁰¹ C. Cerqueira, J. Y. Qin, H. Dang et al. Evidence of Pure Spin-Current Generated by Spin Pumping in Interface-Localized States in Hybrid Metal–Silicon–Metal Vertical Structures, *Nano Lett.* 2019, 19, 1, 90-99.
- ¹⁰² Fabian Cadiz, Abdelhak Djeflal, Delphine Lagarde et al. Electrical Initialization of Electron and Nuclear Spins in a Single Quantum Dot at Zero Magnetic Field. *Nano Letters* 2018 18 (4), 2381-2386.
- ¹⁰³ G. Lampel. Nuclear dynamic polarization by optical electronic saturation and optical pumping in semiconductors. *Phys. Rev. Lett.* 1968, 20, 491.
- ¹⁰⁴ D. T. Pierce, F. Meier. Photoemission of spin-polarized electrons from GaAs. *Phys. Rev. B* 1976, 13, 5484.
- ¹⁰⁵ A. Djeflal, F. Cadiz, M. Stoffel. CoFeB/MgO/Ge spin photodiode operating at telecommunication wavelength with zero applied magnetic field. *Phys. Rev. Applied* 2018, 10, 044049.
- ¹⁰⁶ Yu. G. Galitsyn, D. V. Dmitriev, V.G. Mansurov et al. Critical phenomena in the β -(2×4)- α (2×4) reconstruction transition on the (001) GaAs surface. *JETP Lett.* 2005, 81, 629.
- ¹⁰⁷ A.Y. Cho. GaAs epitaxy by a molecular beam method: observations of surface structure on the (001) surface. *J. Appl. Phys.* 1971, 42, 2074.
- ¹⁰⁸ J. H. Neave, B. A. Joyce, P. J. Dobson et al. Dynamics of film growth of GaAs by MBE from RHEED observations. *Appl. Phys. A.* 1983 31(1).
- ¹⁰⁹ R. L. Fagaly. Superconducting quantum interference device instruments and applications. *Review of Scientific Instruments*, 2006, 77(10).

Bibliography

- ¹¹⁰ H. J. Zhu, M. Ramsteiner, H. Kostial et al. Room-temperature spin injection from Fe into GaAs. *Phys. Rev. Lett.* 2001, 87, 016601.
- ¹¹¹ A. T. Hanbicki, B. T. Jonker, G. Itskos et al. Efficient electrical spin injection from a magnetic metal/tunnel barrier contact into a semiconductor. *Appl. Phys. Lett.*, 2002, 80, 1240–1242.
- ¹¹² O. M. J. van't Erve, G. Kioseoglou, A. T. Hanbicki et al. Comparison of Fe/Schottky and Fe/Al₂O₃ tunnel barrier contacts for electrical spin injection into GaAs. *Appl. Phys. Lett.* 2004, 84, 4334–4336.
- ¹¹³ C. Adelmann, X. Lou, J. Strand et al. Spin injection and relaxation in ferromagnet-semiconductor heterostructures. *Phys. Rev. B: Condens. Matter Mater. Phys.* 2005, 71, 121301(R).
- ¹¹⁴ O. M. J. van't Erve, G. Kioseoglou, A. T. Hanbicki et al. Remanent electrical spin injection from Fe into AlGaAs/GaAs light emitting diodes. *Appl. Phys. Lett.* 2006, 89, 072505.
- ¹¹⁵ N. Nishizawa, H. Munekata. Efficient spin injection through a crystalline AlO_x tunnel barrier prepared by the oxidation of an ultra-thin Al epitaxial layer on GaAs. *J. Appl. Phys.* 2013, 114, 033507.
- ¹¹⁶ B. L. Liu, M. S n s, S. Couderc et al. Optical and electrical spin injection in spin-LED. *Phys. E*, 2003, 17, 358–360.
- ¹¹⁷ X. Jiang, R. Wang, R. M. Shelby et al. Highly spin-polarized room-temperature tunnel injector for semiconductor spintronics using MgO (100). *Phys. Rev. Lett.* 2005, 94, 056601.
- ¹¹⁸ Y. Lu, V. G. Truong, P. Renucci et al. MgO thickness dependence of spin injection efficiency in spin-light emitting diodes. *Appl. Phys. Lett.* 2008, 93, 152102.
- ¹¹⁹ V. G. Truong, P. H. Binh, P. Renucci et al. High speed pulsed electrical spin injection in spin-light emitting diode. *Appl. Phys. Lett.*, 2009, 94, 141109.
- ¹²⁰ M. Ramsteiner, H. Y. Hao, A. Kawaharazuka et al., Electrical spin injection from ferromagnetic MnAs metal layers into GaAs *Phys. Rev. B* 66, 081304(R),2002.
- ¹²¹ X. Y. Dong, C. Adelmann, J. Q. Xie et al., Spin injection from the Heusler alloy Co₂MnGe into Al_{0.1}Ga_{0.9}As/GaAs heterostructures. *Appl. Phys. Lett.* 86, 102107 (2005).
- ¹²² M. Ramsteiner, O. Brandt, T. Flissikowski et al., Co₂FeSi/GaAs/(Al,Ga)As spin light-emitting diodes: Competition between spin injection and ultrafast spin alignment. *Phys. Rev. B* 78, 121303(R), 2008.
- ¹²³ C. H. Li, G. Kioseoglou, A. T. Hanbicki et al., Electrical spin injection into the InAs/GaAsInAs/GaAs wetting layer. *Appl. Phys. Lett.* 91, 262504 (2007).
- ¹²⁴ V. F. Motsnyi, P. Van Dorpe, W. Van Roy et al., Optical investigation of electrical spin injection into semiconductors. *Phys. Rev. B* 68, 245319, 2003.
- ¹²⁵ X. Jiang, R. Wang, S. van Dijken et al., Optical Detection of Hot-Electron Spin Injection into GaAs from a Magnetic Tunnel Transistor Source. *Phys. Rev. Lett.* 90, 256603, 2003.
- ¹²⁶ C. H. Li, G. Kioseoglou, O. M. J. van 't Erve et al., Electrical spin pumping of quantum dots at room temperature. *Appl. Phys. Lett.* 86, 132503 (2005).
- ¹²⁷ L. Lombez, P. F. Braun, P. Renucci et al., Electrical spin injection in InAs/GaAs p-doped quantum dots through Co/Al₂O₃/GaAs tunnel barrier. *phys. stat. sol. (c)* 4, No. 2, 567– 569 (2007).

Bibliography

- ¹²⁸ M. I. Dyakonov, V. L. Perel. *Optical Orientation* ed F Meier and BP Zakharchenya. Elsevier Science Publishers B. V., Amsterdam, 1984, 8, 22–24.
- ¹²⁹ M. I. Dyakonov. *Spin Physics in Semiconductors*, Springer, Berlin, 2008, 12–13.
- ¹³⁰ N. C. Gerhardt, S. Hövel, C. Brenner et al. Electron spin injection into GaAs from ferromagnetic contacts in remanence. *Appl. Phys. Lett.* 2005, 87, 032502.
- ¹³¹ S. Hövel, N. C. Gerhardt, M. R. Hofmann et al. Room temperature electrical spin injection in remanence. *Appl. Phys. Lett.* 2008, 93, 021117.
- ¹³² L. Grenet, M. Jamet, P. Née et al. Spin injection in silicon at zero magnetic field. *Appl. Phys. Lett.* 2009, 94, 032502.
- ¹³³ J. Zarpellon, H. Jaffrès, J. Frougier et al. Spin injection at remanence into III-V spin light-emitting diodes using (Co/Pt) ferromagnetic injectors. *Phys. Rev. B: Condens. Matter Mater. Phys.*, 2012, 86, 205314.
- ¹³⁴ A. Sinsarp, T. Manago, F. Takano et al. Electrical spin injection in perpendicular magnetized FePt/MgO/GaAs heterostructures at room temperature. *Supercond. Novel. Magn.* 2007, 20, 405–408.
- ¹³⁵ C. Adelman, J. L. Hilton, B. D. Schultz et al. Spin injection from perpendicular magnetized ferromagnetic δ -MnGa into (Al, Ga)As heterostructures. *Appl. Phys. Lett.* 2006, 89, 112511.
- ¹³⁶ S. H. Liang, T. T. Zhang, P. Barate et al. Large and robust electrical spin injection into GaAs at zero magnetic field using an ultrathin CoFeB/MgO injector. *Phys. Rev. B: Condens. Matter Mater. Phys.* 2014, 90, 085310.
- ¹³⁷ P. Barate, S. H. Liang, T. T. Zhang et al. Bias dependence of the electrical spin injection into GaAs from CoFeB/MgO injectors with different MgO growth processes. *Phys. Rev. Appl.* 2017, 8, 054027.
- ¹³⁸ S. Ikeda, K. Miura, H. Yamamoto et al. A perpendicular-anisotropy CoFeB/MgO magnetic tunnel junction. *Nat. Mater.* 2010, 9, 721–724.
- ¹³⁹ H. X. Yang, M. Chshiev, B. Dieny et al. First-principles investigation of the very large perpendicular magnetic anisotropy at Fe/MgO and Co/MgO interfaces. *Phys. Rev. B* 84, 054401 (2011).
- ¹⁴⁰ B. S. Tao, P. Barate, J. Frougier et al. Electrical spin injection into GaAs based light emitting diodes using perpendicular magnetic tunnel junction-type spin injector. *Appl. Phys. Lett.* 2016, 108, 152404.
- ¹⁴¹ F. Cadiz, A. Djéffal, D. Lagrade et al. Electrical initialization of electron and nuclear spins in a single quantum dot at zero magnetic field. *Nano Lett.* 2018, 18, 2381–2386.
- ¹⁴² W. G. Wang, S. Hageman, M. Li et al. Rapid thermal annealing study of magnetoresistance and perpendicular anisotropy in magnetic tunnel junctions based on MgO and CoFeB. *Appl. Phys. Lett.* 2011, 99, 102502.
- ¹⁴³ N. Miyakawa, D. C. Worledge and K. Kita. Impact of Ta diffusion on the perpendicular magnetic anisotropy of Ta/CoFeB/MgO. *IEEE Magn. Lett.* 2013, 4, 1000104.
- ¹⁴⁴ B. Tao, P. Barate, X. Devaux et al. Atomic-scale understanding of high thermal stability of the Mo/CoFeB/MgO spin injector for spin-injection in remanence. *Nanoscale*, 2018, 10, 10213.

Bibliography

- ¹⁴⁵ R. H. Horng, P. Han, D. S. Wu. Phosphor-free white light from InGaN blue and green light-emitting diode chips covered with semiconductor-conversion AlGaInP epilayer. *IEEE Photonics Technol. Lett.* 2008, 20, 1139.
- ¹⁴⁶ W. Lee, M. H. Kim, D. Zhu et al. Growth and characteristics of GaInN/GaN multiple quantum well light-emitting diodes. *J. Appl. Phys.* 2010, 107, 063102.
- ¹⁴⁷ H. J. Chang, T. W. Chen, J. W. Chen et al. Current and strain-induced spin polarization in InGaN/GaN superlattices. *Phys. Rev. Lett.* 2007, 98, 136403.
- ¹⁴⁸ J. H. Lee, I. H. Choi, S. Shin et al. Room-temperature ferromagnetism of Cu-implanted GaN. *Appl. Phys. Lett.* 2007, 90, 032504.
- ¹⁴⁹ S. Nakamura, M. Senoh, S. Nagahama et al. InGaN multi-quantum-well-structure laser diodes with cleaved mirror cavity facets. *Jpn. J. Appl. Phys.* 1996, 35, L217.
- ¹⁵⁰ C. Gao, O. Brandt, H. P. Schonherr et al. Thermal stability of epitaxial Fe films on GaN (0001). *Appl. Phys. Lett.* 2009, 95, 111906.
- ¹⁵¹ O. Ambacher, Growth and applications of group III-nitrides. *J. Phys. D: Appl. Phys.* 1998, 31, 2653.
- ¹⁵² B. Beschoten, E. Johnston-Halperin, D. K. Young et al. Spin coherence and dephasing in GaN. *Phys. Rev. B* 2001, 63, 121202.
- ¹⁵³ S. Krishnamurthy, M. Van Schilfgarde, N. Newman. Spin lifetimes of electrons injected into GaAs and GaN. *Appl. Phys. Lett.* 2003, 83, 1761.
- ¹⁵⁴ I. A. Buyanova, M. Izadifard, W. M. Chen et al. On the origin of spin loss in GaMnN/InGaN light-emitting diodes. *Appl. Phys. Lett.* 2004, 84 2599–601.
- ¹⁵⁵ I. A. Buyanova, M. Izadifard, L. Storasta et al. Optical and electrical characterization of (Ga, Mn)N/InGaN multiquantum well light-emitting diodes. *Journal of Electronic Materials*, 2004, 33, 5, 467-471.
- ¹⁵⁶ I. A. Buyanova, J. P. Bergman, W. M. Chen et al. Optical study of spin injection dynamics in InGaN/GaN quantum wells with GaMnN injection layers. *J. Vac. Sci. Technol. B*, 2004, 22, 6, 2668.
- ¹⁵⁷ W. M. Chen, I. A. Buyanova, K. Nishibayashi et al. Efficient spin relaxation in InGaN/GaN and InGaN/GaMnN quantum wells: An obstacle to spin detection. *Appl. Phys. Lett.* 2005, 87, 192107.
- ¹⁵⁸ F. V. Kyrychenko, C. J. Stanton, C. R. Abernathy et al. Investigation of a GaMnN/GaN/InGaN structure for spin LED. *AIP Conference Proceedings*, 2005, 772, 1319.
- ¹⁵⁹ I. A. Buyanova, W. M. Chen, M. P. Ivill et al. Optical characterization of ZnMnO-based dilute magnetic semiconductor structures. *J. Vac. Sci. Technol. B*, 2006, 24 259–62.
- ¹⁶⁰ L. C. Chen, C. H. Tien, Y. M. Luo et al. Photoluminescence and spin relaxation of MnZnO/GaN-based light-emitting diodes. *Thin Solid Films*, 2011, 519, 2516–2519.
- ¹⁶¹ S. Jahangir, F. Dogan, H. Kum et al. Spin diffusion in bulk GaN measured with MnAs spin injector. *Phys. Rev. B* 2012, 86, 035315.
- ¹⁶² A. Yanase, N. Hamada, Electronic structure in high temperature phase of Fe₃O₄. *J. Phys. Soc. Jpn.* 1999, 68, 1607.

Bibliography

- ¹⁶³ J. Tang, M. Myers, K. A. Bosnick et al. Magnetite Fe₃O₄ nanocrystals: spectroscopic observation of aqueous oxidation kinetics. *J. Phys. Chem. B* 2003, 107, 7501.
- ¹⁶⁴ M. Fonin, R. Pentcheva, Y. S. Dedkov et al. Surface electronic structure of the Fe₃O₄ (100): evidence of a half-metal to metal transition. *Phys. Rev. B* 2005, 72, 104436.
- ¹⁶⁵ T. Kouno, K. Kishino, M. Sakai. Lasing action on whispering gallery mode of self-organized GaN hexagonal microdisk crystal fabricated by RF-plasma- assisted molecular beam epitaxy. *IEEE J. Sel. Top. Quant. Electron* 2011, 47, 1565–1570.
- ¹⁶⁶ Y. T. Evgeny, I. Zutic. *Handbook of Spin Transport and Magnetism* (CRC Press, 2011).
- ¹⁶⁷ G. D. Chen, M. Smith, J. Y. Lin et al. Fundamental optical transitions in GaN. *Appl. Phys. Lett.* 1996, 68, 20, 2784–2786.
- ¹⁶⁸ I. A. Buyanova, M. Izadifard, W. M. Chen et al. spin injection and spin loss in GaMnN/InGaN light-emitting diodes. *Proc. AIP Conf.* 2005, 772, 1399–1400.
- ¹⁶⁹ M. H. Ham, S. Yoon, Y. Park et al. Electrical spin injection from room-temperature ferromagnetic (Ga, Mn)N in nitride-based spin-polarized light-emitting diodes. *J. Phys., Condens. Matter*, 2006, 18, 32, 7703–7708.
- ¹⁷⁰ D. Banerjee, R. Adari, S. Sankaranarayan et al. Electrical spin injection using GaCrN in a GaN based spin light emitting diode. *Appl. Phys. Lett.* 2013, 103, 24, 242408-1–242408-4.
- ¹⁷¹ J. Y. Chen, C. Y. Ho, M. L. Lu et al. Efficient spin-light emitting diodes based on InGaN/GaN quantum disks at room temperature: A new self- polarized paradigm. *Nano Lett.* 2014, 14, 6, 3130–3137.
- ¹⁷² A. Bhattacharya, Z. Baten, T. Frost et al. Room temperature GaN-based edge-emitting spin-polarized light emitting diode. *IEEE Photonics Technology Letters*, 2017, 29, 3, 338-341.
- ¹⁷³ A. Bhattacharya, M. Z. Baten, I. Iorsh et al. Room-temperature spin polariton diode laser. *Phys. Rev. Lett.* 2017, 119, 067701.
- ¹⁷⁴ J. Y. Chen, T. M. Wong, C. W. Chang et al. Self-polarized spin-nanolasers. *Nature Nanotechnology*, 2014, 9, 845–850.
- ¹⁷⁵ H. X. Yang, A. D. Vu, A. Hallal et al. Anatomy and giant enhancement of the perpendicular magnetic anisotropy of cobalt-graphene heterostructures. *Nano Lett.*, 2016, 16(1), 145-151.
- ¹⁷⁶ S. Yuasa, A. Fukushima, H. Kubota et al. Giant tunneling magnetoresistance up to 410% at room temperature in fully epitaxial Co/MgO/Co magnetic tunnel junctions with bcc Co(001) electrodes. *Appl. Phys. Lett.* 2006, 89, 042505.
- ¹⁷⁷ H. Ohmori, T. Hatori, S. Nakagawa. Fabrication of MgO barrier for a magnetic tunnel junction in as-deposited state using amorphous RE-TM alloy. *J. Magn. Magn. Mater.* 2008, 320, 22, 2963-2966.
- ¹⁷⁸ R. Matsumoto, S. Nishioka, M. Mizuguchi et al. Dependence on annealing temperatures of tunneling spectra in high-resistance CoFeB/MgO/CoFeB magnetic tunnel junctions. *Solid State Comm.* 2007, 143, 574–578.
- ¹⁷⁹ X. G. Zhang, W. H. Butler. Large magnetoresistance in bcc Co/MgO/Co and FeCo/MgO/FeCo tunnel junctions. *Phys. Rev. B*, 2004, 70, 172407.

Bibliography

- ¹⁸⁰ S. Yuasa, A. Fukushima, H. Kubota et al. Giant tunneling magnetoresistance up to 410% at room temperature in fully epitaxial Co/MgO/Co magnetic tunnel junctions with bcc Co (001) electrodes. *Appl. Phys. Lett.* 2006, 89, 042505.
- ¹⁸¹ H. S. Craft, J. F. Ihlefeld, M. D. Losego et al. MgO epitaxy on GaN (0002) surfaces by molecular beam epitaxy. *Appl. Phys. Lett.* 2006, 88, 212906.
- ¹⁸² J. O. Hauch, M. Fonin, M. Fraune et al. Fully epitaxial Fe (110)/MgO (111)/Fe (110) magnetic tunnel junctions: Growth, transport, and spin filtering properties. *Appl. Phys. Lett.* 2008, 93, 083512.
- ¹⁸³ V. K. Lazarov, S. H. Cheung, S. A. Chambers et al. The structure and magnetic properties of Fe thin films grown on (1×1) and ($\sqrt{3} \times \sqrt{3}$) R30° reconstructed MgO (111). *Microsc. Microanal.* 2007, 13, 1044.
- ¹⁸⁴ N. Khalid, J. Y. Kim, A. Ionescu et al. Barnes. Structure and magnetic properties of an epitaxial Fe(110)/MgO(111)/GaN(0001) heterostructure. *J. Appl. Phys.* 2018, 123, 103901.
- ¹⁸⁵ P. Potapov, P. Longo, and E. Okunishi., "Enhancement of noisy edx hrstem spectrum-images by combination of filtering and PCA." *Micron*, 2017, 96, 29-37.
- ¹⁸⁶ Y. Nukaga, M. Ohtake, M. Futamoto, F. Kirino, N. Fujita and N. Inaba, *IEEE Transactions on Magnetism*, 2009, 45, 2519-2522.
- ¹⁸⁷ S. H. Liang, Z. W. Yu, X. Devaux, A. Ferri, W. C. Huang, R. Desfeux, X. G. Li, S. Migot, D. Chaudhuri, H. X. Yang, M. Chshiev, C. P. Yang, B. Zhou, J. H. Fang, S. Mangin and Y. Lu. "Quenching of Spin Polarization Switching in Organic Multiferroic Tunnel Junctions by Ferroelectric "Ailing-Channel" in Organic Barrier." *ACS Appl. Mater. Interfaces*, 2018, 10 (36), 30614–30622.
- ¹⁸⁸ S. Ikeda, K. Miura, H. Yamamoto, K. Mizunuma, H. D. Gan, M. Endo, S. Kanai, J. Hayakawa, F. Matsukura and H. Ohno, *Nat. Mater.*, 2010, 9, 721–724.
- ¹⁸⁹ S. H. Liang, T. T. Zhang, P. Barate, J. Frougier, M. Vidal, P. Renucci, B. Xu, H. Jaffres, J-M. George, X. Devaux, M. Hehn, X. Marie, S. Mangin, H. X. Yang, A. Hallal, M. Chshiev, T. Amand, H. F. Liu, D. P. Liu, X. F. Han, Z. G. Wang and Y. Lu, *Phys. Rev. B: Condens. Matter Mater. Phys.*, 2014, 90, 085310.
- ¹⁹⁰ H. X. Yang, A. D. Vu, A. Hallal, N. Rougemaille, J. Coraux, G. Chen, A. K. Schmid, and M. Chshiev, *Nano Lett.*, 2016, 16 (1), 145–151.
- ¹⁹¹ O. Benamara, E. Snoeck, T. Blon and M. Respaud, *Journal of Crystal Growth* 312 (2010) 1636–1644.
- ¹⁹² G. Kresse and J. Hafner. Ab initio molecular dynamics for liquid metals, *Phys. Rev. B*, 1993, 47, 558(R).
- ¹⁹³ G. Kresse and J. Furthmüller, Efficiency of ab-initio total energy calculations for metals and semiconductors using a plane-wave basis set. *Comput. Mater. Sci.* 1996, 6, 15.
- ¹⁹⁴ G. Kresse and J. Furthmüller, Efficient iterative schemes for ab initio total-energy calculations using a plane-wave basis set. *Phys. Rev. B*, 1996, 54, 11169.
- ¹⁹⁵ J. P. Perdew, K. Burke, and M. Ernzerhof, Generalized Gradient Approximation Made Simple. *Phys. Rev. Lett.* 1996, 77, 3865.
- ¹⁹⁶ B. Dieny and M. Chshiev, *Rev. Mod. Phys.*, 2017, 89, 025008.

Bibliography

- ¹⁹⁷ D.S. Wang, R.Q. Wu, and A.J. Freeman, *Phys. Rev. B*, 1993, 47, 14932.
- ¹⁹⁸ S. G. Krishnan, M. V. Reddy, M. Harilal, B. Vidyadharan, I. I. Misnon, M. Hasbi, A. Rahim, J. Ismail and R. Jose, *Electrochimica Acta*, 2015, 161, 10, 312-321.
- ¹⁹⁹ K. Refson, R. A. Wogelius, D. G. Fraser, M. C. Payne, M. H. Lee, and V. Milman, *Phys. Rev. B*, 1995, 52, 10823.
- ²⁰⁰ F. J. A. den Broeder, W. Hoving and P. J. H. Bloemen, *Journal of Magnetism and magnetic materials*, 1991, 93, 562-570.
- ²⁰¹ M. T. Johnson, P. J. H. Bloemen, F. J. A. den Broeder and J. J. de Vries, *Rep. Prog. Phys.* 1996, 59, 1409-1458.
- ²⁰² D. J. H. Lambert, D. E. Lin, R. D. Dupuis. Simulation of the electrical characteristics of AlGaIn/GaN heterojunction bipolar transistors. *Solid-State Electronics*, 2000, 44: 253-257.
- ²⁰³ M. Farahmand, C. Garetto, E. Bellotti et al. Monte Carlo simulation of electron transport in the III-nitride wurtzite phase materials system: binaries and ternaries. *IEEE Transactions on Electron Devices*, 2001, 48, 3.
- ²⁰⁴ M. Jullière. Tunneling between ferromagnetic films. *Phys. Lett. A*, 1975, 54, 225.
- ²⁰⁵ J. M. Slaughter. Materials for magnetoresistive random access memory. *Annu. Rev. Mater. Res.* 2009, 39: 277–296.
- ²⁰⁶ V. A. Dediu, L. E. Hueso, I. Bergenti et al. Spin routes in organic semiconductors. *Nat. Mater.* 2009, 8, 707.
- ²⁰⁷ D. Sun, M. Fang, X. S. Xu et al. Active control of magnetoresistance of organic spin valves using ferroelectricity. *Nature communications*, 2014, 5, 4396.
- ²⁰⁸ E. Y. Tsybal, A. Gruverman, V. Garcia et al. Ferroelectric and multiferroic tunnel junctions. *MRS Bull.* 2012, 37, 2: 138-143.
- ²⁰⁹ V. Garcia, M. Bibes, L. Bocher et al. Ferroelectric control of spin polarization. *Science*, 2010, 327, 5969: 1106-1110.
- ²¹⁰ D. Pantel, S. Goetze, D Hesse et al. Reversible electrical switching of spin polarization in multiferroic tunnel junctions. *Nat. Mater.* 2012, 11, 289.
- ²¹¹ S. Jiang, H. Wan, H. Liu et al. High β phase content in PVDF/CoFe₂O₄ nanocomposites induced by DC magnetic fields. *Appl. Phys. Lett.* 2016, 109(10), 102904.
- ²¹² B. B. Tian, J. L. Wang, S. Fusil et al. Tunnel electroresistance through organic ferroelectrics. *Nat. Commun.* 2016, 7, 11502.
- ²¹³ V. Garcia, M. Bibes, Ferroelectric tunnel junctions for information storage and processing. *Nat. Commun.* 2014, 5, 4289.
- ²¹⁴ M. Gajek, M. Bibes, S. Fusil et al. Tunnel junctions with multiferroic barriers. *Nat. Mat.* 2007, 6, 296.
- ²¹⁵ G. F. Goya, T. S. Berquo, F. C. Fonseca et al. Static and dynamic magnetic properties of spherical magnetite nanoparticles. *Journal of Applied Physics*, 2003, 94(5): 3520-3528.
- ²¹⁶ M. Probst, R. Haight. Diffusion of metals into organic films. *Appl. Phys. Lett.* 1997, 70, 1420.

Bibliography

- ²¹⁷ Z. H. Xiong, D. Wu, Z. V. Vardeny et al. Giant magnetoresistance in organic spin-valves. *Nature* 2004, 427, 821.
- ²¹⁸ J. H. Park, E. Vescovo, H. J. Kim et al. Magnetic properties at surface boundary of a half-metallic ferromagnet. *Phys. Rev. Lett.* 1998, 81, 1953.
- ²¹⁹ T. Furukawa. Ferroelectric properties of vinylidene fluoride copolymers. *Phase transitions* 1989, 18, 143.
- ²²⁰ X. Su, F. Zuo, J. A. Schlueter et al. Structural disorder and its effect on the superconducting transition temperature in the organic superconductor k -(BEDT-TTF)₂Cu[N(CN)₂]Br. *Phys. Rev. B* 1998, 57, R14056.
- ²²¹ S. Jesse, B. J. Rodriguez, S. Choudhury et al. Direct imaging of the spatial and energy distribution of nucleation centres in ferroelectric materials. *Nat. Mat.* 2008, 7, 209.
- ²²² J. H. Park, E. Vescovo, H. J. Kim et al. Direct evidence for a half-metallic ferromagnet. *Nature* 1998, 392, 794.
- ²²³ E. Liu, Y. Yin, L. Sun et al. Increasing spin polarization in Fe₃O₄ films by engineering antiphase boundary densities. *Appl. Phys. Lett.* 2017, 110, 142402.